Cross-Section Measurements of Star Configurations in Neutron-Deuteron Breakup at 16.0 MeV

by

Alexander S. Crowell

Department of Physics
Duke University

Date

Approved:

Calvin R. Howell, Supervisor

Robert P. Behringer

Mark C. Kruse

Roxanne P. Springer

Werner Tornow

Dissertation submitted in partial fulfillment of
the requirements for the degree of
Doctor of Philosophy in the Department of
Physics in the Graduate School
of Duke University

2001

Abstract

(Physics – TUNL)

Cross-Section Measurements of Star Configurations in Neutron-Deuteron Breakup at 16.0 MeV

by

Alexander S. Crowell

Department of Physics
Duke University

Date

Approved:

Calvin R. Howell, Supervisor

Robert P. Behringer

Mark C. Kruse

Roxanne P. Springer

Werner Tornow

An abstract of a dissertation submitted in partial
fulfillment of the requirements for the degree
of Doctor of Philosophy in the Department
of Physics in the Graduate School
of Duke University

2001

Abstract

Cross-Section Measurements of Star Configurations in Neutron-Deuteron Breakup at 16.0 MeV

Modern nonrelativistic calculations using effective nucleon-nucleon (NN) potentials have proven very successful in predicting many observables in the three-nucleon (3N) system. This success has been tempered however by some significant discrepancies between theoretical predictions and the available experimental data. Three of the most notable are the triton binding energy defect, the vector analyzing power puzzle in nucleon-deuteron elastic scattering, and the star anomaly in neutron-deuteron (nd) breakup. This last phenomenon is the motivation for the work described in this dissertation.

The star condition is defined as the exit configuration in the center-of-mass system where the momentum vectors of the three outgoing particles are of equal magnitude and separated by 120°. The plane containing these three vectors can be perpendicular to the incident neutron beam (the "space star"), coincident with the incident beam (the "coplanar star"), or somewhere between these two extremes (an "intermediate star"). Previous measurements of the space-star cross section at

10.3 MeV [Ste89, Geb93] and 13.0 MeV [Str89, Set96] give values significantly larger than rigorous calculations (more than 25% higher at 13.0 MeV). The most recent measurement of the coplanar-star cross section at 13.0 MeV [Set96] was in relatively good agreement with theory. Why does rotating the star plane by 90° create such a large discrepancy in one configuration but not another?

In the quest to answer this question, a spatial-orientation study of the star cross section was undertaken at the Triangle Universities Nuclear Laboratory (TUNL) at an incident neutron energy of 16.0 MeV. Cross section measurements of the space-, coplanar-, and an intermediate-star configuration were made using a shielded neutron source and active deuteron target. All three emitted particles were detected to kinematically overdetermine the breakup reaction. Simultaneous measurement of *nd* elastic scattering provided the absolute normalization for the cross sections.

No attempt was made to unfold finite-geometry and energy-resolution effects from the data. Instead theoretical calculations were smeared over the finite geometry and resolution of the experiment with a Monte-Carlo simulation. Comparison of the space-star data to finite-geometry calculations shows the data to be three standard deviations higher than theory, confirming the existence of the star anomaly at 16.0 MeV. Cross sections for the coplanar star are also modestly higher than theory, while the intermediate-star data are in agreement with calculations within statistical uncertainties. The presence of a resonance in the 3N continuum could help explain the star anomaly and other outstanding questions in *nd* breakup. Future measurements in kinematically incomplete *nd* breakup should help to confirm or refute the existence of such a resonant state.

Acknowledgements

Thanking everyone who had a role in my thesis work is quite a task. I feel sort of like a producer at the Academy Awards who has less than a minute to recognize all the people who made his movie a success. In the face of such a daunting challenge, I'll give it my best shot and hope that the folks I have missed will forgive me.

First and foremost I would like to thank my advisor, Dr. Calvin Howell. We have been working together on various projects ever since I enrolled at Duke over eight years ago. I have grown to appreciate Calvin's enthusiasm as well as his determination to fully understand things (even when it meant staying at the lab well past my bedtime). I am also impressed that he treated me not just as his graduate student, but as a colleague.

Secondly, I'd like to recognize the contributions of my colleagues in the Neutron Time-Of-Flight (NTOF) group at TUNL. Dr. Werner Tornow was an invaluable source of knowledge for few-body nuclear physics and spent many long hours making changes to the Monte-Carlo simulation code in spite of his numerous duties as Director of the lab. I'd also like to thank him for having faith in me to maintain the TUNL computer network this past year. Dr. Richard Walter taught me everything I know about tuning beam and the physics behind how the accelerator works. There have been many graduate students and post-docs in the group who have helped me at one time or another: Dinko González, Frank Salinas, Chris Roper, Steve Churchwell, and Qiankun Chen. I especially want to thank Liz Neidel for being a good friend and someone I could vent with. And last but not least I thank my officemate Rob Macri for helping me with the data analysis and making sure life didn't get too

serious around the office.

NTOF is very fortunate to have the help of many folks outside of Duke. Drs. Caesar Jackson, Ron Pedroni, and Ben Crowe graciously took shifts on my runs and generally made my life easier. My collaborators from the China Institute of Atomic Energy, H. Tang and Z. Zhou, were a great help and also opened my eyes to a culture I knew little about. Finally, I would be remiss if I didn't acknowledge the tremendous contributions from our colleague, Dr. Henryk Witała, who generated the nuclear amplitudes that were used in all our theoretical calculations.

None of the work at TUNL would be possible without our support and technical staff. Thanks to Paul Carter, Richard O'Quinn, John Dunham, Sidney Edwards, and Pat Mulkey for keeping the accelerator and electronics working so that I could take my data. My friendship with each of them is a source of great joy, but I must single out my 7 AM conversations with Richard as I finished the graveyard shift as some of my most memorable moments in graduate school.

One of the main reasons I chose to come to Duke for graduate school was that all the graduate students seemed so happy and were a lot of fun to be around. I soon discovered I had made a good choice as the camaraderie with my fellow classmates and those before and after us was truly what kept us going despite grueling homework assignments, qualifying exams, and the other rigors of graduate life. Diversions such as basketball, bridge, golf, and movies brought us closer together and also helped us maintain our sanity. I can't name everyone, but I want to offer a special thanks to Greg, Josh, Eric (Wulf), Eric (Tuba), Mari, Ben, Shane, Nate, Abby, Bob, Bill, Linda, and Jeff for making my time here so enjoyable. (Extra special thanks goes to our "Duke Mom", Donna Ruger, for taking care of each one of us as if we were her

own children.)

I certainly couldn't have gotten this far without the unconditional love and support of my family. I thank my brother for always keeping me on my toes and making sure that I didn't let success go to my head. I thank my mom and dad for instilling in me the belief that I could do anything I set my mind to and for being so very patient all these years. I'd also like to thank my "new" family, the Bachs, for all their encouragement and interest in my studies. Additionally, there are three other very special people who influenced my life in more ways than I can describe: my late grandparents, Margaret Richter and Ernest and Beulah Crowell. Both my grandmothers made sure I always knew how proud they were of me and how much they loved me. My grandfather was the first in his family to go to college and was given the nickname "Doc" because of it. He was so pleased when I would show him my report cards and when I decided to go to Wake Forest University for college. Because my education was so important to him, I proudly dedicate this dissertation to his memory and will think of him fondly any time someone calls me "Dr. Crowell".

The stage crew is telling me my time is up, so I had better finish. Of course I saved the best for last. My final tribute is to my loving wife, Lauren. She only experienced my first years of graduate school vicariously through e-mails, phone calls, and visits. But she was always there the last five and a half years right by my side. She has been there to comfort, encourage, listen, and support in every way she could. I can't imagine how I would ever have finished without her. Thank you so much, sweetheart.

Contents

List of Figures

List of Tables

Chapter 1

Introduction

This dissertation describes the measurement of neutron-induced deuteron breakup cross sections at 16.0 MeV for three kinematic configurations where the momentum vectors of the three outgoing particles are separated by 120° in the center-of-mass system. Measurement of the cross sections for these *star* configurations was motivated by many factors. First, the neutron-deuteron (nd) breakup data taken in previous experiments for the space-star configuration at 10.3 and 13.0 MeV show significant discrepancies with theoretical predictions [Ste89, Str89, Geb93, Set96], while the most recent data for the coplanar-star configuration at 13.0 MeV was in relatively good agreement [Set96]. Secondly, prior to this measurement, no nd breakup data existed at 16.0 MeV. Finally, because the space-star cross-section has been shown to be insensitive to the choice of nucleon-nucleon potential used for calculations, it should be easier to discern the effects of three-nucleon forces in this system than in other configurations [Klo73, Wit88].

In Section 1.1 of this chapter, a background of three-body effects in other fields

of physics will be given. Evidence of three-body effects in nuclear systems will also be presented. The motivations for studying the three-nucleon (3N) system will be discussed in more detail in Section 1.2. Finally, in Section 1.3 a description of the general techniques used in this measurement will be outlined.

1.1 Background

Ever since the discovery that the atomic nucleus was composed of individual particles known as protons and neutrons, nuclear physicists have been interested in understanding the *strong* interaction that binds these constituents together. The earliest systems studied were naturally those of one and two nucleons. As part of the description of the three-nucleon system, theorists proposed that a force dependent simultaneously on the quantum numbers and coordinates of all three nucleons but not reducible into two-body pair-wise forces might be needed. The concepts for such a force have their origins as early as 1939 [Pri39]. Searches for evidence of these so-called *three-nucleon forces* began in earnest more than 30 years ago when advances in computational techniques allowed calculations of observables in the 3N system to be performed and compared to experimental data.

Three-nucleon force (3NF) effects originate mostly as a result of neglecting the internal degrees of freedom of the nuclear constituents (that is, details of the quark substructure of neutrons and protons are ignored by the effective theories utilized in the calculation of experimental observables). Chiral perturbation theory, a low-energy effective field theory, shows tremendous promise for providing a detailed description of 3N dynamics using the appropriate degrees of freedom and having the symmetries of the more fundamental theory, quantum chromodynamics(QCD). In

the meantime, *ad hoc* effective potential models based on meson-exchange theory are used. The predictions of observables in the two-nucleon (2N) system by these models are excellent, but there are notable failures in predictions for the 3N system.

Efforts to describe physical systems with effective models that ignore some internal degrees of freedom are not unique to nuclear physics. Researchers in all fields of physics strive to keep models as simple as possible and hope to reproduce the major properties of a particular system with acceptable precision. Most models are based on the simplest structures in the system: the interaction of two bodies (planets, molecules, atoms, nucleons) with no internal degrees of freedom. The extension of these effective models to the three-body system inevitably leads to three-body effects in some configurations where the internal degrees of freedom are important. In this section, examples of three-body effects in celestial mechanics, atomic and molecular systems, and nuclear systems will be given. As will be shown in these examples, the length scale for three-body effects extends from thousands of kilometers down to just a few femtometers and these effects also encompass all the fundamental forces of nature.

1.1.1 Celestial Mechanics

Perhaps the most famous (or *infamous*) example of the three-body problem in physics comes from the realm of celestial mechanics. The Earth-Moon-Sun system (and also the somewhat simpler Earth-Moon-satellite system) has garnered the attention of many reknown physicists and mathematicians during the last three or four centuries. None other than Isaac Newton was reputed to have told to the astronomer Edmond Halley [Dan88] that trying to calculate the motion of the Moon

> ...made his head ache and kept him awake so often that he would

think of it no more.

Whole books have been devoted solely to this subject [Mar90] and numerous advances in the techniques of classical mechanics evolved from the study of the celestial three-body problem.

The fundamental force for the celestial three-body problem is naturally gravity. The attractive force between two bodies of masses M and m can be determined from Newton's law of gravity,

$$\vec{F}_g = \frac{GMm}{r^2}\,\hat{r}\,, \tag{1.1}$$

where G is Newton's gravitational constant and r is the distance separating their centers. (Note that this equation is only strictly valid for point masses or bodies with spherical symmetry.) The associated potential energy function is given by

$$U_g\,(r) = -\frac{GMm}{r}\,. \tag{1.2}$$

The total potential energy for the three-body system is found from the principle of superposition. Summing up the potentials in a pair-wise manner gives

$$U_g = -G\left(\frac{m_1 m_2}{r_{12}} + \frac{m_1 m_3}{r_{13}} + \frac{m_2 m_3}{r_{23}}\right)\,. \tag{1.3}$$

For the Earth-Moon-satellite system the above treatment implies that the force on the satellite would be just the vector sum of the Earth's gravitational force and that of the Moon. This approach breaks down though because the presence of the Moon influences the gravitational force due to the Earth (and vice versa). The Earth is deformed by the Moon through tidal forces, and thus the Earth's attraction of the satellite is no longer simply described as in the two-body case. In the absence of a fundamental theory, a three-body force can be designed to account phenomenologically for the deviation of the Earth from spherical symmetry. Inclusion of tidal

effects in a fundamental way eliminates the need for a three-body force term. As is the case in all three-body "problems", three-body forces are only required when certain internal degrees of freedom are neglected.

1.1.2 Atomic and Molecular Systems

Three-body forces have been used in the description of atomic and molecular interactions since Axilrod and Teller [Axi43] calculated a non-additive contribution to the potential energy for a system of three inert gas atoms. The typical molecular dimension of approximately 0.5 nm dictates that the electromagnetic force is the dominant mechanism for interaction (the gravitational force between two molecules is some thirty orders of magnitude smaller). The traditional treatment of long-range intermolecular forces (that is, the electron clouds of the interacting molecules do not overlap) divides the attractive contributions into three components:

1. Electrostatic contributions arise from the interaction of permanent dipole moments between two polar molecules. The interaction of two permanent dipoles is attractive and because the electron charge distribution is not distorted in either molecule the interaction energy is termed a first-order energy [Mai81].

2. Inductive forces arise between one molecule with a permanent dipole moment and another non-polar molecule. The permanent dipole distorts the electron charge distribution in the neutral molecule and induces a dipole moment in it. The induced dipole then interacts with the inducing dipole to produce an attractive force.

3. Dispersion forces provide the only contribution to the interaction energy for two neutral molecules. Even though a molecule may not possess a permanent

dipole moment, its electrons are in continuous motion so that the electron density oscillates in time and space. At any instant in time a molecule may possess an instantaneous dipole moment which fluctuates as the electron density fluctuates. The instantaneous dipole moment in one molecule induces an instantaneous dipole moment in a second molecule. In other words, the dispersion energy is a result of correlations between the electron density fluctuations in the two molecules [Mai81].

The potential energy function for the long-range interaction of pairs of molecules can be written compactly as:

$$U(\mathbf{r}, \boldsymbol{\omega}) = U_{el}(\mathbf{r}, \boldsymbol{\omega}) + U_{ind}(\mathbf{r}, \boldsymbol{\omega}) + U_{disp}(\mathbf{r}, \boldsymbol{\omega}) \tag{1.4}$$

where $\boldsymbol{\omega}$ specifies the relative orientation of the two interacting molecules. For the interaction of two polar molecules all three terms will be present. The last two terms will contribute for the interaction between a polar molecule and a non-polar one. Only the dispersion term remains for the interaction of two non-polar molecules.

The potential energy function for the long-range interaction of two neutral atoms can be calculated from second-order quantum mechanical perturbation theory with the perturbing potential having a dipole form. The resulting dispersion energy is given by

$$U_{disp} = \frac{C_6}{r^6} \tag{1.5}$$

where the coefficient C_6 is determined from the dipole oscillator strengths for transitions from the ground state to excited states and the corresponding energy levels.

The simultaneous interaction of three molecules can be treated in a similar fashion. The simplest three-body system consists of three inert gas atoms labeled a, b, and c separated by distances r_{ab}, r_{ac}, and r_{bc} where θ_a, θ_b, and θ_c are the internal

angles of a triangle *abc*. By extending the perturbative treatment of the two-body case as far as the third-order energy $E_0^{(3)}$, it was shown [Axi43] that the leading terms for the dispersion energy are

$$U_{disp}^{abc}(r_{ab}, r_{bc}, r_{ac}) = \frac{C_6^{ab}}{r_{ab}^6} + \frac{C_6^{bc}}{r_{bc}^6} + \frac{C_6^{ac}}{r_{ac}^6} + \frac{\nu_{abc}(3\cos\theta_a \cos\theta_b \cos\theta_c + 1)}{(r_{ab} r_{bc} r_{ac})^3} \quad . \tag{1.6}$$

The first three terms in Equation 1.6 represent the interaction energies of the molecules taken in pairs. If the long-range potentials were pair-wise additive, these three would be the only terms. The fourth term, however, is non-additive and is known as the Axilrod-Teller triple-dipole term. The sign of the triple-dipole energy depends on the geometry of the triangle formed by the three molecules. For acute triangles the triple-dipole energy is positive, while for obtuse angles it is negative. This effect tends to stabilize near-linear arrays of molecules while destabilizing most triangular arrangements [Mai81].

Higher order contributions from instantaneous quadrupole moments and other multipoles can be included in calculations of three-body effects as well. The principal three-body terms are $(DDD)_3$ (the Axilrod-Teller term), $(DDQ)_3$, $(DQQ)_3$, and $(QQQ)_3$ where D and Q represent the dipole and quadrupole contributions, and the subscript, 3, indicates these energies are calculated in the third-order of perturbation theory [Bel70]. The terms including quadrupole contributions fall off more rapidly with distance than the triple-dipole: $(DDQ)_3$ goes as r^{-11}, $(DQQ)_3$ as r^{-13}, and $(QQQ)_3$ as r^{-15}. Because the perturbative analysis used to extract these terms is only valid at large molecular separations, the Axilrod-Teller energy tends to be the dominant many-body term.

Research continues in the field of atomic and molecular physics in efforts to improve the description of the forces that govern the interactions of low-density gases and fluids. Two examples of experimental and theoretical research into three-body

effects in molecular systems found in the current literature include an investigation of the structure function of gaseous Kr by low-momentum neutron diffraction [Gua99], and a comparison of integral equation methods and molecular dynamics simulations in describing the structural and thermodynamic properties of supercritical Ar [Bom01].

1.1.3 Nuclear Systems

Many experiments using high-energy accelerators have established that nucleons are not simple fundamental particles, but are instead aggregate systems composed of smaller constituents known as quarks which interact via the exchange of particles called gluons. The well-accepted theory to describe these quark-gluon interactions is quantum chromodynamics (QCD). In principle, all nuclear phenomena should be derivable from QCD by posing nuclear systems as a many-body problem involving the interactions of quarks and gluons. However appealing this perspective may be, the solution of such a problem is not tractable for a couple of reasons. First, the large coupling constant of the strong interaction ($\alpha_S \gtrsim 1$) prevents the use of perturbative techniques at the distance and energy scales relevant to nuclei. Secondly, the dimensions of the eigenstate basis needed to account for the numerous degrees of freedom of a many-quark-gluon system (unlike photons, the propagators of the electromagnetic force, gluons can interact with themselves, presenting greater complexities for calculation) exceeds the computational capabilities present today, even for simple nuclei. In practice, nuclear phenomena must be explained by approximations and effective models rather than in terms of the most fundamental interactions.

The dynamic and static properties of low-energy scattering and bound state nuclear systems are best described by the nonrelativistic Schrödinger equation em-

ploying effective nucleon-nucleon (NN) potentials. The potentials which most realistically model the NN interaction are based on the principle that the nuclear force is propagated by the exchange of particles known as mesons. The intermediate- and long-range parts of all modern NN potentials (CD-Bonn, AV18, Nijmegen I and II) are based on the exchange of known mesons, while the more nebulous short-range repulsive part typically contains some purely phenomenological components. By construction, NN potentials reproduce the two-nucleon scattering data and properties of the deuteron by fitting any free parameters in the models to these observables.

NN potentials have been used to calculate observables in the three-nucleon (3N) system with most results in excellent agreement with the available experimental data [Glö96]. There are some serious discrepancies between theoretical predictions and data in the 3N system, however; three of the most notable are the triton binding energy problem, the A_y puzzle, and the star anomaly. The star anomaly is the impetus for the measurements described in this dissertation and will be explained in more detail in Section 1.2. The triton binding energy defect and A_y puzzle have sufficiently different signatures to warrant separate discussions.

Triton Binding Energy Defect

The underbinding of the triton by rigorous calculations using modern potentials that are based on two-nucleon (2N) dynamics has been seen as one of the strongest pieces of evidence for the existence of 3NFs. The binding of the triton is strongly correlated with the s-wave strength in the NN potential. Modifying this part of the NN potential to correct the binding defect is not an option though, because a broad range of nuclear data would no longer be properly predicted. Likewise, modifying the off-energy-shell behavior of the NN force does not seem to be the

Potential Model	^3H Binding Energy (MeV)	Reference
CD-Bonn	8.00	[Mac96]
Argonne V18	7.62	[Wir95]
Nijmegen II	7.62	[Sto94]
Experiment	8.48(2)	

Table 1.1: Calculations of the triton binding energy for three modern NN potentials in comparison to experiment. All theoretical predictions were made using charge-dependent 34-channel Faddeev calculations [Mac96]. The experimental value for the triton binding energy comes from [Gib88].

complete solution either. Table 1.1 shows the predictions of three modern potentials compared to the experimental triton binding energy of 8.48 MeV. The Argonne V18 (AV18) and Nijmegen II (Nijm-II) potential models predict the same binding energy even though their treatment of off-shell effects are somewhat different. The CD-Bonn potential comes the closest to reproducing the experimental value of the triton binding energy. The increased binding energy of the CD-Bonn potential over the other two is attributed to the nonlocal construction of the CD-Bonn potential, while the other two are local potentials. Nevertheless, it too underbinds the triton. (More details about the concept of nonlocality will be discussed in Section 2.3.)

As another possible explanation for the triton binding energy defect, it has been proposed that relativistic corrections could be non-negligible [Fri83]. Various approaches have been applied in the effort to incorporate relativistic dynamics into 3N calculations. One approach employed the Bethe-Salpeter equations with covariant, multirank separable interactions derived from different meson-exchange potentials [Rup92]. This study found an increase of ~ 0.3 MeV in the triton binding energy due to relativity. A second approach was based upon variational Monte-Carlo calculations using a relativistic Hamiltonian [Car93]. Here, relativity had the effect of

reducing the triton binding energy by ~ 0.34 MeV. In comparing this result to that from the first approach, Carlson *et al.* [Car93] concluded that "relativistic corrections to the binding energies may depend strongly on the method used to generalize the non-relativistic Hamiltonian for use in relativistic calculations." While more refined relativistic treatments may indeed one day solve the triton binding energy defect, Rupp and Tjon [Rup92] warn that reproducing the binding energy does not necessarily guarantee accurate predictions of other experimental observables such as the 3N charge form factors.

The lack of success from other methods in solving the binding energy defect has been seen as evidence that 3NFs could play a significant role in the 3N system. The definition of a true three-body force is usually given as a force that depends in an irreducible way on the simultaneous coordinates, momenta, spins, and internal quantum numbers of the three interacting particles [Gib88]. Because the long-range part of the NN interaction is well-described by the single exchange of pi-mesons (pions), one obvious approach to the construction of a 3NF starts with two-pion-exchange (2πE). A basic diagram for this process is shown in Figure 1.1. The shaded region represents any non-nucleonic contribution and is most commonly described in terms of the $\Delta(1232)$ resonance. Early calculations with the Tucson-Melbourne (TM) [Coo79], Brazil (BR) [Coe83, Rob86], and Urbana (UR) [Car83, Sch86] 3NFs based solely on 2πE overbound the triton by about 1.5 MeV when a standard value of the πN form factor cutoff ($\Lambda = 5.8\ m_\pi$) was used [Che86]. Later versions of the TM 3NF [Coo93] incorporated the exchange of the more massive rho-meson (in ρ-π and ρ-ρ diagrams) because the ρ-interactions provided a repulsive contribution to the binding energy, in effect cancelling out some of the 2π attraction. Even without including the ρ-exchange, it was shown that through judicious choices of

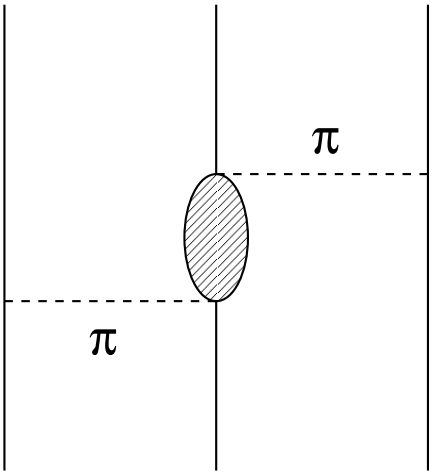

Figure 1.1: Basic diagram for the two-pion-exchange contribution to a three-nucleon force. The shaded structure represents the $\pi N \rightarrow \pi N$ amplitude and can be any contribution except a forward propagating nucleon state. The most common contribution is from the Δ-isobar which dominates πN scattering at energies below 300 MeV.

the form factor cutoff, Λ, that the experimental binding energy of the triton could be reproduced by numerous modern NN potentials when supplemented with the TM 2π-3NF [Nog97]. This treatment yields a number of 3N Hamiltonians which produce the same (correct) triton binding energy. While this approach is more phenomenological than fundamental, using such models allows a meaningful search to be conducted in the 3N continuum for 3NF effects in elastic scattering and nucleon-breakup observables.

A_y Puzzle

Many low-energy elastic scattering observables in the 3N system (that is, for *nd* and *pd* scattering) are well predicted by rigorous calculations using modern NN potentials. The differential cross-section predictions are, in fact, so accurate (to

within 1% of the experimental data [Wit89]) that they will be used to determine the beam-target luminosity for normalization of the nd breakup cross sections in the current experiment (see Section 5.3.2). One observable that does show a significant discrepancy between measurement and calculation is the vector analyzing power, $A_y(\theta)$, for Nd elastic scattering. The vector analyzing power quantifies a dependence of the scattering cross section on the interaction of the spins of the beam and target nuclei. The $A_y(\theta)$ is defined as

$$A_y(\theta) \equiv \frac{\sigma_\uparrow(\theta) - \sigma_\downarrow(\theta)}{\sigma_\uparrow(\theta) + \sigma_\downarrow(\theta)} \tag{1.7}$$

where $\uparrow$ and $\downarrow$ indicate the spin orientation of the incoming nucleon. Discrepancies of up to 30% between the measured $A_y(\theta)$ and theoretical predictions at the analyzing power maximum have been seen for both nd and pd elastic scattering at low energies (below 30 MeV). To illustrate this so-called "A_y puzzle", data and rigorous calculations for the nd vector analyzing power at an incident neutron energy of 3 MeV are shown in Figure 1.2.

First attempts to solve the A_y puzzle were based on modifying the NN potential in such a way that predictions of 2N observables would not be disturbed. Sensitivity studies have shown that $A_y(\theta)$ has a strong dependence on the ${}^3P_j$ partial waves [Wit91]. By multiplying these partial-wave interactions by various strength factors, Witała *et al.* [Wit91] showed it was possible to "fix" the A_y puzzle while keeping other low-energy observables in agreement with the two-body data. This procedure resulted in a NN potential with relatively large charge-independence breaking (CIB) and charge-symmetry breaking (CSB). In fact, the magnitude of the CIB and CSB in the resulting potential was inconsistent with theoretical expectations based on meson-exchange theory [Tor98]. An extensive study by Hüber *et al.* [Hüb98] recently examined the question of whether reasonable changes to different parts of the NN

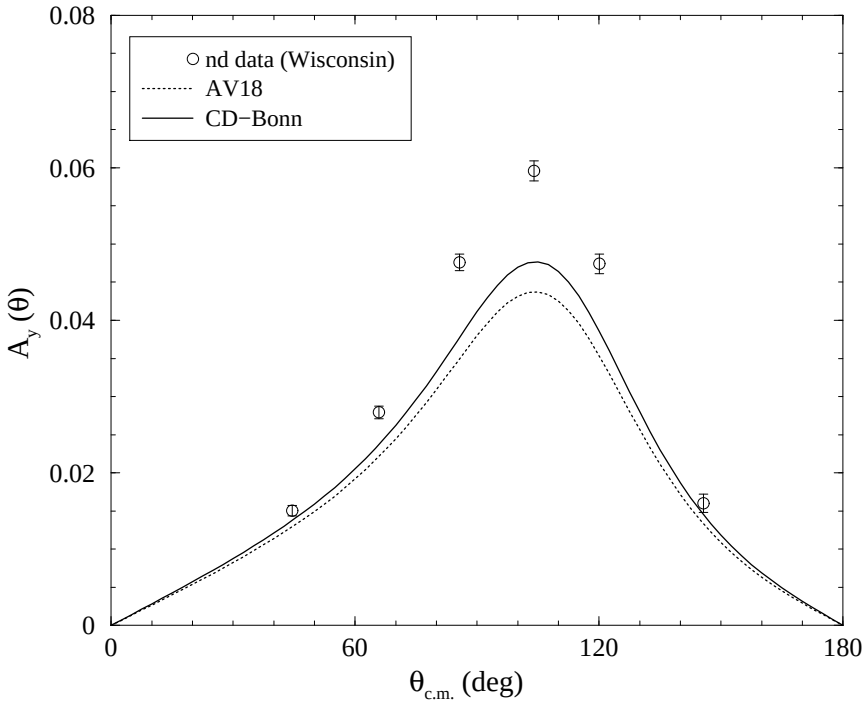

Figure 1.2: Comparison of data and calculations for the nd vector analyzing power, $A_y(\theta)$, at an incident neutron energy of 3.0 MeV. The data are from the Wisconsin group [McA94] and the calculations are rigorous 3N solutions in a Faddeev scheme by the Bochum-Cracow group [Wit01] for two modern NN potentials.

potential could resolve the A_y puzzle; the authors concluded that such changes could not.

Other attempts to solve the A_y puzzle have relied on the inclusion of 3NFs. In contrast to the triton binding energy problem, the addition of a traditional 3NF does not seem to be the solution. Calculations with the AV18 NN potential and the UR 3NF model showed only a slight improvement in the discrepancy [Kie95], while predictions of various NN potentials and the 2πE TM 3NF model actually amplified the difference between theory and data [Wit94]. The failure of traditional 3NFs to solve the A_y puzzle should not be too surprising. In attempts to make calculations with 3NFs as simple as possible, momentum-dependent force terms (in particular those terms proportional to $\vec{l}$) have been ignored. Given the inherent relationship between the analyzing power and the spin of the incident nucleons, it seems likely that additional spin-dependent 3NF components are needed in future calculations. Hüber *et al.* [Hüb98] suggest that the inclusion of spin-orbit terms ($\vec{l} \cdot \vec{s}$) into 3NF calculations would be the next step in the search for a solution to the A_y puzzle.

1.2 Motivation

Nucleon-deuteron (Nd) breakup has proven to be a realm rich with information in the quest to understand better 3N dynamics [Tjo81]. Because the kinematics of the breakup reaction allows the geometry of the nucleons in the exit channel to be varied in a continuous manner, scattering observables can be studied in configurations that show different sensitivities to NN potentials and 3NF models. One aim of these studies is to extract information from the three-body system about the 2N force that is not available from free two-nucleon processes [Wit88]. An example of such

an observable is the neutron-neutron scattering length, a_{nn}. Three other important goals in studies of Nd breakup are:

1. To search for kinematical configurations which are most sensitive to 2N-force properties, thus serving as a testing ground for different NN potential models [Klo73].

2. To search for kinematical configurations which are least sensitive to the details of NN potential models; under these conditions discrepancies between experiment and theory could indicate the influence of 3NFs [Klo73].

3. To search for kinematical configurations which are most sensitive to specific 2N-force components, such as the $^1S_0$ force or the tensor force [Wit88].

As mentioned in Section 1.1.3, one of the largest discrepancies between experiment and theory in the 3N system occurs for the space-star configuration in nd breakup, and is commonly referred to as the *star anomaly*. The star condition is defined as the exit configuration in the center-of-mass system where the momentum vectors of the three outgoing particles are of equal magnitude and separated by 120°. This situation is illustrated in Figure 1.3. The plane containing the three momentum vectors for the star condition can have any orientation with respect to the incident beam axis. When the star plane is perpendicular to the beam axis, the configuration is known as the *space star*. When the plane is coincident with the beam axis, the configuration is known as the *coplanar star*. There can be any number of star configurations between these two extremes. One such configuration measured in the current experiment will be referred to as an *intermediate star*.

Energy and momentum conservation reduces the number of independent momentum components of the three exit nucleons to five. By fixing the positions of

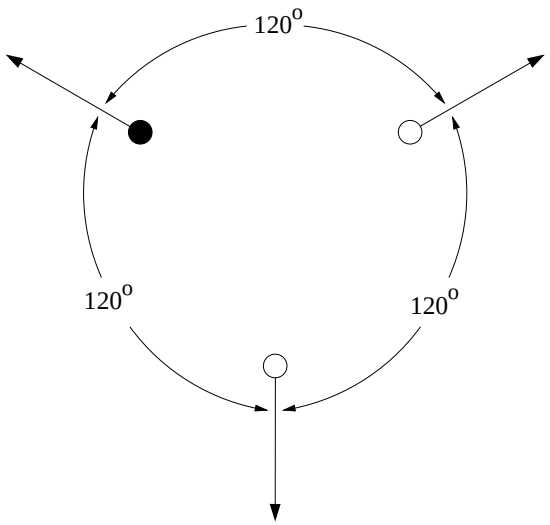

Figure 1.3: Momentum diagram of the star configuration in the center-of-mass system. The momentum vectors of the three nucleons in the exit channel are of equal magnitude and separated by 120°.

two detectors and imposing a coincidence requirement, four angles are specified (two each in θ and ϕ), leaving one kinematic degree of freedom. Measurement of the energies of both detected particles thus overdetermines the kinematics and requires that the particle energies lie on a curve, or *locus*. For the detection of two neutrons in coincidence in *nd* breakup, a kinematic locus in the E_{n1}-E_{n2} plane is defined (see Figure 1.4). A parameterization of this locus into discrete steps of arc-length (S) allows observables to be conveniently plotted as a function of a single parameter, S. The initial starting point (S=0) is defined as the point at which E_{n1} is a maximum for $E_{n2} = 0$ and S increases in a counter-clockwise manner around the curve. (As can be seen in Figure B.3, for some configurations the locus does not intersect the energy axes. In these situations, the S=0 point is defined where both particle energies have reached their minimum value.)

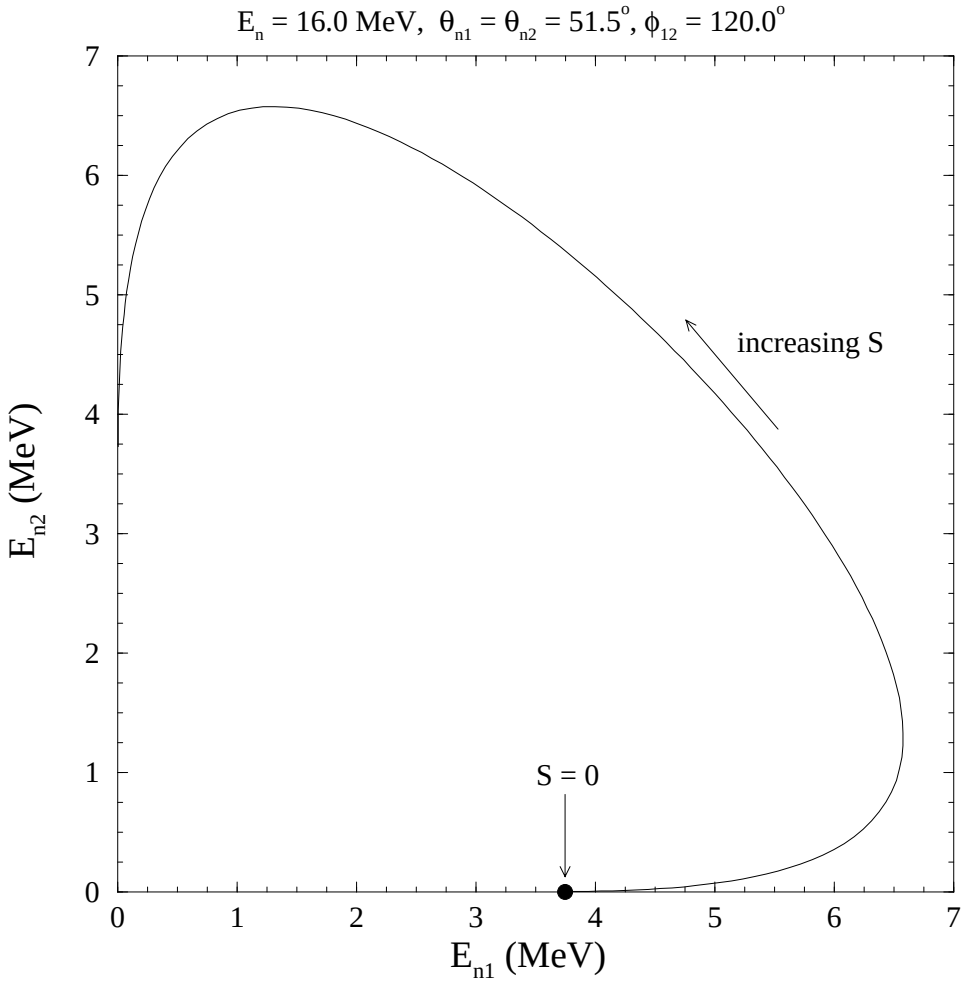

Figure 1.4: Kinematic locus for the space-star configuration. The locus is determined by the incident neutron energy and the angles of the two neutron detectors. All *nd* breakup cross sections will be presented as a function of arc-length (S) along the locus.

The space-star configuration initially garnered the interest of nuclear physicists because it fulfilled the second criterion listed in the beginning of this section; it showed little sensitivity to different NN force models, making it a promising place to search for 3NF effects [Klo73]. The models at that time consisted only of simple s-wave interactions. Later calculations using modern potentials have shown that higher partial waves have a non-negligible contribution [Glö96]. Nevertheless, the space-star configuration remains insensitive to the details of various modern NN potential models. As shown in Figure 1.5, the difference between the two extreme calculations at the space-star point is only 0.8%. The conclusion of Kloet and Tjon [Klo73] holds true; deviations between data and calculation could be the signature of 3NF effects, or of some other physics that is not currently included in standard potential models.

The star anomaly in nd breakup was first reported by Strate *et al.* [Str89] at an incident neutron energy of 13.0 MeV. An independent measurement has subsequently confirmed the large discrepancy at this energy [Set96]. In addition, the cross-section data from two independent measurements at 10.3 MeV [Ste89, Geb93] are significantly higher than calculations, although the discrepancy is not as large as at 13.0 MeV. Comparisons of the results of these measurements to calculations are made easier by averaging the experimental data in the region where the calculated cross section is relatively constant. This averaging is weighted by the statistical errors of each datum and reduces the statistical uncertainty of each measurement to less than $\pm 1\%$. The systematic uncertainty reported for each experiment is then folded with the statistical uncertainty. The average cross sections about the space-star point for the four nd measurements and for three pd breakup measurements at 10.5 [Gro96], 13.0 [Rau91], and 19.0 MeV [Pat96] are shown in Figure 1.6. The solid curve in

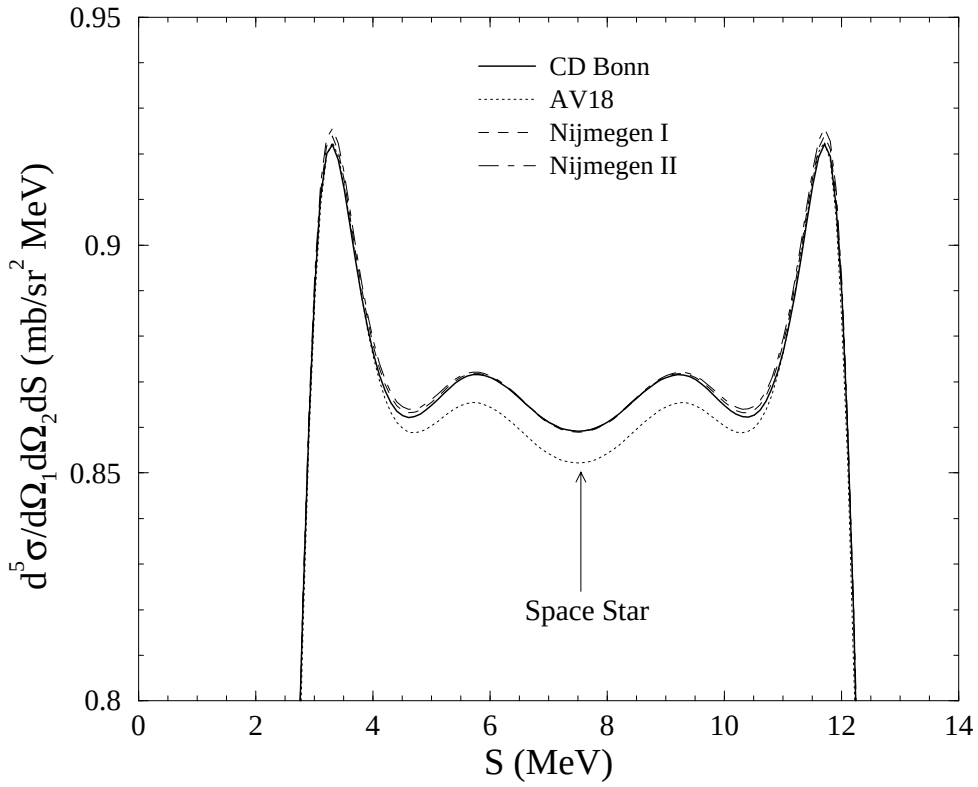

Figure 1.5: Sensitivity of space-star cross-section calculations to four different modern NN potentials. Note the suppressed zero on the vertical axis.

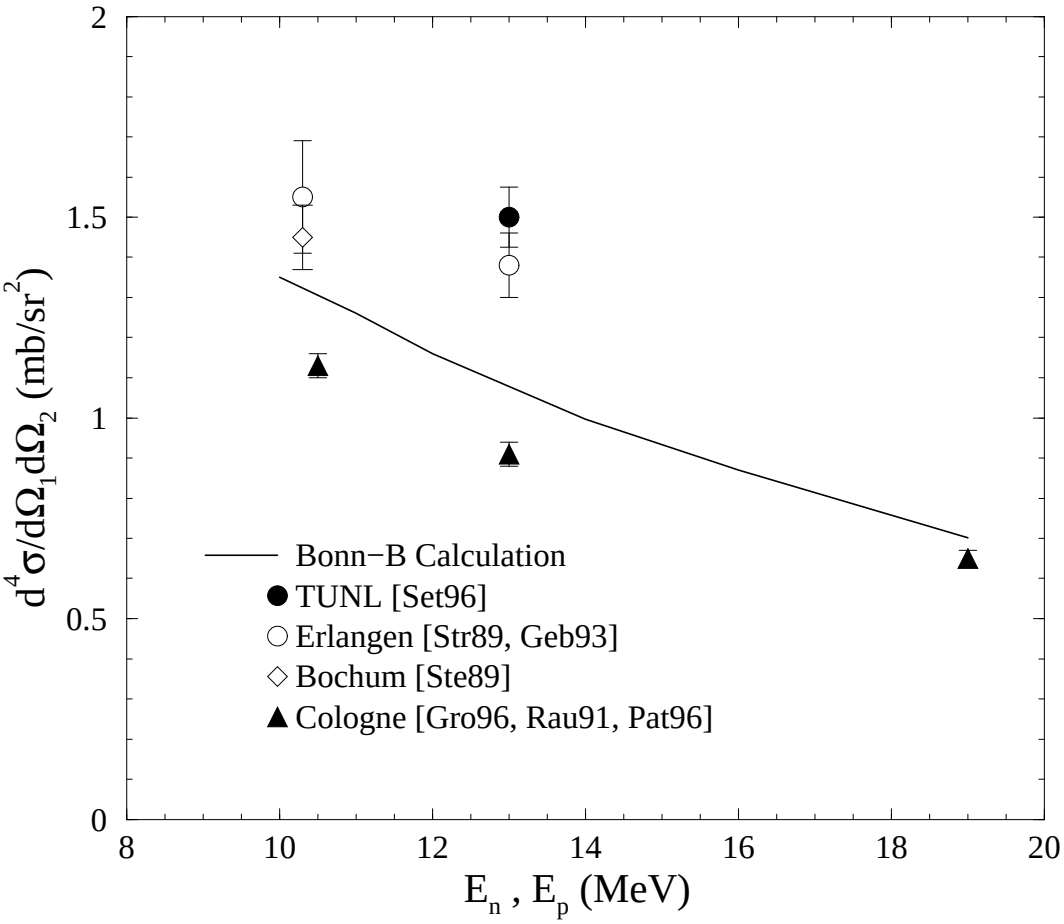

Figure 1.6: Average cross section in the region of the space-star point. The solid circle represents the TUNL *nd* datum [Set96], the open circles are the Erlangen *nd* data [Str89, Geb93], the open diamond is the Bochum *nd* datum [Ste89], and the solid triangles are the Cologne *pd* data [Gro96, Rau91, Pat96]. The curve is an *nd* point-geometry calculation with the Bonn-B NN potential at the kinematics for the space-star point. The error bars are the combined statistical and systematic uncertainty for each measurement.

Figure 1.6 is a point-geometry calculation using the Bonn-B NN potential. The *nd* data at 13.0 MeV have the largest disagreement with calculation. The average of the two points at 13.0 MeV is more than 30% higher than calculation. The *nd* data at 10.3 MeV is in better agreement with calculation (their average is only 10% higher than calculation); however, this discrepancy does represent a two standard deviation difference. The *pd* data consistently fall beneath the calculated values, with the difference growing smaller with increasing energy. This trend tends to corroborate the speculation that Coulomb effects may be significant [Alt94].

The situation for the coplanar-star configuration is somewhat murkier. First measurements of the coplanar-star cross section at 13.0 MeV [Str89] were significantly higher than calculation. However, remeasurement by Setze *et al.* [Set96] found relatively good agreement between data and calculation. Setze *et al.* [Set96] explained the discrepancy as being due to systematic problems in the method used by Strate *et al.* [Str89] to account for their accidental-coincidence background. No other *nd* data for the coplanar-star configuration has been published. Some *pd* data exist at two higher energies: at 22.7 MeV the data agree almost perfectly with calculation [For85], while at 65.0 MeV the data are higher than predicted [Zej97].

The motivation for the current experiment is based on multiple reasons:

1. No breakup data has been reported at 16.0 MeV. A measurement at this energy for the space-star configuration would "fill in the gap" between data at 13.0 and 19.0 MeV as seen in Figure 1.6. Data at several energies will provide information on the energy dependence of the star anomaly and possibly give new insight about its origins.

2. The disagreement of the space-star data with calculation coupled with the

generally good agreement of the most recent coplanar-star data with prediction at 13.0 MeV certainly raises a major question – why does rotating the star plane by 90° create such a large discrepancy in one configuration but not in another?

3. To this author's knowledge, no breakup data has been reported for configurations of an intermediate-star type. At some point between the space- and coplanar-star extremes, one would assume that measurement and prediction must begin to diverge. A study of the star configuration as a function of the plane orientation would add new information to the inquiry.

1.3 Current Experiment

Motivated by the specific reasons set forth in the previous section and by the broader quest to study 3N dynamics more completely and critically, measurements of the *nd* breakup differential cross sections for the space-star, coplanar-star, and intermediate-star configurations were undertaken at Triangle Universities Nuclear Laboratory (TUNL) at an incident neutron energy of 16.0 MeV. This spatial orientation study had as its main objectives the hope of shedding new light on the origins of the star anomaly and the continuing search for true 3NF effects. For a meaningful comparison to be made between data and calculations, statistical accuracy goals of ±5% were established for 0.5-MeV bins along the kinematic locus. The absolute normalization for the breakup cross sections comes from a simultaneous measurement of the beam-target luminosity as determined from *nd* elastic scattering. Backgrounds from random (or accidental) coincidences are explicitly measured by sampling events arriving at unphysical times. The continuous measurement of the luminosity and explicit measurement of the accidental background are two significant features of the

methodology employed in this experiment.

As with any experiment using neutrons as a probe, large corrections have to be made to account for attenuation of the incident and scattered neutron fluxes. Extensive computer simulations were run using Monte-Carlo techniques to generate these correction factors. Correction factors for detector efficiency were also needed. The absolute detection efficiencies of the liquid scintillators used were obtained in previous independent measurements. No attempt was made to extract a point-geometry cross section from the data by correcting for finite-geometry effects. Instead, the potential-model calculations were performed for the finite geometry of the experiment. Data and calculations could then be identically projected on the ideal kinematic locus for a one-to-one comparison.

The following chapters will present details of the 16.0-MeV breakup measurements. Chapter 2 reviews the theoretical bases for the calculations used in the extraction of and comparison to the data. Chapter 3 describes the methods and equipment that were employed in the experiment. Chapter 4 explains the Monte-Carlo computer simulations that were performed as part of the data analysis. Chapter 5 describes the analysis techniques that were used to determine the breakup cross sections. Chapter 6 summarizes the results of the experiment and suggests possible conclusions that can be drawn. Finally, Appendices A, B, and C present tables of the cross-section results, kinematic quantities of interest, and absolute detector efficiencies.

Chapter 2

Theory

2.1 Introduction

Rigorous 3N calculations based on the Faddeev scheme [Fad61] were used for comparison to the experimental cross sections obtained in this project. Dr. Henryk Witała of the Bochum-Cracow theory group [Glö96] provided the T-matrix amplitudes from the Faddeev solutions for various incident energies and for different modern NN potential models. These amplitudes were then used to generate the cross-section predictions.

This chapter will outline the theoretical framework utilized in these calculations, starting with a general discussion of meson-exchange theory in Section 2.2. A specific meson-exchange potential, the CD-Bonn NN potential, will then be described in some detail in Section 2.3. A review of two-body scattering theory will follow in Section 2.4. The 3N breakup formalism will be discussed in Section 2.5 in terms of two- and three-body forces with the application of calculating cross-section observables.

Finally, a brief explanation of some technical details of the calculations will be given in Section 2.6.

2.2 Meson-Exchange Theory

As described in Section 1.1.3, the fundamental theory of the strong force is now commonly accepted to be quantum chromodynamics (QCD). This belief is fairly recent though; originally meson-exchange theory was thought to represent a complete description of the strong interaction in strict analogy to quantum electrodynamics (QED). Now, meson-exchange theory is understood to be an *effective* description of the full and fundamental theory which is valid in the regime of low-energy nuclear physics.

Currently, the best theoretical predictions of nuclear properties come from effective potential models that are based on meson exchange. In this section meson-exchange theory will be discussed as a prerequisite for understanding these potential models. First, the empirical features of the nuclear force that any realistic model must reproduce are described. Next, a brief history of the development of meson-exchange theory will be outlined. Finally, a description of meson properties and the fundamental principles of meson theory will be given.

2.2.1 Features of the Nuclear Force

Measurements by the earliest nuclear physicists established the foundation on which theoretical models of the nuclear strong force were based. In particular, five empirical properties were identified as being fundamental to the nuclear force. These five features provide the criteria which all models purporting to describe the NN

interaction must fulfill:

1. The nuclear force has a finite (or *short*) range. As a first estimate, the range of the nuclear force must be shorter than interatomic distances because only the electromagnetic interaction is needed to explain known phenomena on this scale. A lower, more precise limit comes from the saturation properties of nuclei. For example, the binding energy per nucleon is nearly constant for nuclei with $A > 4$. Also, the nuclear density remains roughly the same, with the radius of heavy nuclei being proportional to $A^{1/3}$. From these observations, Wigner concluded that the range of the nuclear force was approximately equal to the radius of the alpha particle (~ 1.7 fm) [Wig33].

2. The nuclear force is attractive at intermediate distances (*intermediate* refers to the total range of the nuclear force, which is divided into short, intermediate, and long range parts). The most obvious evidence for this feature is nuclear binding. For example, the ^{3}He nucleus (two protons and one neutron) would be torn asunder by Coulomb repulsion if not for the nuclear attraction. Further evidence comes from the analysis of NN scattering data; the s-wave phase shifts are positive (corresponding to attraction) at energies less than 300 MeV [Mac89].

3. The nuclear force has a repulsive core. Compelling proof of short-range repulsion can once again be found in NN scattering data. At energies above 300 MeV (at higher energies, smaller distance scales are probed) the s-wave phase shifts become negative.

4. The nuclear force has a tensor component. The presence of a quadrupole moment for the deuteron ground state is the most striking evidence for this

feature. The ground state ($l = 0$) wavefunction would be spherically symmetric (and thus have no electric quadrupole moment) if not for a noncentral nuclear force component that mixes states of different angular momenta. Further proof of an admixture of angular momentum states in the deuteron ground state can be seen in its nonzero magnetic moment.

5. The nuclear force has a strong spin-orbit component. Evidence for this property is a bit more subtle; the triplet p-waves from phase shift analyses at high energies can only be reproduced by adding a spin-orbit term to the central and tensor nuclear force components.

2.2.2 Brief History

For physicists in the 1930's, the most striking feature of the nuclear force was the short range of the interaction. This characteristic was in stark contrast with the extended range of influence exhibited by the fundamental forces understood at that time, gravitation and electromagnetism. The first theoretical attempts focused on deriving a force of finite range from some more fundamental concept. In 1935 the Japanese physicist Hideki Yukawa proposed, in analogy to the successful theory of quantum electrodynamics (QED), that the nuclear force could be propagated by the exchange of a particle of *nonzero* mass [Yuk35]. These massive particles eventually received the name *mesons* [Bha39], and thus the meson-exchange picture of the nuclear force was born.

Yukawa's original formulation was carried out using the framework of classical field theory. The derivation of the Coulomb potential in QED is given here as an example of this methodology. The electromagnetic interaction is propagated by a

field of massless particles known as photons. In the static limit, the field equation that is fulfilled in this situation is the Poisson equation of classical electrodynamics:

$$-\nabla^2 V(\mathbf{r}) = e\,\delta^{(3)}(\mathbf{r}) . \tag{2.1}$$

The solution to this second-order differential equation is the well-known Coulomb potential:

$$V(r) = \frac{e}{4\pi}\frac{1}{r} . \tag{2.2}$$

In analogy, the meson-exchange theory of the nuclear interaction postulates a field of massive particles that must fulfill a field equation known as the Klein-Gordon equation,

$$(\Box + m^2)\,\varphi(x) = g\,\overline{\psi}(x)\,\psi(x) , \tag{2.3}$$

where $\hbar$ and c have been set equal to 1 for simplicity. (Note that the Klein-Gordon equation reduces to the Schrödinger equation in the non-relativistic limit.) Assuming that the nucleon which is the source of the meson field is infinitely heavy and fixed at the origin, Equation 2.3 reduces to

$$(-\nabla^2 + m^2)\,\varphi(\mathbf{r}) = g\,\delta^{(3)}(\mathbf{r}) \tag{2.4}$$

which has as its solution, the Yukawa potential:

$$\varphi(r) = \frac{g}{4\pi}\frac{e^{-mr}}{r} . \tag{2.5}$$

The exponential form gives the nuclear force the desired finite range. For a massless particle the Yukawa potential simply reduces to the Coulomb form.

After several false steps, such as misidentifying the muon as Yukawa's nuclear field carrier, nuclear physicists finally discovered the *pion* and determined that it did indeed interact strongly with nuclei. One of the more significant theoretical advances

of that era was the proposition by Taketani, Nakamura, and Sasaki (TNS) in 1951 [Tak51] that the nuclear interaction could be subdivided into three regimes. For an internucleon distance, r, these regions are defined as follows:

1. a long-range ("classical") region ($r \gtrsim 2$ fm),

2. an intermediate-range ("dynamical") region (1 fm $\lesssim r \lesssim 2$ fm), and

3. a short-range ("core") region ($r \lesssim 1$ fm).

This subdivision has been of great value in understanding the nuclear force because it allows a step-by-step exploration of the NN interaction and permits different derivations for different parts of the force when necessary [Mac89].

Perhaps the most important contribution of the TNS approach was that it allowed different meson-exchange interactions to be associated with the three separate regimes of the nuclear force. For instance, it is well-understood that in the classical region one-pion exchange (OPE) is the dominant process. That OPE is responsible for the long-range part of the nuclear interaction should not be surprising since a single pion has the smallest mass of any of the mesons or multipion configurations. In the dynamical region two-pion exchange (TPE) processes are the most important, but the exchange of heavier mesons can also be relevant. Many processes are at work in the core region. Multipion exchanges, heavy mesons of various kinds, and on a more fundamental level quark-gluon exchanges, all contribute to the short-range repulsive nature of the nuclear force.

2.2.3 Fundamental Concepts of Meson Exchange

The derivation of the Yukawa potential in the previous section was performed in the framework of classical field theory to show clearly how the short-range nature of the nuclear force is generated by massive particle exchange. More advanced theoretical treatment of meson exchange, however, necessitates the use of quantized field theory. This approach was developed for QED and relies on perturbation techniques for evaluating the interactions that are present. The small electromagnetic coupling constant ($\alpha_{EM} = \frac{1}{137}$) makes perturbative treatments attractive in QED because only a few terms need to be evaluated before convergence is achieved. The large coupling constants of interactions between mesons and baryons (typically on the order of 10) call into question whether perturbation theory can be applied for the nuclear force [Mac89]. A reasonable justification can be found in the TNS conjecture if one considers only the long-range and intermediate regions where there are but a finite number of perturbative contributions. Predictions generated by perturbation theory for these regions are expected to be quite good. In the short-range region, the extended structure of hadrons dictates that the meson-exchange picture should break down, so the limits of perturbation techniques here are irrelevant.

One-Boson Exchange

The lowest-order contribution to NN scattering in the framework of perturbation theory is one-boson exchange (OBE). The Feynman diagram depicting this process in the center of mass of the two interacting nucleons is shown in Figure 2.1. Evaluation of Figure 2.1 according to the Feynman rules [Bjo64] results in an amplitude of

$$-i\,\bar{V}_\alpha\,(q',q) = \frac{\bar{u}_1(\mathbf{q}')\,\Gamma_1^{(\alpha)}\,u_1(\mathbf{q})\,P_\alpha\,\bar{u}_2(-\mathbf{q}')\,\Gamma_2^{(\alpha)}\,u_2(-\mathbf{q})}{(q'-q)^2 - m_\alpha^2} \tag{2.6}$$

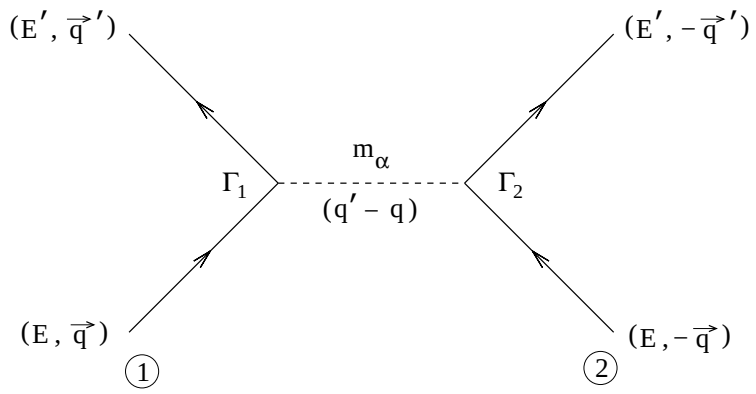

Figure 2.1: Feynman diagram of the one-boson exchange (OBE) contribution to NN scattering in the center of mass system. The solid lines represent nucleons and the dotted line denotes a boson of mass, m_α. The notation is consistent with that used by Machleidt [Mac89].

where $\Gamma_i^{(\alpha)}$ $(i = 1, 2)$ are the vertices representing the boson-nucleon interactions, u_i and $\bar{u}_i$ are the Dirac spinors representing the incoming and outgoing nucleons, and P_α divided by the denominator is the boson propagator. The one-boson exchange potential (OBEP) is defined as the sum of the one-particle exchange amplitudes of the mesons included in the model (see Figure 2.2):

$$V_{\text{OBEP}} = \sqrt{\frac{M}{E'}}\sqrt{\frac{M}{E}}\sum_{\alpha=\pi,\eta,\rho,\omega,\delta,\sigma}\bar{V}_\alpha\left(\mathbf{q}',\mathbf{q}\right)\times\mathcal{F}_\alpha^2\left(\mathbf{q}',\mathbf{q};\Lambda_\alpha\right), \tag{2.7}$$

where $E = \sqrt{M^2+\mathbf{q}^2}$, $E' = \sqrt{M^2+\mathbf{q}'^2}$, M is the nucleon mass, and $\mathcal{F}_\alpha\left(\mathbf{q}',\mathbf{q};\Lambda_\alpha\right)$ are form factors applied to the meson-nucleon vertices. These form factors are introduced to account for the aggregate structure of the meson-nucleon vertex and have the analytical form

$$\mathcal{F}_\alpha\left[(\mathbf{q}'-\mathbf{q})^2\right] = \frac{\Lambda_\alpha^2 - m_\alpha^2}{\Lambda_\alpha^2 + (\mathbf{q}'-\mathbf{q})^2}, \tag{2.8}$$

where Λ_α is the "cutoff mass". The cutoff mass suppresses the contribution of high momenta (that is, small distances) and is related to hadron size. Because the hadron

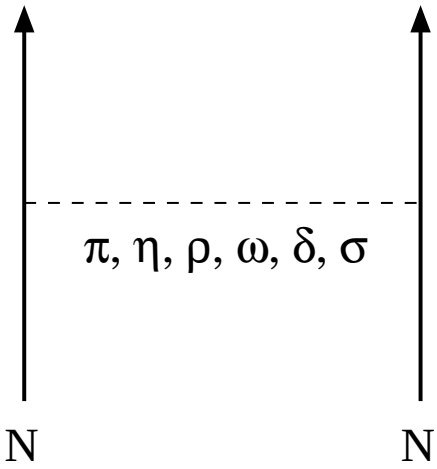

Figure 2.2: Diagram of the one-boson exchange (OBE) model for the nuclear force. The mesons that serve as propagators of the force are shown. Note that the σ-meson is a fictitious particle created to describe multiple-meson contributions in the framework of single boson exchange.

size cannot be calculated from QCD, the cutoff masses used in OBE models are determined from empirical fits to NN data.

Meson-Nucleon Coupling

The guts of the physics involved in meson-exchange theory is found in the meson-nucleon coupling vertices, $\Gamma_i^{(\alpha)}$. These vertices are derived from Lagrangians specific to the types of fields that are involved. The three most relevant fields in low-energy nuclear physics are

1. the pseudoscalar (ps) field,
2. the scalar (s) field, and
3. the vector (v) field.

The commonly used interaction Lagrangians that couple these fields to the nucleon are given by

$$\mathcal{L}_{ps} = -g_{ps}\,\bar{\psi}\,i\,\gamma_5\,\psi\,\varphi^{(ps)} \tag{2.9}$$

$$\mathcal{L}_{s} = g_{s}\,\bar{\psi}\,\psi\,\varphi^{(s)} \tag{2.10}$$

$$\mathcal{L}_{v} = -g_{v}\,\bar{\psi}\,\gamma^{\mu}\,\psi\,\varphi^{(v)}_{\mu} - \frac{f_v}{4M}\,\bar{\psi}\,\sigma^{\mu\nu}\,\psi\,(\partial_{\mu}\,\varphi^{(v)}_{\nu} - \partial_{\nu}\,\varphi^{(v)}_{\mu}) \tag{2.11}$$

where ψ denotes nucleon fields and φ denotes meson fields. In Equation 2.11 the first term is called the vector (v) coupling and has as its coupling strength, g_v. The second term is called the tensor (t) coupling and has strength, f_v. The influence of the various fields on the nuclear force are found by evaluating Equation 2.6 with the interaction Lagrangians shown above. Details of these lengthy and complex calculations are given by Machleidt [Mac86]. A summary of these results has been compiled in Table 2.1.

Realistic Mesons

The next step in the treatment of meson-exchange theory is to consider the physical manifestations of the fields that have so far only been discussed theoretically. In the mass range below the nucleon mass there exist four nonstrange mesons (masses are given in parentheses in units of MeV and come from the Particle Data Group evaluation [Cas98]): $\pi\,(138)$, $\eta\,(549)$, $\rho\,(770)$, and $\omega\,(782)$. The π and η mesons are pseudoscalar particles, while the ρ and ω mesons are vector in nature. Just above the nucleon mass is an isovector scalar meson, $\delta\,(983)$. Due to its large mass and small coupling constant, the δ meson makes a relatively minimal contribution to the nuclear force. Likewise, contributions from the η meson are almost negligible due to its very small coupling constant and large mass compared to the π meson. Those

Coupling	**Bosons (coupling strength)**		**Predicted Force Characteristics**			
	I = 0 [1]	I = 1 $[\tau_1 \cdot \tau_2]$	Central [1]	Spin-Spin $[\sigma_1 \cdot \sigma_2]$	Tensor $[S_{12}]$	Spin-Orbit $[\mathbf{L} \cdot \mathbf{S}]$
ps	η (weak)	π (strong)	–	Weak, coherent with v, t	Strong	–
s	σ (strong)	δ (weak)	Strong, attractive	–	–	Coherent with v
v	ω (strong)	ρ (weak)	Strong, repulsive	Weak, coherent with ps	Opposite to ps	Strong, coherent with s
t	ω (weak)	ρ (strong)	–	Weak, coherent with ps	Opposite to ps	–

Table 2.1: Meson types and their effects on the different aspects of the nuclear force as obtained from OBE. The letter I denotes the boson isospin. The characteristics shown here are the results of calculations by Machleidt [Mac89].

researchers responsible for the early development of the Bonn NN potential noticed that a good fit of NN data favored a vanishing η contribution [Mac87].

The mesons with the greatest effects on the nuclear force are π, ρ, and ω. As the lightest meson, the pion provides the long-range part of the nuclear force, and due to its pseudoscalar nature, the tensor component. This tensor force is reduced at short range by the ρ meson. The ω meson is responsible for the spin-orbit force component and the nuclear short-range repulsion. Together these three mesons explain most of the important features of the nuclear force that were outlined in Section 2.2.1. The one feature that is not accounted for by these mesons is the attraction at intermediate distances.

In theory, an scalar-isoscalar boson with a mass of 500-700 MeV could explain the attraction at intermediate distances. No experimental evidence has ever been found to support this supposition, however. Current understanding instead ascribes the intermediate attraction to two-particle exchanges, primarily 2π-exchange processes. The appealing simplicity of a potential based solely on OBE led theorists to attempt to reproduce the effects of multiple-meson exchange by a single fictitious scalar boson known as the σ meson. The mass and coupling constant of the σ meson are free parameters that are adjusted to fit the NN experimental data.

General Form of the Nuclear Potential

Modern NN potentials that are based on meson exchange are available in either configuration-space or momentum-space formulations. The choice of which basis to use depends on the type of calculations being performed and what processes are being studied. For example, calculations of observables for *pd* scattering which explicitly include the Coulomb interaction have come primarily from the Pisa group

and are performed exclusively in a configuration-space basis [Kie94]. Observables for *nd* breakup on the other hand have been usually calculated in a momentum-space basis using the Faddeev equations [Glö96]. Regardless of which basis is used, the NN potential can typically be expressed as a sum of spin, isospin, and angular momentum operators. For instance, the following equation shows the operator structure for each spin-isospin state in one simple configuration-space formulation:

$$V(r) = V_C(r) + V_T(r)\, S_{12} + V_{LS}(r)\, \mathbf{L}\cdot\mathbf{S}. \tag{2.12}$$

In Equation 2.12, central, tensor, and spin-orbit force terms are represented by V_C, V_T, and V_{LS} respectively, and the corresponding operators are 1, S_{12}, and $\mathbf{L}\cdot\mathbf{S}$. The S_{12} operator is the usual configuration-space tensor operator given by

$$S_{12} = 3\frac{(\boldsymbol{\sigma}_1\cdot\mathbf{r})(\boldsymbol{\sigma}_2\cdot\mathbf{r})}{r^2} - \boldsymbol{\sigma}_1\cdot\boldsymbol{\sigma}_2\ , \tag{2.13}$$

and $\mathbf{S} = \frac{1}{2}(\boldsymbol{\sigma}_1 + \boldsymbol{\sigma}_2)$ is the total spin. The contributions of the π, ρ, ω, and σ mesons to each of the three force terms in Equation 2.12 are shown in figures in Machleidt's paper [Mac89]. In Figure 2.3, a plot of the total nuclear potential is given as a function of the internucleon distance, r, for the AV14 NN model [Wir84] with a total nucleon spin of $S = 0$ and total isospin of $T = 1$. (The "14" indicates the number of different operators used in the model.) The dominant meson-exchange processes for each distance region are noted by the particles that are believed to be responsible. Note that this particular potential exhibits features of the nuclear force that were described in Section 2.2.1 (that is, short-range repulsion, intermediate attraction, and finite range).

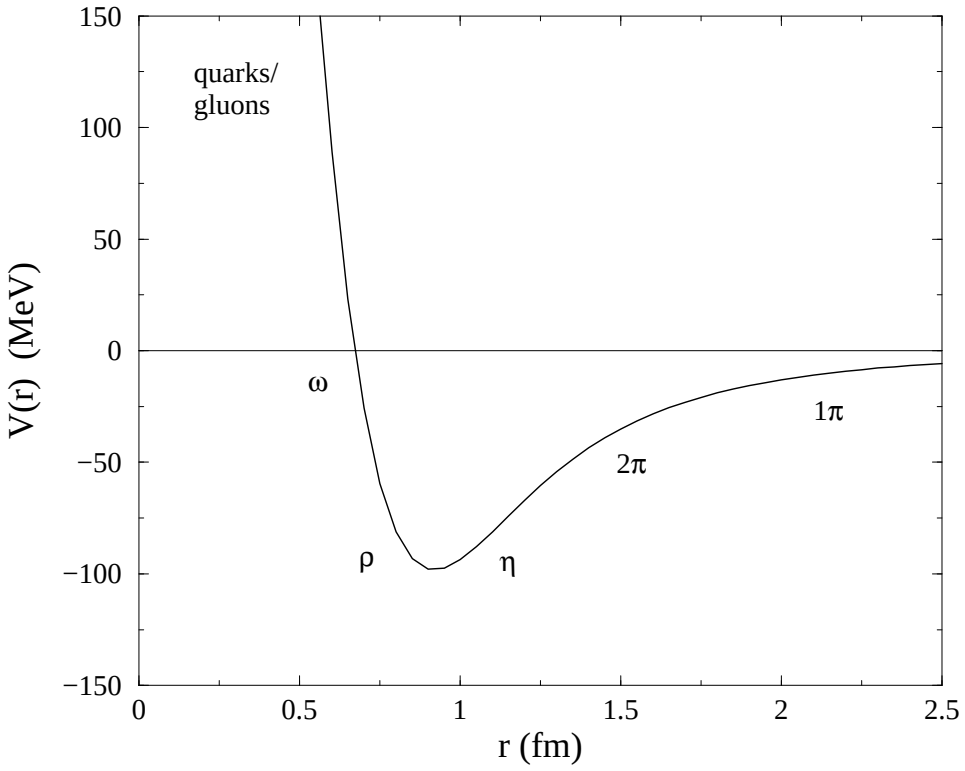

Figure 2.3: A plot of the AV14 NN potential as a function of internucleon distance, r, for total nucleon isospin of $T = 1$ and total nucleon spin of $S = 0$. The dominant meson-exchange processes for each distance region are labeled.

2.3 CD-Bonn NN Potential Model

In 1987 a comprehensive field theoretic meson-exchange model for the NN interaction, known as the Bonn full model, was published [Mac87]. This model has been widely used in the nuclear physics community for many years for predictions of various observables. An updated version of this model, called the CD-Bonn potential, is now available [Mac01]. The CD-Bonn potential has three main advantages over its predecessor:

1. It provides the most accurate fit to the world proton-proton (pp) and neutron-proton (np) data of any NN potential model [Mac01]. For the 2932 pp data below 350 MeV available in the year 2000, CD-Bonn has a fit with a χ^2/datum of 1.01, and for the 3058 nd data the χ^2/datum is 1.02.

2. It incorporates a comprehensive and sophisticated treatment of the charge dependence (the "CD" in "CD-Bonn") of nuclear forces. In particular, it provides a sound basis for studying the important concepts of charge-symmetry breaking (CSB) and charge-independence breaking (CIB).

3. It provides a different off-shell behavior than many commonly used local potentials because it is based on inherently nonlocal covariant Feynman amplitudes for OBE. This nonlocality tends to increase the binding energies for nuclei that have traditionally been underbound by other local potential models.

Each of these advantages will be discussed in some length in the following subsections.

Particle	Mass (MeV)	$g^2/4\pi$	f/g	Λ (GeV)
$\pi^{\pm}$	139.56995	13.6		1.72
π^0	134.9764	13.6		1.72
$\rho^{\pm}$, ρ^0	769.9	0.84	6.1	1.31
ω	781.94	20.0	0.0	1.5

Table 2.2: Basic constants and parameters used in the CD-Bonn NN potential model [Mac01]. The hadron masses are from the Particle Data Group evaluation [Cas98].

2.3.1 General Concepts

Like the Bonn full model, the CD-Bonn potential is based on meson exchange. All mesons with masses below the nucleon mass are included (π, η, ρ, and ω). In addition, two fictitious scalar-isoscalar bosons (σ_1 and σ_2) are introduced as representations of two-meson-exchange processes.

As mentioned in Section 2.2.3, the nucleon-coupling constant of the η-meson is very small, so for practical purposes this meson contributes little to the model. The primary mesons of interest are thus π, ρ, and ω. The masses, nucleon-coupling constants ($g^2/4\pi$), ratios of vector to tensor coupling constants (f/g), and cutoff masses (Λ) that are used in the CD-Bonn model for these mesons are given in Table 2.2. It is important to note that most of these parameters are determined from empirical and semiempirical sources – only the cutoff masses are allowed to vary when fitting the NN database [Mac01].

OBE models typically represent the intermediate nuclear attraction due to 2π-exchange diagrams with a single scalar-isoscalar boson, commonly referred to as σ. To reproduce the NN data accurately though, other two-meson-exchange diagrams must also be included; the most important contribution is $\pi\rho$ exchange which provides some partial cancellation to the 2π attraction [Mac01]. The simulation of

$2\pi + \pi\rho$ exchanges are then no longer purely of a scalar, isoscalar nature and the σ approximation breaks down. One solution to this problem is to readjust the parameters of the σ boson in each partial wave. A second solution is to use two separate boson masses to cover better the broad range that multimeson-exchange affects. In the CD-Bonn potential, the parameters (mass, coupling, cutoff mass) for two scalar-isoscalar bosons, σ_1 and σ_2, are adjusted in each partial wave for each of the three NN interactions: proton-proton (pp), neutron-proton (np), and neutron-neutron (nn).

2.3.2 Charge Dependence

The hypothesis that the interaction between nucleons in the same spin-angular momentum state is identical for pp, np, and nn systems (correcting for the Coulomb force in the pp system) was first proposed in 1936 [Bre36]. This hypothesis is known as *charge independence*. Charge independence can also be stated as a symmetry principle of invariance under any rotation in isospin space. Any evidence of violation of this principle is referred to as *charge independence breaking* (CIB).

A less restrictive symmetry principle that the interaction between like nucleons (that is, pp and nn systems) is identical was espoused a year earlier in 1935 [Fee35]. This proposition is known as *charge symmetry* and is related to invariance under a rotation of 180° about the y-axis in isospin space where the positive z-direction is associated with the positive charge. In analogy to CIB, any violation of this principle is known as *charge symmetry breaking* (CSB).

Experimental and theoretical investigations searching for and explaining CIB and CSB have been active for many decades [Mac89]. The most direct evidence for CIB and CSB in the nuclear force comes from the singlet ($^1S_0$) nucleon-nucleon

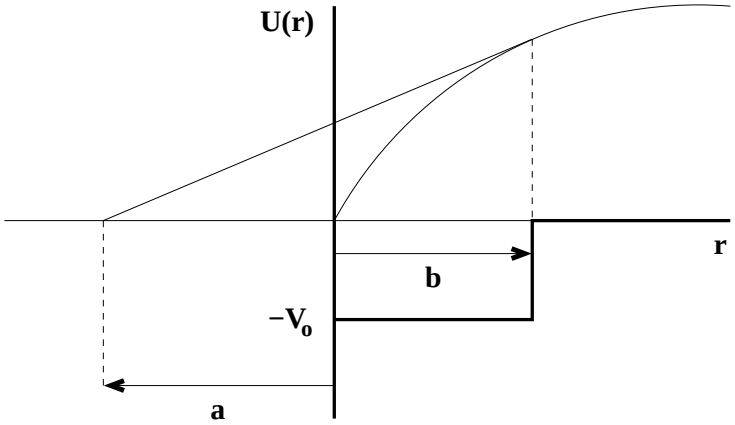

Figure 2.4: The radial wave function, $U(r)$, for an unbound two-particle scattering system is shown. The depth, $-V_0$, and range, b, of the nuclear potential are also illustrated. The radial-axis intercept of the line tangent to the wave function at the range of the potential gives the scattering length, a.

scattering lengths, a_{NN}. The scattering length is a very sensitive measure of the strength of the nuclear force. Formally, the scattering length, a, is defined in the limit of zero-energy scattering between two particles,

$$\lim_{k \to 0} \sigma = 4\pi a^2, \tag{2.14}$$

where σ is the scattering cross section. Intuitively, the scattering length can be understood in terms of the radial wave function and potential for a two-nucleon scattering system. As depicted in Figure 2.4, the scattering length is given by the radial-axis intercept of the line tangent to the wave function at the range of the interaction potential. For an unbound system like that shown in Figure 2.4, the scattering length is negative. For bound systems, a is positive.

The latest experimental values for the $^1S_0$ NN scattering lengths are

$$a_{pp}^N = -17.3 \pm 0.4 \text{ fm} \quad [\text{Mil90}], \tag{2.15}$$

$$a_{nn}^N = -18.9 \pm 0.4 \text{ fm} \quad [\text{How98}, \text{Gon99}], \text{and} \tag{2.16}$$

$$a_{np} = -23.740 \pm 0.020 \text{ fm} \quad [\text{Dum83}], \tag{2.17}$$

where the superscript N refers to the nuclear part of the interaction (electromagnetic effects have been removed from the experimental values). The differences in these scattering lengths imply that CSB and CIB are broken by the following amounts:

$$\Delta a_{\text{CSB}} \equiv a_{pp}^N - a_{nn}^N = 1.6 \pm 0.6 \text{ fm} \tag{2.18}$$

$$\Delta a_{\text{CIB}} \equiv a_{pp}^N - a_{np} = 6.44 \pm 0.40 \text{ fm} . \tag{2.19}$$

The $^1S_0$ NN scattering lengths thus show a small amount of CSB and a larger signature of CIB. The current understanding of these two effects and their treatment in the CD-Bonn model will be discussed in the following two subsections.

Charge Symmetry Breaking

The most basic cause for CSB in the nuclear force is the difference in the masses of the neutron (939.56563 MeV/c^2) and the proton (938.27231 MeV/c^2). The larger neutron mass dictates that less kinetic energy is available in the *nn* system as compared to the *pp* system. The nucleon mass difference also affects the OBE diagrams (Figure 2.1), but only by a negligible amount [Mac01]. Recent charge-dependent nuclear models (such as AV18 and the Nijmegen potentials) have only included these two effects, which together account for just 15% of the observed CSB. Li and Machleidt [Li98a] found that the major part of CSB came from irreducible two-boson-exchange (TBE) diagrams. When added with the kinetic energy and OBE effects

discussed above, calculations of CSB from 2π- and $\pi\rho$-exchange diagrams give a total measure of CSB, $\Delta a_{\rm CSB} = 1.508$ fm [Mac01], which is consistent with the empirical evaluation (Equation 2.18). Because of the significant influence of TBE on CSB, these processes are included in the CD-Bonn model through the σ_1 and σ_2 OBE parameterization that was discussed earlier.

Charge Independence Breaking

The difference in mass for the charged and neutral pions is the primary cause of CIB in the NN interaction (see Table 2.2 for these masses). The largest CIB effect comes from the one-pion-exchange (OPE) diagram and accounts for about 50% of the observed $\Delta a_{\rm CIB}$ [Mac01]. The OPE potential, $V^{\rm OPE}$, for pp scattering is given by

$$V^{\rm OPE}\,(pp) = V_{\pi^0}\ , \tag{2.20}$$

while for np scattering in the $T = 1$ isospin state

$$V^{\rm OPE}\,(np, T = 1)\ = -V_{\pi^0} + 2V_{\pi^\pm}\ . \tag{2.21}$$

These potentials would be identical if the pion masses were the same. The np potential is weaker than the pp one because of the pion mass difference, however, and thus is associated with a more negative scattering length. All modern NN potential models include this CIB effect that comes from the OPE diagram.

The pion mass splitting also contributes to CIB through 2π-exchange and other two-boson-exchange diagrams that involve pions. Calculations of these contributions by Li and Machleidt [Li98b] indicated that two-boson-exchange (TBE) accounts for approximately 20% of the CIB in the nucleon scattering lengths. Nucleon mass splitting contributes another 5% to CIB, but approximately 25% of the CIB in the

nucleon scattering length is still unexplained. The CD-Bonn potential model treats this discrepancy in a phenomenological way — the parameters of the σ_1 and σ_2 mesons are adjusted in the $^1S_0$ channel to reproduce the empirical np data [Mac01]. Other charge-dependent models do not include the TBE effects directly, but instead treat everything except the OPE contribution phenomenologically.

2.3.3 Nonlocality

The concept on nonlocality is strongly related to "off the energy shell" (off-shell) effects in the nuclear many-body system. NN potentials are constructed to reproduce the world two-nucleon scattering data and the properties of the deuteron. Given sufficient, high-quality data, these potentials can be fixed to extraordinary accuracy for "on the energy shell" (on-shell) processes. [On-shell processes are those in which the total energy of the two nucleons is the same before and after the interaction, as in free-space NN scattering.] For a nucleus with more than two nucleons ($A > 2$), the energy of the A-particle system is conserved, but that does not imply that energy is conserved in any given interaction between two nucleons in the nucleus. The two interacting nucleons may have different energies before and after they interact. Theoretical calculations of properties such as the nuclear binding energy must include the off-shell NN interaction for $A > 2$ nuclei. Unfortunately direct measurements of the off-shell NN interaction are not possible; only theory can provide this information [Mac96].

High-quality modern potentials such as AV18 and Nijm-II employ a local version of the OPE potential for the long-range part of the nuclear interaction. For example,

for *pp* scattering

$$V_\pi^{\rm loc}(\mathbf{r}) = \frac{g_\pi^2}{12\pi}\left(\frac{m_\pi}{2M}\right)^2\left[\left(\frac{e^{-m_\pi r}}{r}-\frac{4\pi}{m_\pi^2}\delta^{(3)}(\mathbf{r})\right)\boldsymbol{\sigma_1}\cdot\boldsymbol{\sigma_2} + \left(1+\frac{3}{m_\pi r}+\frac{3}{(m_\pi r)^2}\right)\frac{e^{-m_\pi r}}{r}S_{12}\,\right], \tag{2.22}$$

where m_π is the neutral pion mass and M is the proton mass. The intermediate and short-range parts are parametrized in different ways, but nevertheless rely on local functions: AV18 uses Woods-Saxon type functions while Nijm-II applies a local Yukawa formulation [Mac96]. Exponential form factors (which are also local) are used by both potentials for regularization at short distances. These local formulations are easy to use in configuration-space calculations and thus enjoy much popularity.

Local representations of the OPE potential such as Equation 2.22 are only approximations of the full relativistic Feynman amplitudes, however. The Feynman amplitude shown in Equation 2.6 is in general nonlocal because the Fourier transform into configuration space introduces functions of r and r', the relative distances between the two incoming and outgoing nucleons. The full OPE potential for *pp* scattering in momentum space is

$$\bar{V}_\pi(\mathbf{q}',\mathbf{q}) = -\frac{g_\pi^2}{4M^2}\frac{(E'+M)(E+M)}{(\mathbf{q}'-\mathbf{q})^2+m_\pi^2}\left(\frac{\boldsymbol{\sigma_1}\cdot\mathbf{q}'}{E'+M}-\frac{\boldsymbol{\sigma_1}\cdot\mathbf{q}}{E+M}\right) \times\left(\frac{\boldsymbol{\sigma_2}\cdot\mathbf{q}'}{E'+M}-\frac{\boldsymbol{\sigma_2}\cdot\mathbf{q}}{E+M}\right). \tag{2.23}$$

In the static approximation, $E'\approx E\approx M$, this equation reduces to

$$V_\pi^{\rm loc}(\mathbf{k}) = -\frac{g_\pi^2}{4M^2}\frac{(\boldsymbol{\sigma_1}\cdot\mathbf{k})(\boldsymbol{\sigma_2}\cdot\mathbf{k})}{\mathbf{k}^2+m_\pi^2} \tag{2.24}$$

where $\mathbf{k}=\mathbf{q}'-\mathbf{q}$. Note that Equation 2.24 is just the Fourier transform of the local OPE potential (Equation 2.22). One should also notice that for an on-shell process (i.e., for $|\mathbf{q}'|=|\mathbf{q}|$), Equations 2.24 and 2.23 are equivalent, showing that nonlocality only affects the OPE potential off-shell.

The obvious question that should be raised at this point is: how drastic an effect does the local approximation have? In Figure 1 of Machleidt's paper [Mac96], the half off-shell ${}^3S_1$-${}^3D_1$ amplitude that can only be produced by tensor forces is shown. Calculations with the full OPE potential (Equation 2.23) are compared to those using the static/local approximation (Equation 2.24) and clearly show that the local approximation substantially increases the tensor force off-shell [Mac96].

In Section 1.1.3, off-shell effects were mentioned as a possible explanation for the triton binding energy defect. As shown in Table 1.1, the CD-Bonn potential came closer to predicting the observed triton binding energy than two other local potentials. In fact, about 50% of the gap between predictions of local potentials and experiment is accounted for by the nonlocality of the CD-Bonn model. Similar results have been reported for calculations of the α-particle binding energy [Nog00]. The remaining discrepancy between CD-Bonn predictions and experiment may be due to further relativistic corrections (a brief discussion of this hypothesis was given in Section 1.1.3) or other sources of nonlocality. Note that the CD-Bonn potential includes only nonlocalities from meson exchange; additional contributions are expected from the nucleonic quark substructure at short-range [Sie95].

2.4 Review of 2N Scattering Theory

The Hamiltonian for a two-particle system from classical mechanics has the general form

$$H = \frac{\mathbf{p}_1^2}{2m_1} + \frac{\mathbf{p}_2^2}{2m_2} + V(|\mathbf{r}_1 - \mathbf{r}_2|) \ . \tag{2.25}$$

Making the usual operator transformation, $\mathbf{p} \rightarrow \frac{\hbar}{i}\nabla$, the Schrödinger equation for this Hamiltonian becomes

$$\left[-\frac{\hbar^2}{2m_1}\nabla_1^2 - \frac{\hbar^2}{2m_2}\nabla_2^2 + V(|\mathbf{r}_1 - \mathbf{r}_2|)\right]\psi(\mathbf{r}_1, \mathbf{r}_2) = E\,\psi(\mathbf{r}_1, \mathbf{r}_2) \tag{2.26}$$

in configuration space. A few simple substitutions,

$$\mathbf{r} = \mathbf{r}_1 - \mathbf{r}_2\,, \tag{2.27}$$

$$\mathbf{R} = \frac{m_1\mathbf{r}_1 + m_2\mathbf{r}_2}{m_1 + m_2}\,, \tag{2.28}$$

$$M = m_1 + m_2\,, \quad \text{and} \tag{2.29}$$

$$\mu = \frac{m_1 m_2}{m_1 + m_2}\,, \tag{2.30}$$

decomposes the problem nicely into the motion of the center-of-mass (CM) and motion relative to the CM. Using these substitutions, the transformed Schrödinger equation is then given by

$$-\frac{\hbar^2}{2\mu}\nabla^2\,\psi(\mathbf{r}) + V(r)\,\psi(\mathbf{r}) = E\,\psi(\mathbf{r})\,. \tag{2.31}$$

The two-body scattering problem thus becomes equivalent to the motion of one particle of mass μ under the influence of a central potential V and the free motion of the CM.

Equation 2.31 can be simplified somewhat by setting $\hbar^2/2\mu = 1$ and defining the free Hamiltonian, $H_0 = -\nabla^2$. Switching to Dirac notation, the Schrödinger equation can be written concisely as

$$(H_0 + V)\,|\psi_k\rangle = E_k|\psi_k\rangle \tag{2.32}$$

where $E_k = k^2 \geq 0$ are the eigenvalues corresponding to solutions in the continuum which describe scattering. An alternate way of writing Equation 2.32 is

$$|\psi_k\rangle = |\phi_k\rangle + G(E_k)\,V|\psi_k\rangle \tag{2.33}$$

where $|\phi_k\rangle$ is the solution of the homogeneous equation,

$$(H_0 - E_k)\,|\phi_k\rangle = 0\ , \tag{2.34}$$

and $G\,(E_k)$ is the free Green's function,

$$G\,(E_k) = \frac{1}{E_k - H_0 + i\epsilon}\ , \tag{2.35}$$

where ϵ is an infinitesimal quantity that is eventually put to zero. $G\,(E_k)$ can also be interpreted as the propagator of the state of energy E_k by the free Hamiltonian, H_0. Multiplying Equation 2.33 from the left by $G^{-1}\,(E_k) = E_k - H_0 + i\epsilon$ reproduces Equation 2.32 and shows the two representations to be equivalent.

Premultiplying Equation 2.33 by the potential, V, yields

$$V|\psi_k\rangle = V|\phi_k\rangle + VG\,(E_k)\,V|\psi_k\rangle\ . \tag{2.36}$$

An energy-dependent transition operator, $T\,(E_k)$, can then be defined such that

$$T\,(E_k)|\phi_k\rangle = V|\psi_k\rangle\ . \tag{2.37}$$

Substitution of Equation 2.37 into Equation 2.36 shows that the transition operator obeys the integral equation,

$$T\,(E_k) = V + VG\,(E_k)\,T\,(E_k)\ , \tag{2.38}$$

which is also known as the Lippmann-Schwinger equation [Lip50]. Equation 2.38 can be generalized for any energy, but $E = E_k = k^2$ corresponds to the physical scattering case. Matrix elements of the transition operator are given by

$$T_{k'k} = \langle k'|T\,(E_k)|k\rangle\ . \tag{2.39}$$

When $k^2 = k'^2$ these matrix elements are on-shell because for two-body scattering the energy k^2 must be conserved. If three or more particles are involved, however, the

two-body T-matrix may go off shell. (Matrix elements $\langle k'|T\left(E_k\right)|k\rangle$ with $k^2 \neq k'^2$ are technically termed "half off-shell" or simply half-shell, while elements $\langle k'|T\left(E\right)|k\rangle$ with $E \neq k^2 \neq k'^2$ are termed "completely off-shell". Note that completely off-shell matrix elements can be expressed in terms of half-shell ones [Pre75].)

In the asymptotic expansion of the wave function that solves the Schrödinger equation (Equation 2.32) into incident and scattered waves, the coefficient in front of the scattered wave is known as the scattering amplitude, $f\left(\mathbf{k}', \mathbf{k}\right)$, and is defined by the following equation:

$$\begin{aligned} f\left(\mathbf{k}', \mathbf{k}\right) &= -2\pi^2 \int e^{-i\mathbf{k}'\cdot\mathbf{r}'}\, V(r')\, \psi_k\left(\mathbf{r}'\right) d^3r' \\ &= -2\pi^2 \left\langle \phi_{k'}|V|\psi_k\right\rangle \\ &= -2\pi^2 \left\langle \phi_{k'}|T\left(E_k\right)|\phi_k\right\rangle . \end{aligned} \tag{2.40}$$

For elastic scattering ($k^2 = k'^2$), the scattering amplitude can simply be expressed in term of the angle, θ, between $\mathbf{k}$ and $\mathbf{k}'$:

$$f_k\left(\theta\right) = -2\pi^2 \langle \mathbf{k}'|T\left(E = k^2\right)|\mathbf{k}\rangle . \tag{2.41}$$

All the information about elastic two-body scattering is contained in $f_k\left(\theta\right)$, which is proportional to the on-shell T-matrix elements, T_{kk}. An expansion of the scattering amplitude into different angular momentum states (or *partial waves*) is often informative in studying scattering processes. The partial wave expansion of the scattering amplitude is

$$f_k\left(\theta\right) = \sum_{l=0}^{\infty} \sqrt{4\pi(2l+1)}\, \frac{1}{k}\, e^{i\delta_l}\, \sin\delta_l\, Y_l^0\left(\theta\right) , \tag{2.42}$$

where δ_l is the phase shift of the lth partial wave, and Y_l^0 is the standard spherical harmonic function.

An observable of great interest in two-body scattering experiments is the differential cross section. The scattering cross section is basically the probability that

an interaction will take place between two particles. A direct relation between the scattering amplitude and scattering cross section can easily be shown (see Sitenko [Sit91] for example); the squared modulus of the scattering amplitude determines the scattering cross section per unit solid angle:

$$\frac{d\sigma}{d\Omega} = |f_k(\theta)|^2 . \tag{2.43}$$

Substituting Equation 2.41 into Equation 2.43, the differential cross section for elastic scattering expressed in term of the T-matrix elements becomes

$$\frac{d\sigma}{d\Omega} = 4\pi^4 |\langle \mathbf{k}'|T(E_k)|\mathbf{k}\rangle|^2 . \tag{2.44}$$

Thus the procedure for calculating the scattering cross section reduces to the task of determining the T-matrix elements for a given two-body potential, V, from the Lippmann-Schwinger equation (Equation 2.38).

2.5 3N Breakup Formalism

The quantum-mechanical three-body problem is considerably more complex than the two-body one. The three particles in the exit channel of a reaction can be arranged in various configurations. For example, two particles can form a bound state while the third particle is separated by enough distance that no interaction takes place between it and the bound pair. Such a configuration is referred to as a two-body fragmentation channel. In another configuration, the three particles can be far enough apart that negligible interaction takes place between them. Such an arrangement where the three particles can be treated as free particles is known as the breakup channel. (A third configuration which is just a special case of the breakup channel exists where two of the particles may exit with equal or very nearly equal

momenta and will therefore continue to interact with each other for a long period of time. This kinematic situation is known as a final-state interaction and can cause a large enhancement in the breakup cross section.)

The Hamiltonian for the scattering of three nucleons under the influence of the nuclear potential is given by

$$H = \sum_{i=1}^{3} \left(\frac{\mathbf{p}_i^2}{2m_i} + V_i \right) + V_4 \tag{2.45}$$

where $V_i = V_{jk}$ represents a pair-wise interaction between particles j and k (that is, V_1 would represent the potential between particles 2 and 3 while particle 1 is free). The potential V_4 represents the influence of a possible three-nucleon force (3NF). This contribution will be neglected in the discussion of three-body solutions using only two-nucleon forces in Section 2.5.1. Afterwards, the effects of 3NFs on the three-nucleon equations will be discussed in Section 2.5.2.

The 2N and 3N scattering problems share the common feature that all the physics can be condensed into one operator, the transition- or simply T-matrix. As shown in Section 2.4, solving the 2N scattering problem meant determining T from the the Lippmann-Schwinger equation. The Lippmann-Schwinger equation for three particles has serious drawbacks, however, the most important being that there is no unique solution [Glö96]. Faddeev discovered that an appropriate rearrangement of the Lippmann-Schwinger equation into three coupled integral equations would remedy the problems associated with a direct approach [Fad61]. Faddeev also worked out in detail the mathematical properties of his equations [Fad65]. The three most important properties are:

1. The once-iterated kernel is connected.

2. For the short-range nuclear force, the kernel is compact. This property guar-

antees the convergence of a numerically discretized form of it [Glö96].

3. The solution of the Faddeev equations is unique.

A heuristic approach for obtaining the Faddeev equations is presented in the following section in an attempt to make the derivation more physically transparent than would be possible by a more formal algebraic method.

2.5.1 Scattering With 2N Forces Only

Consider a system of three nucleons, numbered 1, 2, and 3, where particles 2 and 3 are bound to each other (forming a deuteron) and particle 1 is free in the initial state. The three particles will interact via pair-wise forces. An infinite multiple-scattering series diagram is shown in Figure 2.5 for the breakup process, where all nucleons in the final state are free. From the diagrams in Figure 2.5, the infinite series for the breakup operator, $U_0^{(1)}$, can be expressed as

$$U_0^{(1)}\phi_1 = V_3\phi_1 + V_2\phi_1 + V_1G_0V_3\phi_1 + V_3G_0V_3\phi_1 + V_3G_0V_2\phi_1 + \cdots \tag{2.46}$$

where the initial state is denoted by ϕ_1 and the free three-particle propagator between consecutive pair-wise interactions by G_0. The structure of Equation 2.46 leads to the physical interpretation of the multiple-scattering series as a sum of contributions from processes where nucleons interact for a short time and then move freely.

The infinite series of processes represented pictorially by Figure 2.5 and mathematically by Equation 2.46 needs to be split into three parts so that a Faddeev approach can be applied. One obvious way to rearrange the terms in Equation 2.46 is to combine all processes that end with one particular pair interaction on the left.

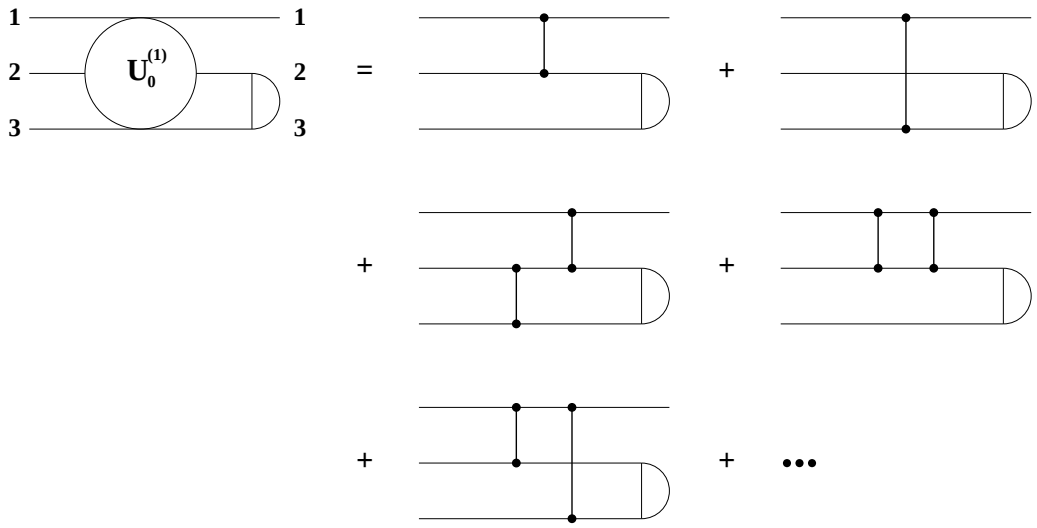

Figure 2.5: Infinite multiple-scattering series diagram for the *nd* breakup reaction. In the initial state nucleons 2 and 3 are bound together, forming a deuteron, and nucleon 1 is free. The three nucleons in the final state are all free. All of the physics of the breakup process are thus contained in the sum over terms which are composed of interactions between pairs and free propagations in between [Glö96].

The breakup operator thus becomes

$$\begin{aligned} U_0^{(1)}\phi_1 &= (V_3 + V_3\,G_0\,V_3 + V_3\,G_0\,V_2 + \cdots)\,\phi_1 + \\ &\quad (V_2 + V_2\,G_0\,V_2 + V_2\,G_0\,V_3 + \cdots)\,\phi_1 + \\ &\quad (V_1\,G_0\,V_2 + V_1\,G_0\,V_1\,G_0\,V_2 + \cdots)\,\phi_1 \\ &\equiv (U_0^{(1,3)} + U_0^{(1,2)} + U_0^{(1,1)})\,\phi_1\ . \end{aligned} \tag{2.47}$$

A little inspection reveals that the new breakup operators, $U_0^{(1,i)}$, satisfy the following system of coupled equations:

$$\begin{aligned} U_0^{(1,3)}\phi_1 = &\ V_3\,\phi_1 + &&\ V_3\,G_0\left(U_0^{(1,3)} + U_0^{(1,2)} + U_0^{(1,1)}\right)\phi_1 \\ U_0^{(1,2)}\phi_1 = &\ V_2\,\phi_1 + &&\ V_2\,G_0\left(U_0^{(1,3)} + U_0^{(1,2)} + U_0^{(1,1)}\right)\phi_1 \\ U_0^{(1,1)}\phi_1 = &&&\ V_1\,G_0\left(U_0^{(1,3)} + U_0^{(1,2)} + U_0^{(1,1)}\right)\phi_1\ . \end{aligned} \tag{2.48}$$

Grouping the breakup operators with the same second index on the left hand side, the equation for $U_0^{(1,3)}$ for example becomes

$$(1 - V_3\,G_0)\ U_0^{(1,3)}\phi_1 = V_3\,\phi_1 + V_3\,G_0\left(U_0^{(1,2)} + U_0^{(1,1)}\right)\phi_1\ . \tag{2.49}$$

Inverting the term to the left of $U_0^{(1,3)}$, Equation 2.49 turns into

$$U_0^{(1,3)}\phi_1 = t_3\,\phi_1 + t_3\,G_0\left(U_0^{(1,2)} + U_0^{(1,1)}\right)\phi_1 \tag{2.50}$$

where the quantity t_3 is defined by

$$t_3 \equiv (1 - V_3\,G_0)^{-1}\ V_3\ . \tag{2.51}$$

A little rearrangement and inspection reveals that t_3 is just the two-body transition operator for particles 1 and 2 in the space of three nucleons and that it obeys the

Lippmann-Schwinger equation (Equation 2.38). A similar treatment of the expressions for $U_0^{(1,2)}$ and $U_0^{(1,3)}$ produces a set of three coupled Faddeev equations:

$$\begin{aligned} U_0^{(1,3)}\phi_1 = &\quad t_3\,\phi_1 + \quad t_3\,G_0\left(U_0^{(1,2)} + U_0^{(1,1)}\right)\phi_1 \\ U_0^{(1,2)}\phi_1 = &\quad t_2\,\phi_1 + \quad t_2\,G_0\left(U_0^{(1,3)} + U_0^{(1,1)}\right)\phi_1 \\ U_0^{(1,1)}\phi_1 = &\qquad\qquad\quad t_1\,G_0\left(U_0^{(1,3)} + U_0^{(1,2)}\right)\phi_1\ . \end{aligned} \tag{2.52}$$

The derivation so far has treated the nucleons as identical particles, so the final step is to antisymmetrize the breakup amplitude as required by the Pauli exclusion principle. The initial state, ϕ_1 is replaced by the linear combination

$$\phi_a \equiv \phi_1 + \phi_2 + \phi_3 \tag{2.53}$$

where for ϕ_i the ith particle is free and the other two form the two-body bound state, which is assumed to be antisymmetric [Glö96]. This assumption guarantees that Equation 2.53 is antisymmetric in all three particles. Repeating this procedure for ϕ_2 and ϕ_3, the properly antisymmetrized breakup amplitude is given by

$$U_0\,\phi_1 \equiv U_0^{(1)}\,\phi_1 + U_0^{(2)}\,\phi_2 + U_0^{(3)}\,\phi_3 = \sum_i \sum_k U_0^{(k,i)}\,\phi_k \equiv \sum_i U_{0,i}\,\phi_1\ . \tag{2.54}$$

The resulting three equations for $U_0^{(k)}$ are just cyclic and anticyclic permutations of each other. Introducing a permutation operator, P_{ij}, which exchanges nucleons i and j, one finds that knowledge of only $U_{0,1}$ is sufficient to describe fully the 3N scattering problem:

$$U_{0,2} = P_{12}\,P_{23}\,U_{0,1} \tag{2.55}$$

$$U_{0,3} = P_{13}\,P_{23}\,U_{0,1} \tag{2.56}$$

A couple of more definitions to simplify notation,

$$P \equiv P_{12}\,P_{23} + P_{13}\,P_{23} \tag{2.57}$$

and

$$T \equiv U_{0,1} \ , \tag{2.58}$$

allows the Faddeev equations to be written in the compact form

$$T\,\phi = t\,P\,\phi + t\,P\,G_0\,T\,\phi \tag{2.59}$$

where the index 1 has been dropped from t and ϕ. The three-body breakup amplitude also has a simple form,

$$U_0 = (1 + P)\,T \ . \tag{2.60}$$

2.5.2 Inclusion of 3N Forces

The concept of three-nucleon forces (3NFs) was discussed in some detail in Section 1.1. Quark physics, meson theory, and relativistic treatments all indicate that 3NFs should be present in the 3N system. However, the form of such forces and the extent that they contribute to 3N observables are open questions that require investigation. Inclusion of various 3NF models into the breakup formalism described above allows calculations to be performed that show the effects 3NFs may have on different observables.

The full 3N Hamiltonian given in Equation 2.45 has a potential term, V_4, representing the influence of a possible 3NF. Inclusion of this term modifies the Faddeev equations obtained in the case of pure 2N interactions. A derivation similar to that in Section 2.5.1 can be performed to obtain these modified equations. Details of such an approach are given in references contained in the review paper by Glöckle *et al.* [Glö96]; only the final results are presented here.

Two coupled equations can be written for T, the operator describing pair-wise interactions in the 3N system, and T_4, the operator representing the irreducible

three-body force,

$$T\,\phi = t\,P\,\phi + t\,P\,G_0\,T\,\phi + t\,G_0\,T_4\,\phi \tag{2.61}$$

$$T_4\,\phi = (1+P)\;t_4\,\phi + (1+P)\;t_4\,G_0\,T\,\phi\;, \tag{2.62}$$

where the three-body t-matrix, t_4, generated by V_4 has a Lippmann-Schwinger form,

$$t_4 = V_4 + V_4\,G_0\,t_4\;. \tag{2.63}$$

Given these results, the full breakup operator turns out to be a fairly obvious generalization of Equation 2.60:

$$U_0 = (1+P)\,T + T_4\;. \tag{2.64}$$

2.5.3 Calculating Breakup Cross Sections

The scattering cross section is directly related to the amplitude, $\langle\phi_0|U_0|\phi\rangle$. The central problem for 3N scattering thus is to solve the integral equations for the T-matrix (Equation 2.59 for 2N interactions only or Equation 2.61 for 2N+3NF calculations). Once the T-matrix is known, the breakup amplitude is easily found with Equation 2.60 or Equation 2.64 and cross sections can be generated.

The initial channel state, $|\phi\rangle$, carries information about the spin quantum numbers, m_n and m_d, of the projectile neutron and target deuteron, respectively, as well as the deuteron wave function, φ_d, and the momentum, $\mathbf{q}_0$, of the neutron relative to the deuteron. This state thus takes the form:

$$|\phi\rangle = |\varphi_d\,m_d\rangle\;|\mathbf{q}_0\,m_n\rangle\;. \tag{2.65}$$

For the nd breakup process all three particles are free in the exit channel. The final channel state, $|\phi_0\rangle$, therefore describes the relative motions of the three particles and their spin quantum numbers.

The description of the relative motions of three particles is most easily accomplished through the standard Jacobi representation. A diagram of the linear and angular momentum coupling scheme used in this parameterization is shown in Figure 2.6. The Jacobi momenta are defined in the standard way by

$$\mathbf{p}_i = \frac{1}{2}\left(\mathbf{k}_j - \mathbf{k}_k\right) , \tag{2.66}$$

$$\mathbf{q}_i = \frac{2}{3}\left(\mathbf{k}_i - \frac{1}{2}\left(\mathbf{k}_j + \mathbf{k}_k\right)\right) , \tag{2.67}$$

for $ijk = 123$ and other cyclic permutations, and where the $\mathbf{k}_i$ are the individual laboratory momenta of the three particles. Any of the three pairs of Jacobi momenta may be used to describe the free motion, so the subscripts are typically dropped. The final channel state can then be written concisely as

$$|\phi_0\rangle = |\mathbf{p}\,\mathbf{q}\,m_1\,m_2\,m_3\rangle \tag{2.68}$$

with the m_i representing the spin quantum numbers of the three nucleons.

The breakup cross section can be calculated from the ratio of two quantities: the flux of particles scattered into the momentum volume elements $d\mathbf{p}$ and $d\mathbf{q}$ per unit time, and the incoming particle flux, $\mathbf{j}$. The scattered flux as determined from time-dependent scattering theory is given by

$$\begin{aligned} dN &= 2\pi\,|\langle\phi_0|U_0|\phi\rangle|^2 \int d\mathbf{p}\,d\mathbf{q}\,\delta\left(\frac{3q_0^2}{4m} + \epsilon_d - \frac{p^2}{m} - \frac{3q^2}{4m}\right) \\ &= 2\pi\,|\langle\phi_0|U_0|\phi\rangle|^2\,k_E\,d\Omega_1\,d\Omega_2\,dE_1 , \end{aligned} \tag{2.69}$$

where k_E is the phase-space factor or density of final states [Glö96]. As discussed in Section 1.2, the breakup cross section is most conveniently expressed in terms of a single variable, S, which parameterizes the kinematic locus. The phase space factor, k_E, therefore is transformed from a function of one neutron energy to a function of

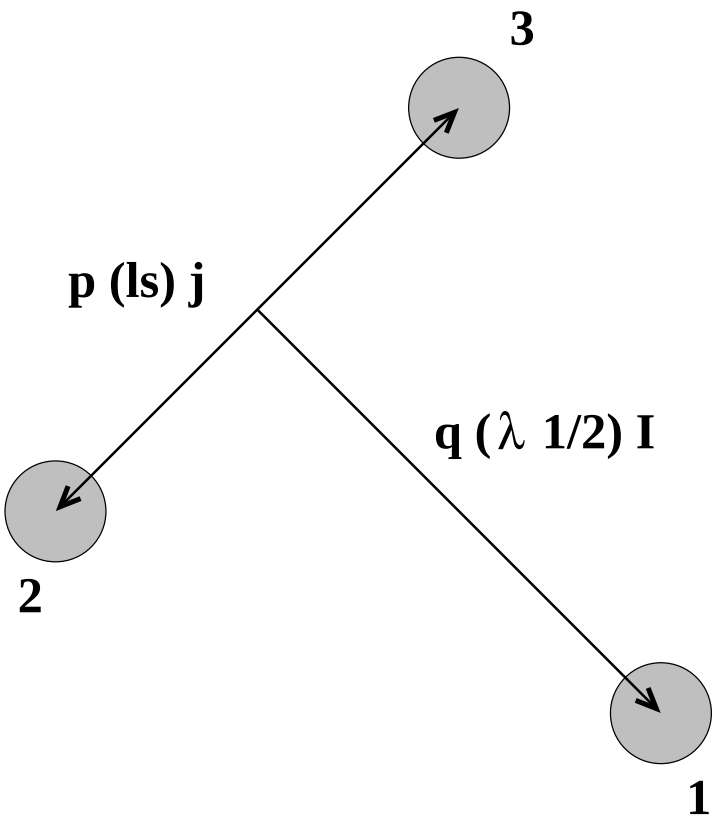

Figure 2.6: Jacobi linear and angular momentum coupling scheme for the 3N system. Particles 2 and 3 are treated as a subsystem with a relative linear momentum of p between them. The orbital angular momentum, l, and spin, s, of this subsystem couple to the total angular momentum of j. Particle 1 then couples to the center-of-mass of the 2-3 subsystem with a relative linear momentum of q. The corresponding orbital angular momentum is λ and the spin of the nucleon is $\frac{1}{2}$ which couple to a total angular momentum of I.

path length by the following expression:

$$k_S \equiv k_E \frac{dE_1}{dS} = \frac{m^2 k_1^2 k_2^2}{\sqrt{k_1^2 \left(2k_2 - \hat{k}_2 \cdot (\mathbf{q}_0 - \mathbf{k}_1)\right)^2 + k_2^2 \left(2k_1 - \hat{k}_1 \cdot (\mathbf{q}_0 - \mathbf{k}_2)\right)^2}} \ . \quad (2.70)$$

With the incoming projectile flux given as

$$|\mathbf{j}| = \frac{1}{(2\pi)^3} \frac{3|\mathbf{q}_0|}{2m} \ , \quad (2.71)$$

the five-fold differential cross section in the center of mass system is:

$$\frac{d^5\sigma}{d\Omega_1 d\Omega_2 dS} = (2\pi)^4 |\langle \phi_0 | U_0 | \phi \rangle|^2 \frac{2m}{3q_0} k_S \ . \quad (2.72)$$

Because the present work was performed with an unpolarized beam, the final magnetic quantum numbers must be summed over and the initial ones must be averaged. The averaging process introduces a statistical spin factor of

$$g = \frac{1}{(2s_d + 1)(2s_n + 1)} = \frac{1}{6} \quad (2.73)$$

where s_d is the spin of the deuteron and s_n is the spin of the neutron. The breakup cross section for an unpolarized beam and target is finally expressed as

$$\frac{d^5\sigma}{d\Omega_1 d\Omega_2 dS} = \frac{1}{6} (2\pi)^4 \sum_{m1,m2,m3} |\langle \phi_0 | U_0 | \phi \rangle|^2 \frac{2m}{3q_0} k_S \ . \quad (2.74)$$

2.6 Calculation Details

The calculations of the Bochum-Cracow theory group are performed in momentum space and in a partial-wave representation. Working in a momentum space basis is a natural consequence of using meson-exchange potentials that are derived from Feynman diagrams in momentum space (recall Figure 2.1 and the corresponding amplitude, Equation 2.6) [Glö83]. Momentum space calculations also provide a valuable

alternative to coordinate space treatments by generating independent results which can be compared for the purposes of establishing numerical levels of accuracy. Such comparisons have been performed by Friar *et al.* [Fri95] and have shown that the two approaches agree to better than 1%.

A partial-wave representation for the calculations is possible because the T-matrix can be decomposed into parts that correspond to states of fixed total angular momentum due to the rotational invariance of the 2N interaction [Glö83]. This property is advantageous for low energies where the nucleons only feel the short-range nuclear interaction in a relatively small number of angular momentum states. Empirical studies indicate that in higher angular momentum states the nucleons pass with little interaction. The partial-wave expansion can therefore be truncated at a relatively small number of terms, making the calculations more numerically tractable.

As was the case for linear momentum in the 3N system, the Jacobi scheme shown in Figure 2.6 also defines the angular momentum coupling that will comprise the partial-wave basis states. The orbital angular momentums and spins are combined to form the total angular momentum by the standard relations:

$$\mathbf{j} = \mathbf{l} + \mathbf{s} \tag{2.75}$$

$$\mathbf{I} = \boldsymbol{\lambda} + \frac{\vec{1}}{2} \tag{2.76}$$

$$\mathbf{J} = \mathbf{j} + \mathbf{I}\,. \tag{2.77}$$

The partial wave basis states of a total three-nucleon angular momentum are then given as

$$|\phi_0\rangle = |pq\,(ls)j\,(\lambda\frac{1}{2})I\,(jI)J\rangle\ . \tag{2.78}$$

The short-range nature of the nuclear interaction allows states beyond a certain total

angular momentum, j_{max}, to be neglected for the two-body subsystem. All calculations used in the present work were performed with $j_{max} = 3$. This truncation reduces the infinite system of coupled integral equations for $\langle\phi_0|T|\phi\rangle$ to approximately 60 equations.

T-matrix amplitudes that include 3NFs were calculated by the Bochum-Cracow theory group for an incident neutron energy of 16.0 MeV using the CD-Bonn potential and the Tuscon-Melbourne (TM) 3NF [Coo79, Coo93]. The 2N+3NF calculations were exact solutions of the Faddeev equations. Cross sections generated from these amplitudes were compared to 2N-only calculations (see Section 6.2.4) and demonstrated explicitly the effect that the TM 3NF has for the space-, coplanar-, and intermediate-star configurations. All partial waves up to $J_{max} = \frac{3}{2}$ were included in the 2N+3NF calculations. At the low energies in this project, this cutoff represents a sufficient number of terms for numerical convergence (note that the Bochum-Cracow group has obtained converged breakup results at energies up to 200 MeV with $J_{max} = \frac{11}{2}$ [Wit01]). The particular form of the TM 3NF used included only 2π exchange diagrams. The effect of ρ-π diagrams was found to be small and that due to ρ-ρ diagrams was negligible [Wit01]. A value of $\Lambda = 4.856\ m_\pi$ was chosen for the πN form factor cutoff so as to reproduce the experimental triton binding energy when used in conjunction with the CD-Bonn NN potential.

Further details on the technical aspects of the calculations, accuracy tests, and applications can be found in the review paper by Glöckle *et al.* [Glö96].

Chapter 3

Experimental Details

3.1 Introduction

In this experiment differential cross sections for the kinematically complete neutron-induced deuteron breakup reaction were measured for three orientations of the star plane: the space star (SST), the coplanar star (CST), and the intermediate star (IST). In addition, data for a neutron-proton (np) final-state-interaction (FSI) were accumulated simultaneously with the SST data. These measurements were made at an incident neutron energy of 16.0 MeV in the shielded neutron-source target area at Triangle Universities Nuclear Laboratory (TUNL). The momenta of the two emitted neutrons and the energy of the proton from neutron-deuteron (nd) breakup were measured, thus over-determining the reaction kinematics. The two neutrons were detected in a specially designed array of twelve liquid scintillators. The recoil proton was detected in the target scintillator, which was a C_6D_{12} liquid deuterated scintillator. A simultaneous measurement of nd elastic-scattering events

was made to provide an absolute normalization for the *nd* breakup cross section. The data were accumulated over a period of three years and represent approximately 2500 hours of actual accelerator time, about 40% of which was spent on development and 60% on production.

3.2 Ion Production and Beam Transport

The 16.0 MeV neutron beam needed for this experiment was produced via the ^{2}H(d, n)^{3}He source reaction by bombarding a deuterium gas cell with a 13.3 MeV deuteron ion beam. The ^{2}H(d, n)^{3}He reaction will be discussed in Section 3.3.1 in some detail. This section will cover the production of the deuteron ion beam, its acceleration, and beam transport to the deuterium gas cell target. For reference, a floor plan of the accelerator bay and target areas at TUNL is shown in Figure 3.1.

3.2.1 Negative Ion Source

The deuterons employed in the ^{2}H(d, n)^{3}He source reaction are produced by an ion source located on the low energy end of the accelerator bay. A 50-keV dc deuteron ion beam is extracted from the duoplasmatron of a direct extraction negative ion source (referred to as DENIS II). A schematic of DENIS II is shown in Figure 3.2 . The negative ion beam originates in the "source head" (an evacuated region including the source magnet, probe, and filament, which is held at an electric potential of 50 kV relative to ground) and is accelerated down to ground potential, thus producing an ion beam having an energy of 50 keV.

The basic premise of the duoplasmatron source is to boil off electrons from a heated cathode and bombard atoms of an injected gas to form positive and negative

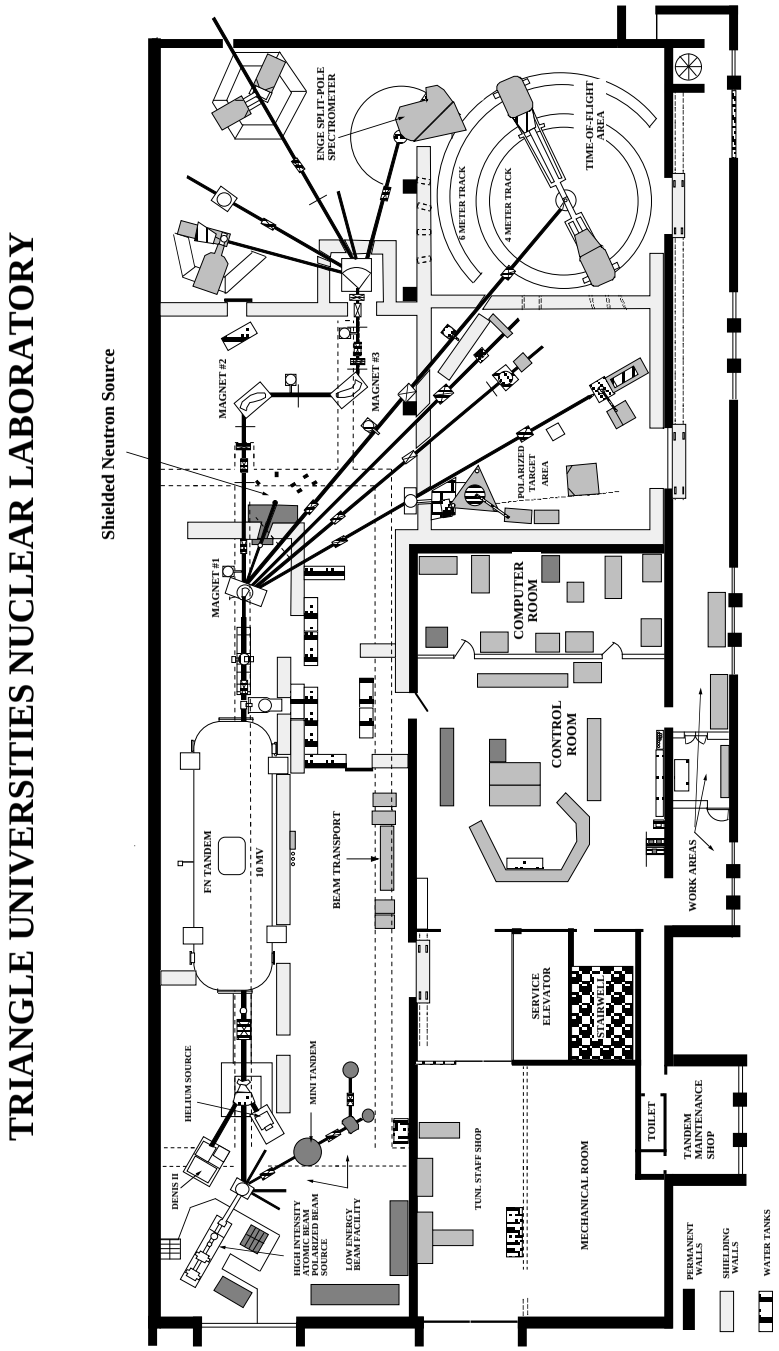

Figure 3.1: Triangle Universities Nuclear Laboratory (TUNL) floor plan. This experiment was performed in the "Shielded Neutron Source" area.

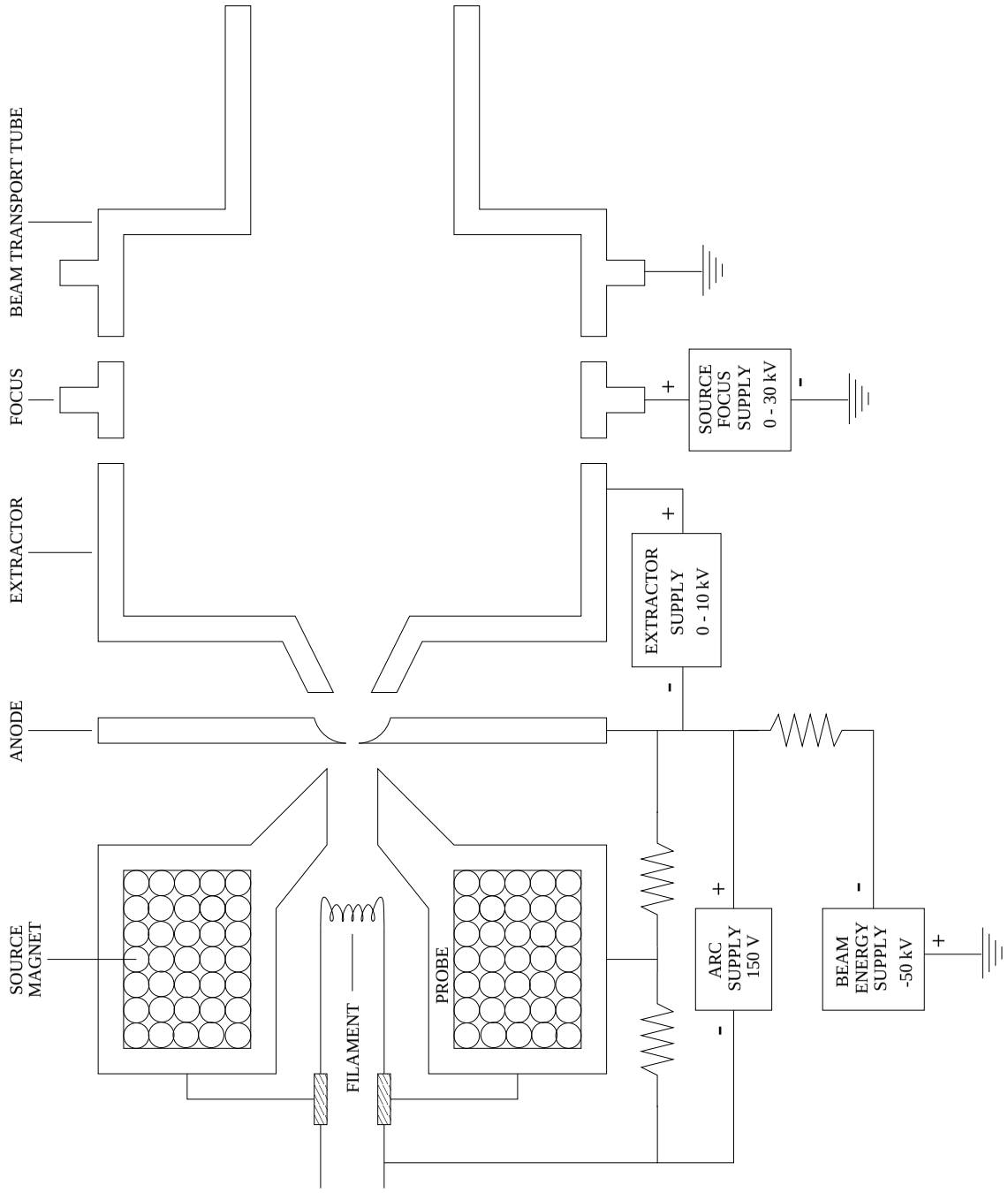

Figure 3.2: Schematic of the Direct Extraction Negative Ion Source (DENIS II) at TUNL.

ions. The heated cathode or filament in DENIS II is made of a fine nickel mesh saturated with "emission" carbonates (that is, carbonates with a very low work function with respect to thermionic emission). An arc discharge is struck between the filament and the anode electrode in a gas with a pressure of about 10^{-2} torr. The discharge is sustained by maintaining a voltage difference of about 150 V between the filament and anode electrode. Radial motion of the electrons is constrained by applying a solenoidal magnetic field in the region between the filament and the anode. For a deuteron ion beam, deuterium gas is leaked into the region between the hot filament and anode. (Hydrogen gas can instead be used for proton beams and even various species of carbon ions can be produced by mixing carbon dioxide gas with the hydrogen.) The electrons in the arc flow from the filament toward the more positive potential at the anode and collide with deuterium atoms on the way, producing a plasma of ions. An electron can either be absorbed by an atom thereby creating a negative ion, or it can knock an electron off an atom producing a positively charged ion. An intense arc of D^+ and D^- ions is thus created, with the D^+ ions forming a very dense central core and the D^- ions forming a less dense halo around the core. Most of the D^- ions are accelerated toward the anode, while some D^+ ions also move toward the anode due to potential gradients set up by space charge effects. Because the D^- ions are to be extracted, the aperture in the anode is slightly offset from the geometrical center of the source head. A high density plasma of D^- ions is thus formed in the region of the anode aperture. The large pressure gradient across the aperture causes D^- ions to migrate through the opening, creating a second plasma of ions just on the other side of the anode aperture, thus the name "duoplasmatron". Negative ions in the second region are extracted by applying an electric field between the anode and an extractor electrode. The extracted beams are then focused by an

electrostatic lens before being accelerated to the full beam-transport energy of 50 keV. An analyzing magnet downstream is used to select out the 50-keV D^- ions and to bend the D^- beam onto axis for injection into the FN Tandem accelerator. A series of electrostatic lenses and magnetic steerers are used to focus and steer the beam into the accelerator.

3.2.2 Tandem Accelerator

The accelerator used in this experiment is the model FN Tandem Van de Graaff. The fundamental principles of the FN Tandem accelerator are straightforward. A centralized metal electrode, known as the terminal, is charged to a very high positive potential. A negatively charged ion beam, such as the D^- beam from DENIS II, is transported inside an evacuated tube toward the terminal, accelerating to higher energies as it approaches the terminal. The D^- ions pass through a thin carbon foil located at the center of the terminal causing two electrons to be stripped away, leaving positively charged D^+ ions. The D^+ ions are then accelerated away from the positively-charged potential terminal, and exit the accelerator with an energy equal to the injection energy plus twice the potential energy of the ions at the terminal. The name "Tandem" refers to the two accelerations (one before stripping and one after) that the ions experience.

A schematic of the FN Tandem at TUNL is shown in Figure 3.3. The high positive potential at the terminal is established by a Pelletron charging system developed by National Electrostatics Corporation (NEC). The terminal is basically a large Faraday cage which is inductively charged by two chains. The Pelletron chains are made of metal pellets connected by insulating nylon links and are charged by an induction scheme that does not use rubbing contacts or corona discharges. For

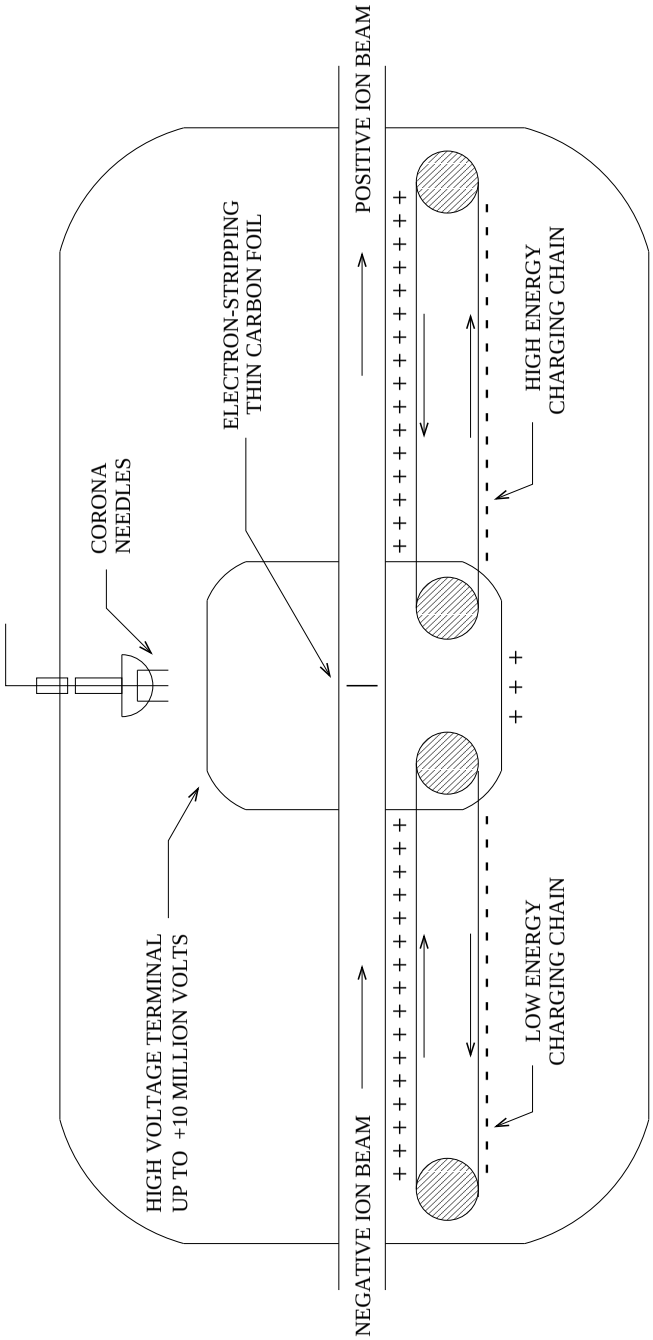

Figure 3.3: Schematic of the Model FN Tandem Van de Graaff accelerator at TUNL.

a positive terminal Pelletron, the negatively-charged inductor electrode pushes electrons off the pellets while they are in contact with the grounded drive pulley. Since the pellets are still inside the inductor field as they leave the pulley, they retain a net positive charge. The chain then transports this charge to the high-voltage terminal, where the reverse process occurs. When it reaches the terminal, the chain passes through a negatively-biased suppressor electrode which prevents arcing as the pellets make contact with the terminal pulley. As the pellets leave the suppressor, charge flows smoothly onto the terminal pulley, giving the terminal a net positive charge.

To maintain a constant and stable terminal voltage, a feedback system is needed to regulate charge deposited and removed from the terminal. A fixture of sharp metal needles (called the corona needles) mounted on a moveable arm is used to draw charge away from the terminal via coronal discharge. Control slits downstream from the 20-70 analyzing magnet (to be discussed in Section 3.2.3) provide an error signal that is used to adjust the variable resistance in the corona assembly. More or less charge is then drawn from the terminal through the corona needles to lower or raise the terminal potential as needed to maintain the desired beam energy. The terminal potential was set to a nominal voltage of approximately 6.65 MV to accelerate the D^+ beam to the necessary 13.3 MeV energy for this experiment.

3.2.3 Beam Transport

Upon exiting the accelerator, the D^+ beam is focused by a pair of magnetic quadrupole lenses and then steered into the 20-70 analyzing magnet (referred to as "Magnet #1" in Figure 3.1). The 20-70 analyzing magnet derives its name from the fact that an incoming beam can exit the magnet vacuum chamber through any of its

fixed ports that are located in the angle range from 20° to 70°. In this experiment the D^+ beam was deflected into the 20° beam line for neutron production at the "Shielded Neutron Source" target area. Located just downstream from the analyzing magnet on the 20° beam line are a pair of horizontal slits which provide accelerator control feedback. When the accelerator terminal potential is well-matched to the field in the 20-70 magnet, the beam will pass through the center of the gap between the control slits. The slits are set to intercept a small amount of beam from the outer edges of the beam envelope, so a well-centered beam will lose beam current equally to slits on opposite sides of the beam axis. If however the beam energy varies slightly due to variations in the terminal voltage, more beam will strike one of the control slits than the other. An error signal is then generated based on the difference in the slit currents, and this signal is used to adjust the amount of charge drawn from the terminal by the corona needles. After traversing the control slits, the beam particles pass through a magnetic steerer, a beam profile monitor, two sets of collimators, and then onto the deuterium gas cell target. The measurements of the beam currents on the collimators and the beam profile provide crucial information for tuning the D^+ beam to the neutron-production target.

3.3 Neutron Production and Collimation

3.3.1 Neutron Production

The dc deuteron ion beam from the accelerator was used to produce a 16.0 MeV neutron beam via the $^2\mathrm{H(d,n)}^3\mathrm{He}$ reaction by bombarding a deuterium gas cell filled to a pressure of approximately 7.8 atm. A schematic of the gas cell target used

for these measurements is shown in Figure 3.4. This gas cell was the same one as described in the dissertation of H.R. Setze [Set94]. Research grade deuterium gas with a purity of 99.99% was used in the neutron-production cell. The gas in the cell was isolated from the beam line vacuum by a 0.25 mil (6.35 μm) Havar beam-entrance foil, and the end of the cell was capped by a gold beam stop with a thickness of 0.051 cm. The beam stop was silver-soldered to the body of the gas cell which was made of copper to provide good heat conduction between the beam stop and cooling coils. Distilled water, which was cooled by the laboratory 10° C circulating water system, was pumped through the copper cooling coils to remove the heat deposited by the beam from the cell. In addition, compressed air was directed onto the beam stop and outside of where the entrance foil was located in the cell to provide further cooling. Energy losses of the deuteron beam through the gas and Havar foil resulted in a 300 keV spread in neutron beam energy. The complete assembly was electrically isolated from the rest of the beam pipe and the charge deposited in the stop by the beam was sent to ground via a beam current integrator. The integrator gave one pulse per fixed amount of charge. These output pulses (BCI) were then counted in a scaler.

The $^{2}\mathrm{H}(\mathrm{d},\mathrm{n})^{3}\mathrm{He}$ reaction is frequently used to produce neutrons in the energy range between 7 and 20 MeV because of its large cross section at 0° with respect to other neutron-production reactions [Dro78]. Other properties which make this reaction well-suited for use as a collimated neutron source are that neutrons emitted at 0° are the most energetic neutrons emanating from the reaction, and because both neutron energy and cross section decrease rapidly with increasing angle. In addition, the +3.3 MeV Q-value (the difference in the mass energies of the reacting nuclei and the reaction product nuclei) for the $^{2}\mathrm{H}(\mathrm{d},\mathrm{n})^{3}\mathrm{He}$ reaction gives more than a 5

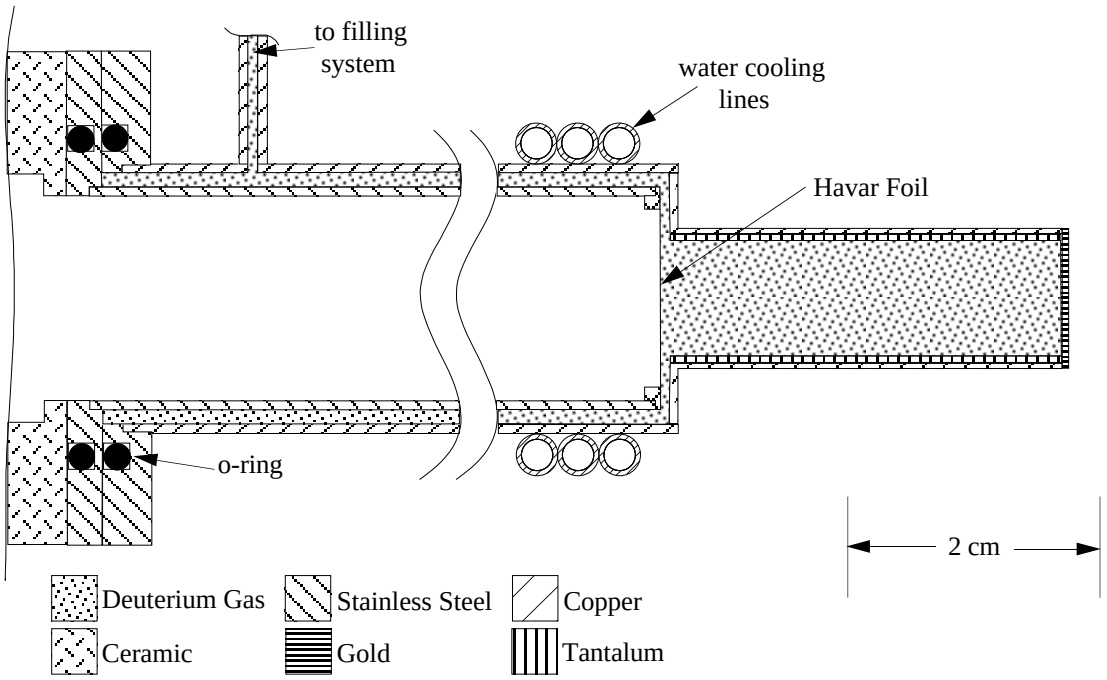

Figure 3.4: Deuterium gas cell used to generate a 16.0 MeV neutron beam from the $^{2}\mathrm{H(d,n)}^{3}\mathrm{He}$ source reaction.

MeV separation between the monoenergetic group at 0° and the continuum neutrons originating from deuteron breakup reactions in the gold beam stop or from the three- and four-body breakup reactions in the deuterium gas, ^{2}H(d, n)dp and ^{2}H(d, n)ppn, respectively.

3.3.2 Neutron Shielding and Collimation

Despite the fact that neutron energy and cross section decrease rapidly with increasing angle in the ^{2}H(d, n)^{3}He source reaction, a substantial number of neutrons are produced at all angles. These neutrons will only serve to increase accidental counting rates in detectors and further obscure the scatttering processes being studied. Traditionally neutron physics has been performed with either shielded detectors or shielded sources to reduce detector counting rates from background processes. Because shielding a large number of detectors in setups with complicated geometries is not practical, the decision was made to create the "Shielded Neutron Source" target area at TUNL (see Figure 3.1). To shield the target area from most background neutron and gamma radiation produced at the production cell and farther upstream from slits, a multi-layered wall composed of concrete, steel, iron, lead, and paraffin was designed and installed between the neutron-production cell on the 20° beam line and the target area (see Figure 3.6). As shown in Figure 3.6, an opening with a rectangular cross section allows the neutrons produced in production gas cell at 0° to reach unobstructed the center detector located on the target-area side of the shielding wall. A double-truncated collimator made from tapered rectangular copper and polyethylene bars was fitted inside the opening in the shielding wall. The collimator was designed with the purpose of minimizing the amount of neutron in-scattering from the sides of the collimator while allowing the center detector to be exposed

to a spatially homogeneous field of unscattered neutrons from the production cell. Specific details of the collimator design can be found in the dissertation of H.R. Setze [Set94].

3.3.3 Neutron Source Reaction Measurement

Previous measurements of *nd* breakup in the Shielded Neutron Source target area at TUNL were performed at an incident neutron energy of 13.0 MeV [Set94, Gon97, Sal98]. Increasing the incident neutron energy to 16.0 MeV for the measurements described here raised two important questions: (1) How "clean" would the neutron source reaction be; that is, what is the relative intensity of the monoenergetic neutrons to the neutrons with a continuum of energies from the breakup processes in the source? (2) How effective is the shielding wall for the most energetic neutrons and γ-rays? The first of these questions was addressed by measuring a time-of-flight (TOF) spectrum of the source reaction for neutrons emitted near 0°. The deuteron beam was pulsed to enable measurement of the velocity distribution of the neutrons incident on the deuterated scintillator (DS). In these TOF measurements the start signal to the time-to-digital converter (TDC) was taken from a liquid scintillator detector mounted at 0° at a flight path of approximately 5.25 m from the gas cell, and the stop signal was derived from the signal from a capacitive pickoff unit that was located immediately in front of the production gas cell. Pulsed deuterons were produced by "chopping" and "bunching" the ion beam before injection into the tandem accelerator. (A thorough description of the chopping and bunching techniques used at TUNL can be found in the dissertation of C.R Howell [How84].)

The TOF spectrum that was accumulated is shown in Figure 3.5. There is an approximately 6 MeV energy difference between the monoenergetic peak and the

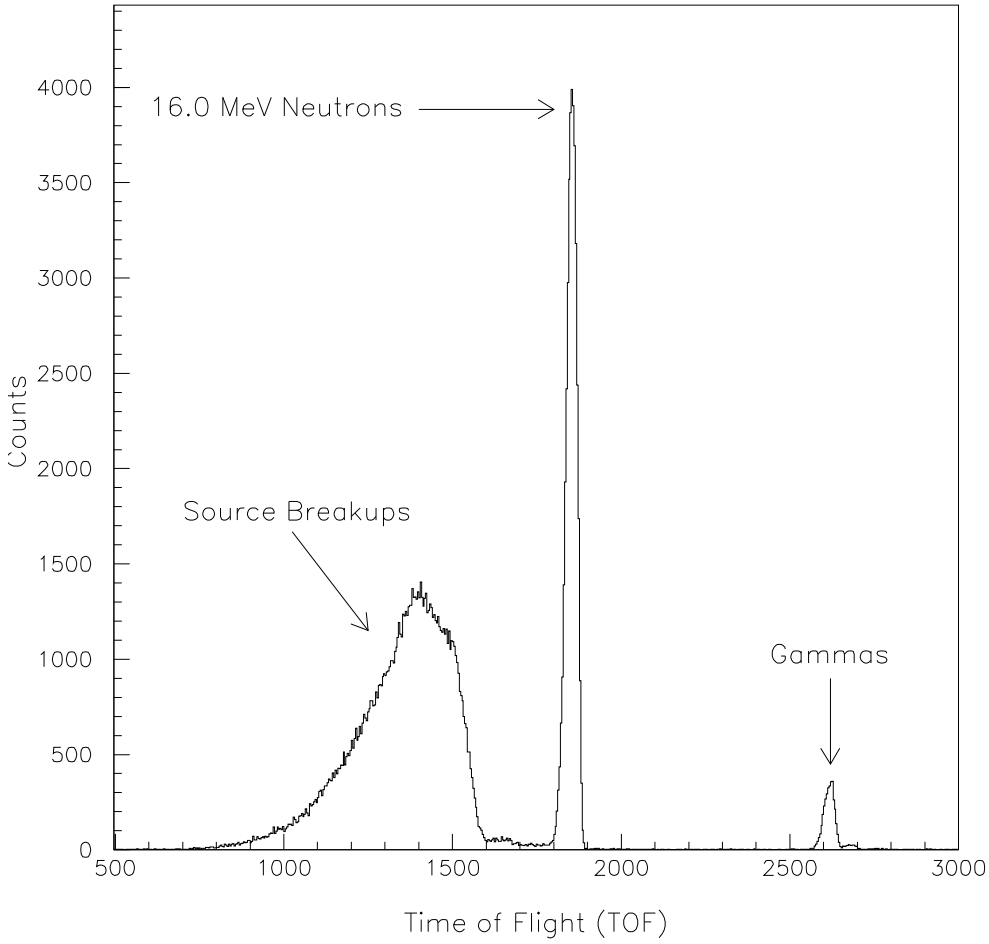

Figure 3.5: Time-of-flight spectrum for the ^{2}H(d, n)^{3}He source reaction near 0°. This measurement was made with a pulsed neutron beam. A hardware energy threshold of approximately 2 MeV and hardware gamma discrimination were applied. Time increases from right to left in this spectrum and the time calibration is 0.1 ns/channel. Earliest in time is the prompt flash of γ-rays, mostly from deuteron-induced reactions in the gold beam stop, followed by the monoenergetic 16.0-MeV group of neutrons, and finally by the continuum of "source breakup" neutrons.

rise of the continuum neutrons. The ratio of monoenergetic neutrons to continuum neutrons with energies above 2 MeV is about 1:5. The intensity of the continuum neutrons with respect to the monoenergetic peak is much larger than at 13.0 MeV. The implication of this result is that background levels will be higher in this experiment than in the previous ones performed in the Shielded Neutron Source target area, because the continuum neutrons only contribute to the background processes. A longer data accumulation time is needed at this slightly higher energy to achieve the same statistical precision goals as at 13.0 MeV.

The answer to the second question was determined by measuring the ratio of the particle flux at 0° (on the axis of the incident neutron beam) to that at the position of the inner edge (the corner of the detector at the smallest angle) of the detector. This measurement was done with a 1-cm wide by 2.5-cm high by 2-cm thick plastic scintillator detector. The flux at the inner edge of the neutron detector was 10^{-4} of that on the incident beam axis at the same distance from the neutron production cell. This ratio is the same as measured at 13.0 MeV, suggesting that the relative contributions of sample uncorrelated backgrounds will be about the same as in the 13.0-MeV experiments.

One final concern is the TOF separation of the *nd* elastically-scattered monoenergetic neutrons from the elastically-scattered continuum neutrons. This separation is critical in the technique used to determine the beam-target luminosity, which is needed to normalize the breakup cross section. Section 5.3 describes the technique used to extract the beam-target luminosity. A sample TOF spectrum for elastic scattering is shown in Figure 5.1 and indicates that the separation of the monoenergetic elastics from the continuum elastics is adequate for determining monoenergetic elastic yields without significant contamination from the continuum neutrons.

Configuration	θ_{n1}	θ_{n2}	ϕ_{12}	Average Flight Path
SST	51.5°	51.5°	120.0°	161.6 cm
FSI	51.5°	51.5°	180.0°	161.6 cm
CST	71.2°	71.2°	180.0°	129.4 cm
IST	68.6°	68.6°	150.0°	132.4 cm

Table 3.1: Detector angles and average flight paths for configurations studied.

3.4 Experimental Setup

Top and frontal views of the target area arrangement used in this experiment are shown in Figure 3.6. The detector geometries for the four breakup configurations studied in this work are listed in Table 3.1. A 16.0-MeV collimated neutron beam (described earlier) was incident on a C_6D_{12} liquid deuterated scintillator. This scintillator served as the deuterium target and as a detector for the elastically-scattered recoil deuterons and breakup protons produced therein. (Because of its location and the fact that all events were required to be in coincidence with this scintillator, it is referred to as the *center detector*.) An array of twelve liquid scintillators was used to detect the scattered neutrons from the reactions of interest. To maximize counting statistics and to measure systematic effects more accurately, a special detector mounting stand was designed and built at TUNL. The mounting stand consisted of a central bearing mechanism to which support arms for the neutron detectors were attached. The mounts on the ends of the support arms were constructed so that the detectors could be angled to point directly at the deuterated scintillator target. Each of the twelve detectors was positioned at the same scattering angle, θ, and was separated from one another by 30° in the azimuthal angle, ϕ.

As stated above, one main objective of the design of the detector array (hence

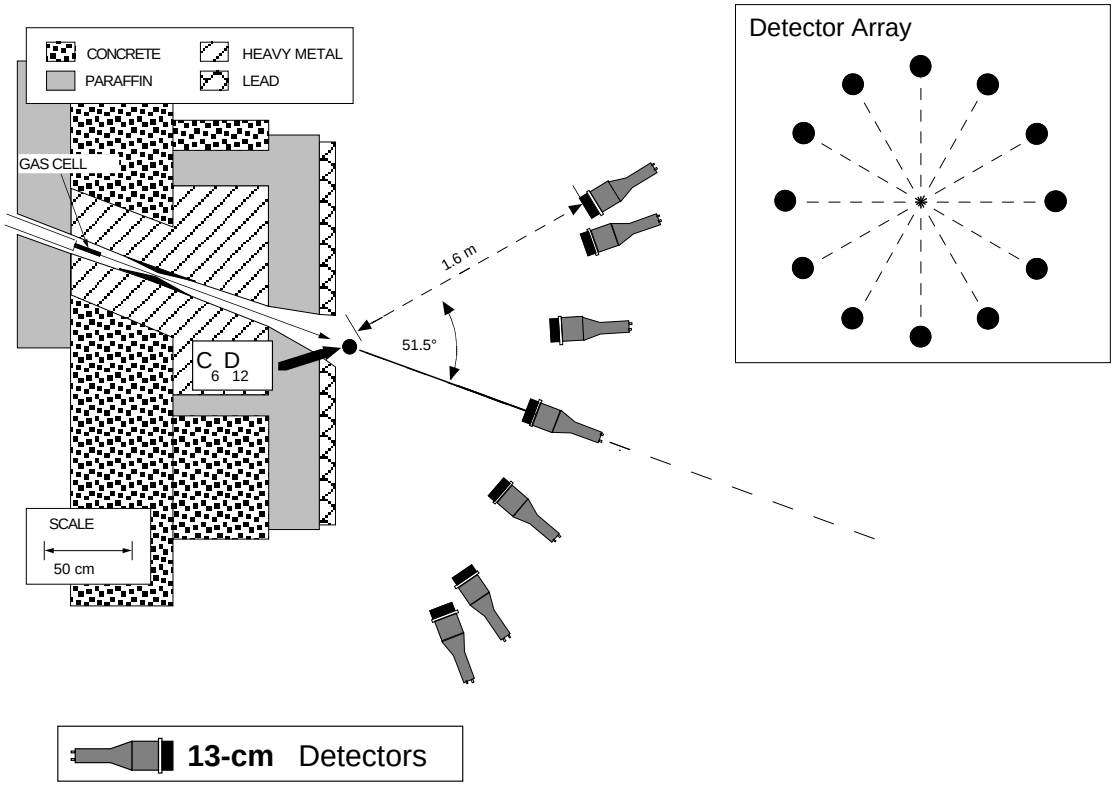

Figure 3.6: Experimental setup for measurements of the space-star cross section at 16.0 MeV. The scale for the top view is indicated in the lower left corner of the drawing. The frontal view of the detector array is not drawn to scale.

forth referred to as the "STAR" array) was to maximize counting statistics. Because all detectors directly measured the star kinematic condition, sufficient statistics (that is, uncertainties of ± 5% or better in 0.5-MeV wide bins along the S-curve) could be accumulated during one experimental run period of 10 days for configurations having average-sized breakup cross sections and normal backgrounds, such as in the case of the space star. Two experimental run periods were required to achieve the desired statistical goals for each of the coplanar- and intermediate-star configurations due to their small cross sections, resulting in lower counting rates and a worse signal-to-noise ratio than for the space star.

The other main objective was to account more thoroughly for systematic effects. The symmetry of the STAR array greatly enhances the understanding of systematics that might affect the measurement. Of particular concern is the determination of the beam-target luminosity from nd elastic scattering. Because this quantity serves to normalize the measured breakup cross section, it must be understood at the ± 1% level. With each of the twelve detectors in the array providing an independent measurement of the luminosity, deviations resulting from errors in positioning detectors, from extra scattering into detectors near the floor, and other factors should be well understood. (See Section 5.3 for more details on the determination of beam-target luminosity.)

A disadvantage to the array design is that only one star kinematic configuration can be measured at a time. Various checks must be performed with each configuration change to ensure that all of the data from the experimental runs constitutes a complete and consistent set of nd breakup cross sections. Another disadvantage is that the twelve detectors only provide one data point for the calibration of the center detector light response function. This dilemma was solved by mounting four extra

Monitor	Angle	Flight Path (cm)
1	91.0°	97.2
2	77.0°	144.2
3	66.0°	176.0
4	34.5°	220.0

Table 3.2: Angles and flight paths for the monitor detectors in the SST measurement.

detectors (referred to as *monitor* detectors) at different scattering angles. Not shown in Figure 3.6, these monitors were positioned at scattering angles on the left side of the incident beam axis (as seen by the neutron beam) and were of a slightly different type than those in the array. All the monitor detectors were mounted in aluminum holders and placed on iron stands bolted to the floor. The heights of the monitors were adjusted with the aid of a surveying telescope, so that the centers of their faces were in the horizontal plane of the neutron beam (about 1.77 m from the lab floor.) Their angles and flight paths for the SST configuration are shown in Table 3.2.

3.5 Detectors

All detectors used in these measurements can be classified as liquid organic scintillators. A scintillator is a substance that emits light in the visible spectrum via atomic and molecular transitions as the material relaxes after ionizing radiation passes through it. The most common organic scintillation materials are aromatic hydrocarbon compounds containing benzene-ring structures [Leo94]. Organic liquid scintillators consist of these materials in a solution of various organic solvents, such as xylene and toluene.

A photomultiplier tube (PMT) is optically coupled to the scintillating material

to convert the emitted light into a useable electrical signal. Light strikes a metal cathode in the PMT causing electrons to be ejected via the photoelectric effect. These photoelectrons are attracted to an emission electrode or *dynode* which is biased to a positive potential relative to the cathode by an external power supply. Secondary electrons are emitted and are accelerated to the next dynode. A typical PMT may have anywhere from 10 to 14 dynodes, each successive one at a slightly more positive electrical potential than the previous stage. This electron-multiplier network can achieve total overall gains of up to 10^7 for conventional PMTs [Leo94]. The final stage or *anode* collects the charge from the electron cascade producing a current pulse of sufficient amplitude that it can be analyzed using commercially available fast electronics.

A scintillator signal can provide a great variety of information. Some of its most important properties are:

1. *Energy Sensitivity.* Above some threshold energy the scintillator light response is directly proportional to the amount of energy deposited in the scintillating material. One of the parameters usually stored in experiments using scintillators is the detector's *pulse height*. A pulse height histogram can be built by digitizing the peak voltage of each scintillator signal or by integrating the total charge in each pulse. Standard energy references, for example, the Compton scattering edge from a γ-ray source like ^{137}Cs , provide the information needed to convert pulse-height histograms to energy spectra. Because typically only a fraction of the interacting particle's kinetic energy is deposited in scintillation detectors, methods such as time-of-flight (to be discussed in Section 3.6.1) are used in combination with particle identification techniques to determine a particle's full kinetic energy.

2. *Fast Time Response.* The rise and decay times of scintillator signals are very short compared to other types of detectors. With decay times on the order of a few nanoseconds, these fast signals make precise timing measurements possible. Furthermore, because the response and recovery times for each event are short, scintillators can handle high counting rates without incurring significant dead-times or pulse pile-up.

3. *Pulse Shape Discrimination.* The decay time constants of many organic scintillators can provide information that allow neutron and γ-ray events to be distinguished by pulse-shape analysis. Most scintillators have a fast and slow decay component to their signals, with the fast component being dominant. Materials exhibiting good pulse shape discrimination (PSD) characteristics have a substantial slow decay component. The stimulation of the slow and fast decay channels is dependent on the ionizing power, $\frac{dE}{dx}$, of the interacting particle. Neutrons, for example, are detected in scintillators through scattering from protons in the hydrocarbon chains (scattering from carbon can also be detected but the light output is much smaller). The relatively large $\frac{dE}{dx}$ of a recoiling proton produces a high density of excited molecules which results in increased intermolecular interactions [Leo94]. These interactions suppress the normal prompt deexcitation process by draining their energies through other channels. The proportion of the fast component emitted relative to the slow component is thus reduced. Events induced by γ-rays, on the other hand, are detected through the usual mechanisms of the photoelectric effect, Compton scattering, and pair production. Because the ionizing power for electrons is much smaller than for protons, the suppression of the fast decay component is lower and the overall decay time of the scintillator signal is somewhat shorter.

Figure 3.7 shows a sketch of scintillator signals for neutron and γ-ray events with the same pulse height. Section 3.6.1 will describe how these signals can be used for particle identification purposes.

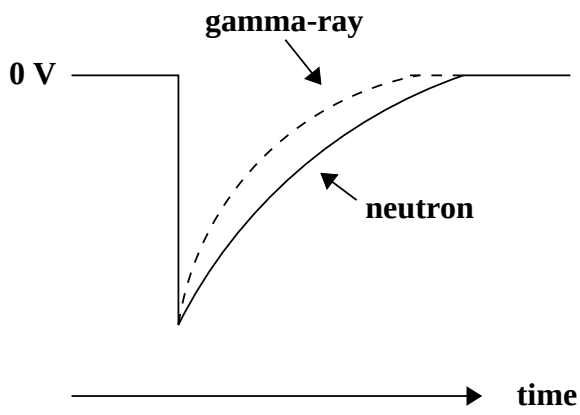

Figure 3.7: Electrical pulses for the detection of a neutron and a γ-ray with the same pulse height in a liquid organic scintillator that has good pulse shape discrimination properties. The differences in the decay times of the signals make particle identification possible.

3.5.1 Center Detector

As mentioned earlier, a C_6D_{12} liquid scintillator served as the active target in the *nd* breakup and *nd* elastic measurements and is known as the center detector (CD). This detector consists of a glass cylinder filled with Nuclear Enterprises' NE-232 scintillating fluid that was mounted upon an RCA 8575 PMT. The glass cylinder has dimensions of 6.39 cm in height, 4.19 cm in diameter, and a wall thickness of 0.2 cm. There is a small bulb on the top front of the cell to allow for thermal expansion of the fluid. The exterior of the cell is covered with white reflector paint and thin aluminum foil except on the bottom surface where the cell is coupled to the PMT. The cell is directly mounted on a PMT with a 2-inch diameter to which it is

optically coupled by a thin film of Bicron Corporation's BC-630 optical grease. A very thin ($\approx$ 0.03 cm) mu-metal shield caps the cell and PMT to maintain a light-tight environment and to shield the early stages of the PMT from stray magnetic fields.

The NE-232 scintillating fluid has a density of 0.96 g/cm^3 and a rather large ratio of 1.96 deuterium atoms for each carbon atom. Neutrons incident on the CD can interact with deuterons via *nd* elastic scattering, *nd* breakup, scatter from carbon nuclei, or pass through without interaction. Charged particles from the scattering and breakup processes travel some distance in the scintillator's active volume and lose kinetic energy. The resulting excitations decay in a few nanoseconds and emit light in the blue to ultraviolet region of the electromagnetic spectrum. The PMT converts the light into electrical pulses proportional to the kinetic energy of the recoiling charged particles.

The center detector serves two important functions in *nd* breakup measurements:

1. It provides the start signal for neutron time-of-flight between the active target and the array of neutron detectors. A stop signal from the twelve STAR detectors or one of the four monitor detectors must occur within a specific coincidence window to form an event trigger (electronics details are given in Section 3.6.2). Deuteron beam current on the gas cell was regulated to maintain the start rate from the CD at $\sim$ 400 kHz.

2. It gives a rough determination of the energies of protons in *nd* breakup and deuterons in *nd* elastic scattering. The energy resolution of the CD is very poor, approximately $\pm$ 0.5 MeV, but because the kinematics are over-determined it is sufficient for background reduction in the analysis.

Scintillating Fluid	Density (g/cm^3)	Hydrogen/Carbon Ratio	Wavelength of Maximum Light Emission (nm)
BC-501	0.901	1.287	425
BC-501A	0.874	1.212	425

Table 3.3: Some basic properties of BC-501 and BC-501A scintillation fluids. The quantities come from the Bicron Corporation's product catalog.

3.5.2 Neutron Detectors

Two different neutron detector designs were used in the star cross-section measurements. The two designs are referred to as Bicron and Argonne with the name indicating the source of the fluid containment cell. The scintillator cells for the Bicron detectors were purchased from The Bicron Corporation and filled with BC-501A liquid scintillating fluid before being shipped to TUNL. The cells for the Argonne detectors were built at Argonne National Laboratory and filled at TUNL with Bicron's BC-501 fluid. The two detector designs are very similar with only slight differences in dimension, construction, and scintillating fluid. Also, different PMTs are used in the two designs. A diagram of the two detector designs is shown in Figure 3.8. Table 3.3 shows a comparison of some basic properties of BC-501 and BC-501A scintillating fluids. Twelve Bicron detectors make up the STAR array. Four Argonne detectors are used as beam-target luminosity monitors and provide important data for calibrating the light response function of the CD.

The fluid cells for the Bicron detectors are simple aluminum cylinders with a glass window on one end and a 1-mm thick aluminum plate on the other end. The inner radius is 6.34 cm and the interior depth is 5.08 cm. A Teflon tube is attached to the fluid volume and coiled around the cell to allow for thermal expansion. Some fluid is present in the tube to prevent gas bubbles from entering the active volume of

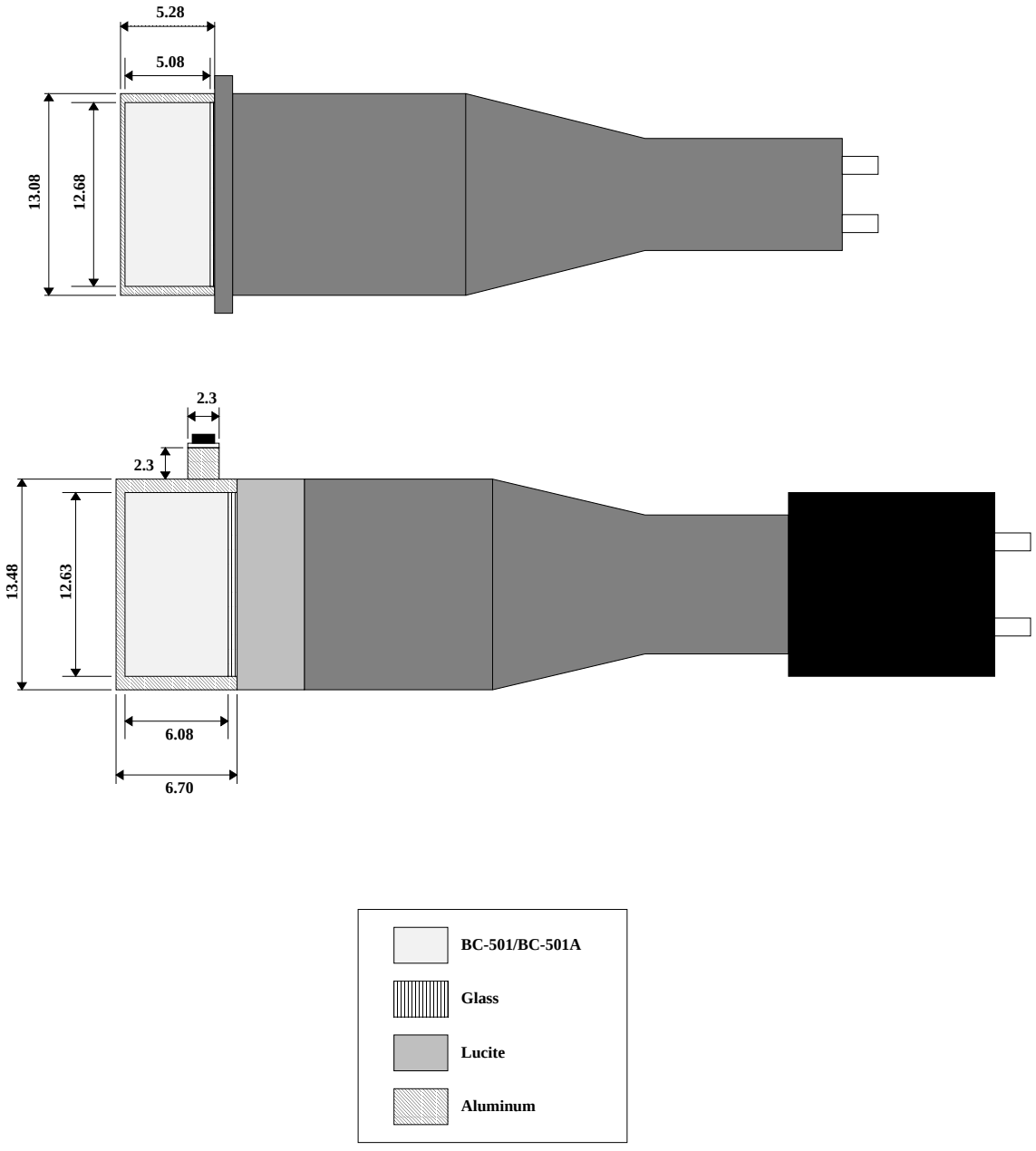

Figure 3.8: Cross-sectional view of Bicron (top) and Argonne (bottom) detectors that were used in the star cross-section measurements. All dimensions are given in cm. Note that detectors are not drawn to scale.

the cell. All interior surfaces except the glass window of the cell are coated with BC-622 reflector paint. The cell is directly coupled to a 12.7-cm diameter flat-face PMT with optical grease. The PMT used is a model R1250 from Hamamatsu Photonics. A magnetic mu-metal shield encases the phototube and base assembly. Flanges on the cell and mu-metal casing are joined with screws to secure the coupling of the scintillator cell to the PMT.

The primary differences between the Argonne and Bicron detector designs are how thermal expansion of the fluid is handled and the coupling of the scintillator to the PMT. The Argonne detectors do not have an expansion chamber; the thermal expansion of the scintillator fluid is compensated for by leaving an argon gas bubble in the cell. The use of argon or another inert gas for the bubble is important because oxygen contamination can reduce the light output of the scintillator by as much as a factor of two [Leo94]. The Argonne cells are also simple aluminum cylinders with a 0.28-cm thick front aluminum face and a 0.3-cm thick back glass plate. Their inner radius is 6.32 cm and their interior depth is 6.08 cm. Amperex model XP2041 PMTs having a 12.7-cm diameter are used with the Argonne cells. Because the faces of these particular PMTs are convex, the cells could not be directly coupled to them. Instead, each cell is coupled to a 5.0-cm thick lucite disk that has been machined on one side to match the curvature of the PMT face. This disk serves to guide the scintillator light into the PMT.

3.6 Detection Electronics

The function of detection electronics is to convert the various electrical signals from detectors into forms useful for interpreting the physical processes in an exper-

iment. A standard called NIM (Nuclear Instrument Module) was established for this purpose in experimental nuclear and high-energy physics. NIM modules manipulate both linear (analog) and logic (digital) signals. Discriminators, amplifiers, gate generators, majority logic units, linear and logic fans, and many other units are examples of NIM electronics. Using combinations of NIM modules and rf wide band pass transmission cables, a circuit can be designed to illuminate a variety of physical phenomena.

As described in Section 3.4, an array of twelve neutron detectors measuring the star kinematic condition and four neutron detectors monitoring the beam-target luminosity via *nd* elastic scattering was utilized in the present work. The detector electronics and trigger circuit are described in this section. In the following subsections, simplified circuit diagrams will be shown whenever possible to elucidate fundamental concepts. Note that the twelve detectors in the STAR array and the four monitor detectors will be generically referred to as *side* detectors.

3.6.1 Neutron Detector Electronics

Only the anode signal from the PMT of each of the side detectors was used in the detection electronics. The anode signal served many purposes:

1. It provided the stop signal for time-of-flight (TOF) measurements. The primary purpose for measuring TOF is to determine the kinetic energy of the detected neutrons. In the *nd* breakup experiments at TUNL, the center detector, as an active target, provided the start signal for a Time-to-Digital Converter (TDC). The stop signal for the TDC was derived from the anode signal of the side detectors. Given the flight path (the distance from the center of the CD to the

center of the side detector cell) and the time measurement from the TDC, the neutron's kinetic energy could be calculated.

2. It gave γ-ray and neutron discrimination. Section 3.5 described how certain scintillators produce signals with different decay times depending on the particle depositing the energy. The scheme employed in the STAR measurements took advantage of this property by using charge integration techniques. For a signal of a certain total integrated charge, more charge will be distributed in the tail of the pulse for neutron events than for γ-ray events. Measuring the total charge and the charge in the tail of a pulse was accomplished by using two channels of a charge-integrating Analog-to-Digital Converter (ADC). One channel was given a short gate (the integration starts with the leading edge and continues for the duration of the width of the gate) starting just before the arrival of the scintillator signal and having a width of approximately 50 ns. The ADC gate input required NIM logic (0 V to -700 mV). The other channel was given a long gate starting at the same time as the narrow one but having a width of 400 ns to integrate the entire pulse. Figure 3.9 shows the relative timing of the analog signal and the two gate signals. Subtracting the charge in the first 50 ns from the total charge yielded the charge in the tail. Plotting the charge in the tail of the pulse versus the total charge in a two-dimensional histogram separated the neutron and γ-rays into distinct islands (see Figure 5.2 for such a histogram). Software cuts were placed around the neutron island to eliminate the γ-ray events.

3. It was used to set a hardware lower-level detection threshold. All logic signals for a detector start with a pulse from a Constant Fraction Discriminator (CFD) module. The threshold setting on the CFD sets the minimum amplitude of an

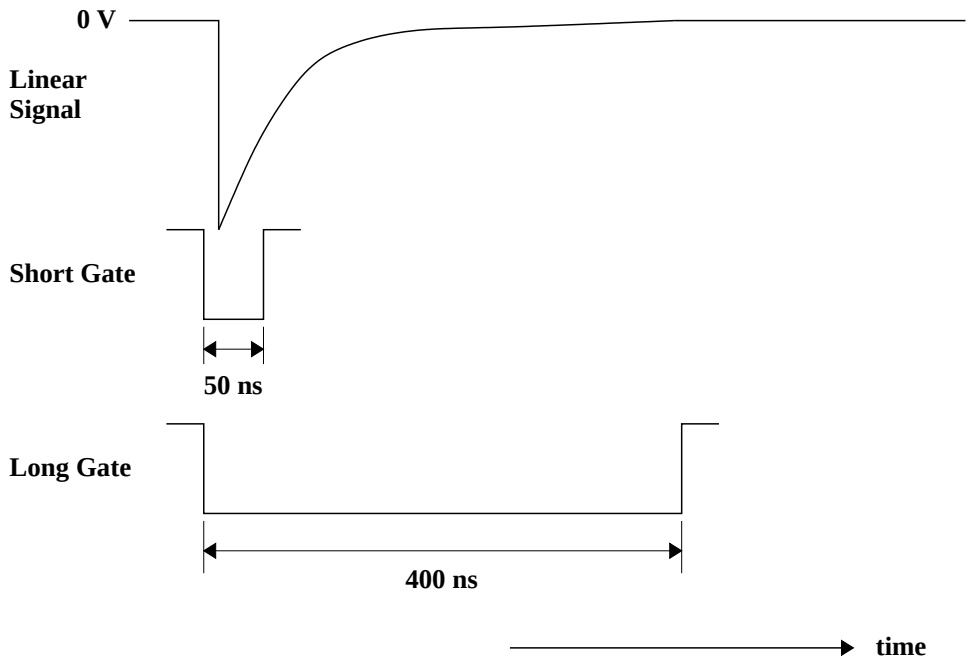

Figure 3.9: A visual representation of the time alignment of gate signals to linear signal at the input to the charge-integrating ADC in the n-γ PSD circuit.

input anode signal that will trigger an output from the module. This threshold serves to eliminate low-level electronic noise and low pulse-height background events. The pulse height of the Compton scattering edge of ^{137}Cs is used to set this threshold. For all the star detectors in the SST configuration the CFD thresholds were set just below one-third of the ^{137}Cs edge. For all other configurations the thresholds were set just below one-quarter of the ^{137}Cs edge.

4. It provided (as an output of the CFD) the timing signal for the trigger circuit. The presence of a side detector timing signal in coincidence with the delayed center detector timing signal was the first-level requirement in the trigger circuit. The alignment of the timing signals at the input to the logic modules used to form the center-side coincidence is shown in Figure 3.10. The time alignment is shown for the earliest possible real event (i.e. a γ-ray flash from a reaction

in the CD). The outputting of the center-side coincidence is determined by the CD timing. For neutron events whose origin was an interaction in the CD, the side detector signal would arrive later in time. The coincidence window permitted measurements of events with side-detector times 300 ns later than the γ-ray flash and 200 ns earlier than the γ-ray flash. With a 1.6-m flight path, neutrons with kinetic energies down to 150 keV were included in the coincidence measurements. Side detector signals arriving earlier than the prompt γ-ray flash are unphysical and must be due to time-uncorrelated events in side and center detectors. These events are referred to as *accidentals*.

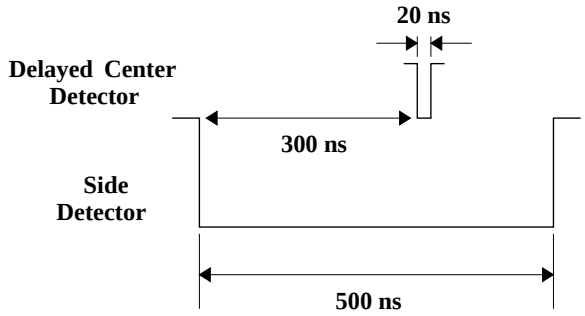

Figure 3.10: Signal alignment for the center detector-side detector coincidence. This coincidence is the first-level requirement in the trigger circuit.

Figure 3.11 is a simplified circuit diagram of the electronics for one neutron detector. The anode signal from the detector is split into two branches by a "magic tee". This passive device is a voltage divider that matches the impedance to 50 Ω in both branches. One of the linear outputs was sent through boxes of RG-58 coaxial cable to delay the signal by about 600 ns. The signal was attenuated to limit the amount of charge going to the ADCs and was passed through a 0.1 μF capacitor to filter out low frequency electrical noise. The filtered and attenuated signal was duplicated by a linear fan module. The duplicate signals were put into two ADC

channels with the long and short gates that were used for the charge integration needed for the PSD.

The other output from the magic tee went into a linear fan module where it was actively summed with a pulser signal (described in Section 3.6.5 in more detail). The linear fan output was the input for the CFD, which set the lower-level detection threshold and produced the timing signals . Next a discriminator was used to regenerate and increase the width of the CFD output signal. One of the outputs of the discriminator was delayed and sent to the TDC as a stop signal for TOF measurements. Another output ("S1") was sent to a logical AND module to form the center-side coincidence, shown in Figure 3.10. The third output was used to generate the long and short gates for the ADCs. Gate signals were only applied to the ADC when the side-detector signal was time correlated with a signal in the CD. This constraint was employed by requiring a logical AND between the delayed side-detector logic signal and the trigger signal. Separate discriminators were used to produce the long- and short-gate signals shown in Figure 3.9.

3.6.2 Center Detector Electronics

The anode signal of the center detector provided timing information from break-up and elastic scattering events. The CD anode signal was fed into a CFD, which set a pulse-height detection threshold and generated a CD timing signal. To include most of the low-energy protons in the FSI configuration, the CFD threshold was set to approximately one-eighth of the pulse height for the Compton edge of a ^{137}Cs γ-ray source (about 800 keV in proton energy). It was set slightly higher for the other configurations studied, because the proton energies were higher in these configurations. The output of the CFD served as the time reference for the event trigger

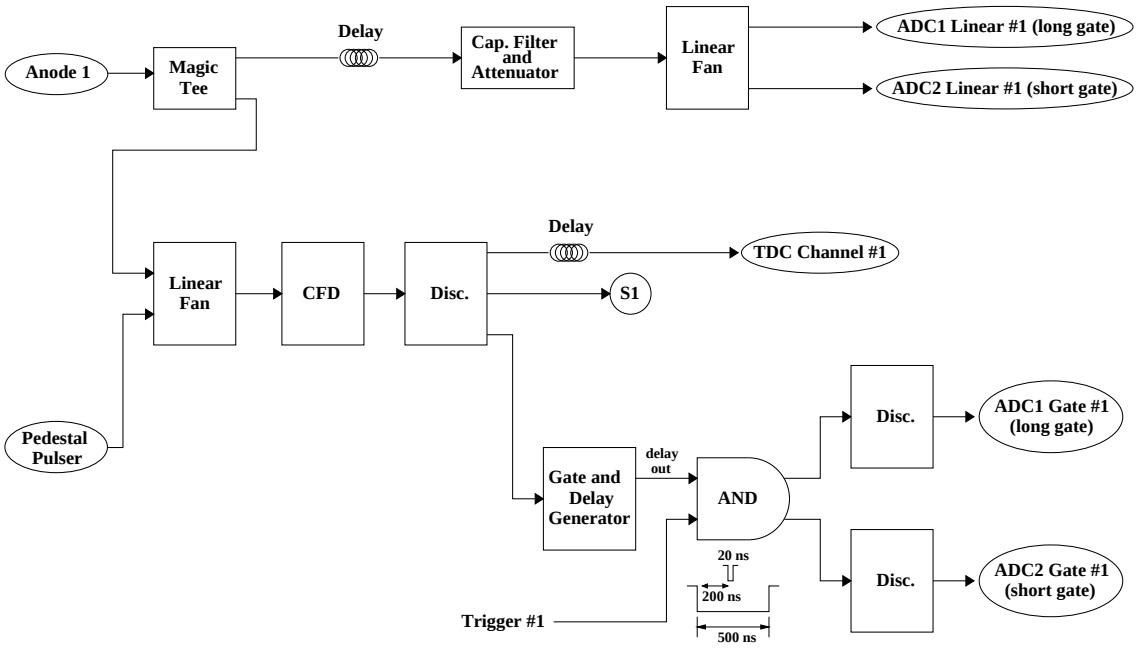

Figure 3.11: Simplified neutron detector electronics circuit for one of the side detectors.

and as the start signal for the TDC.

During the course of the experiment, the pulse-height gains and energy thresholds of the detectors were checked daily using a ^{137}Cs source. A special logic branch was used to take the pulse-height data with the calibration γ-ray sources. Because there were few side-center correlated events with the radioactive sources, it was necessary to trigger the digitizers with individual detector timing signals. A "beam/source box" served the simple function of switching a NIM-logic "TRUE" level between two outputs, either the beam position or source position. In the beam position, the CD CFD output was passed to form the first-level coincidence with the side detectors. The signal was fanned out into 16 separate signals (C1 through C16 in Figure 3.12) which were each put into coincidence with the side detector signals (for example, S1 in Figure 3.11). In the source position, the logical OR of all the neutron detector

CFD outputs was passed to form self-timing coincidences. In this mode each of the neutron detectors was effectively put into coincidence with itself to create the trigger signal for the data acquisition interface.

The dynode signal of the CD was used to generate a pulse-height spectrum. After being delayed, the positive dynode signal was inverted by a linear fan and amplified by a fast amp. The output of the amplifier went into a linear gate module that allowed the signal to pass only when a gate signal was present. The gate signal for the linear gate module was derived from the event trigger. The CD linear signal was then filtered by a 0.1 μF capacitor to reduce low-frequency noise before going to the ADC. The corresponding gate signal at the ADC was also derived from the event trigger. The presence of the linear gate circuit reduced the frequency of CD linear signals from $\sim$ 400 kHz to $\sim$ 400 Hz at the computer interface, therefore substantially reducing pile-up at the ADC.

3.6.3 Trigger Circuit

The trigger circuit had many different functions in the overall detection electronics scheme. As described in the previous two sections, the trigger circuit restricted the number of side detector gate and CD linear signals that make it to the ADCs. Other roles of the trigger circuit were to provide the start signal to the TDC and to strobe the input register that stored the event type pattern.

The input signals to the trigger circuit were the first-level center-side coincidences (designated as CS1 through CS12 in Figure 3.13). Majority logic units were employed to identify events as elastics (*doubles*) or breakups (*triples*). The presence of more than one center-side coincidence indicated a breakup event had occurred and

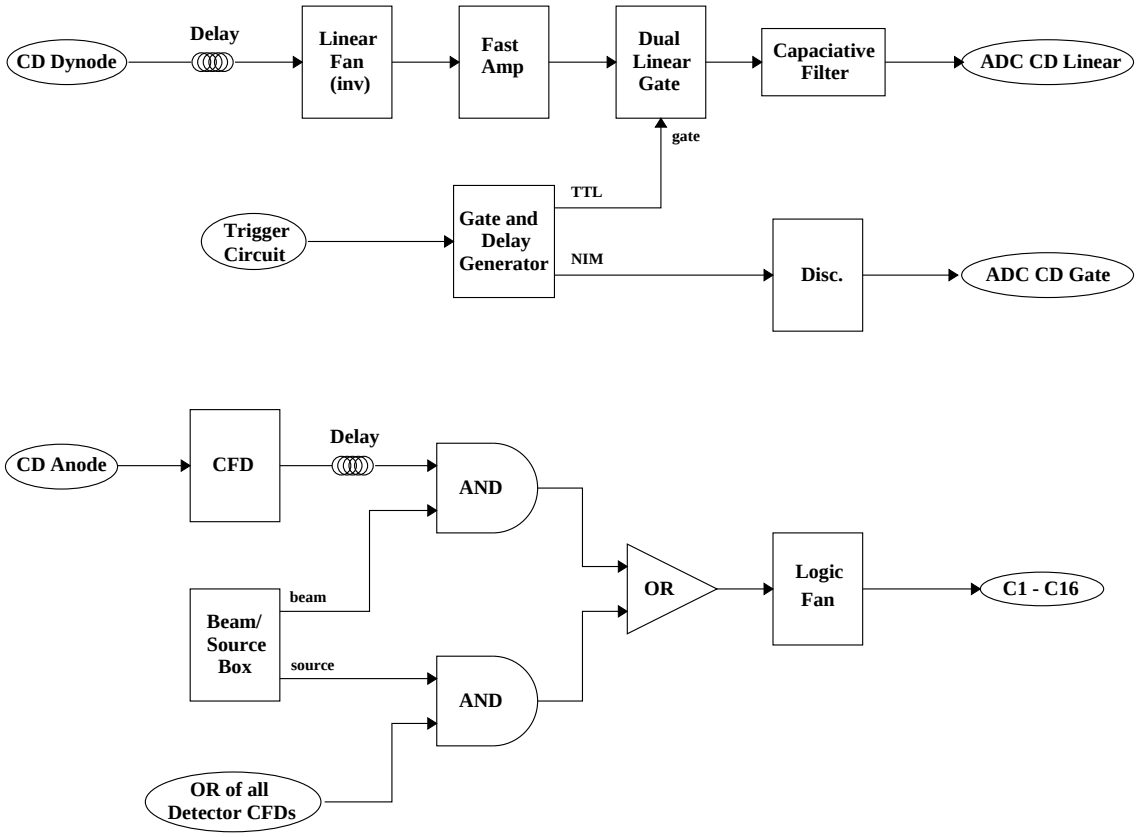

Figure 3.12: Simplified center detector electronics circuit.

generated a veto signal for the elastic branch so as not to double count an event as both a triple and a double coincidence. The logic in Figure 3.13 has been simplified for clarity; the actual units used had only four inputs. Thus, the "AND" and "OR" in Figure 3.13 are merely representations of the many AND and OR units needed to build the equivalent circuit.

Double-coincidences resulting from *nd* elastic scattering have a very large event rate. Attempting to process such a rate would cause an unacceptably large dead-time in the data acquisition (DAQ) system. A prescale circuit was used to reduce the rate of double-coincidence triggers at the DAQ system. The prescale circuit is shown in the lower branch in Figure 3.13. A gate generator was used to widen the logical signal to introduce fixed dead-time for that doubles branch. The prescaled signals were retimed with delayed double-coincidence triggers before being distributed to other parts of the trigger circuit and to the DAQ interface. Scalers were used to count the number of doubles before and after the prescale circuit. The ratio of the values in these scalers gave the prescale factor for double-coincidence events. This factor varied continuously from ~ 10 to ~ 50, depending on the incident beam current and background radiation levels due to beam tuning effects.

A circuit similar to the doubles branch in Figure 3.13 was used for the monitor detectors. The triples, doubles, and monitor triggers were used to tag the event type and to start the digitizers. As shown in Figure 3.14, a separate hit register input signal was created for each trigger type. The logical OR of all three trigger types formed a master trigger signal that was used to generate the gate for the CD linear gate module, strobe the hit register, start the TDC and ADCs, and to gate the Silena ADC. A 12-bit input (or *hit*) register was used to tag the different event trigger types. Channels in the hit register with a high NIM-logic input would have their bits set to

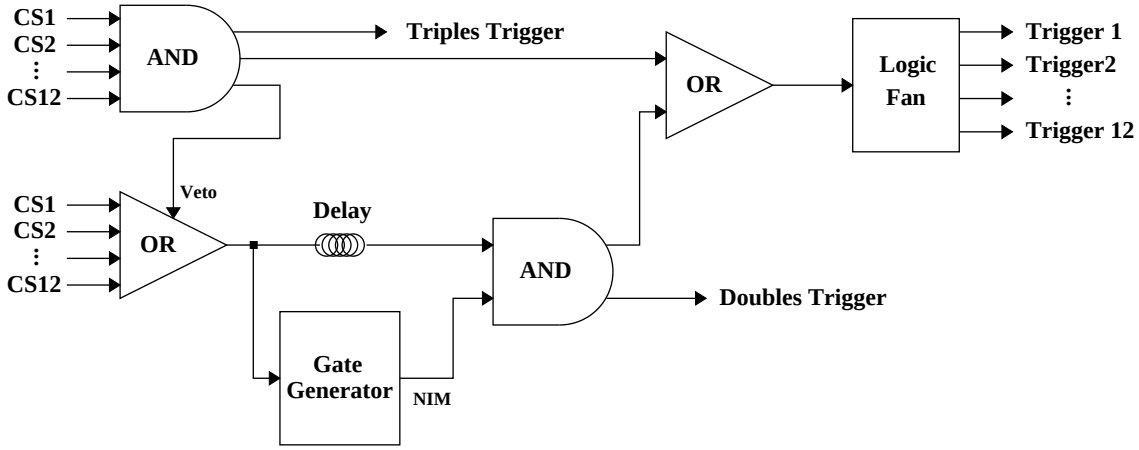

Figure 3.13: Simplified elastic and breakup trigger circuit.

"1" at the arrival of the narrow strobe signal. In addition to the three trigger types shown in Figure 3.14, a 1-Hz clock trigger (used for scaler read-out events) and two kinds of pulser events were also stored in the hit register word. A 50-ns wide start signal activated a common reference oscillator for the 16 channels of the TDC. The arrival of a signal at the input of any of the 16 channels during the 400 ns TAC (Time-to-Analog Conversion) range stopped the counter for that particular channel. The ADC "Gate Enable" signals were very wide ($\sim 1\ \mu$s) pulses that established the time window during which individual channels could integrate charge. The Silena ADC gate signal caused the module to generate a *busy* signal that was used in the veto circuit to hold off subsequent triggers until digitization and conversion of the current event was completed. No data was actually read from the Silena; its only role was to maintain the DAQ dead-time. The Silena busy was cleared after readout of all the digitizers was completed.

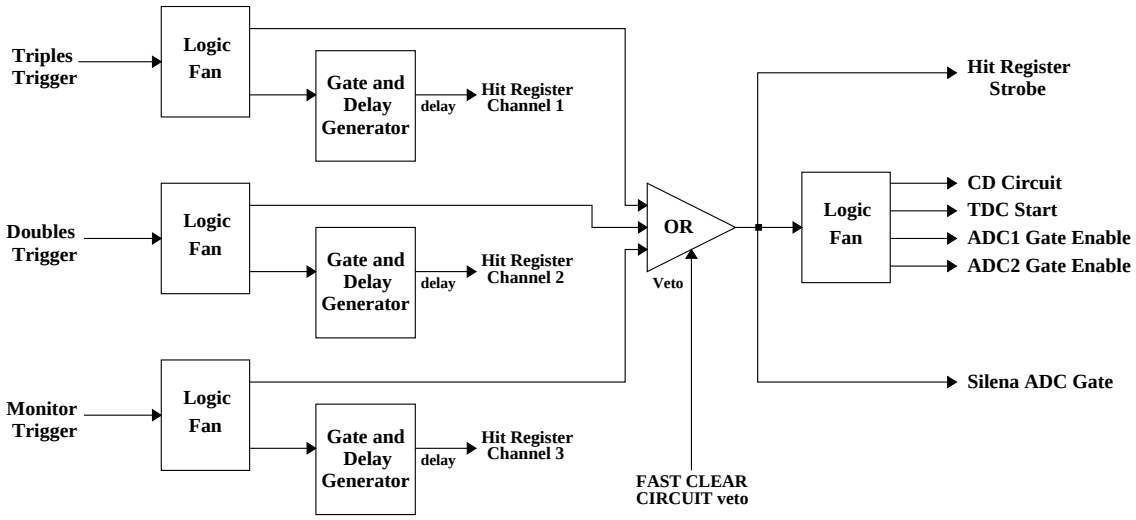

Figure 3.14: Simplified DAQ trigger circuit for event tagging and the starting of digitizing modules.

3.6.4 Veto and Fast Clear Circuit

A veto circuit was implemented to ensure that all digitizers had adequate time for full conversion before new start signals arrived. About 5 μs before the inhibit was released, a *fast clear* signal was sent to reset the hit and data registers of the TDC and ADCs. The circuit used to generate the veto and fast clear signals is shown in Figure 3.15. The DAQ busy signal was generated through a Silena ADC by giving it a gate signal at the same time the digitizers were started. This busy signal remained active while all digitizers were read. The last step in the readout software was to clear the Silena's LAM (Look-at-Me), which stopped the DAQ busy signal. The fall of the DAQ busy signal (usually about 500 μs after the arrival of the Silena gate) generated the fast clear signal. The veto was maintained for approximately 5 μs longer to give the TDC and ADCs enough time to reset completely. The relative timing of the signals involved in the veto and fast clear circuit is shown in Figure 3.16. Additional inhibit signals were fanned into the veto to hold off data acquisition

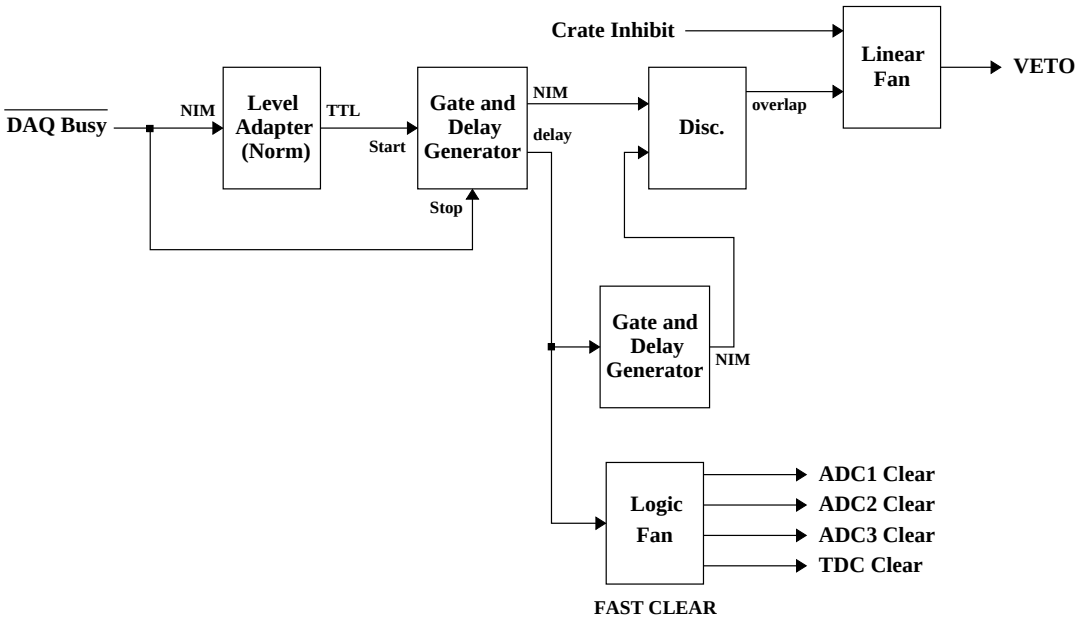

Figure 3.15: Simplified veto and fast clear circuit.

when the beam current went too low or too high or when the preset scaler indicated the end of a run.

3.6.5 Pulsers

When using charge-integrating ADCs for measuring detector pulse heights, any dc level on the linear signal results in a pulse-height offset or *pedestal*. The values of these pedestals must be known accurately to set pulse-height thresholds. The ADC pedestals were continuously sampled during the data taking by gating the ADCs with signals from a pulser that was uncorrelated with the detectors. As shown in Figure 3.17, the pulser was a gate generator that was operated in a self-starting mode (achieved by connecting the NIM output to the start input). The

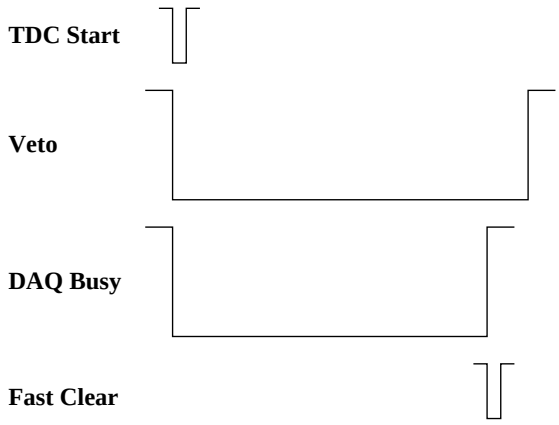

Figure 3.16: Relative timing of signals involved in the veto and fast clear circuit.

width of the NIM output signal was set to generate pulses at a rate of about ~ 1 Hz. The pulser signal was fanned into the side and center detector circuits to satisfy the first-level coincidence requirement. The detector ADC gate signals that were generated from the pulser were uncorrelated in time with any real detector pulses, thus effectively sampling the dc background level on the ADC linear signals. Because the ADCs require negative inputs, only negative dc levels could be measured with this technique. An attempt was made to adjust the front-panel offsets of the last linear fans before the ADCs (see the top right corner of Figure 3.11) to give the linear signals a slight negative level, making it possible to measure the pedestals.

In addition to the pedestal pulser, two LED pulsers were used to monitor the electronics system. Analysis of LED pulser events provided a check on the measurement of data acquisition dead-times and also gave a measure of the TOF "false starts", which are due to the high counting rate of the CD. The LED signals were fed into

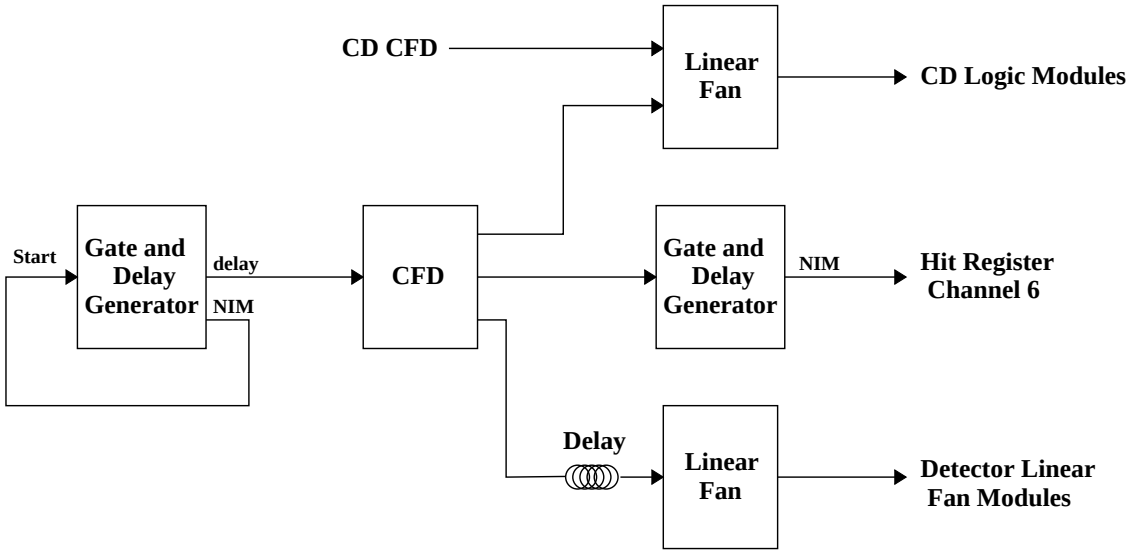

Figure 3.17: Pulser circuit used to measure pulse-height pedestals.

the PMTs of three neutron detectors and the center detector via fiber optic cable. Two independent LED pulser drivers were used, one to simulate double-coincidence events and the other to simulate triples. Fiber optics were attached to detector 4 and the CD for doubles and to detectors 2 and 10 and the CD for triples. The triples pulser driver was set to a repetition rate of $\sim$ 5 Hz while the doubles pulser driver was set somewhat higher to compensate for the prescaling of the elastic triggers. Sync signals from the drivers were sent to the hit register to tag the LED pulser events.

3.7 Data Acquisition

In the previous section the NIM-based electronics used in the shaping and timing of signals from detectors were described. Here the system used to digitize the physical quantities (TOF and pulse height) and to count the logical signals will be

described. The digitization and counting was done using CAMAC (Computer Automated Measurements And Control). The data were stored event by event for off-line analysis. (The large amount of data that was accumulated during experimental runs necessitated compressing the event files and then transferring them from computer hard disk to CDROM media every 24 hours. Backups of multiple CDROMs were subsequently made to magnetic tapes.) Parameters that were recorded for each event included event type, time-of-flight (TOF) and long and short pulse heights (LPH and SPH) for the neutron detector(s) involved, and center detector pulse height (CDPH). The event type was recorded in the data word from a BiRa Model 2351 12-bit input register ("hit register"). The TOF was digitized by a Phillips Model 7186 12-bit, 16-channel Time-to-Digital Converter (TDC). The pulse-height signals were digitized in two Phillips Model 7167 12-bit, 16-channel charge-integrating Analog-to-Digital Converters (ADCs). The CDPH was recorded in a Lecroy Model 2249W 11-bit, 12-channel charge-integrating ADC.

The experiments described in this dissertation were the first at TUNL to utilize the CEBAF Online Data Acquisition (CODA) software. CODA was developed at Jefferson National Laboratory (which is the site of CEBAF) as a modular and scalable Unix-based system using modern network hardware (such as Ethernet) and protocols (TCP/IP). A block diagram of the DAQ hardware in the present setup is shown in Figure 3.18. A Sun Microsystems Sparc Ultra-1 workstation was used as the host computer, and a single-board computer (SBC) residing in a VME crate controlled the event readout and the event data flow through a VME-CAMAC interface module. Currently the SBC is a Motorola Model MVME-162 with a series 68020 (33 MHz) processor. A Model 8210 branch driver by Creative Electronic Systems (CES) in the VME crate interfaces to the CAMAC A-2 crate controller through a standard branch

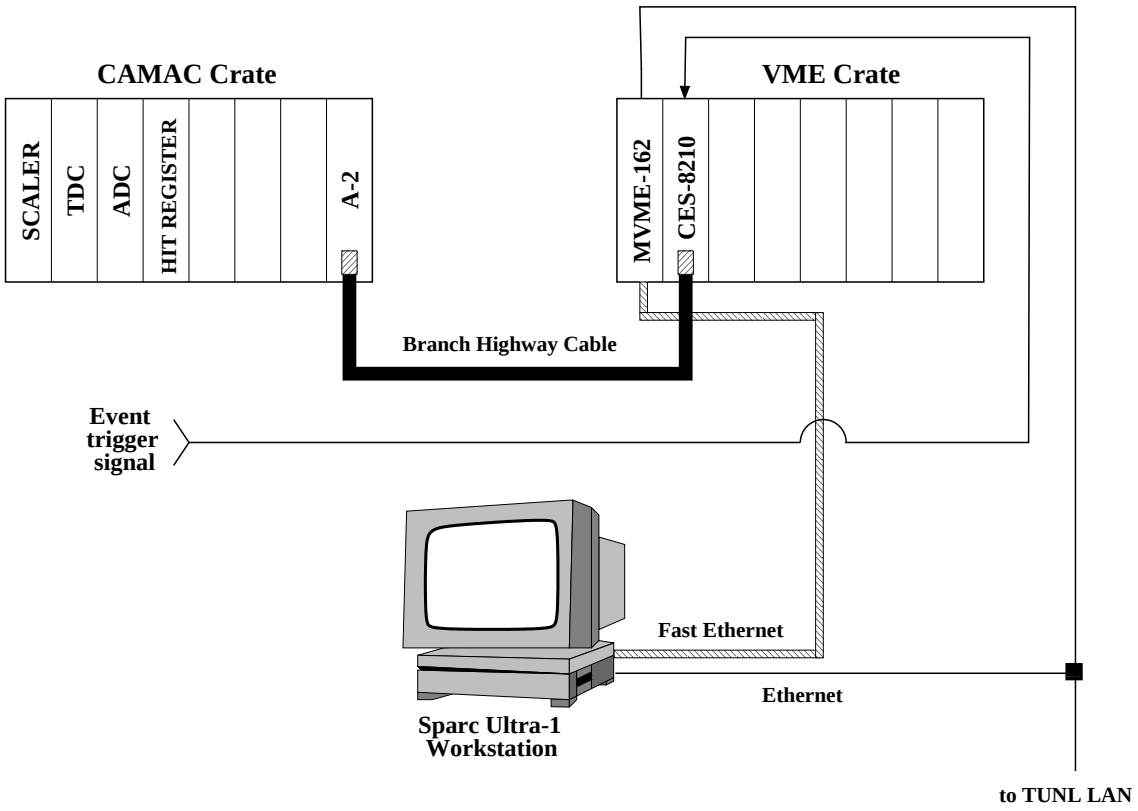

Figure 3.18: Block diagram of data acquisition hardware used in conjunction with CODA software in this experiment.

highway cable. A trigger signal generated in the experimental electronics strobed the CES-8210 causing data from the digitizer modules in the CAMAC crate to be read out. The data are then buffered in the MVME-162 memory and transferred to the DAQ host workstation over Ethernet using standard TCP/IP protocol.

Many days were needed in the early experimental runs to resolve configuration issues between the CODA software and the new hardware setup. Also much time was spent writing the user-specific routines for acquisition and analysis. Finally, before moving into "production" mode, work was necessary to improve the performance and stability of the CODA DAQ system. The average event and data rates were

approximately 420 Hz and 30 kilobytes/sec, respectively, with about a 6% system dead-time.

Chapter 4

Monte-Carlo Simulations

4.1 Introduction

Accurate computer simulations were needed in the *nd* elastic and *nd* breakup analyses to account for effects such as finite geometry, beam-energy spread, and detector time and energy resolution. Monte-Carlo techniques were employed in these simulations which served to facilitate the data analysis and also aided in interpretation of the end results. The three primary goals of the computer simulations were:

1. To calculate the contribution of multiple scattering (MS) events to the center detector pulse-height spectra for *nd* elastic scattering.

2. To generate acceptance- and energy-averaged correction factors for neutron attenuation and detection efficiencies in both the elastic-scattering and breakup measurements.

3. To average theoretical predictions over the finite geometry and energy resolu-

tion of the experimental setup so that direct comparisons of data and theory can be made.

Two separate FORTRAN codes were used for the elastic and breakup simulations. The basic principles common to the two codes will be discussed in Section 4.3.1. Details specific to each scattering process will be described in Sections 4.3.2 and 4.3.3. A description of tests performed to check the accuracy of the breakup code for new detector geometries is given in Section 4.4. The breakup simulations required large libraries of *nd* breakup cross sections for each of the configurations that were studied. The creation of these libraries will be outlined in the following section.

4.2 Cross-Section Libraries

Extensive libraries of *nd* breakup cross sections were generated for the configurations of interest. These libraries were required to span the kinematic regions allowed by the finite geometry of the experimental setup and the energy spread of the incoming neutron beam. Each library stores cross sections at anywhere from 10^5 to 10^6 grid points depending on the sensitivity of the configuration to small changes in angle and energy.

The Monte-Carlo libraries consist of text files which contain point-geometry cross sections that are specified by the incident neutron energy, E_{n0}, and the outgoing neutron production angles, θ_{n1}, θ_{n2}, and ϕ_{12}. Fixing these four parameters determines a kinematic locus, or S-curve. The differential cross sections in each library file are generated in 0.1-MeV steps along this S-curve, starting at the point where the energy of the second neutron is zero. Cross sections are calculated from T-matrix

amplitudes that have been computed by the Bochum-Cracow group. These amplitudes come from rigorous three-nucleon (3N) calculations made utilizing a Faddeev scheme [Glö96]. Amplitudes can be generated for various modern nucleon-nucleon (NN) potential models; all the libraries used in this experiment are based on the charge-dependent Bonn-B NN potential (CD-Bonn) [Mac01]. A FORTRAN code was provided by the Bochum-Cracow group to calculate *nd* breakup cross sections from the T-matrix amplitudes. The Monte-Carlo libraries were generated at TUNL on a PC running the Linux OS with a 600 MHz Alpha processor. Building the libraries for one configuration took approximately three hours of CPU time. This performance compares favorably to calculations done on Cray Y-MP supercomputers for previous experiments of this type.

The libraries were created to span the angular and energy extremes present in the experimental setup. Calculations of the minimum and maximum values of θ_{n1}, θ_{n2}, and ϕ_{12} allowed by finite geometry were performed. An extra tolerance of 0.5°-1.0° was added to these values to ensure the library covered the full kinematic regime. As described in Section 3.3.1, the neutron beam has an energy spread of about 300 keV due primarily to losses in the deuterium gas of the production cell. Cross-section libraries were generated at three discrete incident neutron energies: E_{n0} = 15.85, 16.00, and 16.15 MeV. Finer energy steps were not necessary because the cross sections for all the configurations studied were slowly varying with respect to incident neutron energy. The angular grid spacing used was determined by restricting the cross-section variation between neighboring angles to be less than 4%. Table 4.1 summarizes the angular range spanned and step size used by the libraries for each breakup configuration.

Configuration	θ_{n1} (°)	$\Delta\theta_{n1}$ (°)	θ_{n2} (°)	$\Delta\theta_{n2}$ (°)	ϕ_{12} (°)	$\Delta\phi_{12}$ (°)
SST	46.0-57.0	1.375	46.0-57.0	1.375	109.0-131.0	2.75
FSI	47.0-56.0	0.750	47.0-56.0	0.750	172.0-180.0	1.00
CST	67.2-75.2	1.000	67.2-75.2	1.000	172.0-180.0	1.00
IST	64.6-72.6	1.000	64.6-72.6	1.000	140.0-160.0	2.50

Table 4.1: Angular range and step size for theoretical calculations used to generate the *nd* breakup cross-section libraries for the Monte-Carlo simulations.

4.3 Monte-Carlo Codes

4.3.1 Basic Principles

Both the elastic and breakup simulation codes shared common techniques. Every event that was generated was forced to interact in the center detector (CD). This forced-scattering technique was employed for computational efficiency. Weighting factors that account for the various scattering probabilities are included at the end to normalize properly the different processes that were simulated. Each incident deuteron on the neutron production cell created a neutron that interacted in the CD. Depending on which code is used, the reaction is either an elastic scattering into the angular acceptance of a particular neutron detector, or a breakup event with the neutrons emitted in the direction of two chosen detectors. Each event is started by randomly selecting three points: the first one in the production cell, the second one inside the CD, and the third in one neutron detector. For breakup events, a fourth point is chosen in a second detector. The 300-keV spread in the incident neutron energy from the production cell is modeled by a linear function such that the energies of the produced neutrons vary from the minimum to the maximum value depending on the position in the cell where the neutron was produced. The neutron produced in the cell is then transported to the interaction point in the CD. The attenuation of

the incident neutron through the glass container and in the scintillator fluid of the CD is calculated. After this stage, the differences in the elastic and breakup codes are significant enough to warrant separate discussions.

4.3.2 Simulation for Elastic Scattering

The net yields for *nd* elastic scattering, which are used for the luminosity determination, are taken from the counts in the CD pulse-height spectra. The primary purpose of the elastic scattering simulation is to estimate the background in the CD pulse-height spectra due to events caused by neutrons that scatter multiple times in the CD. Before multiple scattering (MS) processes are considered, *nd* elastic single scattering (SS) is used to determine the time and energy resolution parameters needed as input to the code to reproduce experimental spectra. For all simulated events, several quantities are recorded: the pulse height in the CD, the neutron time-of-flight (TOF), the neutron detection efficiency, the neutron flux transmission from the interaction point in the CD to the front face of the detector, and a probability weighting factor that accounts for the cross section of the scattering process and the energy spread in the CD. The scattering angle is determined from the vector defined by the line connecting the point in the CD with the point in the neutron detector. Given the scattering angle and incident neutron energy, the energies of the recoil deuteron and the scattered neutron are calculated from two-body kinematics. The deuteron energy is converted to pulse height using the measured CD light response function. This pulse-height spectrum is then convoluted with a skewed Gaussian function in an attempt to match the resolution of the CD. The neutron TOF is calculated from the neutron energy and also convoluted with a Gaussian distribution to try to reproduce the net time resolution of the CD and neutron detector.

Single Scattering

Section 5.3.1 gives a detailed description of the procedure used to obtain the elastic yields from the experimental spectra using combinations of gates and simulated results. A brief summary with emphasis on the steps involving the simulation is given here. The first task in the analysis of the elastic scattering data is to reproduce the experimental elastic TOF peak by adjusting the width of the Gaussian smearing function in the simulation. The centroid of the simulated peak is also adjusted to match the experimental one and a normalization factor is applied. Figure 4.1 shows the results of this procedure for one detector in the SST configuration.

The next step is to determine the input parameters necessary in simulating the center detector pulse-height (CDPH) spectrum. The experimental CDPH spectrum is accumulated for events falling in the elastic TOF gate shown in Figure 4.1. A histogram for accidental events is filled concurrently by setting a gate in the unphysical region of the TOF spectrum. These accidentals are subtracted and the remaining background is fit with an exponential function. After subtraction of this residual background, the parameters of the skewed Gaussian function in the simulation are adjusted to reproduce the remaining peak which is presumed to be solely due to single *nd* scattering. Figure 4.2 shows the relatively good agreement between experimental and simulated spectra for one detector in the SST configuration.

The centroid of the simulated spectrum is determined by the measured CD light response function (see Section 5.3.3). If the centroid of the simulated spectrum does not align with the experimental one, then the scattering angle of the detector is likely different from the nominal angle for the configuration. Because of the difficulties in surveying the angles of the out-of-plane detectors in the STAR array, the Monte-

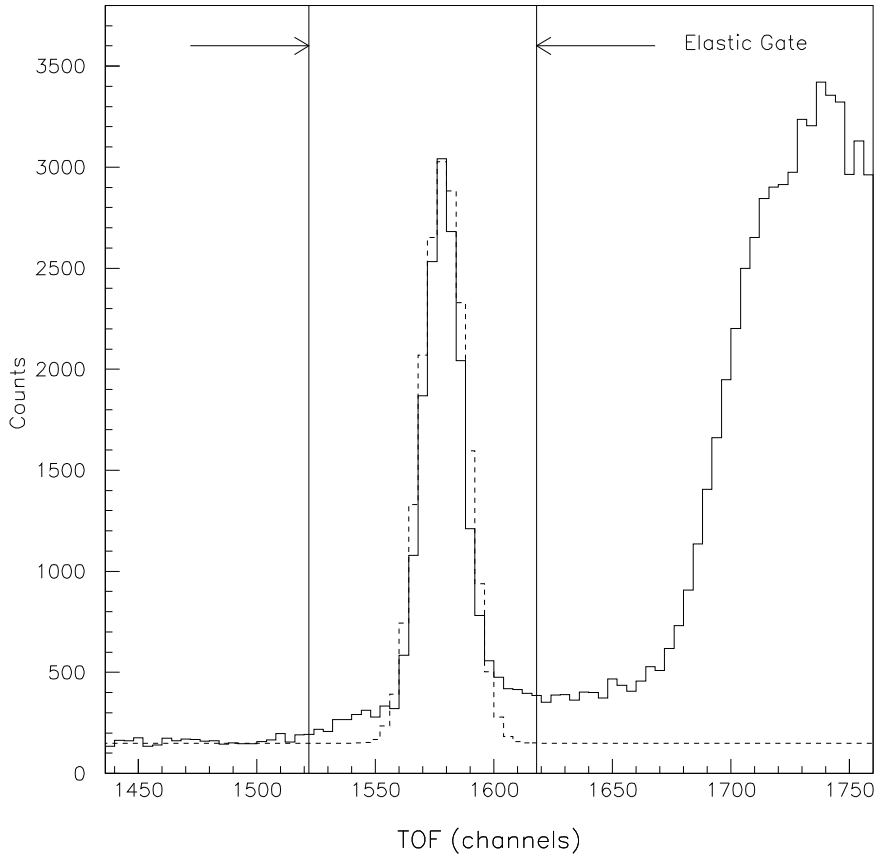

Figure 4.1: Experimental (solid line) and simulated (dotted line) TOF spectra for *nd* elastic scattering. The Monte-Carlo code simulated *nd* elastic single scattering. The time shift and resolution parameters of the simulation were adjusted to reproduce the centroid and FWHM of the experimental peak. The FWHM of the peak in this particular spectrum is approximately 2 ns. Note that a constant background has been added to the simulated spectrum to account for the contribution from accidental (random) coincidences.

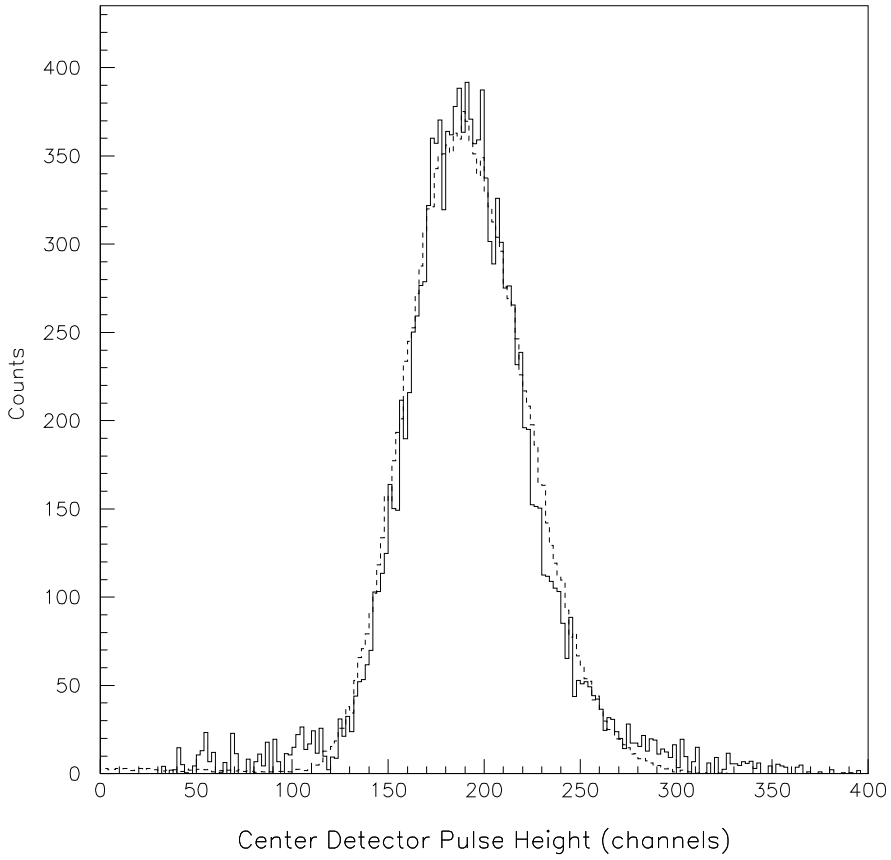

Figure 4.2: Experimental (solid line) and simulated (dotted line) CDPH spectra for *nd* elastic scattering. The measured accidental and fitted residual backgrounds have been subtracted from the experimental spectrum. The Monte-Carlo code simulated the CDPH spectrum for *nd* elastic single scattering. The input parameters for the skewed Gaussian function in the simulation were adjusted to match as closely as possible the features of the experimental spectrum.

Carlo simulation was used to determine the true scattering angles of these detectors with the angles of the in-plane detectors serving as calibration points.

Multiple Scattering

After the time and energy resolution parameters have been set from the single scattering simulation, multiple scattering processes can be turned on in the code. Because triple scattering is expected to contribute less than 1% of the *nd* elastic yields, only double-scattering processes are included in the MS simulations. The physical processes considered were neutron elastic scattering from deuterium and elastic and inelastic scattering of neutrons from carbon.

The probability of multiple scattering in the target is significant because of the large size of the deuterated scintillator relative to the mean-free path of neutrons at the energies in this experiment. The mean-free path of a 16.0-MeV neutron in the deuterated scintillator is about 10 cm, or approximately twice as large as the scintillator's diameter. For this mean-free path, the probability that a neutron will interact once in the scintillator is about 33%. Squaring this single interaction probability gives a rough estimate of the contribution of double scattering as 11%.

Because of the presence of a heavy nucleus such as carbon, a neutron can scatter multiple times in the target and still arrive at the detector with the same TOF as a neutron singly-scattered from deuterium. For example, a neutron can scatter elastically at a moderately large angle from carbon losing little energy in the process and then scatter to a small angle from deuterium with the net scattering angle and energy being the same as a single elastic scattering reaction off of deuterium. Because the TOF technique cannot completely resolve these processes, neutrons from MS form a background beneath the prominent single scattering peak in the TOF spectrum

(see Figure 4.1). Figure 4.3 shows the simulated contribution of the neutrons from MS in the CDPH spectrum to be approximately 8%.

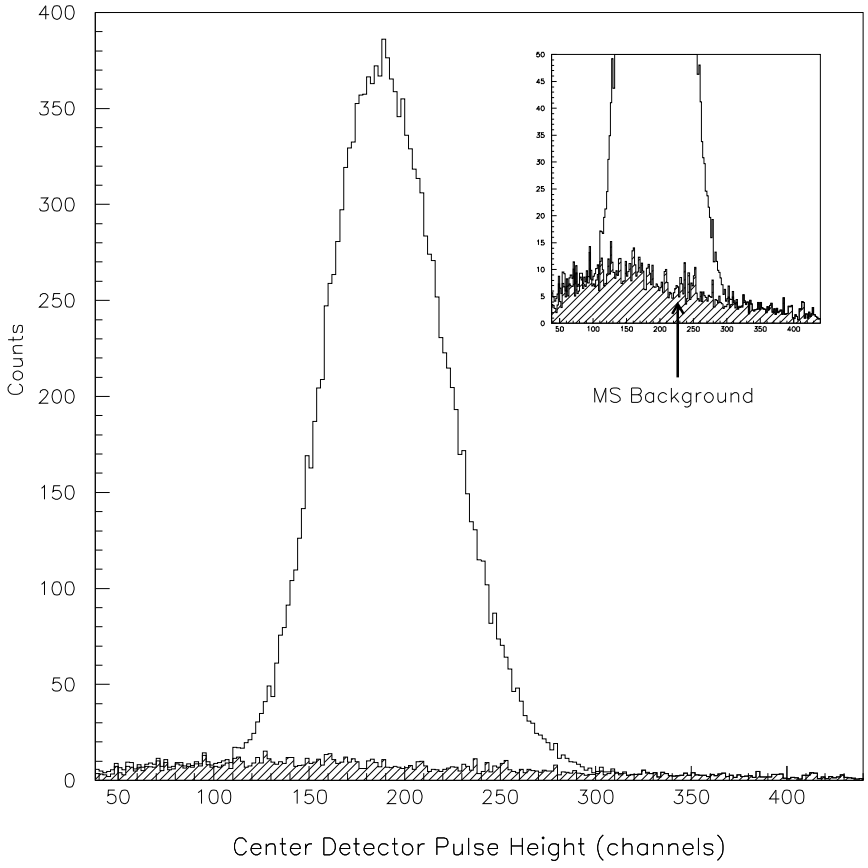

Figure 4.3: Simulated CDPH spectra including single and multiple scattering processes. The inset shows the MS background beneath the dominant single scattering peak. MS events account for approximately 8% of the total counts in the peak.

4.3.3 Simulation for the Breakup Reaction

The results of the breakup simulation were of central importance in determining the cross sections in this experiment and in their interpretation with respect to

theoretical predictions. The experimental data are subject to many effects which must be accurately understood if a meaningful result is to be achieved. Effects that are modeled by the Monte-Carlo simulation include: the attenuation of neutrons as they pass through the scatterer and in their flight through air, the efficiency of the neutron detectors, the time resolution of the detectors, the pulse-height resolution of the CD, and the finite size of the target and detectors.

Only single scattering events were considered in the breakup simulation. This decision was a partially pragmatic one, considering that any realistic simulation of multiple scattering would require a library of *nd* breakup cross sections for all kinematically allowed configurations. More importantly, the effect of MS events in the breakup yields should be quite small. Simulations for *nd* elastic scattering showed that only about 8% of neutrons scatter more than once. The more restrictive kinematic constraints imposed in the breakup analysis should result in very few MS events being included in the final yields.

As mentioned earlier, in the breakup simulation four interaction points are randomly chosen: one in the neutron production cell, one in the CD, and one in each of the two detectors in the breakup pair. The latter three points determined the neutron scattering angles and along with the incident neutron energy defined a kinematic locus. The three particle energies were then calculated in 100-keV steps along the S-curve. The products of the two neutron transmissions and detector efficiencies were computed for each point along the kinematic locus. These values were not necessarily identical to the ones determined in the experiment because of differences in the methods used to calculate the neutron energies in the experiment and simulation. The experimental neutron energies are determined from their TOF values assuming the neutrons have flight paths defined by the distance from the geometric

center of the scatterer to the center of each detector. In the simulation the flight path is the actual distance between the interaction points in the CD and neutron detector. To be able to compare simulated and experimental results, the simulated neutron energies were recalculated using the center-to-center distance as the neutron flight path. The new energies (designated by primes) are thus given by

$$E_i' = \left(\frac{d_i'}{d_i}\right)^2 E_i \tag{4.1}$$

where $i = n1$ or $n2$, representing the energy of the first or second breakup neutron. The center-to-center distance is d_i' and d_i is the actual distance traveled by the simulated neutron.

The proton energy, E_p, in the simulation was calculated from the two neutron energies by conservation of energy

$$E_p = E_{total} - E_{n1} - E_{n2}\ , \tag{4.2}$$

where E_{total} is the energy available to the three nucleons in the exit channel. The available energy is just the incident neutron energy minus the energy needed to breakup the deuteron and is equal to 13.775 MeV for this experiment. The experimental uncertainty in the proton energy due to the poor pulse-height resolution of the CD was reproduced by fitting the total-energy spectrum (see Figure 5.10) with a Gaussian distribution. The proton energy distribution in the simulation was smeared to make the simulated total energy distribution, $E_{n1}' + E_{n2}' + E_p'$, match the experimental spectrum. (Note that $E_p' = E_p$ because the proton energy does not require the corrections that were applied to the neutron energies.)

Attenuation and Efficiency Corrections

The adjusted neutron energies were used in indexing the products of the transmission and efficiency correction factors for consistency with the treatment of the experimental data. The factors themselves were computed using the uncorrected energies and flight paths from the simulation:

$$\begin{aligned} \overline{\alpha}\left(E'_{n1}, E'_{n2}, E'_p\right) &\equiv \alpha\left(E_{n1}\right) \cdot \alpha\left(E_{n2}\right) \quad \text{and} \\ \overline{\epsilon}\left(E'_{n1}, E'_{n2}, E'_p\right) &\equiv \epsilon\left(E_{n1}\right) \cdot \epsilon\left(E_{n2}\right) . \end{aligned} \tag{4.3}$$

The values for $\overline{\alpha}$ and $\overline{\epsilon}$ were averaged into arrays indexed by the three particle energies in 250-keV bins. Figure 5.11 shows these two output arrays projected into the E_{n1}-E_{n2} plane for the SST configuration. The Monte-Carlo code also calculated a weighting factor which was obtained from the Gaussian used to smear the proton energies:

$$\overline{w}\left(E'_{n1}, E'_{n2}, E'_p\right) \equiv w\left(E_p\right) . \tag{4.4}$$

An output array for the weighting factor was also generated in 250-keV bins. These three output arrays were used to calculate the transmission and efficiency correction factors needed in determining the breakup cross section. In addition, they were used to define the boundary of a three-dimensional gate set on the region of experimentally valid data (see Section 5.5.1).

Finite-Geometry Theoretical Predictions

Comparison of the experimental cross sections and theoretical predictions is made difficult by finite geometry and resolution effects. Unfolding finite geometry effects from measurements is an arduous task and can lead to large uncertainties. For this reason an alternate path was chosen. Instead of applying corrections to

the data, the decision was made to fold the finite geometry of the experiment into the theoretical predictions with the Monte-Carlo simulations. In addition to the three output arrays described above, an array of *nd* breakup cross sections was also generated. A multi-parameter linear interpolation algorithm was used to obtain the cross-section values, $\overline{\sigma}\left(E_{n1}, E_{n2}\right)$, between grid points in the relevant cross-section libraries (see Section 4.2). The interpolation parameters used include the scattering angles, incident neutron energy, and the energies of the two breakup neutrons. The cross-section values from the libraries were multiplied by the weight factor (w) and indexed to an output array in the same manner as $\overline{\alpha}$, $\overline{\epsilon}$, and $\overline{w}$:

$$\overline{s}\left(E'_{n1}, E'_{n2}, E'_{p}\right) = \overline{\sigma}\left(E_{n1}, E_{n2}\right) \cdot w\left(E_{p}\right). \tag{4.5}$$

Projection of the finite-geometry theoretical predictions onto the S-curve was performed using the same procedures as the data. A FORTRAN code was used to read in the four Monte-Carlo simulation output arrays for attenuation, efficiency, cross section, and weighting factor. Weight factor elements

$$\mathcal{K}\left(E'_{n1}, E'_{n2}, E'_{p}\right) = \overline{w} \cdot \overline{\alpha} \cdot \overline{\epsilon} \tag{4.6}$$

and cross-section elements

$$\mathcal{W}\left(E'_{n1}, E'_{n2}, E'_{p}\right) = \overline{s} \cdot \overline{\alpha} \cdot \overline{\epsilon} \tag{4.7}$$

were calculated for each energy grid point. The point-geometry locus $\mathrm{S}\left(E^{c}_{n1}, E^{c}_{n2}, E^{c}_{p}\right)$ was calculated by a separate kinematics code in steps of $\Delta\mathrm{S} = 0.5$ MeV (the superscript "c" denotes energies along the ideal point-geometry locus). Projection of the simulated results onto the ideal locus was accomplished by looping over the grid points $\left(E'_{n1}, E'_{n2}, E'_{p}\right)$ that lie within the bounds of the three-dimensional gate. For

each grid point the momentum of each particle was calculated using the nonrelativistic kinematic formula,

$$k'_i = \sqrt{2\,m\,E'_i}\,, \tag{4.8}$$

where $i = n1, n2, p$ and the mass of the proton and neutron are taken to be identical. The simulated events were then projected onto the points chosen along the ideal kinematic locus by the minimum distance method; that is, the quantity

$$K_{min} = \sqrt{\sum_{i=n1,n2,p} (k_i^c - k'_i)^2} \tag{4.9}$$

was minimized [Fin87]. From these projections, the simulated yields curve, $\overline{\Sigma}\,(\mathrm{S}_i)$, is given by

$$\overline{\Sigma}\,(\mathrm{S}_i) = \sum_j \mathcal{W}\,(k'_{n1}, k'_{n2}, k'_p)_j\,, \tag{4.10}$$

and the weight factor curve, $\kappa\,(S_i)$, is given by

$$\kappa\,(\mathrm{S}_i) = \sum_j \mathcal{K}\,(k'_{n1}, k'_{n2}, k'_p)_j\,, \tag{4.11}$$

where the summation index j is over all grid points (k'_{n1}, k'_{n2}, k'_p) that are projected into the S_i bins along the ideal kinematic locus according to the criterion set in Equation 4.9. The finite-geometry theoretical cross section for each S_i bin is given by the expression

$$\frac{d^5\sigma^{MC}}{d\Omega_1 d\Omega_2 d\mathrm{S}}\,(\mathrm{S}_i) = \frac{\overline{\Sigma}\,(\mathrm{S}_i)}{\kappa\,(\mathrm{S}_i)}\,. \tag{4.12}$$

Figure 4.4 shows the theoretical finite-geometry cross section projected onto the E_{n1} vs. E_{n2} plane for the np FSI configuration. Figure 4.5 shows a comparison of the point- and finite-geometry cross sections as a function of S for the np FSI configuration.

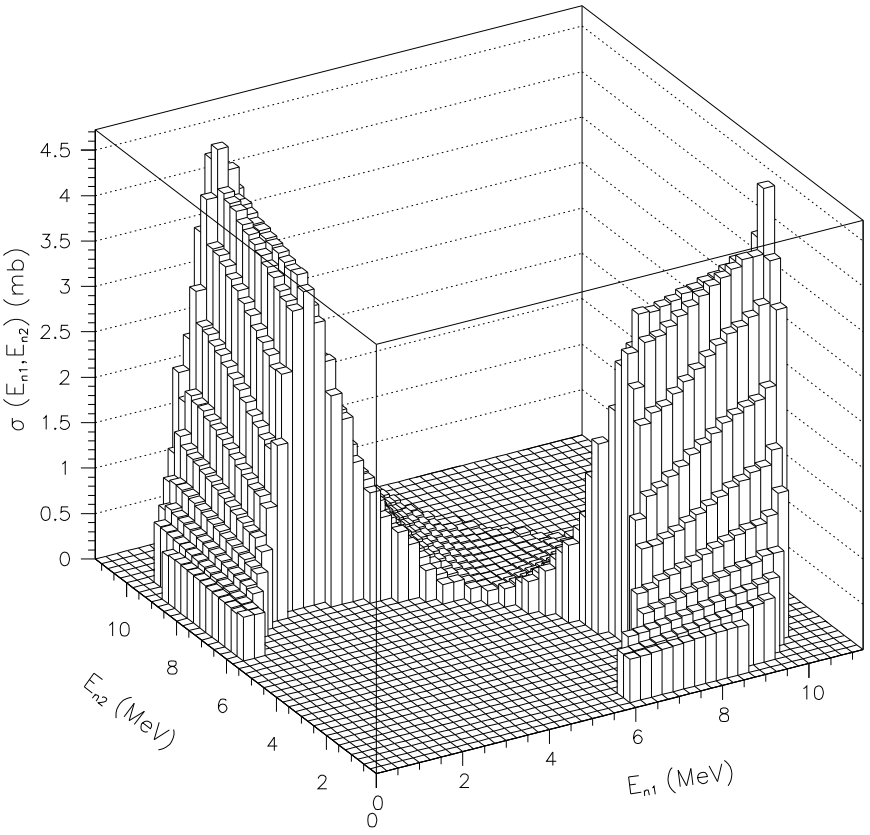

Figure 4.4: Simulated *np* FSI cross section projected onto the E_{n1} vs. E_{n2} plane.

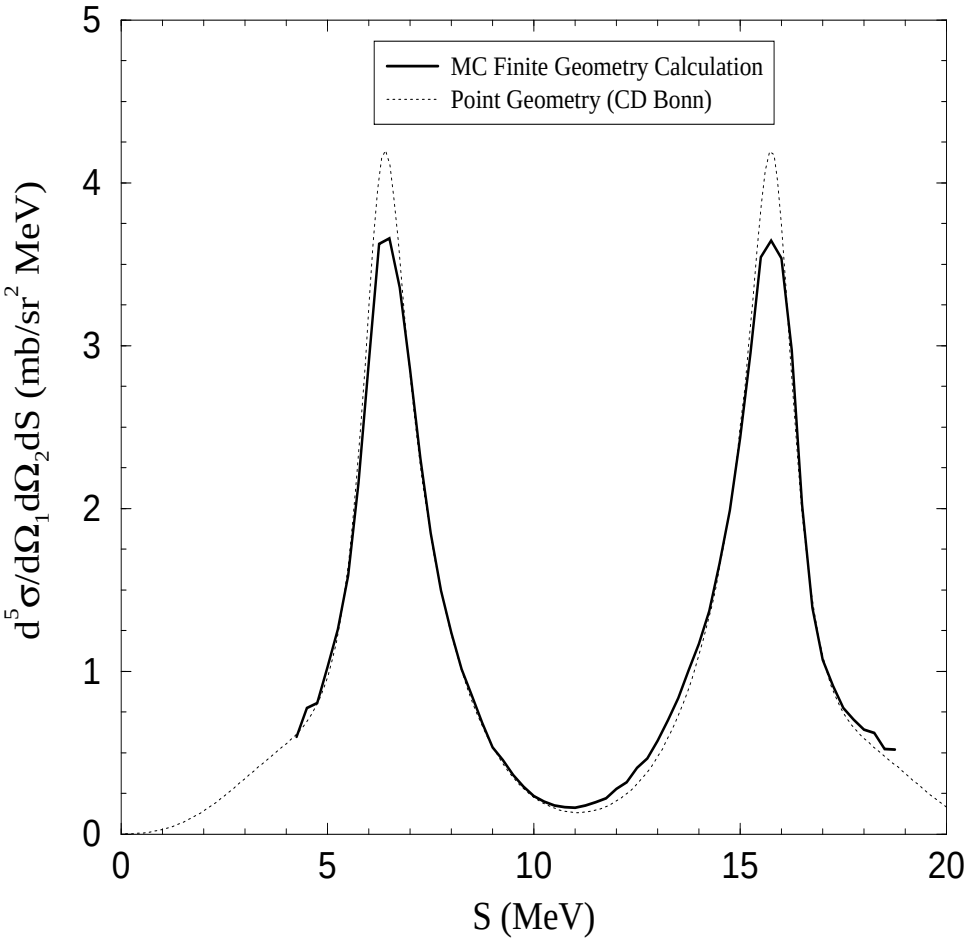

Figure 4.5: Comparison of point- and finite-geometry *nd* breakup differential cross sections for the *np* FSI configuration.

4.4 Simulation Tests

The Monte-Carlo code used in previous *nd* breakup experiments [Set94, Gon97, Sal98] was written for configurations where the two coincident detectors were either in the scattering plane or where one detector was above the plane at an azimuthal angle of 120° with its partner in the scattering plane. The design of the STAR array allows detectors to be above and *below* the scattering plane at azimuthal angles 30° apart. Because the neutron transmission corrections are dependent on the amount of material between the interaction and the detector, the code had to be modified to account for the new geometries introduced in this experiment. After the code was modified, extensive tests were performed to ensure the correction factors were accurate for all detector pairs.

Geometry symmetry-breaking due to the design of the center detector is primarily responsible for the complications in modeling the various detector pairs. Left-right symmetry is preserved by the cylindrical design of the CD scintillator cell; however, up-down symmetry is broken by the photomultiplier tube upon which the cell is mounted. For example, Figure 4.6 shows how a neutron can scatter in the CD such that it travels through the glass face of the PMT before reaching a detector. The extra attenuation for neutrons going to the detectors below the scattering plane is not present for neutrons headed toward detectors above the plane.

The PMT face plate is plano-concave (thinner in the middle than on the sides). At its center the face plate is approximately 1.1-mm thick. On the edges, the glass is about 6.5-mm thick. To avoid the complexities of programming the real geometry, an approximation was made by assuming that the volume of the face plate can be redistributed into a disk of uniform thickness. An effective thickness of 3.8-mm was

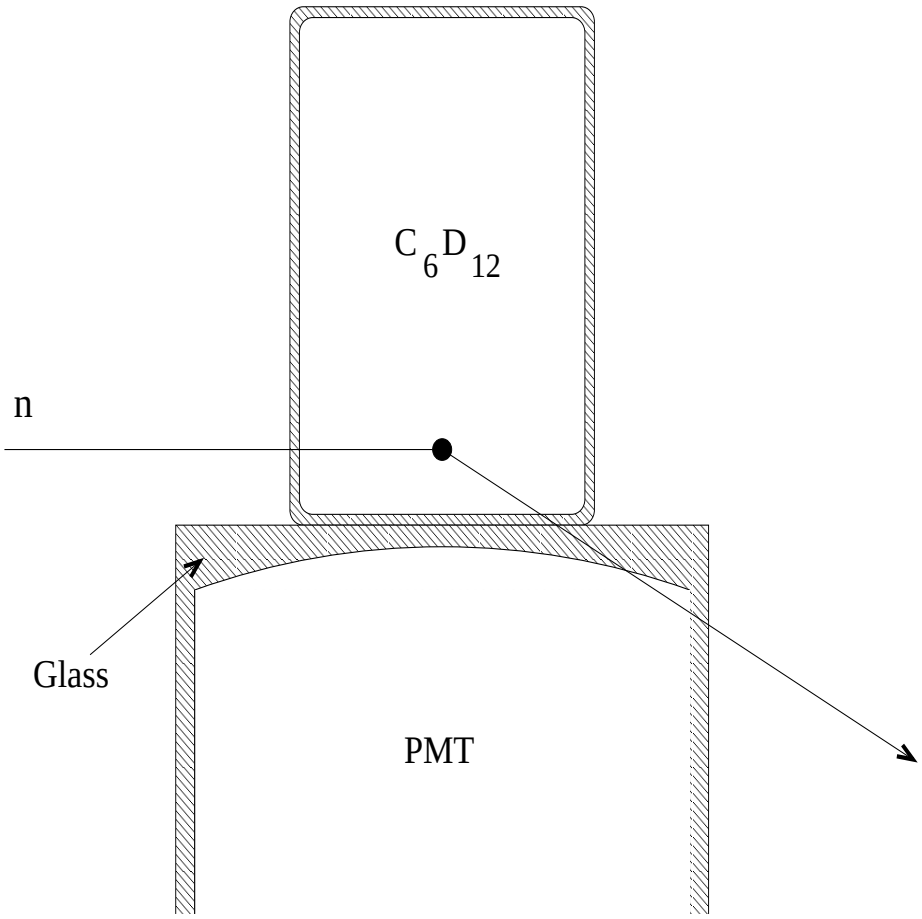

Figure 4.6: A neutron scattering in the CD scintillator cell and passing through the glass face plate of the PMT. Note that this diagram is not drawn to scale. The relative size difference between the diameters of the PMT and scintillator cell is exaggerated for illustrative purposes.

determined in this manner.

Accounting for the symmetry-breaking described above, there exist seven unique detector pairings for the SST configuration that need to be modeled by the Monte-Carlo simulation. Figure 4.7 shows the unique detector pairings with the value of each detector's azimuthal angle, ϕ, labeled. The Monte-Carlo code was modified in such a way that all seven pairs could be simulated with the same program, but different input files.

Simulations were run for the seven unique pairings and the neutron transmission correction factors were projected as a function of S. As shown in Equation 4.3, the output array is actually the product of the transmissions of the neutrons headed toward the two detectors in the pair. The individual correction factors were determined by setting the transmission of the neutrons headed toward one of the detectors to unity. Internal consistency checks could then be performed to ensure that neutrons headed toward a particular detector had the same transmission when the detector was used in a different pairing and that neutrons headed toward detectors with left-right symmetry also had similar correction factors. The difference in transmission factors for a particular detector used in two separate pairs was found to be less than 0.1%. The transmission factors for pairs with left-right symmetry deviated from each other by less than 0.2%. Point-geometry calculations were also made using the code and they produced reasonable results as well. These tests seemed to provide credible evidence that the simulations were properly accounting for the geometry of the experimental set-up.

Another test that was performed to check the accuracy of the simulations focused on the selection of the seed for the code's random number generating routine. The random number generating subroutine was taken from "Numerical Recipes in

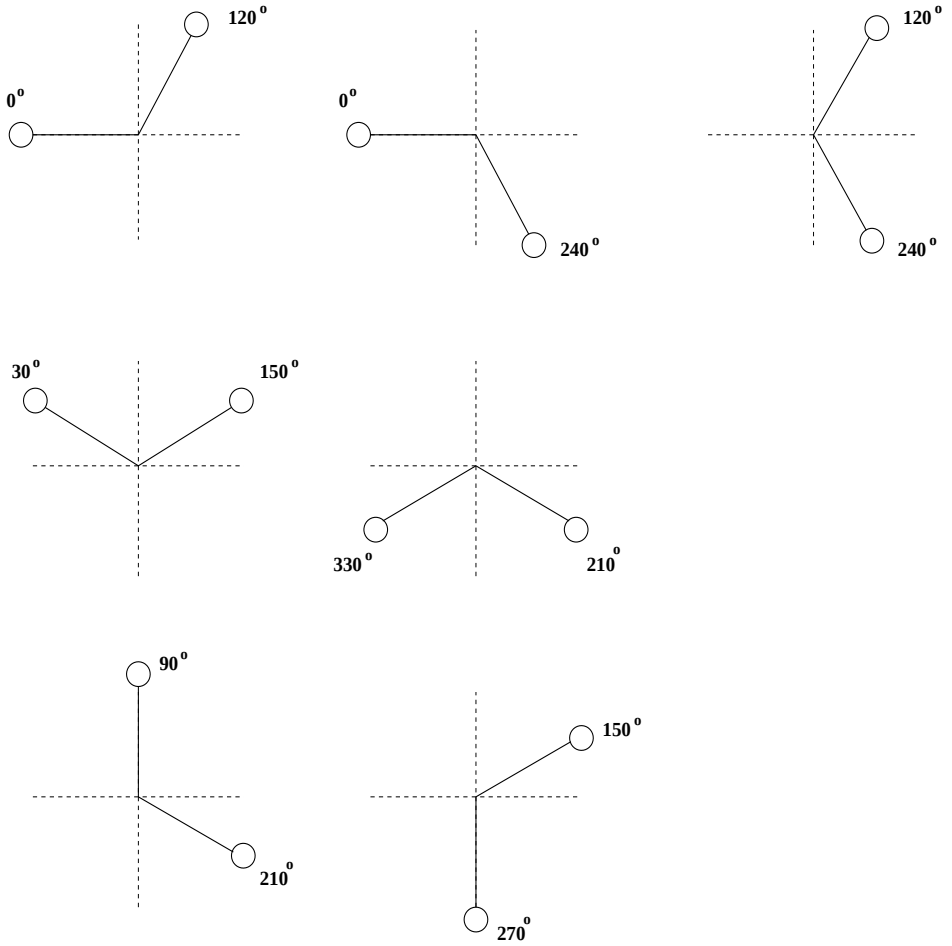

Figure 4.7: The seven unique detector pairings considered in the Monte-Carlo simulations for the SST configuration. The values refer to the ϕ angles of each detector. The neutron beam direction is into the page.

FORTRAN" [Pre92]. Any negative integer value was allowed for the seed. For the test, the simulation was run for three different seed values and the neutron transmission output array was projected onto the S-curve for each case. An evaluation of the three cases was made by comparing the average neutron transmission correction factor calculated from two bins around and including the space-star point ($S = 7.0$, 7.5, and 8.0 MeV). Table 4.2 shows that the correction factors for the three cases had a standard deviation of approximately 0.4% when 100,000 histories were simulated. (Compare this deviation to the expected statistical uncertainty for 100,000 histories, which is just over 0.3%.) This result validates the hypothesis that the random number sequence should converge for any choice of seed if a sufficient number of steps is used.

Random Number Seed	Average Neutron Transmission
-8169	0.4125
-1237	0.4092
-2659	0.4112
Deviation	0.404 %

Table 4.2: Random number generator test results. The average neutron transmission around the space-star point for the detector pair (0°, 120°) is given for different seed values. The standard deviation of the average correction factors is about 0.4%. All simulations were run for 100,000 histories.

Chapter 5

Data Analysis

5.1 Introduction

The physical processes of interest in this work produced a very small fraction of the total number of events collected. Intensive analysis was necessary to extract information on the processes of interest due to the large background that was present. Complete on-line analysis was thus not practical, so the data were stored event by event for later off-line analysis. Because the correlation between the parameters in each event is preserved in event-mode storage, the essential features of each event could be reconstructed in the off-line analysis. Each recorded event contained the event type (double-coincidence or triple-coincidence), the detector hit pattern, the time-of-flight (TOF) and long- and short-gate pulse heights (LPH and SPH) for each neutron detector involved, and the center detector pulse height (CDPH).

The analysis software used in this project was based on the CEBAF Test Package (CTP) system [Woo93]. CTP is a set of software tools that provides a convenient

user interface for standard first-pass analysis of hadronic physics experimental data. These tools permit the user to change analysis parameters, create histograms, and define data cuts (also called tests) without recompiling the analysis code. Using CTP was a natural extension of the decision to employ CODA for data acquisition as both packages are utilized at Jefferson National Laboratory. FORTRAN routines were written to unpack the raw data structures into arrays, sort the data by event type, compute relevant physical quantities, and call the CTP functions that applied cuts and tests to the data before histograms were filled. Histograms were stored in HBOOK format and could be viewed and manipulated with PAW (Physics Analysis Workstation). Both HBOOK and PAW are part of data-analysis packages available from the CERN software library. All analysis was carried out on the TUNL Unix cluster. The FORTRAN routines that make up the analyzer were compiled and linked on both Solaris and Linux platforms. Sparc Ultra 1's and Intel-based PC's served as the hardware for data replay and analysis.

This chapter describes in detail the off-line analysis procedure used to determine the differential cross sections from the raw yields for the measured *nd* breakup configurations. This procedure was implemented in three distinct stages:

1. The *nd* elastic-scattering events were analyzed to determine the integrated beam-target luminosity, $\mathcal{L}_{int}$, which is the product of the neutron flux and the number of scatterers in the target. The luminosity is needed for the absolute normalization of the *nd* breakup cross-section data.

2. The light output response function for the center detector (CD) was found for deuterons from *nd* elastic-scattering data. This function was used to derive the light output response for protons. The proton light output response curve was

used to determine the energies of the protons in the breakup channel from the CD pulse height spectrum.

3. Triple-coincidence events (events with hits in the CD and two neutron detectors) were sorted to obtain the *nd* breakup yields for each configuration being studied. The output files from Monte-Carlo simulations of the experiment (see Section 4.3.3) were used as a three-dimensional gate on the data and provided correction factors for efficiency and attenuation effects. The counts for the breakup reaction were projected into bins of equal energy width along the point-geometry kinematic locus, and a cross section was calculated for each bin.

5.2 General Analysis Issues

5.2.1 Analysis Batches

Production data for the *nd* breakup configurations studied were accumulated over seven experimental periods, each of which lasted from a minimum of five days to a maximum of thirteen days. The seven sets of data were further divided into batches for replay and analysis. A replay batch included data accumulated between detector gain and threshold checks using a ^{137}Cs calibration source. These checks were performed daily, so each batch contains approximately 24 hours of data. Dividing each data set into batches has the benefit that changes in the values of important parameters can be easily monitored throughout the course of a run. For instance, this technique was used to track a continuous decrease in the integrated beam-target luminosity during one run that was due to a small gas leak in the neutron production

cell (see Section 5.3.2). Another example which shows the utility of batch division was in the adjustment of the pulse-shape γ-ray rejection cut to compensate for slight gain shifts in the detector electronics over time. The most important advantage of dividing the data sets into batches is that the systematic uncertainties inherent in the analysis techniques could be estimated by comparing luminosities and cross sections determined in different batches. Table 5.1 shows a summary of the experimental periods. Note that the column labeled "Hours of Data" only includes actual production data-taking time and does not include the many hours of research and development work required to reduce backgrounds and sources of systematic error to acceptable levels.

Analysis Batch Numbers	Configuration(s) Studied	Date of Data Acquisition	Hours of Data
01 - 08	SST/FSI	August 1998	184
09 - 17	CST	October 1998	200
18 - 26	CST	January 1999	218
27 - 38	IST	April 1999	268
39 - 42	IST	May 1999	91
43 - 47	SST/FSI	April 2000	131
48 - 51	SST/FSI	May 2000	91
		Total Hours	1183

Table 5.1: Summary of experimental periods. Each data set was divided into analysis batches for tracking systematic effects. "Hours of Data" includes only actual production data-taking time.

5.2.2 Sorting

The first step after unpacking the raw data structure was to test the value of the hit register. The value of the hit register determined the type of that particular event:

- 1 ≡ breakup (triple-coincidence) event
- 2 ≡ elastic (double-coincidence) event
- 4 ≡ monitor event
- 8 ≡ scaler event
- 16 ≡ LED pulser event
- 32 ≡ pedestal pulser event

Separate off-line analysis codes were written to process the different event types. An additional level of sorting was implemented for breakup events. For each breakup event, a detector hit pattern was created using the TOF of the particles detected in each of the twelve STAR detectors. If the TOF value fell inside a very wide time window, then the bit corresponding to that detector was set to a value of one. The detector hit pattern was used to select the detector configuration for the event.

5.2.3 Accidental Coincidences

In any coincidence experiment there exists the possibility of "accidental" coincidences. These false coincidences are formed by uncorrelated signals that happen to occur within a time difference of each other that is less than the coincidence time window. In this experiment, accidental coincidences can occur between the CD and each of the neutron detectors or between two neutron detectors for triple-coincidence events. For example, consider an event in which a neutron elastically scatters from a deuteron in the CD and heads toward a side detector. Before it reaches the detector however, an uncorrelated particle is detected in the side detector, thus producing a shorter TOF than would be expected. Likewise, an uncorrelated particle can be detected in the CD just prior to the arrival of the neutron that scattered into the side detector, thereby causing a longer TOF than expected. The rate of these accidental

coincidences, A, can be estimated from Poisson statistics as

$$A = R_{ndet}\,(1 - e^{-(R_{CD}\,\tau_w)}) \tag{5.1}$$

where R_{ndet} is the neutron detector counting rate, R_{CD} is the CD counting rate, and τ_w is the width of the coincidence time window. Equation 5.1 reduces to

$$A \approx R_{ndet}\,R_{CD}\,\tau_w \tag{5.2}$$

in the limit where the product $R_{CD}\,\tau_w \ll 1$.

These accidental coincidences (or simply *accidentals*) are truly random in time and produce a flat background in the neutron TOF spectra (see Figure 5.1). Because this background is present in the regions of the TOF spectrum corresponding to the *nd* elastic-scattering peak and the *nd* breakup continuum, a method of accounting for accidentals is necessary to determine the true counts. A measure of the accidental contribution was found by setting a gate in the unphysical region of TOF where the times correspond to velocities greater than the speed of light, specifically earlier than the prompt γ-ray peak. The events falling in this TOF gate are treated in the same manner as the events in the regions of interest. The true counts are obtained by taking the difference between the counts corresponding to TOF values in the accidental region from those with TOF values of the process of interest. This simple method is sufficient for double-coincidence events. Treating the accidentals in triple-coincidence events becomes much more complicated because one or both neutron-CD coincidences could be accidental. All possible combinations of TOF regions must be considered (see Section 5.4.2 for a more thorough discussion).

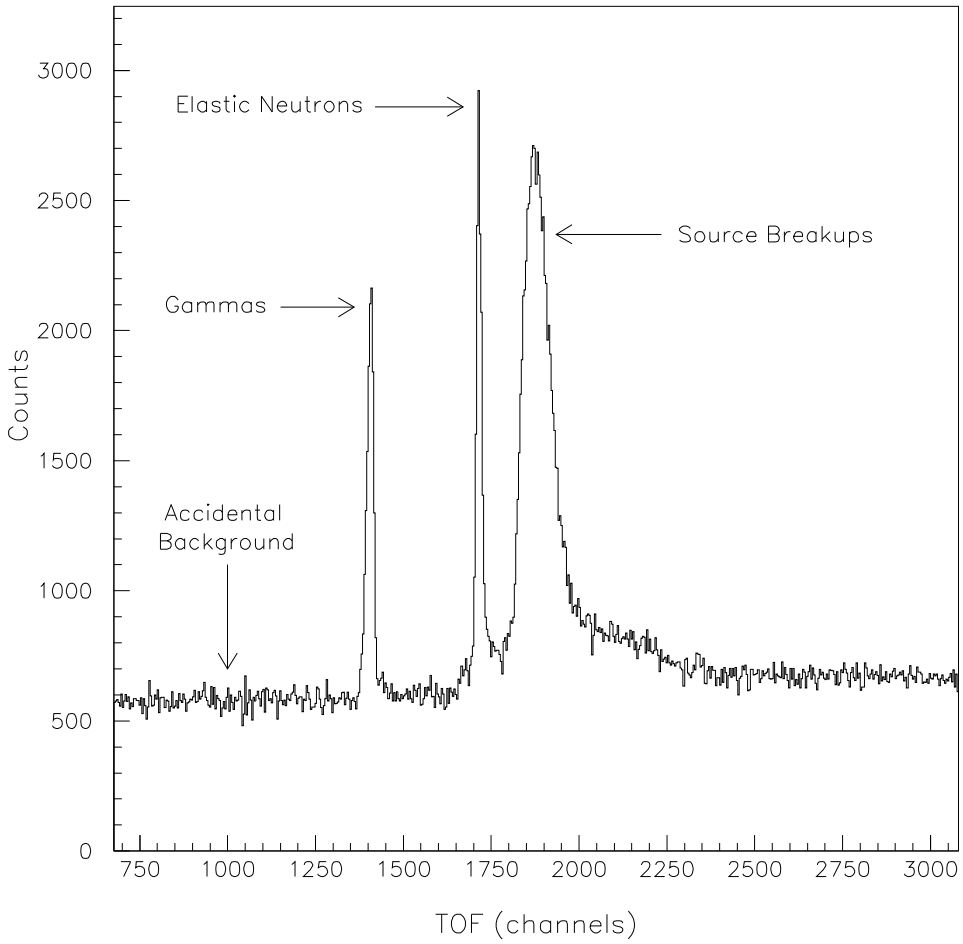

Figure 5.1: A typical TOF spectrum for double coincidences. Time increases from left to right in this spectrum and the calibration is 0.1 ns/channel. A pulse-height cut of one-third of the Compton scattering edge from ^{137}Cs was applied. The gamma peak represents the earliest detected events that originated in the CD. All counts coming before the gamma peak in time are unphysical and thus give a measure of the accidental background present in this measurement. Following the gammas is the peak due to 16.0 MeV incident neutrons scattering elastically from deuterons in the CD to an angle of $\theta_n = 51.5°$. The last feature to note is the broad mound of neutrons labeled "source breakups". As seen in Figure 3.5, secondary reactions in the gas cell produce a continuum of lower energy neutrons. These neutrons can then elastically scatter in the CD and be detected.

5.2.4 Pulse Shape Discrimination

One of the first steps in data reduction was to eliminate γ-ray events through pulse shape discrimination (PSD). Section 3.6.1 described how charge integration techniques were used to identify neutrons and γ-rays. Figure 5.2 shows a two-dimensional PSD histogram with total charge plotted versus charge in the tail of the scintillator pulse. Note that this plot has been rotated to make the neutron and γ-ray islands as vertical as possible and has been shifted an arbitrary amount along the horizontal axis for convenience. The software cut (or *gate*) that was used to eliminate events in which γ-rays were detected is shown between the islands. Because the current version of the CTP software was not capable of using two-dimensional gates, a one-dimensional equivalent had to be fashioned. Points were chosen for the cut in the PAW histogram display and were fit with a 4th order polynomial function. This function was evaluated on an event by event basis and compared to the horizontal axis value for each event. Events that had a horizontal axis value greater than the evaluated function were identified as being due to detected γ-rays and were eliminated from further analysis. Figure 5.3 shows the effects of such a software PSD cut on a typical neutron detector TOF spectrum.

5.2.5 Finite Geometry and Resolution Considerations

In an ideal experiment, a perfectly monoenergetic beam would scatter off of a point target into a point detector. A cross section could then easily be determined from the counts in the detector, and direct comparisons to theoretical predictions would be trivial. Unfortunately, reality dictates that targets and detectors must subtend finite solid angles to accumulate a statistically significant number of events in

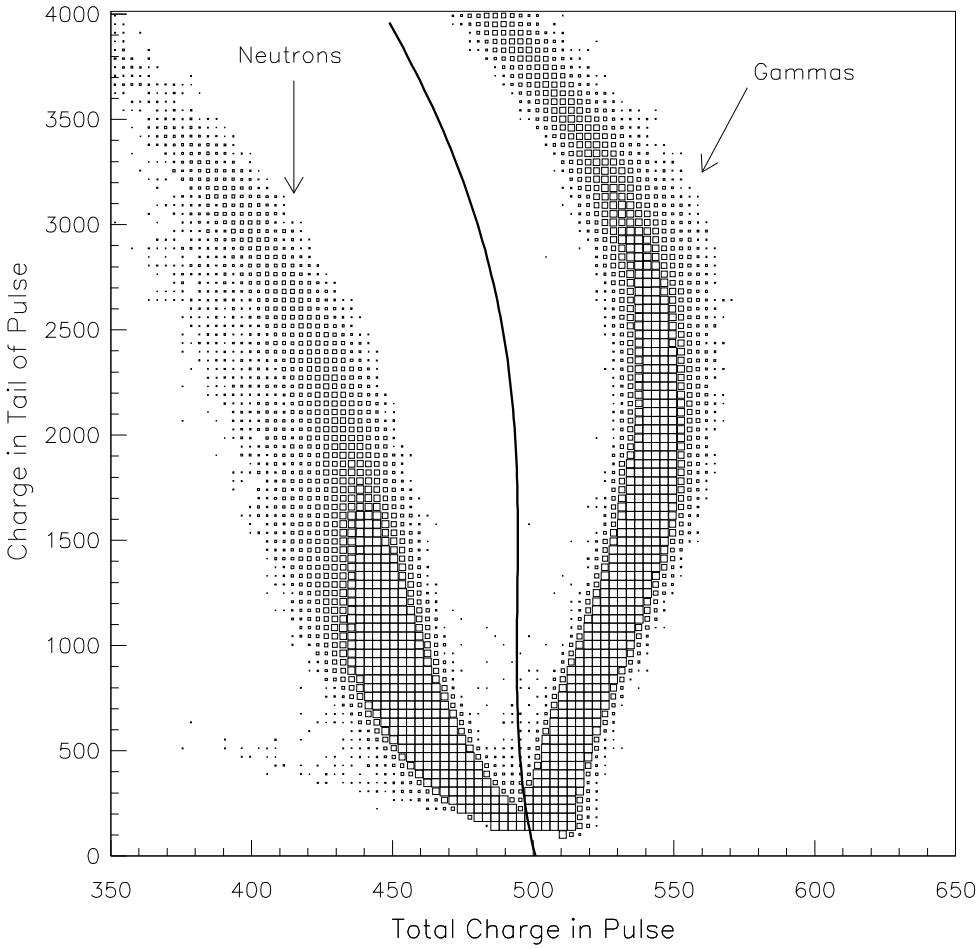

Figure 5.2: Two-dimensional PSD spectrum showing the separation of neutrons and γ-rays at a PH threshold cut of $\frac{1}{4}\times$Cs. Note that the entire spectrum has been rotated to make the islands approximately vertical, and shifted an arbitrary number of channels for presentation. The solid line between the neutron and gamma islands represents the software cut used to eliminate events due to detected γ-rays from further analysis.

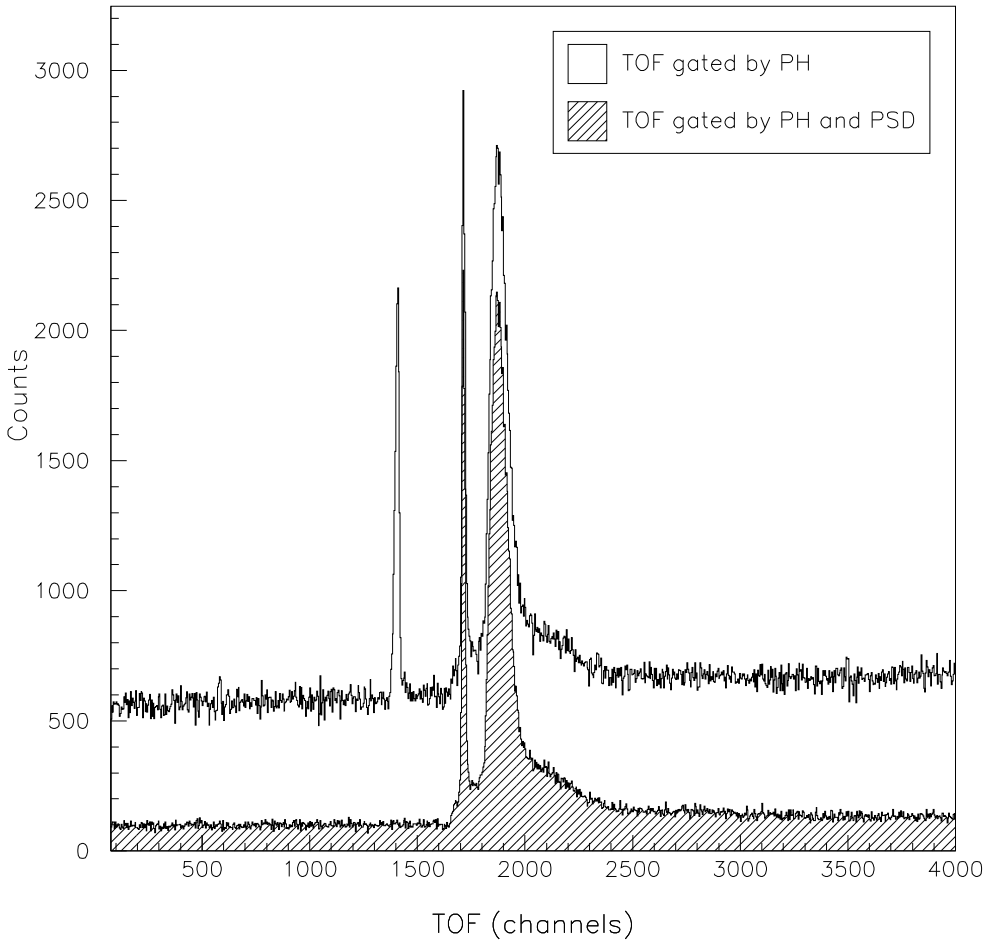

Figure 5.3: The effect of the software PSD cut on a typical TOF spectrum is shown. The hatched histogram is the TOF spectrum with the number of γ-ray detected events reduced by the PSD cut.

a reasonable amount of time. In neutron scattering experiments, effects due to finite geometry can be quite dramatic because of the relatively large detectors and targets required to optimize the counting rate of the process of interest. Likewise, particle beams do not have infinite energy resolution. Neutron production reactions, either in gas cells or solid targets, inevitably generate a spread of particle energies. Energy spread in the beam tends to average the measured physics observables and can make interpretation of results challenging. These finite geometry and energy resolution effects manifest themselves in the experiment through three primary processes: neutron flux attenuation in the target, multiple scattering in the target, and averaging of data over a range of kinematic loci.

Neutron Flux Attenuation

The rather large size of the target (which in this experiment is also the center detector) causes considerable attenuation of the incoming and scattered neutron fluxes. Attenuation also arises from the structural materials in the center detector (that is, the glass cylinder which contains the scintillating fluid and the mu-metal cover which shields the phototube from ambient magnetic fields and also makes the detector light-tight) and even from air scattering between the target and side neutron detectors. Attenuation corrections are necessary in both the elastic and breakup analyses. These corrections can be estimated using the center-to-center distances from CD to each side detector, the thicknesses and densities of the materials through which the neutrons traverse, and the tabulated total neutron cross sections of the nuclei in these materials. The final corrections were made using precise calculations from Monte-Carlo simulations that include the most important experimental effects (see Section 4.3.3).

Multiple Scattering in the Target

There is substantial probability, estimated to be about 30%, that a neutron will scatter at least twice in the target CD used in this experiment before being directed toward one of the side detectors. The dominant multiple-scattering processes are double scattering between two deuterium nuclei or between a deuterium and a carbon nucleus. Multiple scattering must be accounted for in the beam-target luminosity determination because it creates a CD-side detector time-correlated background that is not removed by accidental subtraction techniques. Again, Monte-Carlo simulations are necessary to determine the precise magnitude and shape of these background contributions (see Section 4.3.2).

Smearing of Different Kinematic Loci

The scattering angles quoted in this experiment are measured from the geometrical center of the CD to the center of the front face of the side detectors. The relatively large size of the target and side detectors allows scattering processes that occur at a range of angles around the central value to be detected. For example, in the space-star configuration measured with one detector in the horizontal plane and the other out of the plane with central values of $\theta_1 = \theta_2 = 51.5°$, $\phi_1 = 0°$, and $\phi_2 = 120°$, the angular uncertainties were $\pm 3°$ and $\pm 4°$ in the polar scattering angles, and $\pm 8°$ in the azimuthal scattering angle between the two detectors (ϕ_{12}). The difference in the polar angular uncertainties for the two side detectors is due to the fact that the center detector is a cylinder and thus lacks spherical symmetry. For breakup events, two sets of scattering angles (one for each detector in the coincidence pair) completely determine the kinematic locus of allowed energies for all three outgoing

particles. The angular uncertainties due to finite geometry spread the data about the kinematic locus defined by point geometry. Figure 5.4 shows the point geometry locus for the SST configuration along with other loci within the angular resolution of this experiment.

Energy resolution effects will make similar contributions in smearing the data about the point geometry locus. Variations in the accelerating potential of the tandem can create a spread in the energy of the incident deuteron beam which is then imparted to the neutron beam. Likewise, the length of the deuterium gas cell can create a spread of neutron energies due to energy losses by the deuteron beam in the gas. The breakup cross-section libraries for the Monte-Carlo simulations were generated over a range of neutron energies to account for these resolution effects (see Section 4.3.3).

While the energies of the three outgoing particles can be determined for each event, the real kinematic locus which is correlated with that event cannot be discerned. For this reason the data are projected onto the point geometry or *ideal* locus into energy bins with a width of 500 or 750 keV (depending on the configuration) along S, the arc-length around the locus. It is important to note that finite geometry and energy resolution effects are not deconvoluted from the data. Instead, these effects are folded into the theoretical predictions using Monte-Carlo simulations, thus allowing a one-to-one comparison with the projected data. The relationship between the measured breakup yields and the breakup cross section is given by:

$$\begin{aligned} Y_{bu} &= \frac{d^5\sigma}{d\Omega_1 d\Omega_2 dS} \cdot d\Omega_1 \cdot d\Omega_2 \cdot dS \cdot \alpha_1(E_{n1}) \cdot \alpha_2(E_{n2}) \\ &\quad \cdot \epsilon_1(E_{n1}) \cdot \epsilon_2(E_{n2}) \cdot N_{target} \cdot N_{neutron} \end{aligned} \tag{5.3}$$

where

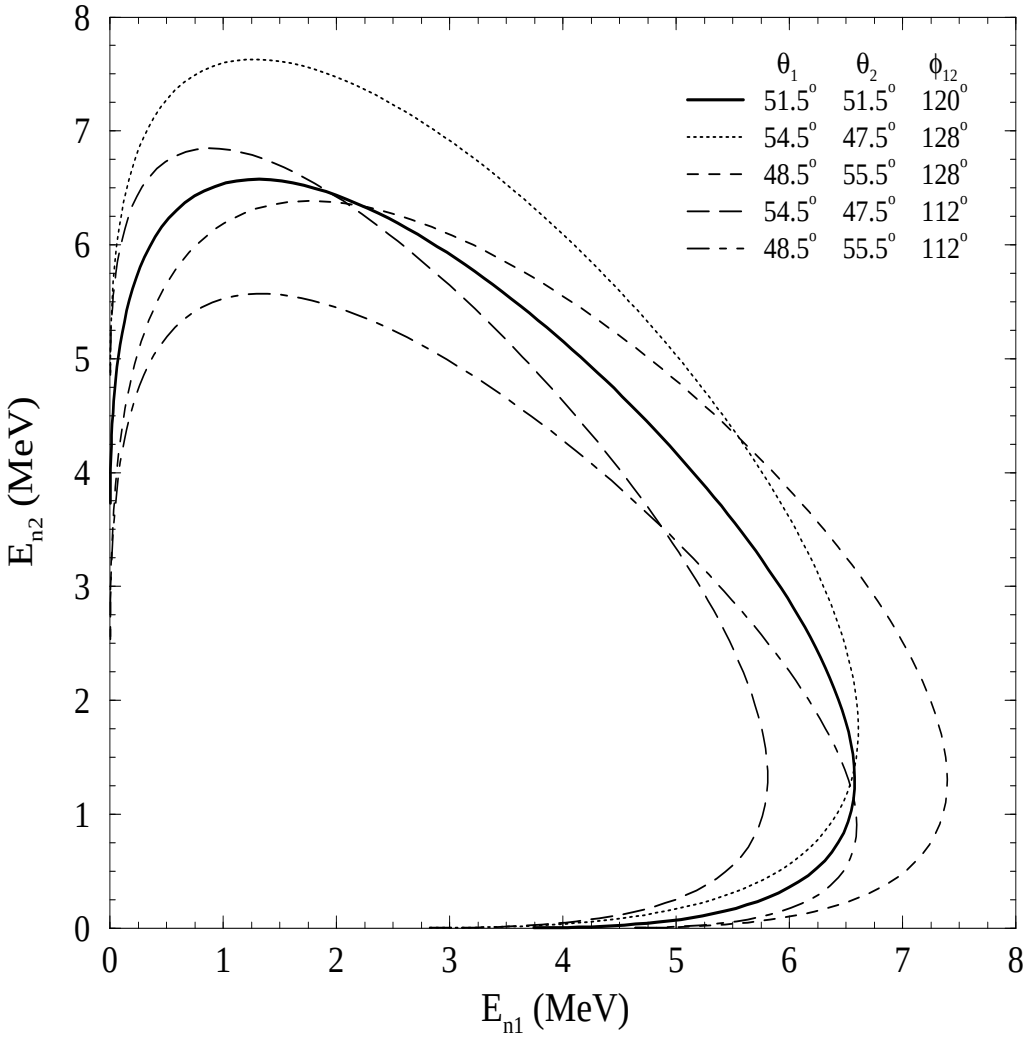

Figure 5.4: Finite geometry effects on kinematics for the SST configuration. The solid curve represents the point geometry or "ideal" locus for the space-star configuration. The other curves show kinematic loci that are within the angular acceptance of this experiment. All kinematic calculations were performed at an incident neutron energy of 16.0 MeV.

Y_{bu} = yields for the nd breakup reaction,

$d\Omega$ = solid angle of the neutron detectors,

dS = bin width along the locus,

ϵ = neutron detector efficiency,

α = transmission of the scattered neutron flux,

N_{target} = number of target nuclei in the scatterer,

$N_{neutron}$ = number of 16.0 MeV neutrons incident on the target.

The product $N_{target} \cdot N_{neutron}$ in Equation 5.3 is just the integrated beam-target luminosity, $\mathcal{L}_{int}$. The determination of $\mathcal{L}_{int}$ will be described in Section 5.3.2. The method for projecting the data onto the ideal kinematic locus will be outlined in Section 5.5.2. Finally, the effective efficiency and transmission terms are determined from the Monte-Carlo simulations of the experiment and will be described in more detail in Section 5.5.1.

5.3 Elastic-Scattering Analysis

Equation 5.3 shows that the relationship between breakup yields and absolute breakup cross section depends on the product of the number density of the target scatterers and incident neutron flux, $N_{target} \cdot N_{neutron}$. This product is referred to as the integrated beam-target luminosity, $\mathcal{L}_{int}$, and serves as an absolute normalization for the cross section. One possible method for finding $\mathcal{L}_{int}$ is to monitor precisely the incident neutron flux and target densities so that each quantity may be determined separately. A more convenient method and the one used in this experiment was to analyze nd elastic-scattering data that were accumulated concurrently with the breakup data. Because the nd elastic-scattering cross section is well known (both

experimentally and theoretically), a comparison of the elastic yields obtained to the elastic yields expected provides a relatively simple method of measuring $\mathcal{L}_{int}$. Of course, factors such as finite geometry, multiple scattering, detector efficiency, and neutron attenuation must be accounted for in this determination.

5.3.1 Obtaining the Elastic Yields

The first step in determining the luminosity is to extract the net *nd* elastic scattering yields. In the replay the different event types were identified by the value of the hit register. For elastic scattering events the hit register value was 2. Two fundamental cuts on the data were initially applied:

1. A pulse-height threshold of $\frac{1}{4}\times$Cs was set in software for all twelve STAR detectors. This threshold corresponds to an equivalent neutron energy cutoff of approximately 0.5 MeV. Note that the software threshold must be set moderately higher than the hardware threshold because the electronic cutoff from the CFD tends to have a broad resolution rather than being infinitely sharp.

2. Pulse shape discrimination techniques were used to eliminate events with γ-rays detected in the side detectors as described in Section 5.2.4.

A TOF histogram was accumulated for all events that passed the pulse-height and PSD requirements (see Figure 5.5). The neutron elastic scattering peak is clearly visible. The broad mound to the right of the elastic peak is the continuum of neutrons from secondary reactions in the gas cell, such as ^{2}H(d, n)ppn and ^{2}H(d, n)dp, that then elastically scatter in the target.

Because some of the *nd* elastic events can occur at the same time as a background event in another detector (that is, the two events occur in time such that their

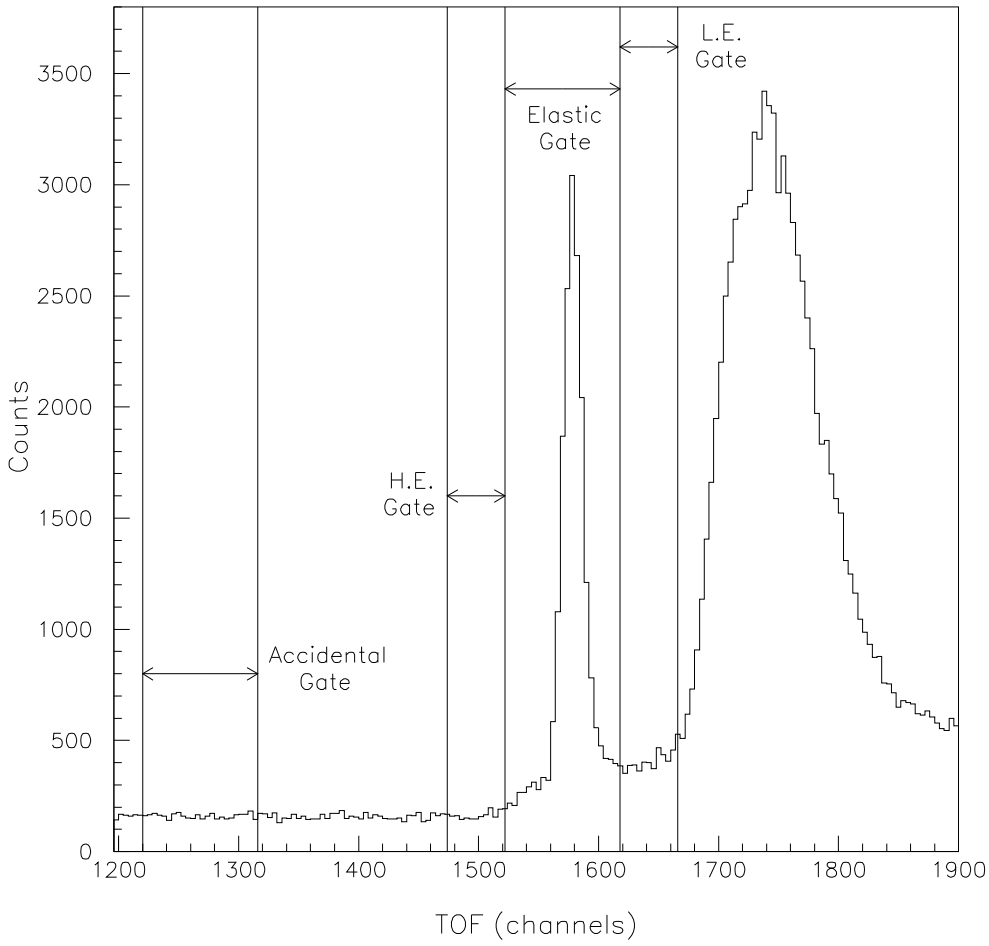

Figure 5.5: Typical TOF spectrum for double-coincidence events. The gates used in the analysis of the elastic-scattering data are shown. Note that the gates for elastic-scattering and accidental regions are set to the same width, while the high-energy (HE) and low-energy (LE) gates are set half as wide. The width of the LE gate was restricted by the separation of the elastic peak and continuum neutron mound. All events in this spectrum passed pulse-height and PSD requirements. The time calibration is 0.1 ns/channel and the CD-side detector center-to-center distance is approximately 160 cm for this particular detector.

signals fall in the electronics coincidence window), these events will be treated as triple coincidences by the electronics (see Section 3.6.3). Figure 5.9 shows this false elastic peak in the triples TOF spectra. It was empirically determined that these triple coincidences make up about 1% of the elastic yields for each detector. As shown in Equation 5.2, the coincidence rate between any two detectors depends on the counting rate in each detector. The number of elastic events lost to false triple coincidences thus varies from detector to detector. To recover these events, test conditions were defined so that the TOF spectra for a particular detector would be incremented whenever a coincidence was formed between it and any of the other eleven detectors in the array. A gate was set around the false elastic peak in this aggregate triple-coincidence spectrum and a simple linear fit was used to account for accidental background (that is, for events where the coincidence was formed by uncorrelated signals in both detectors). Because the triple triggers do not go through the prescale circuit like the double triggers do, the number of extracted yields from the false elastics must be divided by the prescale factor before being added to the net elastic yields.

Three physical processes must be accounted for in obtaining the elastic-scattering yields:

1. A recoil deuteron may not deposit all of its energy in the center detector. If the elastic scattering reaction takes place near the edge of the scintillator volume, the recoil deuteron may exit without depositing all of its energy. Also, as the scattering angle of the neutron increases, the energy of the recoil deuteron increases, resulting in a much longer mean free path in the scintillator fluid. These *edge effects* are simulated by the Monte-Carlo code to determine the percentage of yields lost due to this effect.

2. A neutron can scatter off of more than one nucleus in the target. The relatively large target volume increases the probability that multiple-scattering events from both deuterium and carbon can occur. Monte-Carlo simulations of the double-scattering processes are run to calculate the contributions to the experimental TOF and CDPH spectra.

3. Lower-energy continuum neutrons generated in production cell from the ^{2}H(d, n)ppn and ^{2}H(d, n)dp reactions can scatter successively on carbon and deuterium and arrive at a detector with the same TOF as 16.0 MeV neutrons that scattered only once from deuterium in the CD. These scattered continuum neutrons form a *sample-correlated background* beneath the *nd* elastic-scattering TOF peak. Monte-Carlo simulations and data from the experimental CDPH events in TOF gates adjacent to the elastic-scattering peak are used to separate this background from the *nd* elastic events. These gates are labeled as "LE" and "HE" gates in Figure 5.5.

The procedure used to obtain the yields for elastic scattering was as follows:

1. The experimental *nd* elastic-scattering TOF peak was simulated with a Monte-Carlo (MC) code for single scattering. Time shift and resolution input parameters to the code were adjusted to reproduce the centroid and FWHM of the experimental peak.

2. A gate was set around the elastic-scattering peak and for all events that fell within that gate, the center detector pulse-height (CDPH) spectrum was incremented. This is referred to as the *true + accidental* spectrum. A second gate was set in the accidental region of TOF. For events which fell within this accidental gate, a second CDPH spectrum was incremented. Two more

experimental CDPH spectra were accumulated for events with TOF falling in the low-energy (LE) and high-energy (HE) analysis gates. The accidental spectrum was then subtracted from the *true + accidental* spectrum and the residual background was fit with an exponential function. This background was subtracted, leaving the *true* spectrum. The true spectrum was simulated by the MC with input parameters being adjusted to reproduce the centroid and FWHM.

3. Multiple-scattering (MS) contributions were simulated for events falling in the low-energy, elastic, and high-energy TOF gates. The three MS processes simulated were deuterium-carbon, carbon-deuterium, and deuterium-deuterium double scattering inside the CD scintillator volume. Note that only elastic scattering from carbon was considered. The MS histograms were normalized and subtracted from the corresponding experimental CDPH spectra.

4. Accidental background and MS events were subtracted from the low-energy, high-energy, and true + accidental CDPH spectra. The LE and HE spectra were then averaged channel by channel and normalized to fit the beginning and tail of the true + accidental CDPH spectrum. An exponential fit of the suggested background was made and subtracted from the experimental spectrum.

5. The resulting spectrum after accidental, MS, and sample-correlated background subtraction was integrated to obtain the net elastic yields. Spectra displaying the contributions of each type of background and the final yields are shown in Figure 5.6.

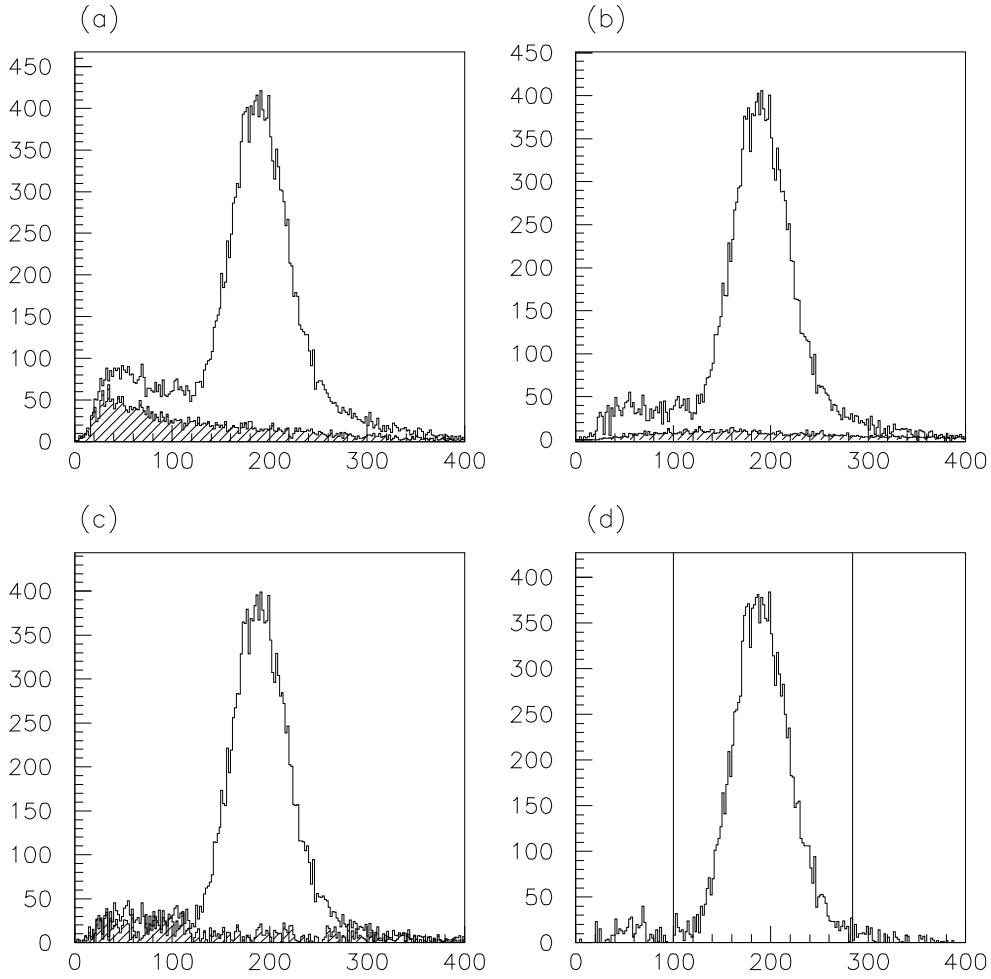

Figure 5.6: CDPH spectra for elastic scattering. Overlays of the background contributions are shown. Threshold and PSD cuts have been applied. (a) CDPH spectra for events falling in the elastic TOF gate and the accidentals gate (shaded). (b) Accidental-subtracted CDPH spectrum shown with the simulated multiple-scattering background. (c) CDPH spectrum with the multiple-scattering background subtracted overlaid with the estimated sample-correlated background spectrum. (d) CDPH spectrum with all background contributions having been subtracted. The counts inside the gate were integrated to get the final elastic yields.

5.3.2 Luminosity Determination

The elastic-scattering yields for a detector at an angle of θ are related to the differential cross section in the lab by

$$Y_{el}(\theta) = \left(\frac{d\sigma}{d\Omega}(\theta)\right)_{lab} \cdot d\Omega \cdot \alpha\left(E_{el}\right) \cdot \epsilon\left(E_{el}\right) \cdot N_{target} \cdot N_{neutron}. \tag{5.4}$$

All the quantities in this equation are known except for the product $N_{target} \cdot N_{neutron}$, which as previously explained is just the integrated beam-target luminosity, $\mathcal{L}_{int}$. The elastic yields, Y_{el}, were determined as explained in the previous subsection. The differential cross section for nd elastic scattering, $\left(\frac{d\sigma}{d\Omega}(\theta)\right)_{lab}$, was computed by the Bochum-Cracow group using rigorous nd calculations [Wit89]. The solid angle of the detector, $d\Omega$, was calculated from its area and flight path. The transmission of the scattered neutron flux through the CD and air, α, was calculated in the Monte-Carlo simulation from well-known neutron total cross sections. Finally, the neutron detector efficiencies, ϵ, were determined in independent measurements [Sal98].

The determination of the absolute breakup cross section from the measured breakup yields also depends on $\mathcal{L}_{int}$ (see Equation 5.3). Therefore, Equation 5.4 was rearranged to determine a value for the luminosity from the elastic yields in each neutron detector:

$$\mathcal{L}_{int} \equiv N_{target} \cdot N_{neutron} = \frac{Y_{el}(\theta)}{\left(\frac{d\sigma}{d\Omega}(\theta)\right)_{lab} \cdot d\Omega \cdot \alpha\left(E_{el}\right) \cdot \epsilon\left(E_{el}\right)} \tag{5.5}$$

Two correction factors to Equation 5.5 were necessary. As described in Section 3.6.3, a prescale circuit was implemented to reduce the high double-coincidence rate resulting from nd elastic scattering at the data acquisition (DAQ) interface. Two scalers were used to count the number of trigger signals before and after the prescale circuit. The ratio of these two scalers gave the *scale factor* which had to be applied

to the yields. The second correction was for the dead-time incurred while the DAQ system was processing events. Section 3.6.4 described the veto circuit that was used to hold off triggers while the digitizing modules were busy. Two scalers were used to count the total number of triggers generated by the detection electronics and the number of triggers that actually were processed by the DAQ system. The ratio of these scalers gave the dead-time correction (DTC) factor.

Luminosities were calculated for the twelve neutron detectors in the STAR array for each replay batch. To permit comparison of different replay batches, the luminosities were normalized by the number of beam current integration (BCI) pulses measured by a scaler for each batch. Equation 5.6 gives the formula used to calculate the integrated beam-target luminosity for each detector for each replay batch:

$$\mathcal{L}_{int} = \frac{Y_{el}(\theta) \cdot \text{scale factor} \cdot \text{DTC}}{\left(\frac{d\sigma}{d\Omega}(\theta)\right)_{lab} \cdot d\Omega \cdot \alpha\left(E_{el}\right) \cdot \epsilon\left(E_{el}\right) \cdot \text{BCI}}. \tag{5.6}$$

An advantage to using nd elastic scattering for normalizing the breakup cross section was that twelve independent normalization factors ($\mathcal{L}_{int}$) could be determined for each replay batch. Because the value determined for the beam-target luminosity should be identical for all the neutron detectors, any deviation in value among the detectors gives a measure of the systematic errors involved in the luminosity determination process. Figure 5.7 shows a plot of integrated beam-target luminosity versus detector number for one batch of data from the SST measurement. Luminosities were determined for the twelve detectors at two different pulse-height thresholds, $\frac{1}{4}\times$Cs and $1\times$Cs. The relative agreement (within statistical uncertainties) of the luminosities at the two different thresholds is a good indication that the thresholds are being set correctly. Luminosities analyzed at both thresholds show a systematic deviation from the average which is likely caused by slight errors in the calculation of attenuation factors for detectors out of the scattering plane. The dispersion (one

standard deviation) in the luminosity data about the average value is approximately ± 1.8%.

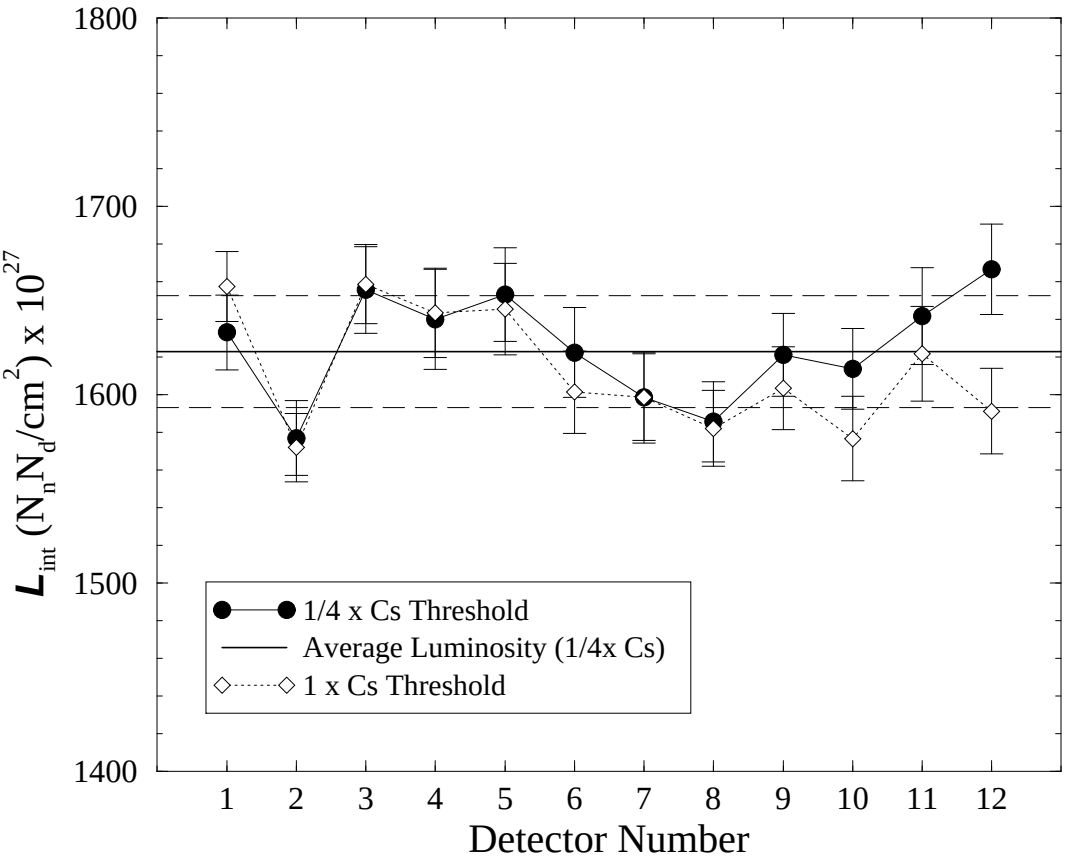

Figure 5.7: Integrated beam-target luminosity, $\mathcal{L}_{int}$, versus detector number for the twelve neutron detectors in the STAR array. The $\mathcal{L}_{int}$ values determined using two different pulse-height thresholds are shown. The error bars on the data represent the statistical uncertainty only. The solid line is the statistically weighted average of the twelve luminosities at a $\frac{1}{4}\times$Cs threshold setting. The long-dashed lines indicate the range of values within one standard deviation of the average luminosity. Note the offset on the vertical scale.

Assuming uncorrelated uncertainties, the square of the total relative uncertainty for $\mathcal{L}_{int}$ can be computed simply as the sum of the squares of the relative uncertainties

in each term of Equation 5.6:

$$\left(\frac{\Delta\mathcal{L}_{int}}{\mathcal{L}_{int}}\right)^2 = \left(\frac{\Delta Y_{el}}{Y_{el}}\right)^2 + \left(\frac{\Delta\sigma_{el}}{\sigma_{el}}\right)^2 + \left(\frac{\Delta d\Omega}{d\Omega}\right)^2 + \left(\frac{\Delta\alpha}{\alpha}\right)^2 + \left(\frac{\Delta\epsilon}{\epsilon}\right)^2. \quad (5.7)$$

The uncertainties for the scale factor, BCI, and DTC were negligible and thus not included in the calculation. The total uncertainty can be separated into statistical and systematic parts. The statistical error on $\mathcal{L}_{int}$ is due entirely to the counting uncertainty in Y_{el} as determined from the numbers of detected foreground and background events. The relative systematic error can be written as

$$\left(\frac{\Delta\mathcal{L}_{int}}{\mathcal{L}_{int}}\right)_{sys} = \left[\left(\frac{\Delta Y_{el}}{Y_{el}}\right)^2_{sys} + \left(\frac{\Delta\sigma_{el}}{\sigma_{el}}\right)^2 + \left(\frac{\Delta d\Omega}{d\Omega}\right)^2 + \left(\frac{\Delta\alpha}{\alpha}\right)^2 + \left(\frac{\Delta\epsilon}{\epsilon}\right)^2\right]^{\frac{1}{2}} \quad (5.8)$$

and varies with analysis batch according to the systematic uncertainty in Y_{el}. This systematic uncertainty is mainly caused by error in the background subtraction technique and is reflected in the standard deviation of the luminosities from detector to detector. The net relative uncertainty of $\mathcal{L}_{int}$ for a data set is the statistically weighted average of the standard deviations obtained for each analysis batch and is approximately $\pm 2.9\%$ for the SST configuration. The systematic error on σ_{el} is estimated to be approximately $\pm 1\%$ and is due to limits on computational precision and the dispersion in predictions based on different modern nucleon-nucleon potential models [Wit89]. The uncertainty in the solid angle comes from measurement error of the detector flight path and varies depending on where the detector is located in the array. It also varies from configuration to configuration because of the different flight paths used (see Table 3.1). The flight paths for those detectors closest to the horizontal scattering plane can be measured to a precision of ± 3 mm, giving an error of $\pm 0.5\%$ for the solid angle in the SST configuration (using an average flight path of ~ 160 cm). The detectors in the top of the array were more difficult to survey. The

$\left(\frac{\Delta Y_{el}}{Y_{el}}\right)$	$\left(\frac{\Delta \sigma_{el}}{\sigma_{el}}\right)$	$\left(\frac{\Delta d\Omega}{d\Omega}\right)$	$\left(\frac{\Delta \alpha}{\alpha}\right)$	$\left(\frac{\Delta \epsilon}{\epsilon}\right)$	Total Systematic Error
$\pm$ 2.9%	$\pm$ 1.0%	$\pm$ 0.5%	$\pm$ 1.3%	$\pm$ 3.0%	$\pm$ 4.5%

Table 5.2: Estimate of systematic errors for the integrated beam-target luminosity determination for the SST configuration.

measurement error in the flight path of these detectors was about ±5 mm, which corresponds to a relative error of about ±0.7% in solid angle for the SST configuration. Because the flight paths for the CST and IST configurations were shorter, the relative systematic error in solid angle was somewhat higher in these configurations than for the SST configuration. The main uncertainty in the neutron transmission factor comes from uncertainties in the total neutron cross sections for the scatterer constituents (carbon, deuterium, silicon, and oxygen). Based on reported errors for these cross sections, the relative systematic error for α is estimated to be ±1.3%. The absolute detector efficiencies were determined in two separate measurements, and assigned a relative systematic uncertainty of ±3%. See the paper by Setze *et al.* [Set96] for a discussion of how the systematic error was assigned for these measurements. Table 5.2 summarizes the systematic uncertainties described here and gives the total systematic error in the beam-target luminosity determination for the SST configuration.

The twelve luminosities that were obtained for each replay batch were statistically averaged to obtain a value for $\overline{\mathcal{L}_{int}}$. The average luminosity per kBCI, average statistical uncertainty, and standard deviation of the individual values from the average for each replay batch of the SST data are shown in Table 5.3. The standard deviation of the individual values of $\mathcal{L}_{int}$ from $\overline{\mathcal{L}_{int}}$ reflects the systematic error associated with this method. The average luminosity normalized by BCI should be

Analysis Batch	kBCI	$\overline{\mathcal{L}_{int}} \times 10^{27}$ (cm^{-2}/kBCI)	Statistical Uncertainty	Standard Deviation
1	8912	1622.824	± 6.568	± 29.702
3	7225	1554.119	± 8.148	± 38.996
4	7969	1548.206	± 6.586	± 53.952
5	5747	1536.518	± 7.271	± 38.677
6	7373	1511.138	± 6.662	± 56.963
7	7309	1515.954	± 7.001	± 48.968
8	5790	1503.528	± 7.413	± 47.596

Table 5.3: Average integrated beam-target luminosity per kBCI for each analysis batch for the SST data with statistical error and standard deviation. Note that batch 2 was omitted from the elastic and breakup analyses because of problems with gain shifts in the electronics for a couple of detectors.

approximately constant from batch to batch due to the fact that the BCI is proportional to the charge deposited by the deuteron beam on the neutron production cell. The neutron flux, however, depends not just on the incident beam current but also on the deuterium gas pressure in the production cell. A slow decrease in gas pressure was observed during the course of most of the experiment and was most likely due to gas leaking around the Havar entrance foil into the evacuated beam line. This decrease means that the values of $\overline{\mathcal{L}_{int}}$ for each batch of data could differ by an amount proportional to the average gas pressure in the cell of each batch. Another factor which could cause changes in the luminosity from batch to batch is the *localized beam heating effect*. In an ideal system, increased deuteron beam current should produce a proportionally higher neutron flux. If the increase in heat due to the higher beam current is not efficiently removed by the cooling system, the local density of gas where the incident deuteron beam passes can be lower than the average density in the cell, resulting in a smaller flux increase than would be expected.

5.3.3 Center Detector Light Response

Besides its important role in determining the absolute normalization factor for the breakup cross section, the analysis of *nd* elastic-scattering data is also vital to the breakup-data analysis because the two-body elastic-scattering process can be used to establish a relationship between pulse height and particle energy in the center detector. In the analysis of the *nd* breakup data, the energy of the two outgoing neutrons is determined from TOF techniques (see Section 5.4), but the energy of the breakup proton must be found from the center detector pulse-height signal. As with all scintillators, the amount of light produced in the center detector is proportional to the amount of energy deposited in the detector by the particle. A *light response function* that quantifies this relation between scintillation light and energy deposition can be found by measuring the pulse heights for charged particles of various known energies. Analysis of *nd* elastic-scattering data allows a light response function for deuterons to be obtained. Tornow *et al.* [Tor86] have shown that for the deuterated scintillator, NE-232, the deuteron light output response function can be related to one for protons by the simple formula

$$L_p(E) = \frac{1}{2} L_d(2E), \tag{5.9}$$

where $L_p(E)$ is the light output of a proton of energy E and similarly for L_d at energy $2E$.

The deuteron light output response function is obtained from the same spectra that are used to determine the elastic-scattering yields. The centroids of the CDPH spectra, after background subtraction, were determined for each detector. Because all the STAR detectors were at the same scattering angle, θ, and thus had approximately the same recoil deuteron energy for *nd* elastic scattering, they provided only one

Monitor	SST		CST		IST	
	θ	E_d	θ	E_d	θ	E_d
1	91.0	10.81	110.3	12.45	107.5	12.26
2	77.0	9.13	89.4	10.64	87.8	10.47
3	66.0	7.55	78.6	9.35	76.3	9.04
4	34.5	2.65	44.0	4.06	42.9	3.89

Table 5.4: Laboratory scattering angles, θ, for the monitor detectors for the three star configurations that were studied and the recoil deuteron energy, E_d, associated with *nd* elastic scattering to each angle. Angles are given in degrees and the recoil energies have units of MeV.

point for the light output response curve. As described in Section 3.4, four monitor detectors were mounted to the left of the STAR array at different scattering angles to provide more calibration points for the light output response curve. Table 5.4 shows the central scattering angles for the monitor detectors for all three star configurations that were studied. This table also gives the recoil deuteron energy associated with *nd* elastic scattering to each angle. Additional data points were obtained from the measurement of the electronic pedestal (which is just the pulse height at zero energy), and from the 180° recoil scattering edge which shows up in the unconditional CDPH spectrum. The centroid channels for the STAR detectors and four monitors were plotted versus the recoil deuteron energy for elastic scattering along with the zero energy and 180° recoil points. Figure 5.8 shows a light response curve for the SST measurement.

For all measurements described in this work, the center detector light output response was best described by a piece-wise continuous fit of two analytical functions. For the SST configuration, the functions coincided at a recoil deuteron energy of 7.55 MeV. Below 7.55 MeV the points were fit with a quadratic function of E. Above 7.55 MeV they were fit with a linear function of E. Along with the relationship between

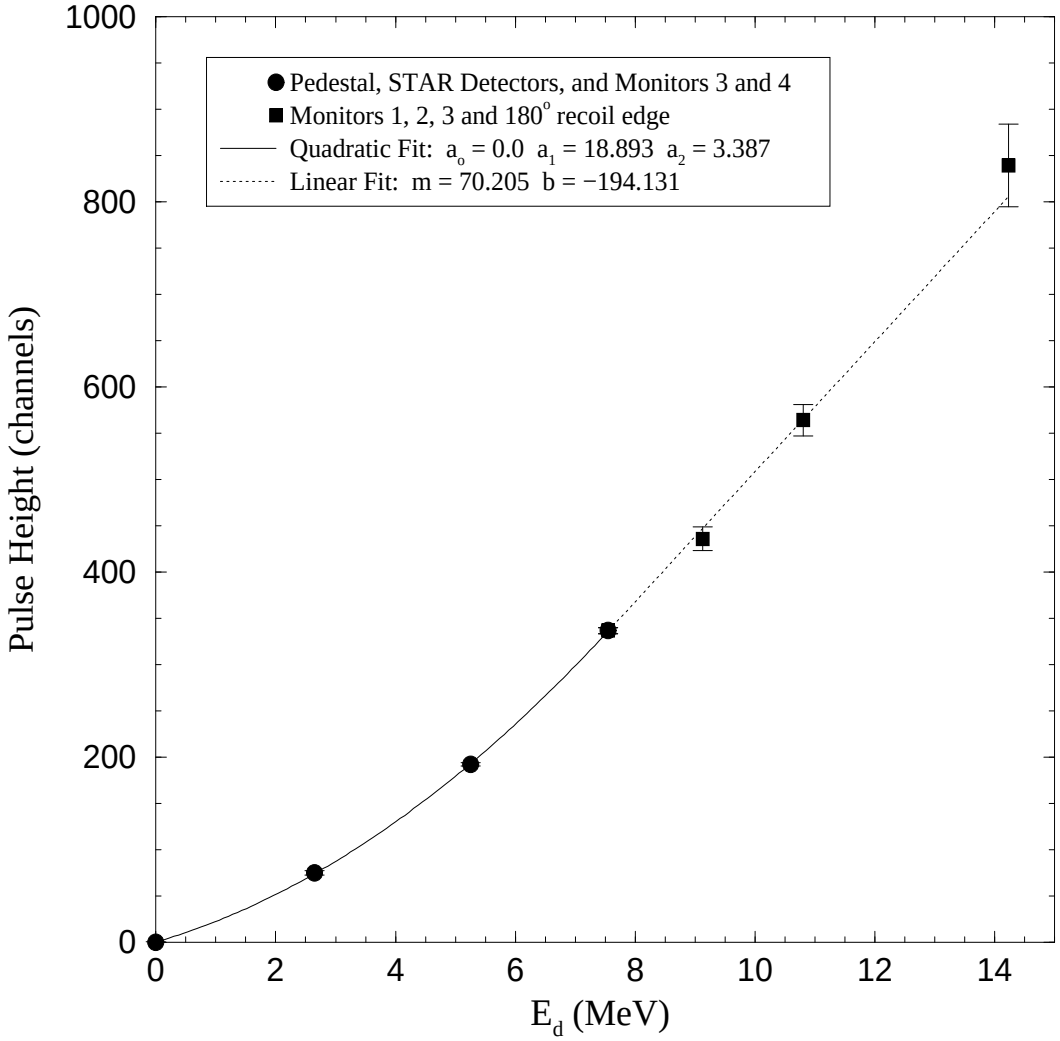

Figure 5.8: Center detector light output response function for the SST measurement. Quadratic and linear fits used to describe the data are shown. The error bars on the data were estimated from the Gaussian fitting procedure that was used to obtain the CDPH centroids. The quadratic and linear functions were constrained so that their values and slopes would coincide at a deuteron energy of 7.55 MeV.

deuteron and proton light output defined in Equation 5.9, these two functions were used to calculate the proton energies for the breakup data.

5.4 Breakup Analysis

Breakup events were identified by their hit register value ($\equiv 1$). Additional sorting was provided by the TDC hit register value (see Section 5.2.2), which helped select out events having the desired detector combinations for the configuration of interest. In the SST configuration for example, only coincidences between detectors that were 120° apart in ϕ (see Section 3.4) were processed. For each event that passed the breakup sorting requirements, the pulse-height and pulse-shape parameters of both neutron detectors were tested to determine if they met the $\frac{1}{4}\times$Cs threshold and PSD cuts that were described earlier for the elastic-scattering data analysis. The kinematic properties of some configurations allowed a software lower-level threshold to be set on the recoil proton pulse height in the CD. Because in the SST configuration the recoil proton energy is always above 4.6 MeV, a software test was applied to the CDPH that cut out events with proton energies that were lower than about 3 MeV. The situation is similar for the CST and IST configurations; the minimum recoil proton energy of interest is quite high, allowing the software threshold to be set high as well. The one configuration where a software lower-level threshold was not possible was the FSI. Here the proton energy dips to approximately 600 keV, which is very close to the hardware threshold. The values chosen for these cuts take into consideration the energy resolution of the center detector and finite geometry effects so as not to cut out any "good" events.

All events that fulfilled the PH, PSD, and CDPH requirements were used to

increment the appropriate TOF spectra. Figure 5.9 shows the TOF spectra for one detector pair in the SST configuration. The gates shown in the figure were used to distinguish between accidentals and true events. The following subsections will describe the treatment of the "True + Accidentals" and "Accidental" events. Note that the gate set around the "True + Accidentals" events will be referred to as "gate 1" and the gate set around the "Accidentals" will be referred to as "gate 2" in the following discussion.

5.4.1 True + Accidentals

All the events that passed the PH, PSD, and CDPH cuts discussed above and which had a neutron TOF that fell inside gate 1 for both detectors were considered to be "True + Accidental" events. Gate 1 was set from ten channels after the elastic-scattering peak all the way up to the channel representing the equivalent neutron energy for the software pulse-height threshold ($\frac{1}{4}\times$Cs in most cases). For these events the energies of both neutrons were calculated from their TOF values. Because TOF is a relative technique, a time reference had to be established to allow absolute quantities such as energy to be determined. The false elastic-scattering peak in the triples spectra (described in Section 5.3.1) provides a convenient time reference. The energy of an incident 16.0-MeV neutron that elastically scatters from deuterium to some angle θ is given by two-body kinematics. The time (t_{el}) it takes a neutron of energy E_{el} to travel a distance l (the flight path of the detector) is then easily calculated from nonrelativistic kinematics. The time difference between an elastic reference event (occurring in channel c_{el} in TOF) and a breakup event (in channel c) is given as

$$\Delta t = t_{cal} \cdot (c - c_{el}) \tag{5.10}$$

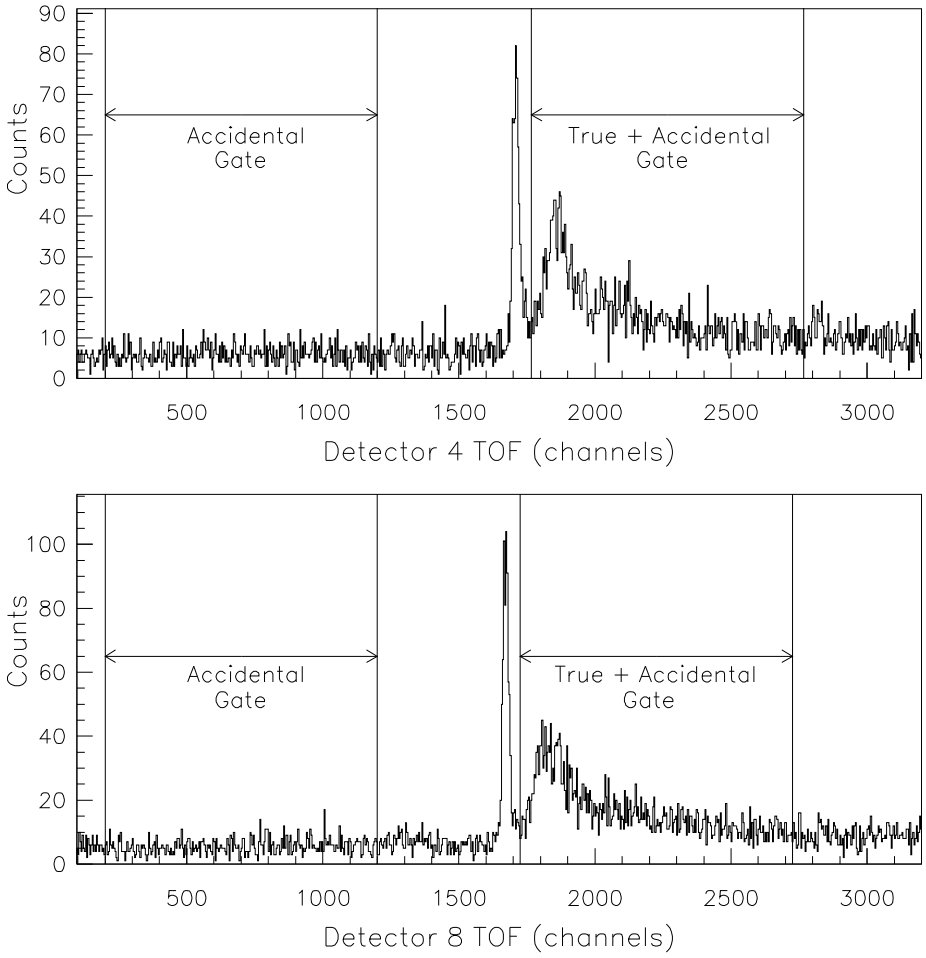

Figure 5.9: Triple-coincidence TOF spectra for a pair of neutron detectors used in the SST configuration ($\theta_4 = 51.5°$, $\phi_4 = 0.0°$, $\theta_8 = 51.5°$, $\phi_8 = 120.0°$) measurements.

where t_{cal} is the time calibration factor with units of ns/channel. In all the measurements described here, the full digitizing range (or TAC range) of the TDC was set to 400 ns and all 12 bits of the data word were used (giving spectra with 4096 channels). The resulting time calibration was thus approximately 0.1 ns/channel. The energy of a neutron event coming later in TOF than the elastic-scattering event can be found from the following equation:

$$E_n = \left(\frac{72.25 \cdot l}{\Delta t + t_{el}} \right)^2 \tag{5.11}$$

where 72.25 comes from the values of the speed of light, c, and the mass of the neutron, and has units of $\mathrm{ns} \cdot \mathrm{m}^{-1} \cdot \sqrt{\mathrm{MeV}}$.

The energy of the breakup proton was calculated from its center detector pulse height by using the light output response function that was found from the elastic-scattering analysis (see Section 5.3.3). The sum of the energies of the three detected particles (two neutrons and the proton) was calculated and a *total energy* histogram was incremented. For true breakup events originating in the center detector, energy conservation requires the total energy of the three particles to be 13.775 MeV, which is just the remaining energy from the 16.0 MeV initial neutron energy after breaking the deuteron (the binding energy of the deuteron is about 2.225 MeV). Figure 5.10 shows a total energy spectrum for the SST configuration. The centroid of the enhancement is at approximately 13.78 MeV. During the analysis, deviations of the centroid of this peak from 13.78 MeV were indications of errors in the energy calibrations from TOF or the CD light output response function.

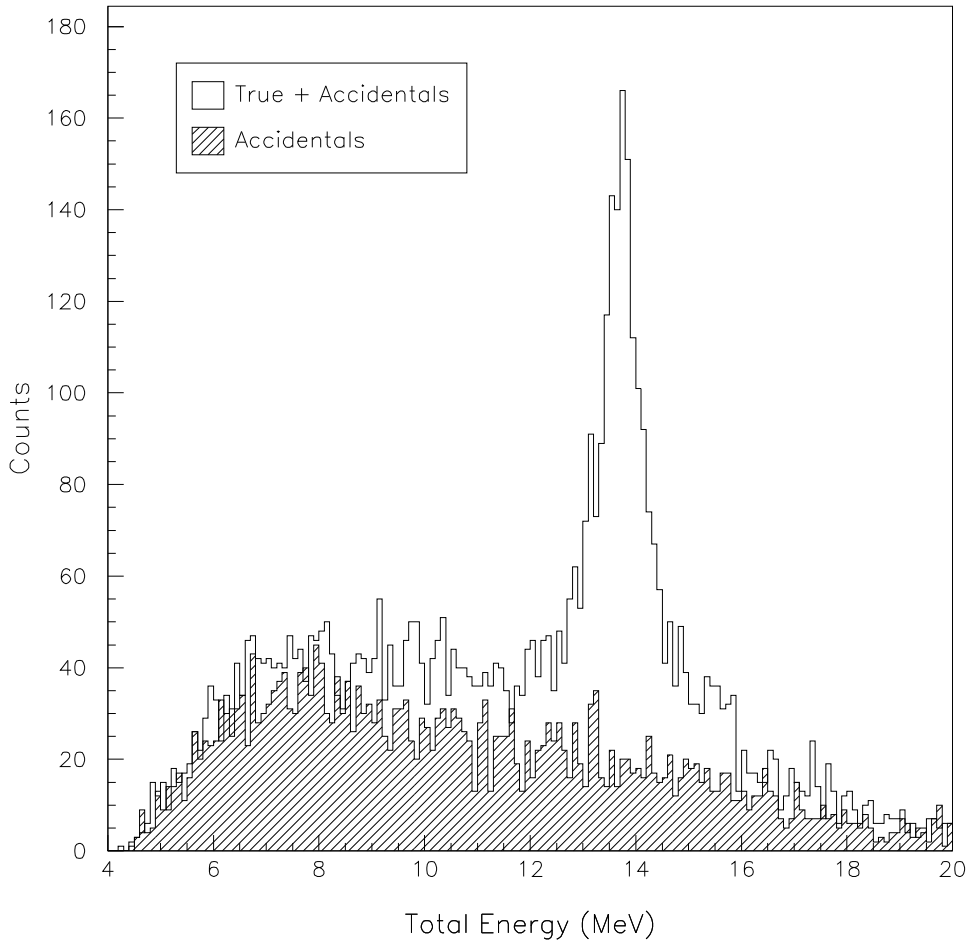

Figure 5.10: Total energy spectrum for the SST configuration at 16.0 MeV. The shaded area comes from accidental events. The centroid of the enhancement is at approximately 13.78 MeV.

5.4.2 Triple-Coincidence Accidentals

Treating accidental coincidences in the breakup analysis is made difficult by the fact that one or both of the detected neutrons in a breakup event could be due to an accidental coincidence between a side detector and the center detector. The triple-coincidence requirement for breakup events means that the simple subtraction technique used in the elastic analysis is no longer sufficient. Instead, all accidental combinations involving the two detectors and the CD must be considered.

Accidentals are time-uncorrelated events that are misidentified as breakup events. In these events, a signal in one or both detectors is produced by room background neutrons. Because these events should be randomly distributed in time, they occur throughout the time coincidence window and show up in all regions of the TOF spectrum, including where valid breakup events are kinematically allowed. The procedure used to identify and process accidentals is described below..

All events fulfilling the PH, PSD, and CDPH test conditions and which had a neutron TOF that fell inside gate 2 were considered to be "Accidental" events. Gate 2 was set in the TOF region before the γ-ray peak because all these events were unphysical (i.e. no time-correlated particles could arrive at the detector before the γ-rays from the reaction in the CD) and was of the same width as gate 1. Because these accidental events are time uncorrelated with the CD, the energy of the associated neutrons cannot be determined from their position in the TOF spectrum. To generate an energy spectrum, the TOF positions of events in gate 2 must be shifted to cover the same time region as events falling in gate 1. The "energies" of the accidental events are then calculated with respect to the elastic peak just as for the events in gate 1. For an event in gate 2 with a TOF in channel c, the "new"

Event Tag	Detector 1 Event Type	Detector 2 Event Type
1	T+A	T+A
2	T+A	A
3	A	T+A
4	A	A

Table 5.5: Identification of true and accidental triple-coincidence types. "T+A" represents a TOF value falling in the true + accidental gate for that detector and "A" represents a value falling in the accidental gate.

TOF channel is

$$c' = (c - c_a) + c_t \tag{5.12}$$

where c_a is the first channel of gate 2 and c_t is the first channel of gate 1. The energy is then calculated using Equations 5.10 and 5.11 with c' having replaced c.

Breakup events were classified into four categories according to the time region in which the TOF value for each of the detected particles in the coincidence fell. Table 5.5 shows the four possible combinations of "True + Accidental" and "Accidental" events and the tags assigned to each. Events of each tag were treated separately in the analysis. Total-energy spectra were accumulated for each kind, and the events for each kind were projected onto the ideal kinematic locus using the same algorithm. In the last stage of analysis, the projected yields of types 2-4 were subtracted from type 1. The procedure for this subtraction was as follows:

1. The projected yields for types 2 and 3 were added together.

2. Type 4 yields were subtracted from the type 1 yields.

3. Because type 4 events also form an accidental background underneath events of types 2 and 3, type 4 yields were subtracted from the yields of both of those types.

4. The background-subtracted type 2 and 3 yields were then subtracted from the background-subtracted type 1 yields.

In summary, the expression for obtaining the "True" triple-coincidence yields is

$$\begin{aligned} Y(T) &= [Y(1) - Y(4)] - [Y(2) - Y(4)] - [Y(3) - Y(4)] \\ &= Y(1) - Y(2) - Y(3) + Y(4) \end{aligned} \tag{5.13}$$

To test this method of handling the random accidental background, data were sorted for triple coincidences involving two detectors that were only 30° apart in ϕ for the CST setup ($\theta_n = 71.2°$). This configuration is not kinematically allowed; therefore, all events must come from accidental coincidences. After processing the data in the manner described above, the total-energy spectrum of the accidental events was subtracted from the total-energy spectrum containing the "True + Accidental" events. The resulting difference spectrum was statistically consistent with zero.

5.5 Determining the Breakup Cross Section

5.5.1 Monte-Carlo Corrections

Two of the largest corrections necessary when extracting an absolute cross section in any experiment involving neutrons are for attenuation and detector efficiency. The attenuation (or conversely the transmission) of the scattered neutron flux depends on the neutron total cross sections of the materials through which the neutron passes and the distance travelled through those materials. As described in Section 5.2.5, finite-geometry effects due to the relatively large size of the scatterer and detectors make a simple calculation of the transmission correction factors difficult. The

spread of energies about the ideal kinematic locus also makes calculating the detector efficiency corrections difficult. Monte-Carlo simulations are needed to determine the correction factors throughout the kinematic range allowed by finite geometry and energy resolution. As discussed in Section 4.3.3, the product of the transmissions and efficiencies for the two breakup neutrons were computed and stored in an array indexed by the three particle energies (E_{n1}, E_{n2}, E_p). The effective transmission and efficiency corrections are thus given as

$$\begin{aligned} \overline{\alpha}\left(E_{n1}, E_{n2}, E_p\right) &\equiv \alpha_1\left(E_{n1}\right) \cdot \alpha_2\left(E_{n2}\right) \quad \text{and} \\ \overline{\epsilon}\left(E_{n1}, E_{n2}, E_p\right) &\equiv \epsilon_1\left(E_{n1}\right) \cdot \epsilon_2\left(E_{n2}\right). \end{aligned} \tag{5.14}$$

The magnitude of these correction factors can be seen in Figure 5.11 where the efficiency and transmission arrays have been projected into the E_{n1}-E_{n2} plane.

The Monte-Carlo code also calculated a weighting factor (w) which was obtained from the normalized Gaussian function used to smear the proton energies (accounting for the poor energy resolution of the center detector). The weighting factor array was used in conjunction with the transmission and efficiency arrays to further restrict the set of events that were included in the final analysis. Only events where the product $\overline{\alpha} \cdot \overline{\epsilon} \cdot w$ was non-zero were passed to the projection subroutine. This condition effectively puts a three-dimensional cut on the kinematic region of interest in E_{n1}-E_{n2}-E_p space (as determined by the Monte-Carlo simulation).

5.5.2 Data Projection

As explained in Section 5.2.5, because the real kinematic locus for an event cannot be determined, the data are projected onto the "ideal" kinematic locus and then compared to theoretical predictions which have been treated in a similar manner.

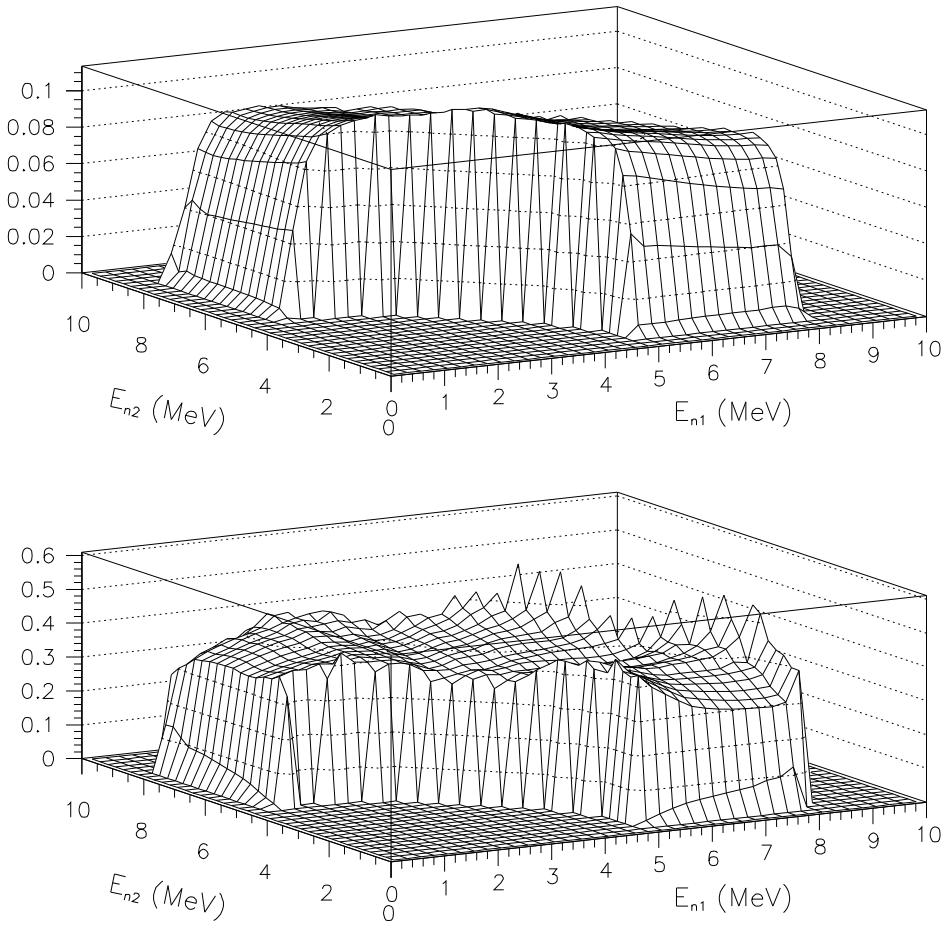

Figure 5.11: Efficiency (top graph) and neutron transmission (bottom graph) arrays projected on the E_{n1} vs. E_{n2} plane for the SST configuration (detector pair θ_1=θ_2=51.5°, $\phi_1 = 0°$, and $\phi_2 = 120°$).

The kinematic locus is parameterized in terms of S, the path length along the ideal kinematic curve. The origin of S (i.e. where S = 0) is traditionally defined as the point where the locus crosses the E_{n1} axis (or where $E_{n2} = 0$). This definition is sufficient for the SST and FSI configurations; however, the ideal loci for the CST and IST configurations never intersect either the E_{n1} or E_{n2} axis. For these two configurations, the origin of S is defined to be the point where E_{n2} reaches its minimum value. In all these situations, S increases as the locus is traversed in the counter-clockwise direction (see Figure 1.4 and Appendix B).

Events which passed the three-dimensional cut generated from the Monte-Carlo simulation had their particle energies converted to momentum by

$$k_i = \sqrt{2mE_i} \tag{5.15}$$

where it was assumed that $m_n = m_p$. The event was then projected from the three-dimensional momentum space into bins along the S-curve by minimizing the quantity

$$K = (k_{n1}^{ideal} - k_{n1})^2 + (k_{n2}^{ideal} - k_{n2})^2 + (k_p^{ideal} - k_p)^2 \tag{5.16}$$

where the superscript *ideal* refers to the momenta of the center of the bins along S used in the projection. The data were binned in 500-keV steps of arc-length S for the CST, IST, and FSI configurations. For the SST configuration the data were summed in 750-keV wide bins to reduce the statistical uncertainties. This method was used in processing both "True + Accidental" and "Accidental" spectra (see Figure 5.12). After subtraction of accidentals, the yields for the breakup reaction were extracted as a function of S.

The theoretical cross-section predictions were averaged over the finite geometry and energy resolution of the experiment and projected onto the ideal kinematic locus using this same algorithm. The projected cross section will be used in comparison

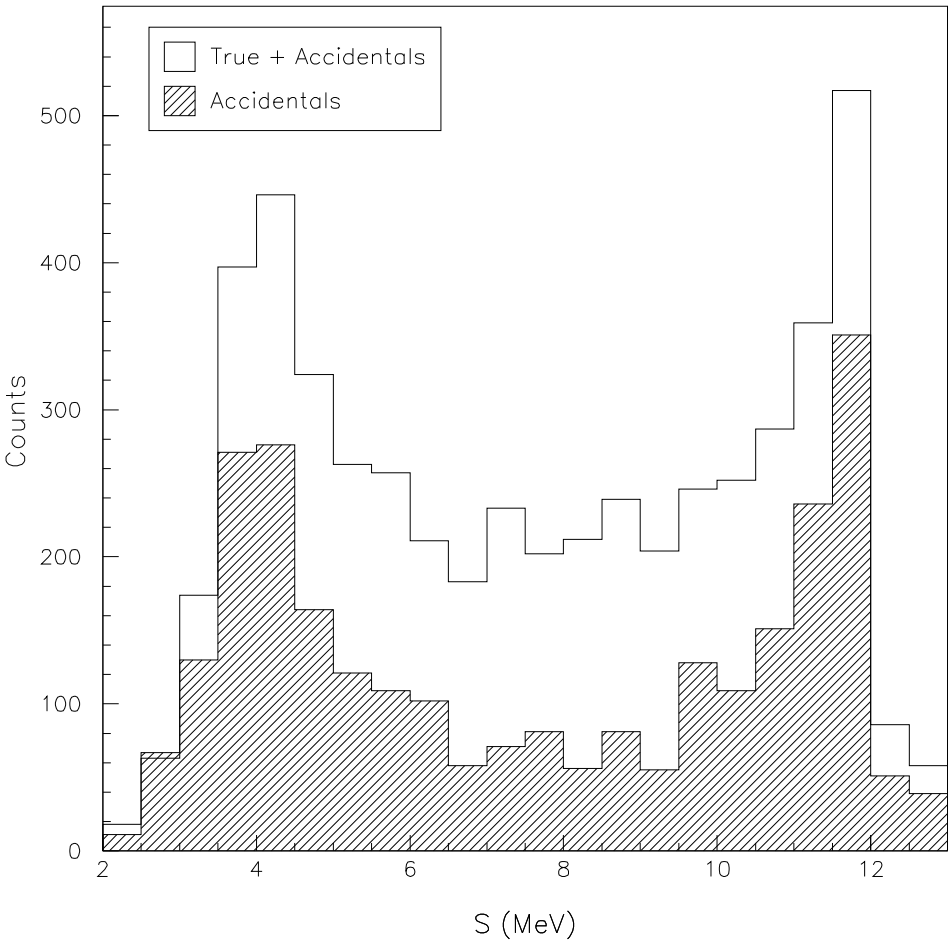

Figure 5.12: "True + Accidental" and "Accidental" yields projected onto the ideal kinematic locus for the SST configuration. Note that these yields only represent about one-quarter of the total data for this configuration.

with the final cross section extracted from the experimental data. Projections of the efficiency and transmission arrays onto S are shown in Figure 5.13 to illustrate the magnitude of the corrections that were applied to the breakup yields to obtain a final cross section.

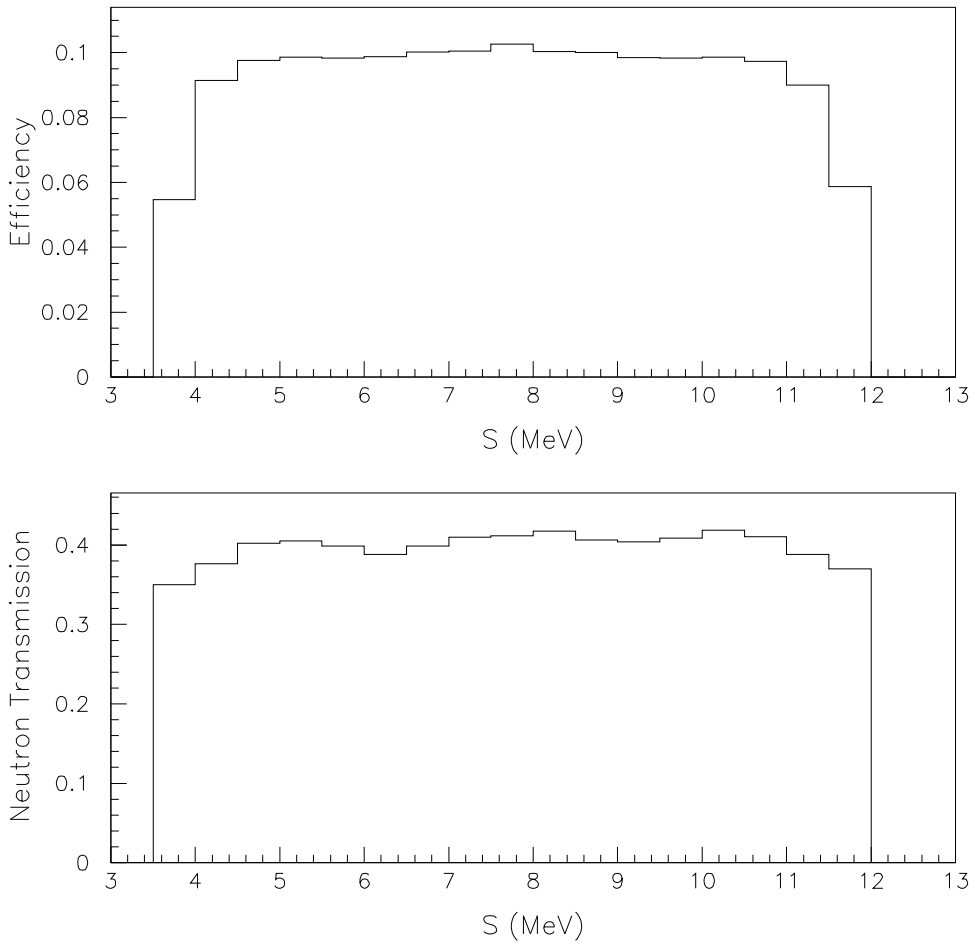

Figure 5.13: Effective efficiency and neutron transmission correction factors projected onto the kinematic locus for the SST configuration (detector pair θ_1=θ_2=51.5°, $\phi_1 = 0°$, and $\phi_2 = 120°$).

5.5.3 Cross-Section Determination

Combining Equations 5.3, 5.5, and 5.14, the breakup cross section in each bin along S can be written as

$$\frac{d^5\sigma}{d\Omega_1 d\Omega_2 dS} = \frac{Y_{bu} \cdot \mathrm{DTC}}{d\Omega_1 \cdot d\Omega_2 \cdot dS \cdot \overline{\alpha} \cdot \overline{\epsilon} \cdot \overline{\mathcal{L}_{int}} \cdot \mathrm{BCI}}. \tag{5.17}$$

During the projection of the breakup yields onto the kinematic locus, two other arrays were generated as a function of S:

$$\mathcal{F}(S) \equiv \sum_i (\overline{\alpha} \cdot \overline{\epsilon} \cdot \omega)_i \quad \text{and} \tag{5.18}$$

$$\mathcal{G}(S) \equiv \sum_i \omega_i \tag{5.19}$$

where the summation was over each point projected into a specific bin along the S-curve. These two arrays were used to determine the product of the neutron transmissions and efficiencies for each point on the locus since

$$\overline{\alpha} \cdot \overline{\epsilon} = \frac{\mathcal{F}(S)}{\mathcal{G}(S)}. \tag{5.20}$$

Substituting this into Equation 5.17, the cross section becomes:

$$\frac{d^5\sigma}{d\Omega_1 d\Omega_2 dS} = \frac{Y_{bu}(S) \cdot \mathrm{DTC} \cdot \mathcal{G}(S)}{d\Omega_1 \cdot d\Omega_2 \cdot dS \cdot \mathcal{F}(S) \cdot \overline{\mathcal{L}_{int}} \cdot \mathrm{BCI.}} \tag{5.21}$$

5.6 Error Analysis

In calculating the total uncertainty in the measured breakup cross section (Equation 5.17), the beam-target luminosity was factored into its constituents so that correlations could be explicitly accounted for. The statistical and systematic errors in the *nd* breakup cross section follow from Equations 5.6 and 5.17 by adding the

uncorrelated errors in quadrature with the statistical error just given by:

$$\left(\frac{\Delta\sigma_{bu}}{\sigma_{bu}}\right)_{stat} = \left[\left(\frac{\Delta Y_{bu}}{Y_{bu}}\right)^2_{stat} + \left(\frac{\Delta Y_{el}}{Y_{el}}\right)^2_{stat}\right]^{\frac{1}{2}}. \tag{5.22}$$

The correlated systematic errors must be treated separately before they can be combined with the uncorrelated errors. A cancellation occurs for correlated errors that appear in both numerator and denominator, which is the case for the attenuation and absolute efficiency correction factors when Equation 5.17 is expanded out. Because the same cross section libraries are used by the Monte-Carlo simulation to calculate the attenuation factors for the luminosity determination and the *nd* breakup cross section, the error in the attenuation for $\mathcal{L}_{int}$ cancels in part the error in the attenuation factor for one of the two breakup neutrons. Using standard propagation of error techniques, these errors are added linearly with a sign indicating whether the factor is in the numerator or denominator as

$$\left(\frac{\Delta\alpha}{\alpha}\right) = \left(\frac{\Delta\alpha_{\mathcal{L}}}{\alpha_{\mathcal{L}}}\right) - \left(\frac{\Delta\alpha_1}{\alpha_1}\right) - \left(\frac{\Delta\alpha_2}{\alpha_2}\right). \tag{5.23}$$

A similar treatment of the absolute detection efficiency yields

$$\left(\frac{\Delta\epsilon^{abs}}{\epsilon^{abs}}\right) = \left(\frac{\Delta\epsilon^{abs}_{\mathcal{L}}}{\epsilon^{abs}_{\mathcal{L}}}\right) - \left(\frac{\Delta\epsilon^{abs}_1}{\epsilon^{abs}_1}\right) - \left(\frac{\Delta\epsilon^{abs}_2}{\epsilon^{abs}_2}\right). \tag{5.24}$$

The total systematic uncertainty in the breakup cross section can then be found by combining the correlated and uncorrelated sources of error in quadrature

$$\begin{aligned}\left(\frac{\Delta\sigma_{bu}}{\sigma_{bu}}\right)_{sys} = \Bigg[&\left(\frac{\Delta Y_{el}}{Y_{el}}\right)^2 + \left(\frac{\Delta\sigma_{el}}{\sigma_{el}}\right)^2 + \left(\frac{\Delta d\Omega_1}{d\Omega_1}\right)^2 + \left(\frac{\Delta d\Omega_2}{d\Omega_2}\right)^2 + \\ &\left(\frac{\Delta d\Omega_{\mathcal{L}}}{d\Omega_{\mathcal{L}}}\right)^2 + \left(\frac{\Delta\alpha}{\alpha}\right)^2 + \left(\frac{\Delta\epsilon^{abs}}{\epsilon^{abs}}\right)^2 + \\ &3\times\left(\frac{\Delta\epsilon^{shape}}{\epsilon^{shape}}\right)^2 + 3\times\left(\frac{\Delta\epsilon^{thresh}}{\epsilon^{thresh}}\right)^2\Bigg]^{\frac{1}{2}}\end{aligned} \tag{5.25}$$

where the α and ϵ^{abs} terms are just the correlated errors from Equations 5.23 and 5.24. ϵ^{shape} and ϵ^{thresh} are the errors in the shape determination of the efficiency curve and in the pulse-height threshold setting for the neutron detectors respectively. These errors are assumed to have a normal distribution and thus contribute a factor of 3 corresponding to the addition in quadrature of the terms used in the luminosity determination and breakup cross section.

Estimates of the magnitude of each term in Equation 5.25 and the sources of these systematic uncertainties are described below:

1. As mentioned in Section 5.3.2, the uncertainty in the yields for *nd* elastic scattering is due mainly to error in the subtraction technique used to eliminate accidental and sample-correlated backgrounds. An estimate of the uncertainty comes from the standard deviation of the luminosities determined for each detector from the average. A statistically weighted average for all analysis batches for the SST configuration gives a net uncertainty of approximately $\pm 2.9\%$.

2. The uncertainty in the *nd* elastic-scattering cross section used (σ_{el}) is approximately $\pm 1\%$ and is due to limits on computational precision and the dispersion in predictions based on different nucleon-nucleon potential models [Wit89].

3. The uncertainty in the solid angles comes from measurement error of the detector flight path and varies depending on where the detector is located in the array. It also varies from configuration to configuration because of the different flight paths used (see Table 3.1). The flight paths for those detectors closest to the horizontal scattering plane can be measured to a precision of ± 3 mm, giving an error of $\pm 0.5\%$ for the solid angle in the SST configuration (using

an average flight path of $\sim$ 160 cm). The detectors in the top of the array were more difficult to survey and therefore increased the measurement error to about $\pm$5 mm, which gives an error of about $\pm$0.7% in solid angle for the SST configuration. Because the flight paths for the CST and IST configurations were shorter, the systematic error in solid angle will be somewhat higher than for the SST configuration.

4. The main uncertainty for the neutron transmission factors comes from uncertainties in the total neutron cross sections for the scatterer constituents (carbon, deuterium, silicon, and oxygen) that were used in the Monte-Carlo simulations. Based on reported errors for these cross sections, the systematic error for α is estimated to be $\pm$1.3%.

5. The uncertainty in the absolute detection efficiency for each neutron detector derives from uncertainty in the normalization of the $^{2}\mathrm{H}(\mathrm{d},\mathrm{n})^{3}\mathrm{He}$ reaction cross section that was used in previous efficiency measurements [Sal98]. The normalization uncertainty was estimated to be $\pm$2.0%. Other uncertainties in the efficiency measurements accounted for a $\pm$2.0% error [Set96]. These errors were uncorrelated and added in quadrature for a total uncertainty of $\pm$3.0%.

6. Efficiency measurements were made with the $^{2}\mathrm{H}(\mathrm{d},\mathrm{n})^{3}\mathrm{He}$ source reaction and compared to those taken with the neutrons from the spontaneous fission of a ^{252}Cf source. The determination of the shape of the efficiency curve for each detector from this comparison was estimated to have an approximate $\pm$1.0% uncertainty [Sal98].

7. The shape and magnitude of the neutron detector efficiency curve depends on the pulse-height threshold setting. The threshold settings are determined by

Source of Uncertainty	Estimated Uncertainty
Elastic Yields	± 2.9%
Elastic Cross Section	± 1.0%
Solid Angle	± 0.5%
Neutron Attenuation	± 1.3%
Detector Efficiency (Absolute)	± 3.0%
Detector Efficiency (Shape)	± 1.0%
Threshold Setting	± 0.5%
Total Uncertainty	± 5.0%

Table 5.6: Summary of systematic uncertainties in the cross-section determination for the SST configuration.

obtaining the Compton scattering edge from ^{137}Cs. An error of ±2 channels in this measurement translates into a threshold uncertainty of about ±0.5%. This uncertainty should be uncorrelated from detector to detector and is assumed to have a normal distribution.

The systematic uncertainties are summarized in Table 5.6 for the SST configuration. As explained above, the solid angle uncertainty will be slightly higher for the CST and IST configurations. The total systematic uncertainty was calculated by adding all the uncertainties in this table in quadrature according to Equation 5.25.

Chapter 6

Results and Conclusions

6.1 The Experimental Cross Sections

Finite-geometry cross sections were determined for the space-, coplanar-, and intermediate-star configurations as well as for an np FSI configuration as a function of S using Equation 5.21. As explained in Section 5.2.1, the data replay was broken up into smaller batches to facilitate fine adjustments in analysis parameters and to track systematic effects. Additionally, the analysis codes treated each breakup detector pair as a separate measurement. Again the primary motivation was to monitor systematic effects. Cross sections for a particular detector pair were determined by statistically averaging the data for all the replay batches. The cross sections for each detector pair were then statistically averaged to give the final results for each configuration. Cross-section data points at the extremes of the S-curves were excluded because the neutron detection efficiency becomes highly dependent upon the precision of the threshold setting and the energy resolution of the detector for

$E_n \lesssim 1.0$ MeV at the $\frac{1}{4}\times$Cs threshold setting.

The cross-section data for the four breakup configurations are compared in Figures 6.1 to 6.4 to rigorous *nd* calculations made using the CD-Bonn NN potential [Mac01]. The dotted curves in these figures represent point-geometry calculations. The solid curves are calculations of the finite-geometry cross sections obtained from Monte-Carlo simulations (as described in Section 4.3.3). The error bars on the data represent statistical uncertainties only. The systematic uncertainty associated with these measurements is approximately ±5.0% (see Section 5.6). Note that this uncertainty can only affect the magnitude of the cross section, not the shape.

Brief observations about these results for each of the configurations are given below. Tables of the cross sections determined for all four configurations can be found in Appendix A.

6.1.1 SST

Results for the space-star configuration are shown in Figure 6.1. The data are consistently higher than both the point-geometry and finite-geometry calculations. (The corrections due to finite-geometry effects are seen to be negligible over the S range of the measured data.) Excluding the point at each end of the measured distribution, the statistically weighted average of the data is 1.024 ± 0.027 mb/sr^2·MeV. When the systematic uncertainty is added in quadrature with the statistical uncertainty, the total error becomes ±0.058 mb/sr^2·MeV. This uncertainty puts the average cross section at approximately three standard deviations higher than the theoretical prediction. Closer inspection of the data reveals that seven of the points are within one (statistical) error bar of the average value with the other three points

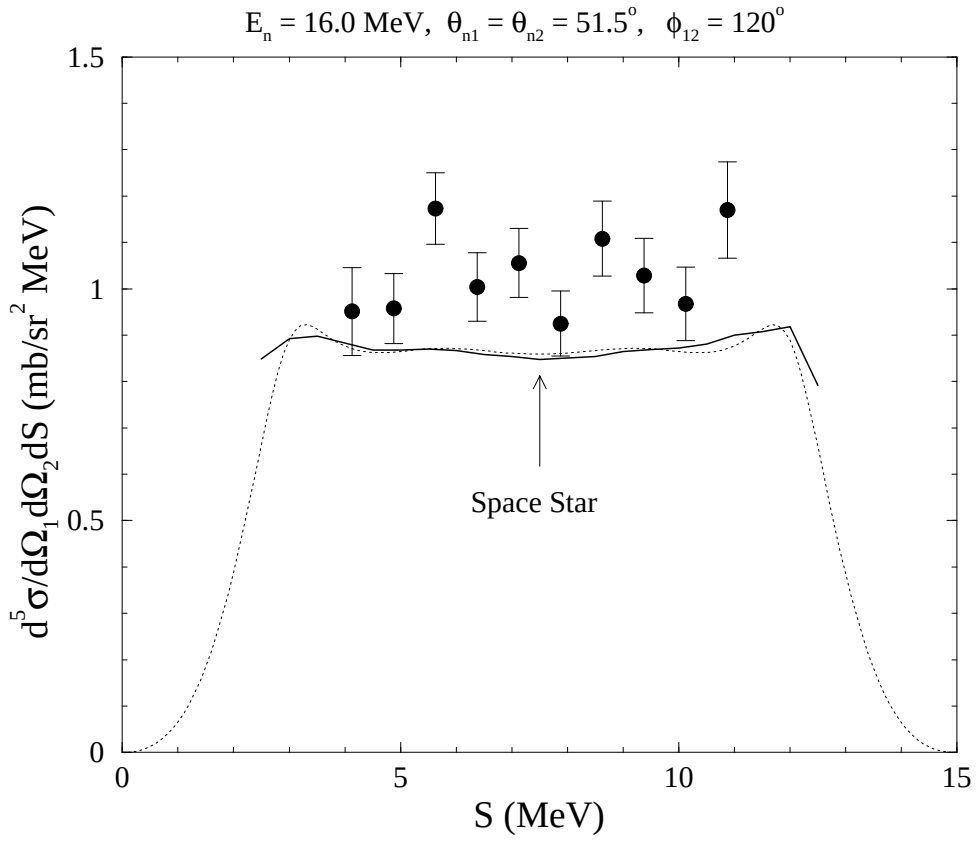

Figure 6.1: Results for the space-star configuration. The dotted curve is the point-geometry calculation. The solid curve is the finite-geometry prediction from Monte-Carlo simulations. The error bars on the data represent the statistical uncertainties only.

less than two error bars away. This distribution is consistent with statistical fluctuations about a constant value. One can conclude then that the flat shape of the SST cross section predicted by calculation is reproduced in the data. The three standard deviation discrepancy in the magnitude of the measured data seems to confirm the existence of the star anomaly at 16.0 MeV. Possible explanations for this phenomenon are offered in Section 6.3.

6.1.2 FSI

Results for the *np* FSI configuration measured concurrently with the space star are shown in Figure 6.2. The measured cross sections are significantly lower than theory in the final-state peaks. The disagreement in the peaks is quite puzzling. The configuration for the FSI was believed to be an excellent place to measure the systematic error in the experimental techniques used by determining a value for the $^1S_0$ neutron-proton scattering length, a_{np}. Previous *nd* breakup measurements at 13.0 MeV [Sal98, Gon99] determined a value for a_{np} that was consistent with that from free scattering. This result for a_{np} gave confidence in the value obtained for the $^1S_0$ neutron-neutron scattering length, a_{nn} in the same experiment. The size of the deviation from the accepted value of a_{np} was expected to give a quantitative indication of the soundness of the experimental techniques used. A rough determination of a_{np} was obtained from the data using the finite-geometry calculation shown in Figure 6.2 and assuming a direct proportionality between a_{np} and the cross section value at the maximum of the FSI peak. In this manner a value of $a_{np} = -18 \pm 2$ fm was obtained, which is is about three standard deviations lower than the accepted value of -23.75 fm. Because it is strongly believed that the systematic uncertainties reported in Section 5.6 represent all substantial sources of error in this measurement, the conclusion is reached that the observed discrepancy between the FSI data and the theoretical predictions is real and that the FSI configuration is not a sound gauge of experimental methodology. Apparently, it was fortuitous that the *np* FSI cross section was in good agreement with theory in the measurements of González *et al.* [Sal98, Gon99].

So far no plausible explanation for the discrepancy has been found. Examination of Figure 6.2 does show the very large effect on the peak height due to the finite-

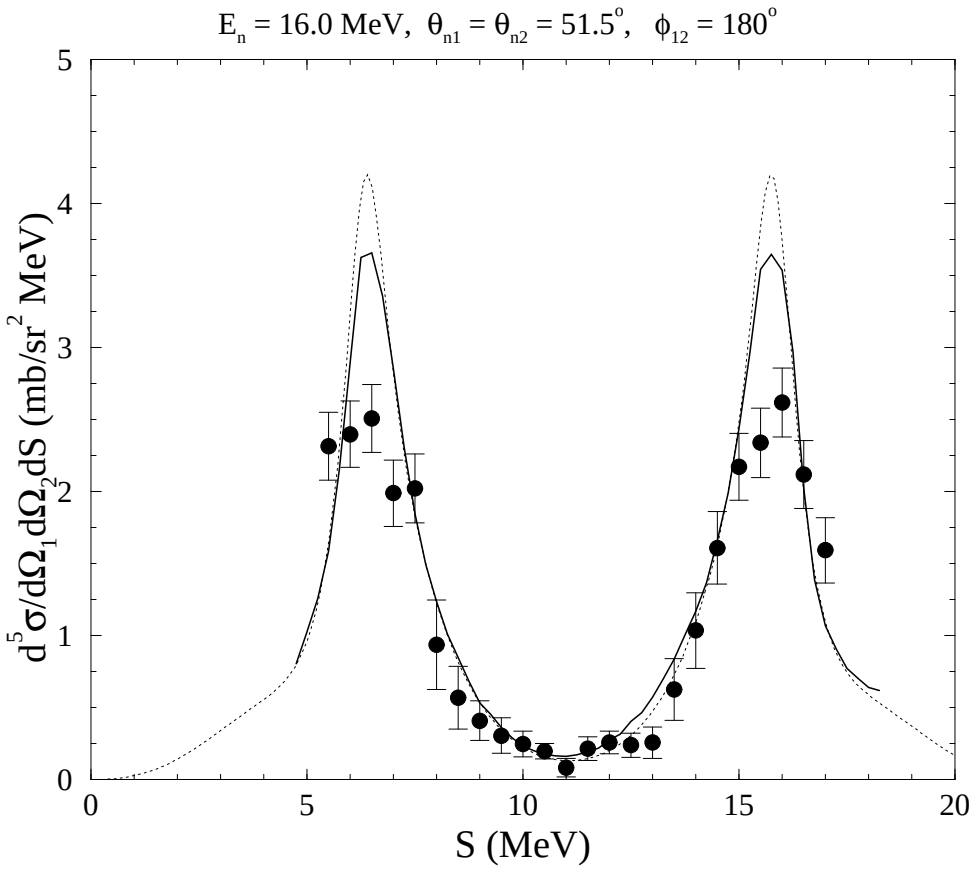

Figure 6.2: Results for the *np* FSI configuration. The dotted curve is the point-geometry calculation. The solid curve is the finite-geometry prediction from Monte-Carlo simulations. The error bars on the data represent the statistical uncertainties only.

geometry of the experiment. It is possible that the finite-geometry corrections are larger than what is currently found from the Monte-Carlo simulations. However, the size of the discrepancy makes it unlikely that this alone could entirely explain the disagreement. One possibility that could seemingly be ruled out is that the absolute normalization is incorrect. Scaling the data to match theory in the peaks not only disturbs the agreement across the rest of the kinematic locus, but it would greatly amplify the space-star discrepancy because the two configurations were measured simultaneously (and thus have the same beam-target luminosities).

6.1.3 CST

Results for the coplanar-star configuration are shown in Figure 6.3. The centroids of the data points are consistently above the finite-geometry prediction (recall that all the data presented in this work reflect the finite geometry of the experiment and thus must be compared to the Monte-Carlo simulated predictions). Because the predicted cross section is fairly constant over the portion of the S-curve measured in this work, the middle four data points could be averaged. The statistically-weighted average of these points gives a value of 0.588 ± 0.024 mb/sr^2·MeV. Adding the systematic error in quadrature raises the uncertainty to ± 0.038 mb/sr^2·MeV. This uncertainty puts the average cross section at about 1.4 standard deviations above the finite-geometry calculation.

The coplanar-star configuration was very difficult to measure experimentally because of the relatively small cross section and the low energies of the breakup neutrons (see Table B.3 for a table of kinematic values for the CST). The analysis was made challenging because the available phase space was smaller than the angular acceptance of the neutron detectors. That is to say, at some point moving across

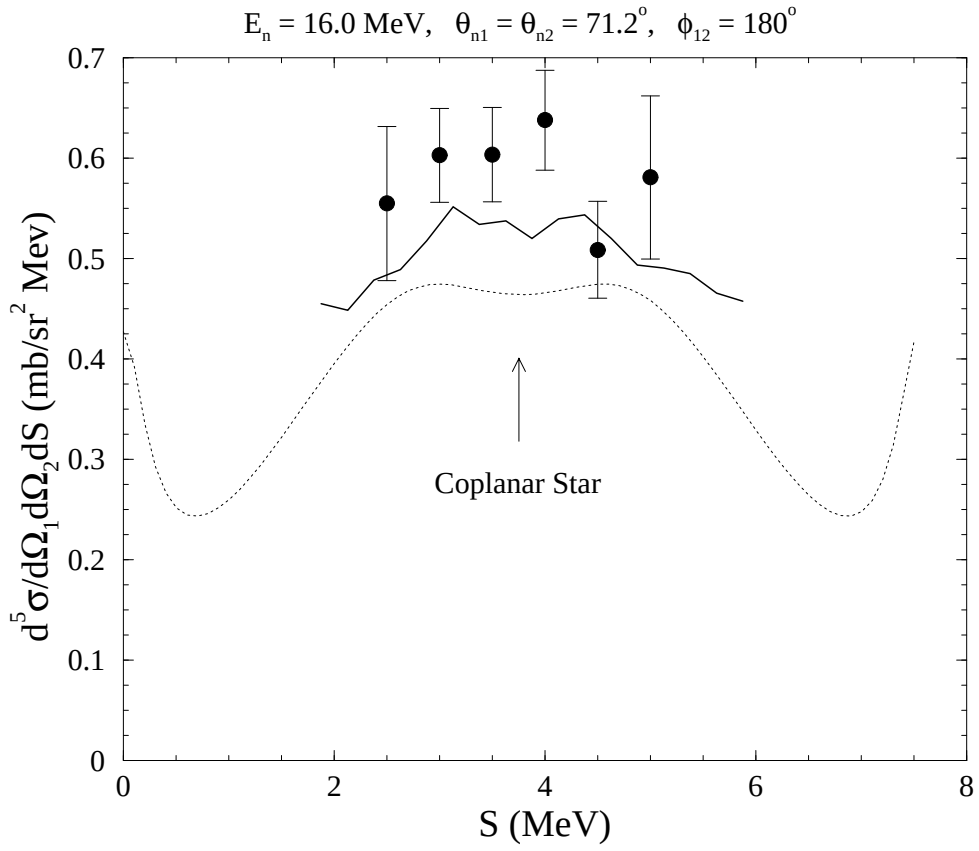

Figure 6.3: Results for the coplanar-star configuration. The dotted curve is the point-geometry calculation. The solid curve is the finite-geometry prediction from Monte-Carlo simulations. The error bars on the data represent the statistical uncertainties only.

the detector face at angles larger than the central angle, the *nd* breakup reaction was no longer kinematically allowed. The finite-geometry calculation is larger than the point-geometry one for this reason – because part of the detector saw no cross section, what cross section was measured was confined to an effectively smaller solid angle.

6.1.4 IST

Results for the intermediate-star configuration are shown in Figure 6.4. The data only represent about 25% of the total accumulated data and should be considered as preliminary. The preliminary cross sections show modest agreement with the finite-geometry predictions.

Unfortunately the IST configuration suffers from many of the same technical challenges as the CST (see Section 6.1.3 above). In addition, during the measurements there was an intermittent timing shift (most likely due to a loose contact on a signal cable in the trigger electronics). The data presented here were from batches where the timing was stable. Analysis of the rest of the data will be much more time-consuming.

6.2 Sensitivity Calculations

The results presented in Section 6.1 inevitably invoke the following fundamental question: what are the differences in the underlying physics for the star and *np* FSI configurations? Because each exit channel configuration in *nd* breakup samples a different region in 3N phase space, the details of the NN force components acting on the interacting particles and the dynamics of the 3N system greatly impact the

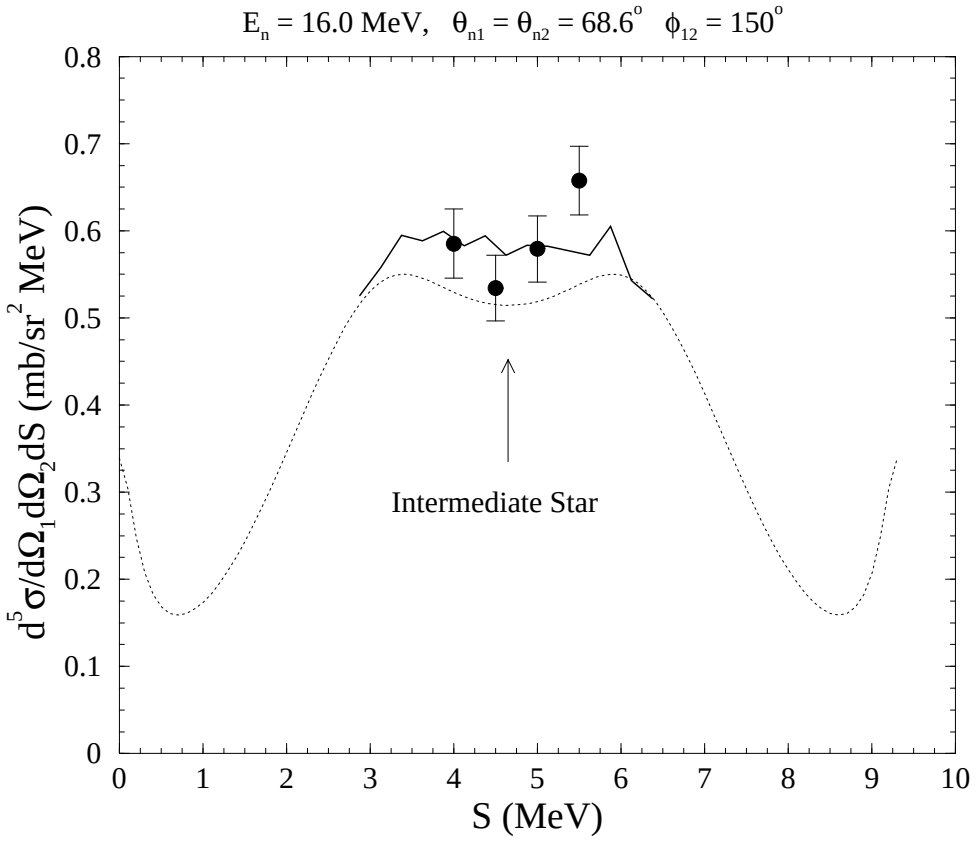

Figure 6.4: Preliminary results for the intermediate-star configuration. The dotted curve is the point-geometry calculation. The solid curve is the finite-geometry prediction from Monte-Carlo simulations. The error bars on the data represent the statistical uncertainties only. Note that these data are about 25% of the total accumulated data for this configuration.

observables for this reaction. One would like to be able to isolate the discrepancy between data and theory for each configuration to certain aspects of the NN potential (hopefully to a part that is less well-understood from a theoretical basis or less precisely determined from empirical studies). Slight modifications to certain components of the NN potential could indeed "fix" the space-star anomaly and the discrepancies between theory and the measured data for the CST and *np* FSI configurations. Of course, these changes are limited by many rigid constraints – a new NN potential must reproduce the 2N world data with very high accuracy, and it must also predict 3N observables to at least the level they are at now. This goal may not be achievable, but identifying the components of the NN potential that are most influential can improve current understanding and possibly benefit future theoretical and experimental studies.

To understand better the differences in the physics of the configurations studied in this work, calculations were performed to determine the dependence of the cross sections to different 2N force components, to the total 3N channel spin (S), and to the 3N orbital angular momentum λ (recall that Figure 2.6 defines the linear and angular momentum coupling scheme used in these calculations). In addition, calculations were performed that included the Tuscon-Melbourne (TM) 3NF [Coo79, Coo93] to see what influence it might have on the breakup cross sections. (Note that all calculations are made for point geometry.) The results of these two types of calculations are presented in the following subsections.

6.2.1 Sensitivity to NN Force Components

The FORTRAN code provided by the Bochum-Cracow group for calculating breakup cross sections was modified so that certain T-matrix elements could be set

to zero (note that this is made possible by the partial-wave representation used in the calculations). Conditional statements were created to select out the elements corresponding to the parameters of interest. In this fashion, the influence of partial waves of definite angular momentum and spin states could be examined.

The first parameter studied was the 2N force components for different orbital angular momenta (l). Calculations were made to isolate the spin singlet, $^1S_0$, and triplet, $^3S_1$-$^3D_1$, components of the $l = 0$ partial wave (s-wave). The contributions of these components are shown in Figures 6.5 to 6.8 along with the total s-wave contribution (which is the quantum mechanical sum of the singlet and triplet amplitudes) and the full calculations using the CD-Bonn NN potential.

Sensitivity calculations to 2N orbital angular momenta for the space-star configuration are shown in Figure 6.5. The primary observation for these calculations is that the SST cross section is almost completely determined by the s-wave strength in the NN potential. Higher-order partial waves have a negligible contribution to the SST cross section.

As shown in Figure 6.6, the np FSI cross section is also primarily determined by the $l = 0$ partial wave. For this configuration, the higher partial waves make a small contribution in the valley between the np final-state peaks. This region offers some very interesting physics in the singlet and triplet components. A broad peak corresponding to nn quasi-free scattering (QFS) can be seen in the $^1S_0$ component. In the $^3S_1$-$^3D_1$ calculation a relatively constant cross section can be seen that is the result of a collinear kinematic configuration. Quasi-free scattering refers to the kinematical situation where one particle in the initial state is a spectator, and so the scattering appears to be merely a two-body event. Around S = 11.0 MeV, the proton from the breakup reaction reaches it minimum energy as it assumes the role

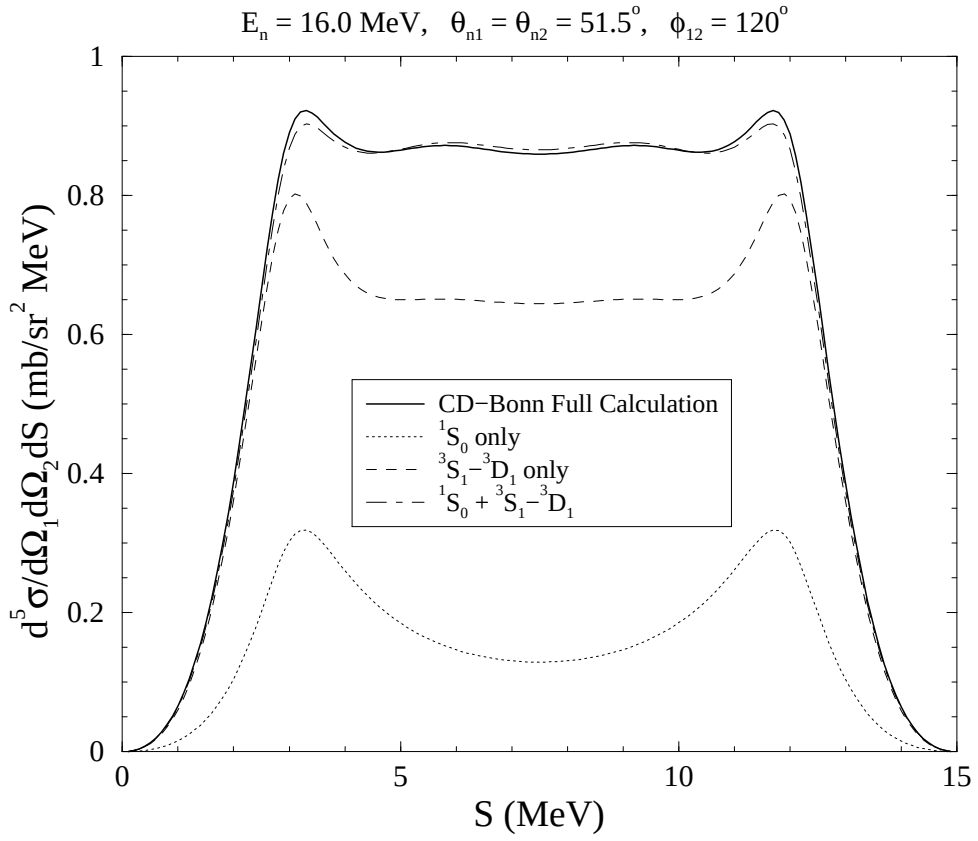

Figure 6.5: Sensitivity of space-star cross-section calculations to different parts of the NN potential.

of the spectator. Because the neutrons interact strongly and are identical particles, their spins must be anti-aligned, and so this arrangement is only possible in the singlet state. A collinear configuration occurs when one particle is at rest in the c.m. system while the other two particles exit with equal but opposite momenta. Again the proton is at a minimum energy, but the two neutrons cannot interact with each other. They instead interact with the proton. The absence of identical particles in the interaction therefore allows the triplet state to be possible. The enhancement around S = 11 MeV that is in each cross-section component does not show up in the full calculation. Therefore, the nuclear amplitudes for the singlet and triplet partial waves must interfere destructively in this region to produce the cross-section valley.

Calculations for the coplanar-star configuration are shown in Figure 6.7. One prominent difference between the CST and SST cross sections becomes immediately obvious: the $l = 0$ partial wave by itself greatly overpredicts the CST cross section. Higher-order partial waves must play a significant role in this configuration. Further calculations in fact showed that inclusion of $l = 1$ states to the $l = 0$ partial wave brings the cross section down to within 10% of that from the full calculation. To achieve even better convergence (within 2% of the full calculation), the $l = 2$ states also need to be included.

As seen in Figure 6.8, the situation for the intermediate-star configuration is fairly similar to that for the coplanar star. Again higher-order partial waves significantly influence the cross section.

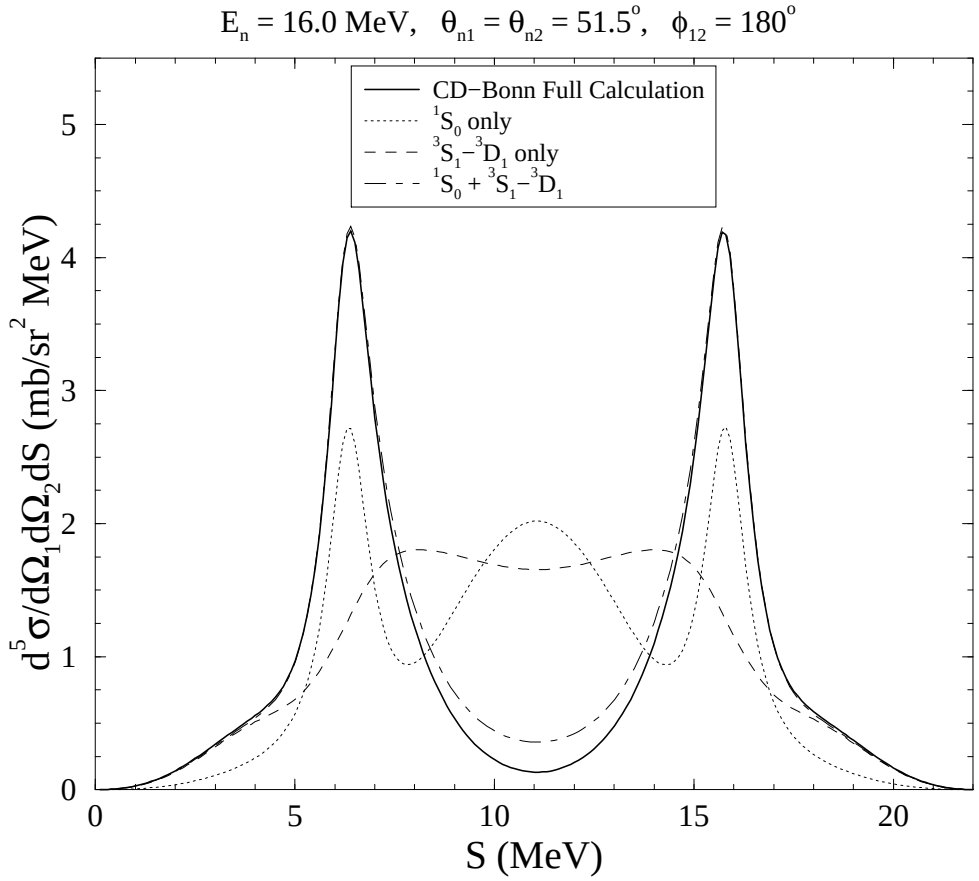

Figure 6.6: Sensitivity of *np* FSI cross-section calculations to different parts of the NN potential.

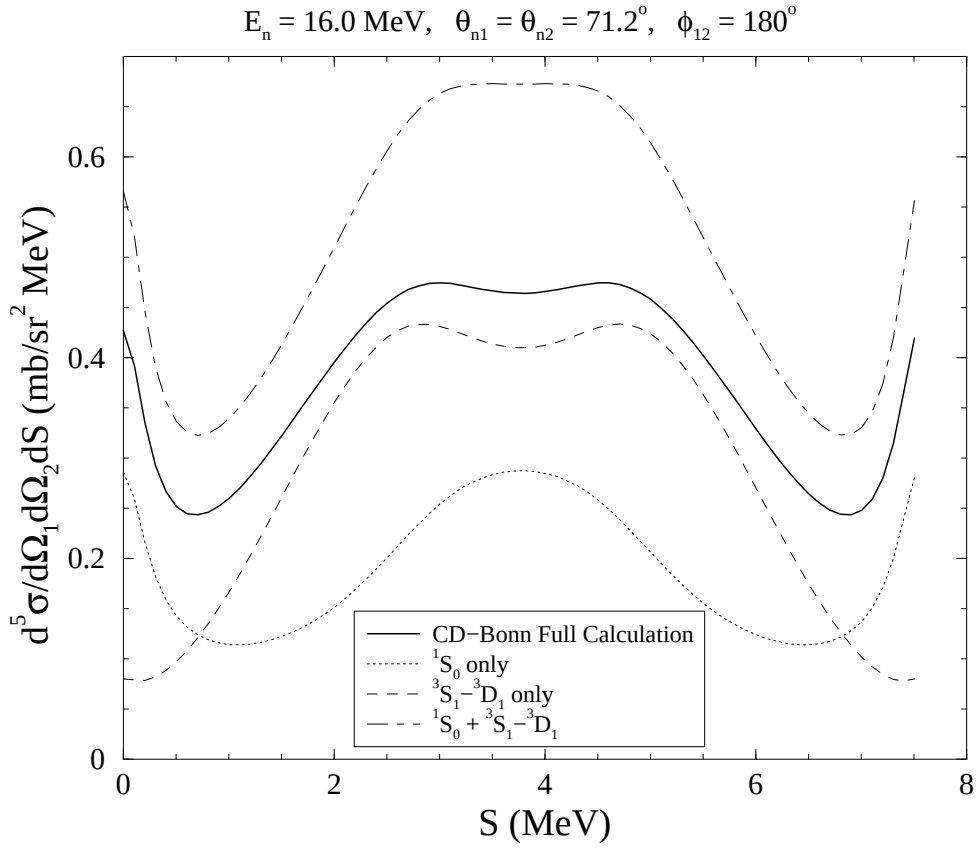

Figure 6.7: Sensitivity of coplanar-star cross-section calculations to different parts of the NN potential.

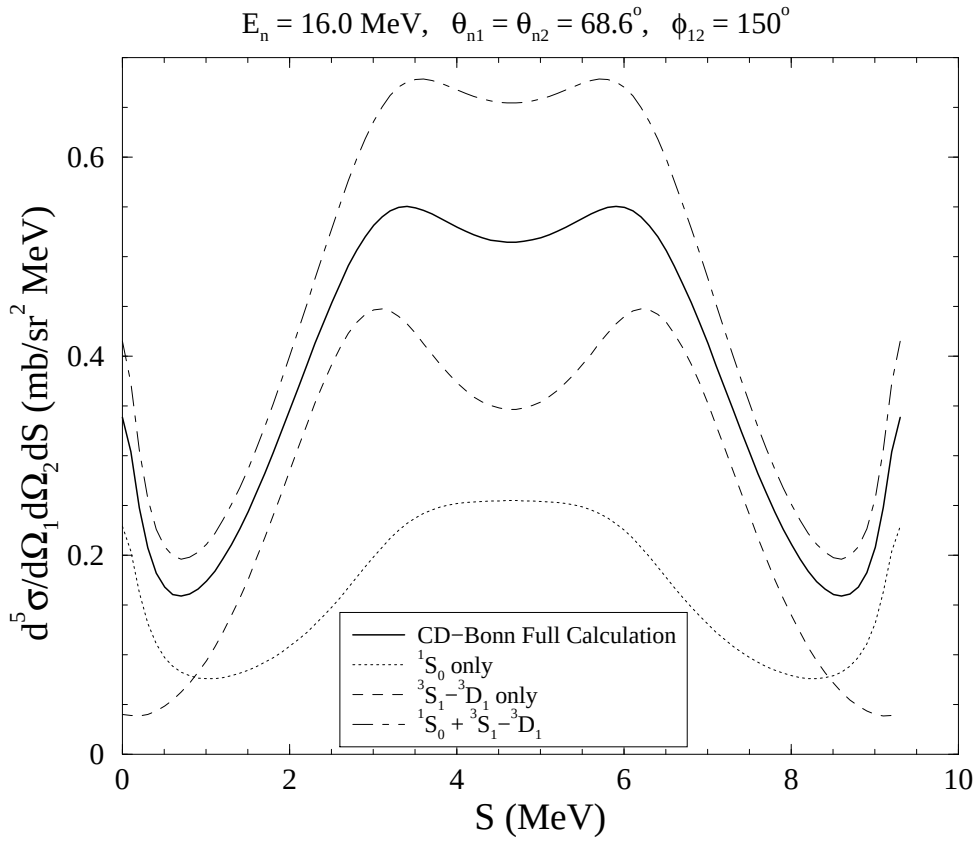

Figure 6.8: Sensitivity of intermediate-star cross-section calculations different parts of the NN potential.

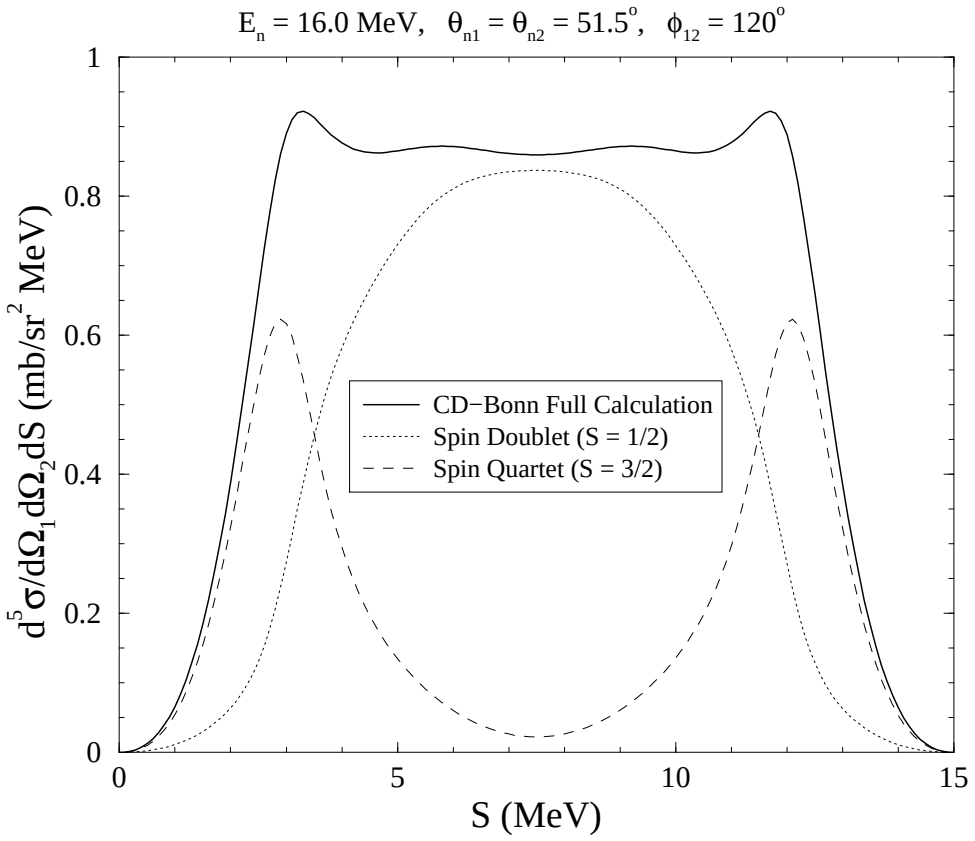

Figure 6.9: Sensitivity of space-star cross-section calculations to the total spin, S, of the 3N system.

6.2.2 Sensitivity to 3N Channel Spin

The second parameter studied was the total channel spin of the 3N system, S. Calculations were made to isolate the spin doublet ($S = \frac{1}{2}$) and the spin quartet ($S = \frac{3}{2}$) contributions to the cross section. These two contributions are shown in Figures 6.9 to 6.12 along with the full calculations using the CD-Bonn NN potential.

Because the sensitivity calculations with respect to 3N channel spin show the same behavior for all four configurations, it is necessary only to give a summary

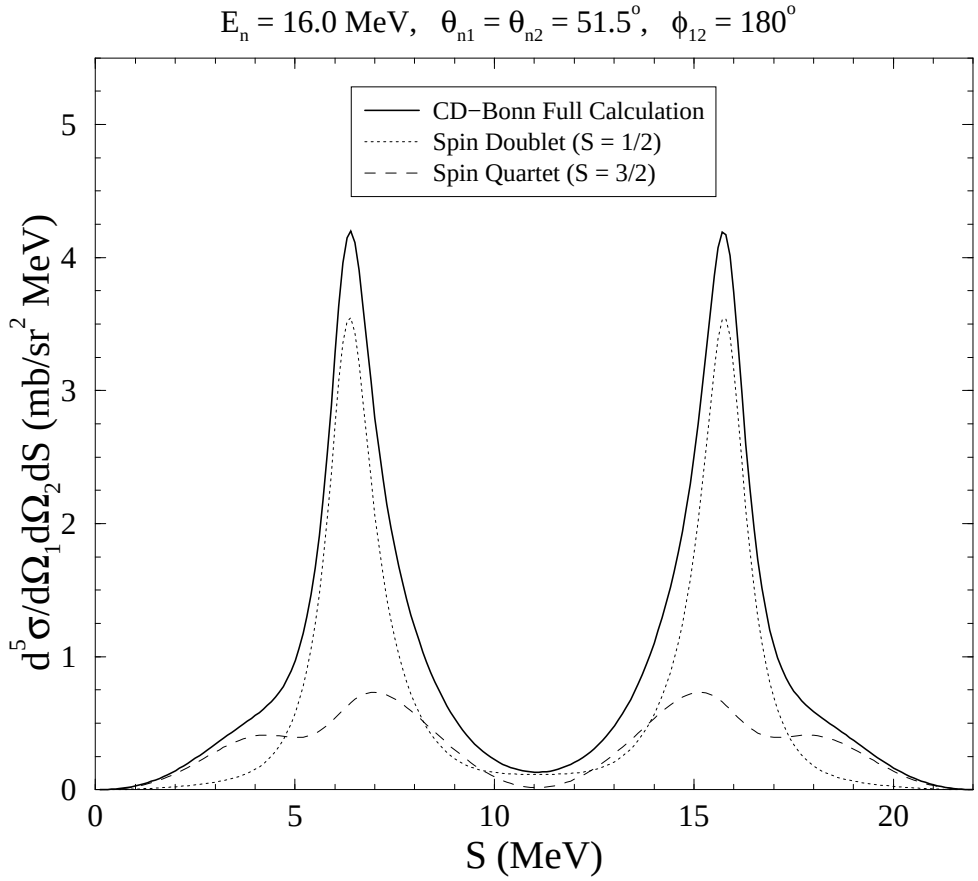

Figure 6.10: Sensitivity of *np*FSI cross-section calculations to the total spin, S, of the 3N system.

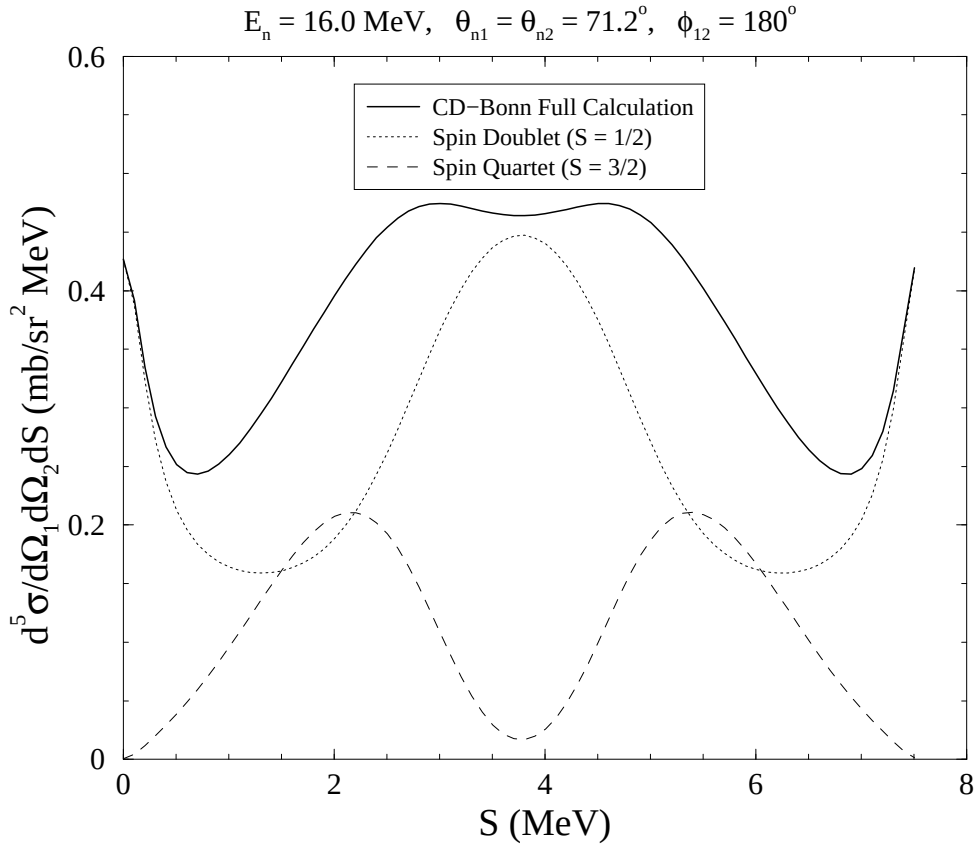

Figure 6.11: Sensitivity of coplanar-star cross-section calculations to the total spin, S, of the 3N system.

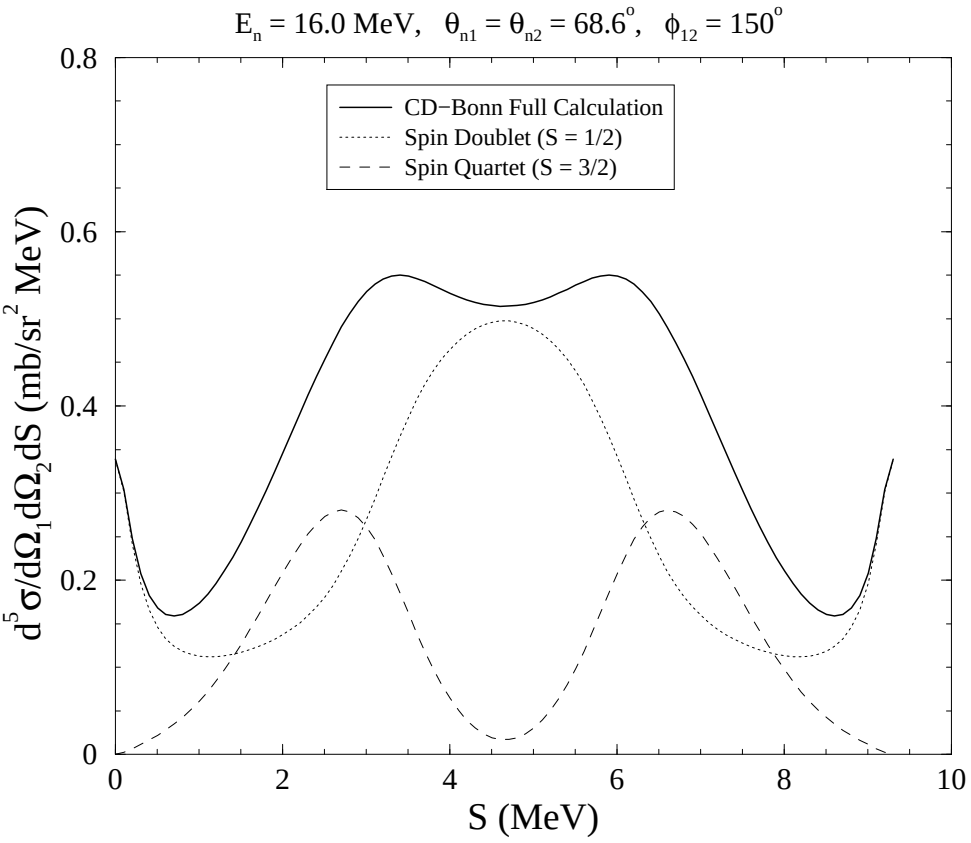

Figure 6.12: Sensitivity of intermediate-star cross-section calculations to the total spin, S, of the 3N system.

here. In all four breakup configurations, the cross-section strength at the star point or FSI peaks is almost entirely due to the spin doublet state. This observation is consistent with that from Koike and Taniguchi [Koi86]. They found that the doublet strength dominated in the breakup reaction at energies below 30 MeV. On the other hand, Nd elastic scattering was dominated by the spin quartet except in the cross-section minimum where the strengths of the two states are nearly equal. As can be seen in Figures 6.9, 6.11, and 6.12, the spin quartet only becomes important as one moves away from the star point. Although the calculated magnitude of the cross sections for the four configurations is dominated by the doublet state, the shape of the distribution along S is determined by the interference of the amplitudes for the spin doublet and quartet. In cases where there is a discrepancy between data and theory, the shapes of the measured cross-section data could provide insight into the relative channel spin strengths for the breakup reaction.

6.2.3 Sensitivity to 3N Orbital Angular Momentum

The final parameter studied was the orbital angular momentum of the 3N system, λ. Cross-section calculations were made in steps of λ where λ was increased by one unit in each step starting with $\lambda = 0$. These studies are shown in Figures 6.13 to 6.16 along with the full calculations using the CD-Bonn NN potential.

The space-star configuration shows perhaps the most interesting behavior with respect to λ. As shown in Figure 6.13, the odd values of λ do not contribute to the cross section at the space-star point. The special symmetry of the space-star configuration means that only amplitudes with even values of λ will contribute to the cross section (because the cross section depends on the product of two spherical harmonic functions). The most significant even λ is $\lambda = 2$, as can be seen in the

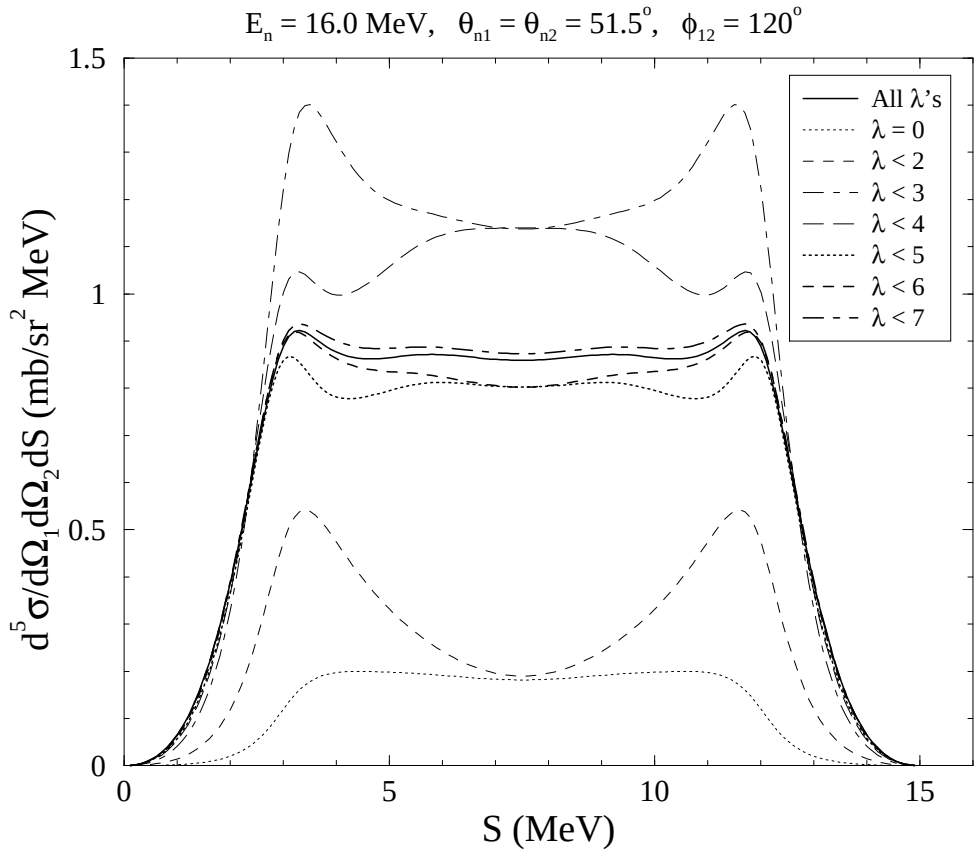

Figure 6.13: Sensitivity of space-star cross-section calculations to the orbital angular momentum, λ, of the 3N system.

large cross-section increase from the $\lambda < 2$ to the $\lambda < 3$ calculation. States with odd values of λ contribute away from the SST point. Reasonable convergence to the full calculation is obtained for states up to $\lambda = 6$.

The *np* FSI configuration does not share the symmetry of the space star and thus receives contributions to the cross-section peaks from even and odd values of λ (see Figure 6.14). As was the case for the space star, the addition of the $\lambda = 2$ state seems to cause the greatest change in the cross section. Convergence to the full calculation is achieved by including all states up to $\lambda = 5$.

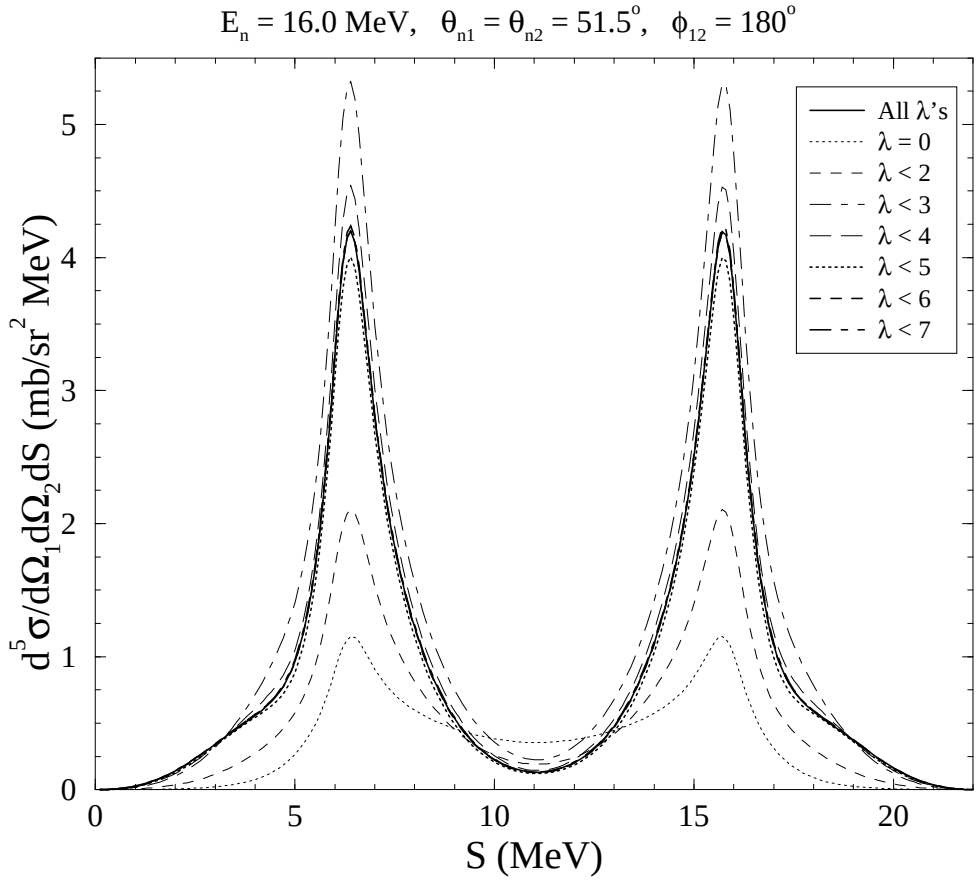

Figure 6.14: Sensitivity of *np* FSI cross-section calculations to the orbital angular momentum, λ, of the 3N system.

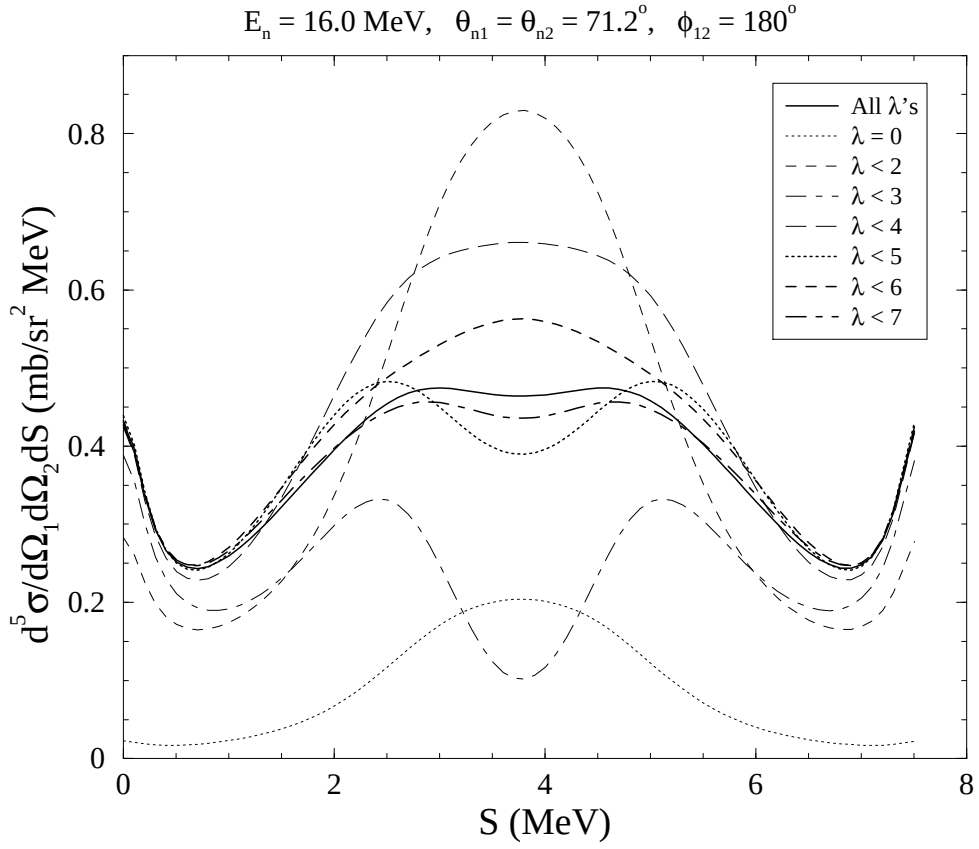

Figure 6.15: Sensitivity of coplanar-star cross-section calculations to the orbital angular momentum, λ, of the 3N system.

As was seen in sensitivity calculations with respect to the 2N orbital angular momentum, the coplanar-star configuration also has a rich structure in its dependence on λ (see Figure 6.15). The λ =0,1,2, and 3 states all strongly impact the magnitude and shape of the CST cross section. In contrast to the SST and *np* FSI configurations, the $\lambda = 2$ state actually brings the cross section down. The higher 3N angular momentum states are also more significant as can be seen by only a moderate level of convergence to the full calculation for $\lambda < 7$.

Calculations for the intermediate-star configuration show some similarities to

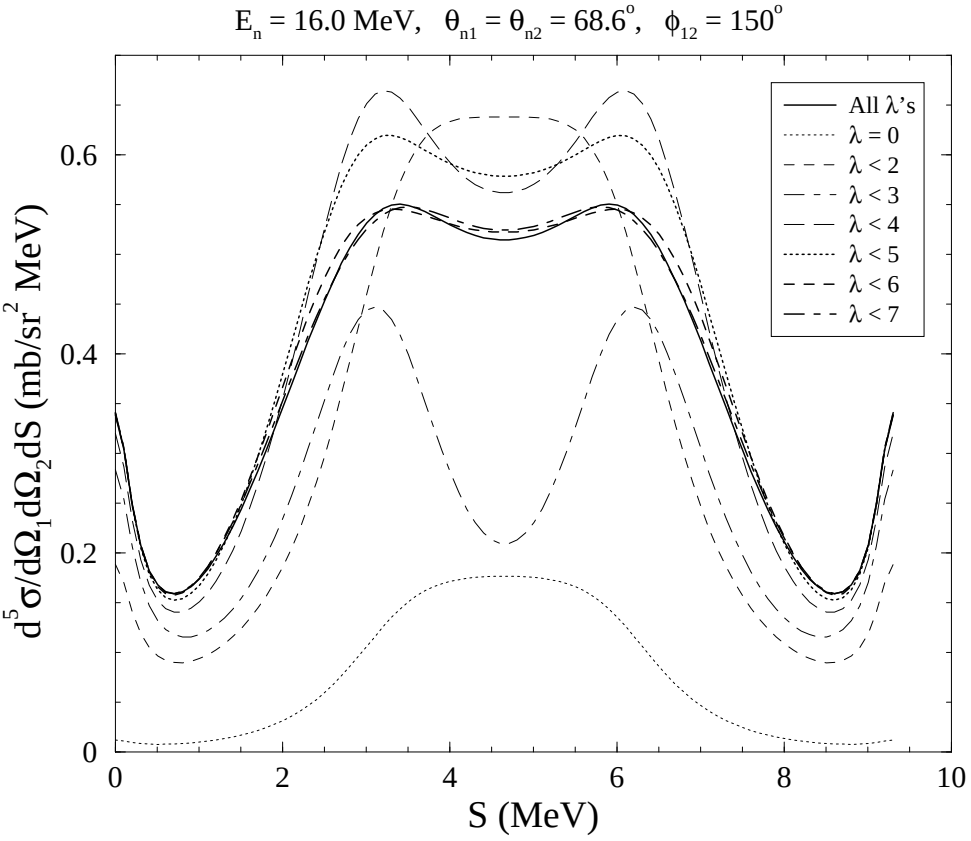

Figure 6.16: Sensitivity of intermediate-star cross-section calculations to the orbital angular momentum, λ, of the 3N system.

those for the coplanar star. Once again the λ =0,1,2, and 3 states all significantly affect the cross section with the $\lambda = 2$ state bringing the cross section down (see Figure 6.16). One difference in the IST calculations is that good convergence is reached by including all states only up to $\lambda = 5$.

6.2.4 Sensitivity to the TM 3NF

The Bochum-Cracow group provided T-matrix amplitudes that were generated with the CD-Bonn NN potential and the TM 3NF. Details of these calculations are

Configuration	Percent Change in Cross Section	Effect of 3NF on the Cross Section
SST	0.07 %	increase
FSI	1.40 %	increase
CST	1.50 %	decrease
IST	1.20 %	decrease

Table 6.1: Summary of calculations with the TM 3NF added to the CD-Bonn NN potential. The percent change in the cross section at the star point and in the np final-state peaks is given in the second column. The third column indicates whether the inclusion of the 3NF increased or decreased the cross section.

given in Section 2.6. Cross sections were then calculated from these amplitudes and compared to cross sections from 2N-only T-matrix elements. The differences in these cross sections were small enough to create difficulty in distinguishing them on a plot. Instead, the results are summarized in tabular form in Table 6.1. Calculations for the space star showed virtually no change in the cross section when the TM 3NF was included. The change in the cross sections for the other configurations was larger, but still represented only a small effect.

6.3 Discussion and Speculations

As was seen in the previous section, explanations for the space-star anomaly are hard to come by. One question that bears asking is, could all the data be somehow incorrect? This possibility seems very unlikely. The data at 10.3 MeV [Ste89, Geb93] and 13.0 MeV [Str89, Set96] are in agreement with one another within the reported systematic uncertainties. These data are from measurements by three independent research groups who used similar experimental techniques but somewhat different experimental setups. To provide a final check on these data, measurements were

made at TUNL at these two energies, and preliminary results corroborate the original findings [Mac00]. Finally, preliminary results from a measurement at 25.0 MeV at the China Institute of Atomic Energy (CIAE) also show a discrepancy between data and theory for the space star [Zho01]. However, the discrepancy is substantially smaller at 25.0 MeV.

A more likely possibility is that some important physics is missing from the theory. This statement is easily made *ad hoc*, but are there any clues as to what the missing ingredient(s) might be? The sensitivity calculations in the previous section are a good first step. Calculations investigating the dependence of the SST cross section on the 2N force showed that the s-wave strength of the NN potential is the primary influence. Could this part of the nuclear force be missing some important physics? It seems doubtful. The singlet s-wave np force is one of the most well-understood parts of the nuclear force due to extensive studies of np scattering. Although the triplet state has not been as thoroughly determined, it is highly constrained by the properties of the deuteron. The nn force is the least determined of the NN s-wave forces, and modeled using the assumption of charge independence. So there is some margin for adjustment of this force. The main constraints on the nn s-wave force strength are the value of the scattering length and the lack of a nn bound state. Computational studies indicate that to increase the calculated SST cross section sufficiently to put it in agreement with data by only changing the strength of the $l = 0$ nn potential requires an nn force strong enough to produce a bound nn state [Wit01]. Modifying the s-wave part of the np potential to correct for the observed discrepancies between data and theory while not disturbing all the numerous 2N and 3N observables that are well-described would be an extremely challenging task that has a low chance for success and certainly beyond the scope of this dissertation.

Given that the inclusion of 3NFs were the "solution" to the triton binding energy problem, could they help resolve the space-star anomaly? The results of Table 6.1 show that the TM 3NF is not the answer at 16.0 MeV (calculations at other energies may show increased sensitivity, but usually only on the order of 1-2%). Other 3NF models would probably give slightly different results, but it is highly unlikely that any of the present 3NF models could produce a large enough change in the cross section to make theory match the space-star data.

One speculation that has recently been proposed as a possible solution for the space-star anomaly is that there could be a broad resonance state in the 3N continuum [How01]. At this time little work has been done to confirm or refute this speculation, but there is a reasonable body of circumstantial evidence to make it worth considering. Some of the more salient pieces of evidence are given below:

1. The energy dependence of the space-star cross section shows that the discrepancy between data and theory has a large enhancement at 13.0 MeV as compared to other energies. This trend is most easily observed by integrating the space-star cross section over the region of the kinematic S-curve where the cross sections are nearly constant. The top graph in Figure 6.17 shows the integrated space-star cross section as a function of energy compared to the theoretical prediction. The bottom graph shows the ratio of the experimental to the calculated value and clearly displays the "peak" at 13.0 MeV. Note that the ratios at the other three energies are in agreement with each other within the systematic uncertainties.

2. Measured cross sections from kinematically incomplete nd breakup experiments studying nn final-state interactions are about 20% higher than theory in the

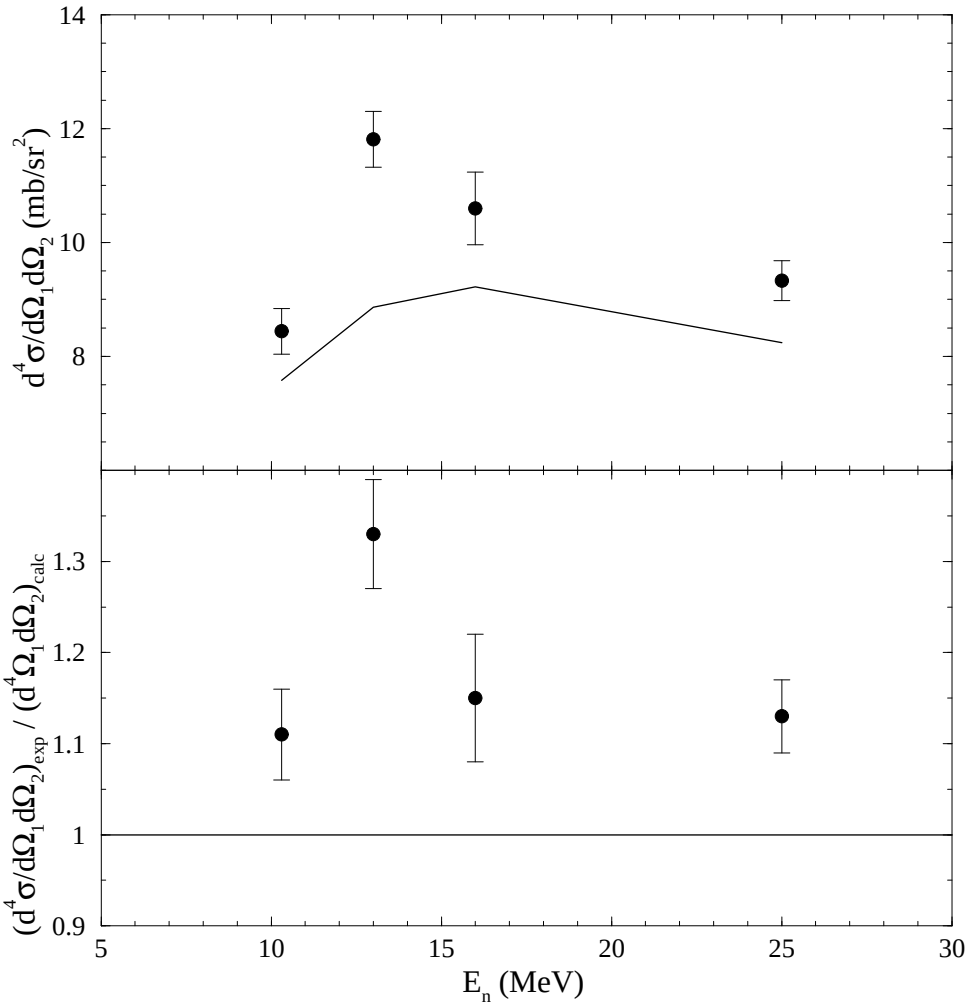

Figure 6.17: The top graph shows the integrated cross section for the space-star configuration. The data at 10.3 MeV are from Stephan *et al.* [Ste89] and Gebhardt *et al.* [Geb93], at 13.0 MeV from Strate *et al.* [Str89] and Setze *et al.* [Set96], and at 25.0 MeV the datum is a preliminary result from Zhou *et al.* [Zho01]. The 16.0 MeV datum is from the present work. The error bars represent the ±5% systematic uncertainty reported in each experiment. The curve is the result of calculations with the Bonn-B NN potential [Mac89]. The bottom graph shows the ratio of these data to the Bonn-B calculation.

region of the proton energy spectrum just below the FSI enhancement for incident neutron energies close to 14 MeV [Tor96]. Measurements of this type seek to determine the $^1S_0$ neutron-neutron scattering length, a_{nn}, by fitting the FSI enhancement with theoretical calculations. The absolute normalization for the cross sections comes from scaling the flat region of the proton energy distribution to match the calculated values. This procedure is justified because calculations with different values of a_{nn} converge in the flat region below the FSI peak. A reanalysis of published data by Tornow *et al.* [Tor96] showed that a normalization factor of ≈ 0.8 was necessary at neutron energies close to 14 MeV, but at 25 MeV and 49.6 MeV this factor was instead one, and at 11.0 MeV the factor was 1.2.

3. The measured total *nd* breakup cross section is higher than calculation in the energy range between 10 and 20 MeV. A plot of the measured total *nd* breakup cross sections and calculation can be found in Figure 32 of the review paper by Glöckle *et al.* [Glö96]. The uncertainties in the data are fairly large, but their centroids are all consistently higher than the theoretical prediction.

4. Values of a_{nn} obtained from kinematically complete *nd* breakup at 13.0 [Gon99] and 25.3 MeV [Huh00] disagree by 2.5 fm (more than four standard deviations given their reported systematic uncertainties of 0.6 and 0.4 fm respectively). The discrepancy is troubling because both groups also measured an *np* FSI and determined values of a_{np} consistent with that measured by direct *np* scattering. The larger value of a_{nn} determined at 13.0 MeV is consistent with values extracted from the *nn* FSI in the ^{2}H(π^-,nn)γ reaction, while the smaller value determined at 25.3 MeV is consistent with the values from other *nd* breakup measurements. Strangely, the *np* FSI data measured in this work are indicative

of a smaller nn scattering length.

While none of the evidence presented above conclusively proves the presence of a resonance state in the 3N continuum, it does raise the possibility that these outstanding problems could be related. For instance, if a resonance did exist it might explain the difference in the values of a_{nn} obtained in nd breakup. An enhancement in the breakup cross section for some configurations in the energy region around 13.0 MeV could lead to the larger value of a_{nn} obtained at 13.0 MeV than was obtained at 25.3 MeV.

At this point one obvious question to ask is, why hasn't this resonance been previously observed? First, based on the space-star data, such a resonance would have a width of at least 4 MeV. This broadness would make identifying it difficult with data alone. Secondly, its channel spin would suppress its influence in the more accurately measured and popularly studied elastic scattering reaction channel. Because the low-energy breakup reaction is most sensitive to the 3N spin doublet arrangement (as seen in the sensitivity calculations of Section 6.2), the resonance would likely have a channel spin of $\frac{1}{2}$. Elastic scattering is dominated by the 3N spin quartet state except in the minimum of the differential cross section where the contribution of the spin doublet is nearly equal to that from the quartet [Koi86]. Measurements in this region are as challenging as those for the breakup reaction because of the increased need to control systematic errors and understand sources of background.

Clearly further experimental study is necessary to confirm or refute the presence of a resonant state in the 3N continuum. Unfortunately, the measurements with the best prospects of discerning the existence of a resonant state are also the most difficult. As mentioned above, high precision measurements of the differential cross-section in the minimum for nd elastic-scattering below 30 MeV would add important

information to the discernment of the existence of a resonant state. Measurements of the total *nd* breakup cross section between 10 and 30 MeV also would be informative and is even more challenging than the elastic-scattering measurements in the minimum of the cross section. Maybe the best place to begin would be cross-section measurements of the kinematically incomplete breakup reaction. Cross-section measurements of the flat region in the proton energy spectrum for neutron energies around 14 MeV would be greatly beneficial in mapping out the energy dependence of the normalization factors.

6.4 In Closing

Cross sections for three star configurations and one *np* final-state interaction configuration in *nd* breakup were measured at an incident neutron energy of 16.0 MeV. These cross sections are the first *nd* breakup data measured at this energy. The data were binned in 500-keV bins for the *np* FSI, CST, and IST configurations and in 750-keV bins for the SST configuration. Statistical uncertainties of approximately $\pm 7\%$ were achieved for each data set. The systematic uncertainty in the measurements was determined to be $\pm 5\%$.

Much success has been achieved in describing data for the 3N system with Faddeev-type calculations that use modern NN potential models. These successes have been tempered however by several notable discrepancies, one of which is the star anomaly. Measurements reported in this dissertation confirm the anomaly for the space-star configuration at 16.0 MeV. The average of the data for the SST configuration is three standard deviations higher than the theoretical predictions. Though the discrepancy between data and theory is less than at 13.0 MeV, it still clearly

exists. The cross-section data for the CST and *np* FSI configurations also disagree substantially with theory. The discrepancy with the CST configuration is interesting but not too surprising. The big surprise in these measurements was the substantially lower cross section at the maximum of the *np* FSI peaks.

The existence of a broad resonance in the 3N continuum is proposed as one plausible explanation for the star anomaly and for the newly observed *np* FSI problem. This speculation opens the possibility that other unresolved problems in *nd* breakup may be related to the same physics. Continued experimental studies (guided by theory) are clearly needed to test this hypothesis in the hope of finally resolving many of the lingering questions in the 3N system.

Appendix A

Cross-Section Tables

Tabulated results of the *nd* breakup cross sections measured in this work are given in Tables A.1 to A.4. The cross sections and their uncertainties have units of mb/sr^2·MeV and the arc-length, S, is given in MeV. The uncertainties for the cross sections represent only the statistical uncertainties.

S	σ	$\Delta\sigma$	S	σ	$\Delta\sigma$
4.125	0.9511	0.0948	7.875	0.9250	0.0698
4.875	0.9574	0.0758	8.625	1.1079	0.0807
5.625	1.1734	0.0772	9.375	1.0286	0.0803
6.375	1.0035	0.0738	10.125	0.9672	0.0791
7.125	1.0555	0.0745	10.875	1.1696	0.1041

Table A.1: Cross-section results for the SST configuration.

S	σ	$\Delta\sigma$	S	σ	$\Delta\sigma$
5.5	2.1088	0.1962	11.5	0.2121	0.0702
6.0	2.3846	0.2017	12.0	0.2165	0.0663
6.5	2.6058	0.2102	12.5	0.2207	0.0699
7.0	2.0478	0.2017	13.0	0.2498	0.0974
7.5	1.7924	0.2050	13.5	0.7277	0.1964
8.0	1.0290	0.2672	14.0	1.0634	0.2385
8.5	0.6608	0.2051	14.5	1.4819	0.2155
9.0	0.4477	0.1280	15.0	2.2454	0.2071
9.5	0.3905	0.1116	15.5	2.2856	0.2159
10.0	0.2230	0.0738	16.0	2.7096	0.2151
10.5	0.1903	0.0491	16.5	2.0503	0.2019
11.0	0.0946	0.0557	17.0	1.5951	0.2000

Table A.2: Cross-section results for the FSI configuration.

S	σ	$\Delta\sigma$
2.5	0.5547	0.0767
3.0	0.6026	0.0467
3.5	0.6034	0.0471
4.0	0.6377	0.0498
4.5	0.5084	0.0482
5.0	0.5807	0.0810

Table A.3: Cross-section results for the CST configuration.

S	σ	$\Delta\sigma$
4.0	0.5853	0.0396
4.5	0.5343	0.0378
5.0	0.5792	0.0381
5.5	0.6577	0.0394

Table A.4: Cross-section results for the IST configuration.

Appendix B

Kinematic Tables and Plots

A FORTRAN code incorporating nonrelativistic three-body kinematics was used to calculate quantities of interest for each of the *nd* breakup configurations studied in this work. Tables B.1 to B.4 show the results obtained for an incident neutron energy of 16.0 MeV and for the neutron detector angles given in the captions. The locus of energies allowed by kinematics is shown for each configuration in Figures B.1 to B.4. The kinematic quantities given in the following tables are defined as:

E_{n1} = laboratory energy of neutron one,
E_{n2} = laboratory energy of neutron two,
E_p = laboratory energy of the proton,
E_{12} = relative energy of neutrons one and two,
E_{13} = relative energy of neutron one and the proton,
E_{23} = relative energy of neutron two and the proton,
S = arc length along the kinematic locus,
θ_p = laboratory polar scattering angle for the proton, and

ϕ_p = laboratory azimuthal scattering angle for the proton.

Each of the star configurations contains one point that was of special interest kinematically:

Space-star point: S = 7.50 MeV,
Coplanar-star point: S = 3.75 MeV, and
Intermediate-star point: S = 4.65 MeV.

The star points can be distinguished in the kinematic tables as the set of parameters for which the relative energies of all three nucleons are nearly identical.

The *np* final-state interaction configuration contains two points of special interest: S = 6.40 MeV and S = 15.70 MeV. These two values of S correspond to the maximum cross sections in the final-state enhancement peaks and are easily identified in the kinematic tables as having relative energies between one neutron and the proton of close to 0.

Space-Star Kinematics								
Laboratory Energy			Relative Energy			Arc	Proton Lab Angle	
E_{n1}	E_{n2}	E_p	E_{12}	E_{13}	E_{23}	S	θ_p	ϕ_p
1.00	6.53	6.25	3.56	2.34	6.76	3.3	44	-22
1.20	6.56	6.01	3.65	2.31	6.70	3.5	45	-25
1.40	6.56	5.81	3.73	2.31	6.62	3.7	46	-27
1.60	6.54	5.64	3.81	2.33	6.52	3.9	46	-29
1.80	6.49	5.49	3.87	2.38	6.41	4.1	47	-31
2.00	6.43	5.35	3.92	2.44	6.29	4.3	48	-33
2.20	6.35	5.23	3.97	2.52	6.17	4.5	48	-35
2.40	6.25	5.12	4.01	2.62	6.03	4.7	49	-37
2.60	6.15	5.03	4.05	2.72	5.89	5.0	49	-39
2.80	6.03	4.94	4.08	2.84	5.74	5.2	49	-41
3.00	5.91	4.87	4.11	2.96	5.58	5.4	50	-43
3.20	5.77	4.80	4.14	3.10	5.43	5.7	50	-45
3.40	5.63	4.75	4.16	3.24	5.26	5.9	50	-47
3.60	5.47	4.70	4.18	3.39	5.10	6.2	51	-49
3.80	5.31	4.66	4.19	3.54	4.93	6.4	51	-51
4.00	5.14	4.63	4.20	3.71	4.75	6.7	51	-53
4.20	4.96	4.61	4.21	3.87	4.58	7.0	51	-55
4.40	4.78	4.60	4.22	4.05	4.39	7.2	51	-57
4.60	4.58	4.59	4.22	4.23	4.21	7.5	51	-60
4.80	4.38	4.60	4.22	4.42	4.03	7.8	51	-62
5.00	4.16	4.61	4.21	4.61	3.84	8.1	51	-64
5.20	3.93	4.64	4.20	4.81	3.65	8.4	51	-66
5.40	3.69	4.68	4.18	5.02	3.46	8.7	51	-69
5.60	3.44	4.74	4.16	5.23	3.26	9.0	50	-71
5.80	3.16	4.82	4.13	5.46	3.07	9.4	50	-74
6.00	2.85	4.92	4.09	5.70	2.87	9.7	50	-77
6.20	2.50	5.07	4.03	5.96	2.67	10.1	49	-81
6.40	2.07	5.30	3.94	6.25	2.47	10.6	48	-85
6.40	0.72	6.66	3.38	6.80	2.47	12.0	42	-79

Table B.1: Kinematics for the space-star configuration with $\theta_{n1} = 51.5°$, $\phi_{n1} = 0.0.°$, $\theta_{n2} = 51.5°$, $\phi_{n2} = 120.0°$. Arc length and energies are given in MeV, angles in degrees.

np Final-State Interaction Kinematics								
Laboratory Energy			Relative Energy			Arc	Proton Lab Angle	
E_{n1}	E_{n2}	E_p	E_{12}	E_{13}	E_{23}	S	θ_p	ϕ_p
1.00	8.10	4.67	5.19	0.71	6.76	4.7	41	180
1.40	8.44	3.94	5.69	0.35	6.62	5.2	42	180
1.80	8.62	3.35	6.10	0.15	6.41	5.7	43	180
2.20	8.71	2.86	6.44	0.05	6.17	6.1	42	179
2.40	8.73	2.65	6.59	0.03	6.03	6.3	42	179
2.60	8.73	2.44	6.74	0.03	5.89	6.5	42	180
2.80	8.71	2.26	6.87	0.05	5.74	6.7	41	180
3.00	8.69	2.09	6.99	0.08	5.58	6.9	41	179
3.20	8.64	1.93	7.11	0.12	5.43	7.1	40	179
3.40	8.59	1.78	7.21	0.18	5.26	7.3	39	180
3.60	8.53	1.65	7.31	0.25	5.10	7.5	38	180
3.80	8.46	1.52	7.40	0.33	4.93	7.7	37	179
4.00	8.38	1.40	7.49	0.42	4.75	7.9	36	180
4.20	8.28	1.29	7.57	0.51	4.58	8.1	34	179
4.40	8.18	1.19	7.64	0.62	4.39	8.4	33	180
4.60	8.07	1.10	7.71	0.74	4.21	8.6	31	179
5.00	7.83	0.94	7.82	0.99	3.84	9.1	26	180
5.40	7.55	0.82	7.91	1.28	3.46	9.5	21	180
5.60	7.40	0.77	7.95	1.44	3.26	9.8	18	180
6.00	7.08	0.70	8.00	1.78	2.87	10.3	11	180
7.00	6.09	0.69	8.01	2.79	1.86	11.7	9	0
7.40	5.60	0.77	7.95	3.26	1.45	12.3	18	0
7.60	5.34	0.84	7.90	3.52	1.24	12.7	22	0
7.80	5.05	0.93	7.83	3.80	1.03	13.0	26	0
8.00	4.73	1.05	7.75	4.09	0.81	13.4	30	0
8.20	4.37	1.21	7.63	4.42	0.60	13.8	33	0
8.40	3.94	1.43	7.46	4.80	0.39	14.3	36	0
8.60	3.38	1.80	7.20	5.28	0.17	14.9	39	0
8.70	2.91	2.16	6.94	5.65	0.07	15.4	41	0
8.60	1.73	3.45	6.03	6.45	0.17	16.6	43	0
8.40	1.34	4.03	5.63	6.64	0.39	17.0	42	0
8.20	1.10	4.48	5.32	6.73	0.60	17.3	42	0

Table B.2: Kinematics for the np final-state interaction configuration with $\theta_{n1} = 51.5°$, $\phi_{n1} = 0.0.°$, $\theta_{n2} = 51.5°$, $\phi_{n2} = 180.0°$. Arc length and energies are given in MeV, angles in degrees.

Coplanar-Star Kinematics								
Laboratory Energy			Relative Energy			Arc	Proton Lab Angle	
E_{n1}	E_{n2}	E_p	E_{12}	E_{13}	E_{23}	S	θ_p	ϕ_p
1.00	2.38	10.39	2.91	4.19	5.56	2.3	9	179
1.10	2.45	10.22	3.08	4.11	5.47	2.4	8	179
1.20	2.51	10.06	3.23	4.05	5.38	2.5	8	180
1.30	2.56	9.92	3.37	4.00	5.29	2.6	7	179
1.40	2.59	9.79	3.50	3.96	5.20	2.7	7	180
1.50	2.61	9.67	3.62	3.94	5.10	2.8	6	180
1.60	2.62	9.55	3.73	3.93	5.00	2.9	6	180
1.70	2.62	9.45	3.83	3.92	4.90	3.0	5	179
1.80	2.61	9.36	3.92	3.94	4.80	3.1	4	179
1.90	2.59	9.29	4.00	3.96	4.70	3.2	4	180
2.00	2.56	9.22	4.07	4.00	4.59	3.3	3	179
2.10	2.51	9.16	4.13	4.04	4.49	3.5	2	180
2.20	2.45	9.12	4.17	4.11	4.38	3.6	1	179
2.30	2.37	9.10	4.19	4.20	4.28	3.7	0	178
2.40	2.27	9.11	4.18	4.31	4.17	3.8	0	0
2.50	2.12	9.15	4.14	4.46	4.06	4.0	2	0
2.60	1.86	9.31	3.97	4.74	3.95	4.2	4	0
2.50	1.18	10.09	3.20	5.40	4.06	5.1	8	0
2.40	1.02	10.35	2.96	5.54	4.17	5.2	9	0
2.30	0.91	10.57	2.75	5.64	4.28	5.4	9	0

Table B.3: Kinematics for the coplanar-star configuration with $\theta_{n1} = 71.2°$, $\phi_{n1} = 0.0.°$, $\theta_{n2} = 71.2°$, $\phi_{n2} = 180.0°$. Arc length and energies are given in MeV, angles in degrees.

Intermediate-Star Kinematics								
Laboratory Energy			Relative Energy			Arc	Proton Lab Angle	
E_{n1}	E_{n2}	E_p	E_{12}	E_{13}	E_{23}	S	θ_p	ϕ_p
1.00	2.84	9.93	2.96	3.97	5.73	2.9	16	-31
1.10	2.90	9.78	3.10	3.91	5.65	3.0	16	-33
1.20	2.95	9.63	3.23	3.86	5.57	3.1	16	-35
1.30	2.98	9.49	3.36	3.82	5.48	3.2	16	-37
1.40	3.00	9.37	3.47	3.79	5.40	3.3	16	-39
1.50	3.02	9.26	3.57	3.78	5.31	3.4	16	-42
1.60	3.02	9.15	3.67	3.77	5.22	3.5	16	-44
1.70	3.02	9.05	3.76	3.78	5.12	3.6	16	-46
1.80	3.01	8.97	3.84	3.79	5.03	3.7	15	-49
1.90	2.99	8.89	3.92	3.81	4.93	3.8	15	-52
2.00	2.96	8.82	3.98	3.84	4.83	3.9	15	-55
2.10	2.92	8.76	4.04	3.88	4.74	4.0	15	-57
2.20	2.87	8.70	4.09	3.94	4.63	4.2	15	-61
2.30	2.82	8.66	4.13	4.00	4.53	4.3	15	-64
2.40	2.75	8.63	4.16	4.07	4.43	4.4	15	-67
2.50	2.67	8.61	4.18	4.15	4.33	4.5	15	-71
2.60	2.58	8.60	4.19	4.25	4.22	4.6	15	-75
2.70	2.46	8.61	4.17	4.37	4.12	4.8	15	-79
2.80	2.33	8.65	4.14	4.51	4.01	5.0	15	-84
2.90	2.14	8.73	4.06	4.69	3.91	5.2	15	-89
3.00	1.84	8.93	3.87	4.99	3.80	5.5	15	-80
2.90	1.10	9.78	3.10	5.65	3.91	6.3	16	-63

Table B.4: Kinematics for the intermediate-star configuration with $\theta_{n1} = 68.6°$, $\phi_{n1} = 0.0.°$, $\theta_{n2} = 68.6°$, $\phi_{n2} = 150.0°$. Arc length and energies are given in MeV, angles in degrees.

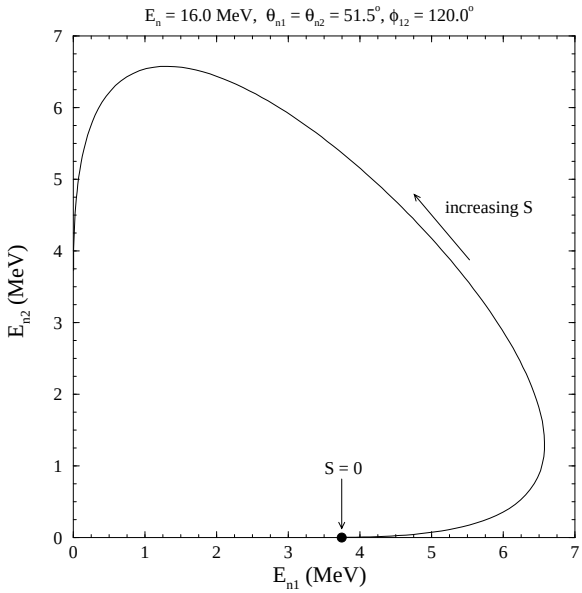

Figure B.1: Kinematic locus for the space-star configuration.

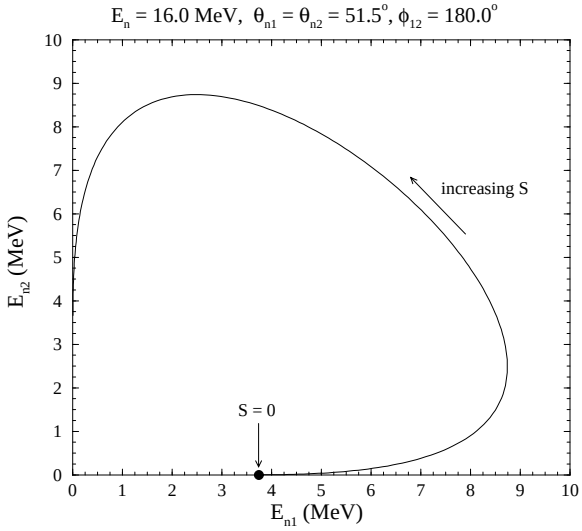

Figure B.2: Kinematic locus for the *np* final-state interaction configuration.

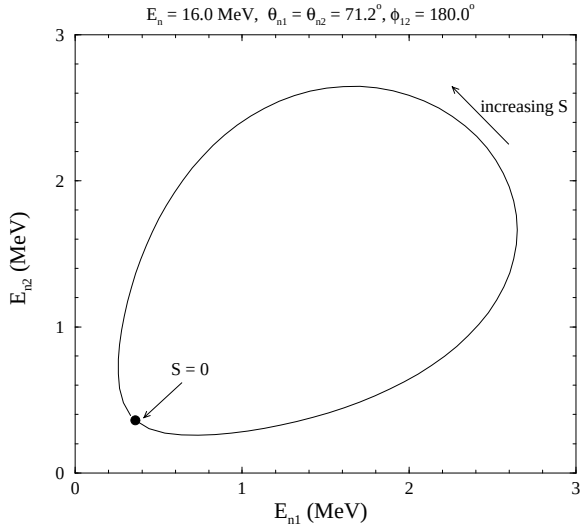

Figure B.3: Kinematic locus for the coplanar-star configuration. Note that the locus does not cross either energy axis. The S=0 point is defined where both neutron energies have reached their minimum value.

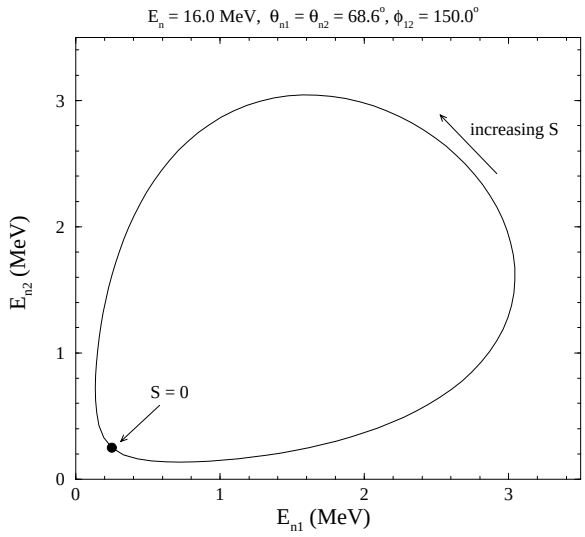

Figure B.4: Kinematic locus for the intermediate-star configuration. Note that the locus does not cross either energy axis. The S=0 point is defined where both neutron energies have reached their minimum value.

Appendix C

Detector Efficiency Tables and Plots

The absolute efficiencies of the neutron detectors were measured previously at TUNL using the ^{2}H(d, n)^{3}He neutron-source reaction and also with the spontaneous fission neutrons from a ^{252}Cf source [Gon97, Sal98]. All of the detectors in the STAR array were of identical construction (from Bicron Corporation) and filled with the same scintillating fluid (BC-501A). One of these detectors was previously calibrated in studies at the Physikalisch-Technische Bundesanstalt (PTB) in Braunschweig, Germany [Gon97]. The light response characteristics of this detector were then incorporated in the PTB group's Monte-Carlo programs, NRESP7 and NEFF7 [Die82].

The PTB Monte-Carlo codes do a good job of reproducing the shape of the detector efficiencies measured with the ^{2}H(d, n)^{3}He reaction and the ^{252}Cf source. A normalization factor was necessary to bring the calculated efficiencies into better agreement with the ^{2}H(d, n)^{3}He data. A comparison of the PTB calculations with the measured efficiencies for one detector is shown in Figure C.1. The calculated

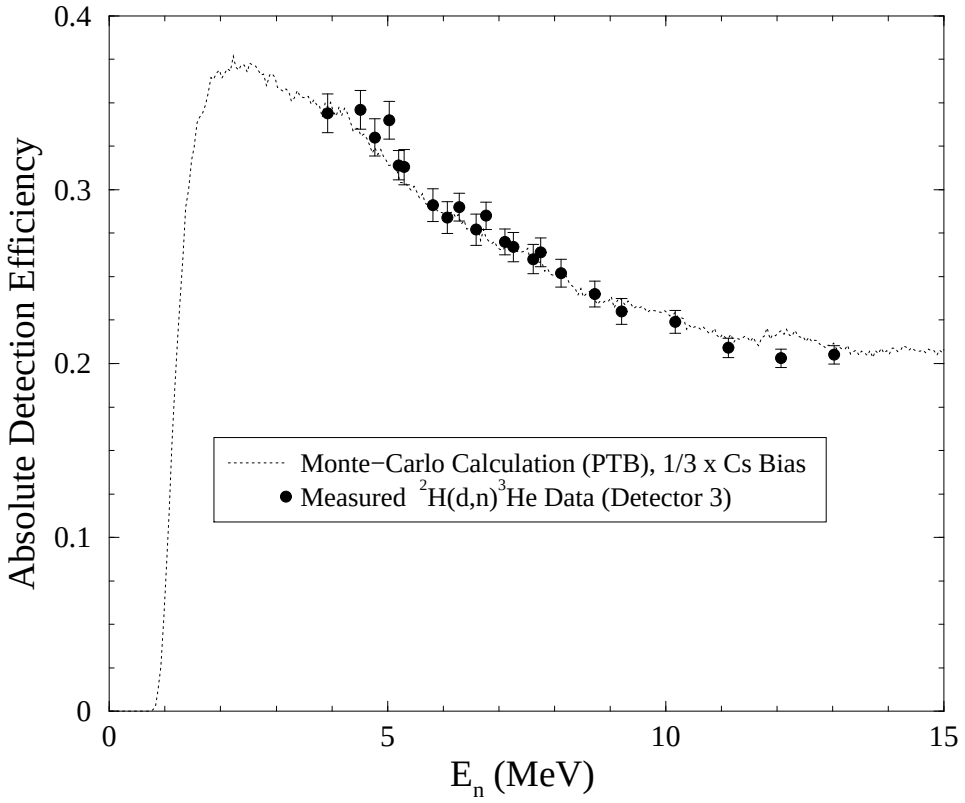

Figure C.1: Comparison of the absolute detection efficiencies obtained from ^{2}H(d, n)^{3}He measurements at TUNL with calculations using the PTB Monte-Carlo code at a pulse-height threshold of $\frac{1}{3}\times$Cs. The simulated efficiency curve is normalized independently for each detector to fit the measured data. For this particular detector, the normalization factor was 1.0.

efficiencies were used in the Monte-Carlo simulations to generate the corrections for the breakup data. A separate normalization factor was then applied when calculating the breakup cross section to account for slight differences in the detectors' measured efficiencies. Table C.1 gives the factors that were applied to the calculated efficiences for each detector.

Detector efficiency is dependent on the pulse-height threshold (or bias) set in the detection electronics (or set in analysis with software). The dependence of efficiency

Detector	PTB Normalization	Detector	PTB Normalization
1	0.988	7	0.950
2	0.988	8	0.975
3	1.000	9	0.964
4	0.975	10	0.974
5	0.956	11	0.975
6	0.968	12	0.975

Table C.1: PTB Efficiency Normalization Factors

on pulse-height threshold is shown in Figure C.2 as determined from simulations with the PTB codes. Note that the normalization factors shown in Table C.1 are bias-independent; that is, normalizing the calculations to the measured efficiencies at one bias also brings the calculations into agreement with the data at other biases. Calculated efficiencies for the two biases used in this work are tabulated in Tables C.2 and C.3. Further details on the efficiency measurements and calculations can be found in the dissertations of D.E. González Trotter [Gon97] and F. Salinas [Sal98].

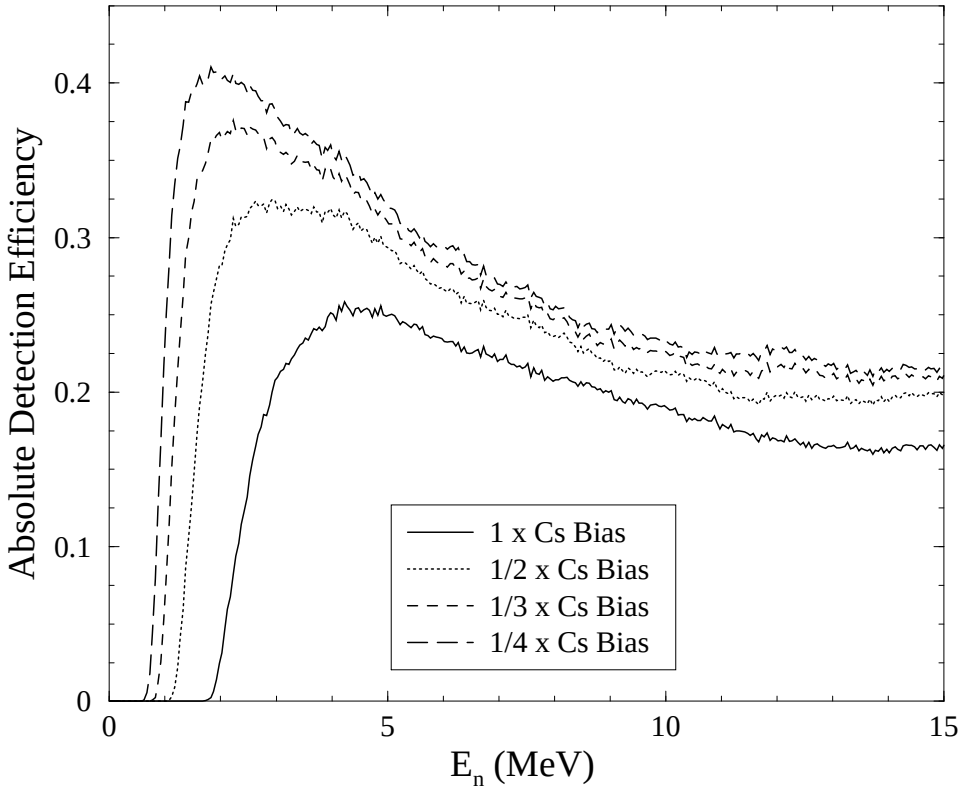

Figure C.2: Comparison of the absolute detection efficiencies obtained in simulations with the PTB Monte-Carlo code (NEFF7) for different pulse-height thresholds (biases).

Energy	Efficiency	Energy	Efficiency	Energy	Efficiency
0.70	0.0000	3.50	0.3529	6.80	0.2701
0.80	0.0023	3.60	0.3490	7.00	0.2657
0.90	0.0256	3.70	0.3488	7.20	0.2652
1.00	0.0812	3.80	0.3418	7.40	0.2642
1.10	0.1515	3.90	0.3472	7.60	0.2625
1.20	0.2152	4.00	0.3451	7.80	0.2532
1.30	0.2630	4.10	0.3475	8.00	0.2520
1.40	0.3002	4.20	0.3467	8.20	0.2495
1.50	0.3241	4.30	0.3398	8.40	0.2395
1.60	0.3417	4.40	0.3354	8.60	0.2414
1.70	0.3489	4.50	0.3308	8.80	0.2360
1.80	0.3644	4.60	0.3293	9.00	0.2385
1.90	0.3670	4.70	0.3210	9.20	0.2358
2.00	0.3643	4.80	0.3201	9.40	0.2316
2.10	0.3695	4.90	0.3194	9.60	0.2314
2.20	0.3766	5.00	0.3141	9.80	0.2304
2.30	0.3688	5.10	0.3135	10.00	0.2293
2.40	0.3717	5.20	0.3042	10.20	0.2264
2.50	0.3728	5.30	0.3038	10.40	0.2219
2.60	0.3712	5.40	0.2997	10.60	0.2198
2.70	0.3659	5.50	0.2990	10.80	0.2175
2.80	0.3596	5.60	0.2976	11.00	0.2168
2.90	0.3668	5.70	0.2908	11.20	0.2123
3.00	0.3588	5.80	0.2906	11.40	0.2156
3.10	0.3566	5.90	0.2871	11.60	0.2118
3.20	0.3563	6.20	0.2840	11.80	0.2205
3.30	0.3527	6.40	0.2773	12.00	0.2176
3.40	0.3538	6.60	0.2774		

Table C.2: Absolute detection efficiencies as determined from the PTB Monte-Carlo code with a pulse-height threshold of $\frac{1}{3}\times$Cs.

Energy	Efficiency	Energy	Efficiency	Energy	Efficiency
0.70	0.0457	3.50	0.3705	6.80	0.2921
0.80	0.1137	3.60	0.3634	7.00	0.2841
0.90	0.1492	3.70	0.3657	7.20	0.2772
1.00	0.2270	3.80	0.3620	7.40	0.2771
1.10	0.2839	3.90	0.3631	7.60	0.2699
1.20	0.3300	4.00	0.3597	7.80	0.2705
1.30	0.3580	4.10	0.3561	8.00	0.2705
1.40	0.3698	4.20	0.3593	8.20	0.2626
1.50	0.3811	4.30	0.3532	8.40	0.2625
1.60	0.3981	4.40	0.3528	8.60	0.2538
1.70	0.3954	4.50	0.3516	8.80	0.2543
1.80	0.4037	4.60	0.3471	9.00	0.2492
1.90	0.4083	4.70	0.3413	9.20	0.2426
2.00	0.4048	4.80	0.3364	9.40	0.2435
2.10	0.4028	4.90	0.3370	9.60	0.2401
2.20	0.4026	5.00	0.3317	9.80	0.2399
2.30	0.3974	5.10	0.3307	10.00	0.2396
2.40	0.4018	5.20	0.3266	10.20	0.2371
2.50	0.3966	5.30	0.3211	10.40	0.2350
2.60	0.3951	5.40	0.3210	10.60	0.2367
2.70	0.3918	5.50	0.3184	10.80	0.2322
2.80	0.3860	5.60	0.3102	11.00	0.2307
2.90	0.3820	5.70	0.3075	11.20	0.2251
3.00	0.3850	5.80	0.3042	11.40	0.2255
3.10	0.3769	5.90	0.3028	11.60	0.2209
3.20	0.3767	6.20	0.2974	11.80	0.2234
3.30	0.3745	6.40	0.2908	12.00	0.2233
3.40	0.3744	6.60	0.2906		

Table C.3: Absolute detection efficiencies as determined from the PTB Monte-Carlo code with a pulse-height threshold of $\frac{1}{4}\times$Cs.

Bibliography

[Alt94] E.O. Alt and M. Rauh. *Proton-Induced Deuteron Breakup Reaction $^2H(p,pp)n$.* Few-Body Systems, **17**(1994) 121–162. 22

[Axi43] B.M. Axilrod and E. Teller. *Interaction of the van der Waals Type Between Three Atoms.* Journal of Chemical Physics, **11**(1943) 299. 5, 7

[Bel70] R.J. Bell. *Multipolar Expansion for the Non-Additive Third-Order Interaction Energy of Three Atoms.* Journal of Physics, **B3**(1970) 751–762. 7

[Bha39] H.J. Bhabha. Nature, **143**(1939) 276. 28

[Bjo64] J.D. Bjorken and S.D. Drell. *Relativistic Quantum Mechanics.* McGraw-Hill, 1964. 31

[Bom01] J.M. Bomont, J.L. Bretonnet, and M.A. van der Hoef. *Comparison Between Integral Equation Method and Molecular Dynamics Simulation for Three-Body Forces: Application to Supercritical Argon.* Journal of Chemical Physics, **114**(2001) 5674–5681. 8

[Bre36] G. Breit and E. Feenberg. *The Possibility of the Same Form of Specific Interaction for All Nuclear Particles.* Physical Review, **50**(1936) 850–856. 41

[Car83] J. Carlson, V.R. Pandharipande, and R.B. Wiringa. *Three-Nucleon Interaction in 3-, 4- and Infinity-Body Systems.* Nuclear Physics, **A401**(1983) 59–85. 11

[Car93] J. Carlson, V.R. Pandharipande, and R. Schiavilla. *Variational Monte Carlo Calculations of ^3H and ^4He with a Relativistic Hamiltonian.* Physical Review, **C47**(1993) 484–497. 10, 11

[Cas98] C. Caso et al. *Review of Particle Physics. Particle Data Group.* European Physical Journal, **C3**(1998) 1–794. 34, 40

[Che86] C.R. Chen, G.L. Payne, J.L. Friar, and B.F. Gibson. *Faddeev Calculations of the 2π-3N Force Contribution to the ^3H Binding Energy.* Physical Review, **C33**(1986) 1740–1752. 11

[Coe83] H.T. Coelho, T.K. Das, and M.R. Robliotta. *Two-Pion-Exchange Three-Nucleon Force and the ^3H and ^3He Nuclei.* Physical Review, **C28**(1983) 1812–1828. 11

[Coo79] S.A. Coon, M.D. Scadron, P.C. McNamee, B.R. Barrett, D.W.E. Blatt, and B.H.J. McKellar. *The Two-Pion-Exchange Three-Nucleon Potential and Nuclear Matter.* Nuclear Physics, **A317**(1979) 242–278. 11, 63, 186

[Coo93] S.A. Coon and M.T. Peña. *Momentum and Coordinate Space Three-Nucleon Potentials.* Physical Review, **C48**(1993) 2559–2575. 11, 63, 186

[Dan88] J.M.A. Danby. *Fundamentals of Celestial Mechanics.* Willmann-Bell, Inc., 1988. 3

[Die82] G. Dietze and H. Klein. *NRESP4 and NEFF4 Monte Carlo Codes for the Calculation of Neutron Response Functions and Detection Efficiencies for NE 213 Scintillation Detectors.* Physikalisch-Technische Bundesanstalt, Bundesallee 100, W-3300 Braunschweig, 1982. 220

[Dro78] M. Drosg. *Unified Absolute Differential Cross Sections for Neutron Production by the Hydrogen Isotopes for Charge-Particle Energies Between 6 and 17 MeV.* Nuclear Science and Engineering, **67**(1978) 190–220. 73

[Dum83] O. Dumbrajs, R. Koch, H. Pilkuhn, G.C. Oades, H. Behrens, J.J. de Swart, and P. Kroll. *Compilation of Coupling Constants and Low-Energy Parameters: 1982 Edition.* Nuclear Physics, **B216**(1983) 277–335. 43

[Fad61] L.D. Faddeev. *Scattering Theory for a Three-Particle System.* Journal of Experimental and Theoretical Physics (U.S.S.R.), **12**(1961) 1014–1019. 25, 52

[Fad65] L.D. Faddeev. *Mathematical Aspects of the Three-Body Problem in the Quantum Scattering Theory.* Israel Program for Scientific Translations, 1965. 52

[Fee35] E. Feenberg and J.K. Knipp. *Intranuclear Forces.* Physical Review, **48**(1935) 906–912. 41

[Fin87] E. Finckh, K. Geissdörfer, R. Lin, S. Schindler, and J. Strate. *Method for Data Analysis of Three Particle Experiments by Monte Carlo Simulation.* Nuclear Instruments and Methods in Physics Research, **A262**(1987) 441–443. 121

[For85] F. Foroughi, H. Vuilleme, P. Chatelain, Ch. Nussbaum, and B. Favier. *Proton Analysing Power and Cross Section Measurement in the d(p,2p)n Reaction for a Configuration Favouring Three-Nucleon Forces.* Journal of Physics G (Nuclear Physics), **11**(1985) 59–68. 22

[Fri83] J.L. Friar. *Three-Body Forces.* In H.O. Meyer, editor, *AIP Conference Proceedings*, volume 97, pages 378–389, 1983. Proceedings of the Conference on The Interaction Between Medium Energy Nucleons in Nuclei. 10

[Fri95] J. L. Friar, G. L. Payne, W. Glöckle, D. Hüber, and H. Witała. *Benchmark Solutions for n-d Breakup Amplitudes.* Physical Review C, **51**(1995) 2356–2359. 62

[Geb93] K. Gebhardt, W. Jäger, C. Jeitner, M. Vitz, E. Finckh, T.N. Frank, Th. Januschke, W. Sandhas, and H. Haberzettl. *Experimental and Theoretical Investigation of the ^2H(n,nnp) Reaction and of the Neutron-Neutron Scattering Length.* Nuclear Physics, **A561**(1993) 232–250. v, 1, 19, 21, 202, 205

[Gib88] B.F. Gibson and B.J.H. McKellar. *The Three-Body Force in the Trinucleons.* Few-Body Systems, **3**(1988) 143–170. 10, 11

[Glö83] W. Glöckle. *The Quantum Mechanical Few-Body Problem.* Springer-Verlag, 1983. 61, 62

[Glö96] W. Glöckle, H. Witała, D. Hüber, , H. Kamada, and J. Golak. *The Three-Nucleon Continuum: Achievements, Challenges and Applications.* Physics Reports, **274**(1996) 107–285. 9, 19, 25, 37, 52, 53, 54, 56, 57, 59, 63, 109, 206

[Gon97] D.E. González Trotter. *Extraction of the $^1S_0$ Neutron-Neutron Scattering Length from a Kinematically Complete N-D Breakup Experiment.* Ph.D. thesis, Duke University, 1997. 76, 124, 220, 222

[Gon99] D.E. González Trotter, F. Salinas, Q. Chen, A.S. Crowell, W. Glöckle, C.R. Howell, C.D. Roper, D. Schmidt, I. Šlaus, H. Tang, W. Tornow, R.L. Walter, H. Witała, and Z. Zhou. *New Measurement of the $^1S_0$ Neutron-Neutron*

Scattering Length Using the Neutron-Proton Scattering Length as a Standard. Physical Review Letters, **83**(1999) 3788–3791. 43, 180, 206

[Gro96] R. Großman, G. Nitzsche, H. Patberg, L. Sydow, S. Vohl, H. Paetz gen. Schieck, J. Golak, H. Witała, W. Glöckle, and D. Hüber. *Low Energy Proton-Deuteron Versus Neutron-Deuteron Breakup in Four Configurations: Implications for Coulomb-Force Effects*. Nuclear Physics, **A603**(1996) 161–175. 19, 21

[Gua99] E. Guarini, G. Casanova, U. Bafile, and F. Barocchi. *Structure of Gaseous Kr in the Low-q region by Neutron Scattering and Interaction Potentials*. Physical Review, **E60**(1999) 6682–6690. 8

[How84] C. R. Howell. *Neutron Scattering from ^{28}Si and ^{32}S: Cross Sections and Analyzing Powers from 8 to 40 MeV*. Ph.D. thesis, Duke University, 1984. 76

[How98] C.R. Howell, Q. Chen, T.S. Carman, A. Hussein, W.R. Gibbs, B.F. Gibson, G. Mertens, C.F. Moore, C. Morris, A. Obst, E. Pasyuk, C.D. Roper, F. Salinas, I. Šlaus, S. Sterbenz, W. Tornow, R.L. Walter, C.R. Whiteley, and M. Whitton. *Toward a Resolution of the Neutron-Neutron Scattering-Length Issue*. Physics Letters, **B444**(1998) 252–259. 43

[How01] C.R. Howell. *Nucleon-Deuteron Breakup: Truths and Implications*. Nuclear Physics, **A689**(2001) 298c–307c. 204

[Hüb98] D. Hüber and J.L. Friar. *The A_y Puzzle and the Nuclear Force*. Physical Review, **C58**(1998) 674–685. 13, 15

[Huh00] V. Huhn, L. Wätzold, Ch. Weber, A. Siepe, W. von Witsch, H. Witała, and W. Glöckle. *New Investigation of the Neutron-Neutron and Neutron-Proton Final-State Interaction in the n-d Breakup Reaction*. Physical Review, **C63**(2000) 014003. 206

[Kie94] A. Kievsky, M. Viviani, and S. Rosati. *Study of Bound and Scattering States in 3-Nucleon Systems*. Nuclear Physics, **A577**(1994) 511–527. 37

[Kie95] A. Kievsky, M. Viviani, and S. Rosati. *Cross Section, Polarization Observables, and Phase-Shift Parameters in p-d and n-d Elastic Scattering*. Physical Review, **C52**(1995) R15–R19. 15

[Klo73] W.M. Kloet and J.A. Tjon. *A Study of Break-up Processes in Neutron-Deuteron Scattering*. Nuclear Physics, **A210**(1973) 380–396. 1, 16, 19

[Koi86] Y. Koike and Y. Taniguchi. *3-Body Calculation of Neutron-Deuteron Elastic-Scattering in the Energy Region from 2.5 MeV up to 50 MeV*. Few-Body Systems, **1**(1986) 13–36. 197, 207

[Leo94] W.R. Leo. *Techniques for Nuclear and Particle Physics Experiments*. Springer-Verlag, 1994. 82, 83, 84, 89

[Li98a] G.Q. Li and R. Machleidt. *Charge Asymmetry of the Nucleon-Nucleon Interaction*. Physical Review, **C58**(1998) 1393–1402. 43

[Li98b] G.Q. Li and R. Machleidt. *Charge Dependence of the Nucleon-Nucleon Interaction*. Physical Review, **C58**(1998) 3153–3162. 44

[Lip50] B.A. Lippmann and J. Schwinger. *Variational Principles for Scattering Processes. I*. Physical Review, **79**(1950) 469–480. 49

[Mac86] R. Machleidt. In M.B. Johnson and A. Picklesimer, editors, *Relativistic Dynamics and Quark-Nuclear Physics*, page 71, 1986. 34

[Mac87] R. Machleidt, K. Holinde, and Ch. Elster. *The Bonn Meson-Exchange Model for the Nucleon-Nucleon Interaction*. Physics Reports, **149**(1987) 1–89. 36, 39

[Mac89] R. Machleidt. *The Meson Theory of Nuclear Forces and Nuclear Structure*. Advances in Nuclear Physics, **19**(1989) 189–376. 27, 30, 31, 32, 35, 37, 41, 205

[Mac96] R. Machleidt, F. Sammarruca, and Y. Song. *Nonlocal Nature of the Nuclear Force and Its Impact on Nuclear Structure*. Physical Review, **C53**(1996) R1483–R1487. 10, 45, 46, 47

[Mac00] R.A. Macri, S. Churchwell, B.J. Crowe III, A.S. Crowell, C.R. Howell, E.M. Neidel, R.S. Pedroni, I. Šlaus, W. Tornow, R.L. Walter, and H. Witała. *Preliminary Analysis for the Space-Star Configurations at 10.3 and 13.0 MeV*. TUNL Progress Report, **XXXIX**(1999-2000) 24–27. 203

[Mac01] R. Machleidt. *High-Precision, Charge-Dependent Bonn Nucleon-Nucleon Potential*. Physical Review, **C63**(2001) 024001. 39, 40, 43, 44, 45, 109, 178

[Mai81] G.C. Maitland, M. Rigby, E.B. Smith, and W.A. Wakeham. *Intermolecular Forces: Their Origin and Determination*. Oxford University Press, 1981. 5, 6, 7

[Mar90] C. Marchal. *The Three-Body Problem*. Elsevier Science Publishers, 1990. 4

[McA94] J.E. McAninch, L.O. Lamm, and W. Haeberli. *Analyzing Power in Neutron-Deuteron Elastic Scattering at $E_l^n ab$ = 3 MeV*. Physical Review, **C50**(1994) 589–601. 14

[Mil90] G.A. Miller, B.M.K. Nefkens, and I. Šlaus. *Charge Symmetry, Quarks and Mesons*. Physics Reports, **194**(1990) 1–116. 43

[Nog97] A. Nogga, D. Hüber, H. Kamada, and W. Glöckle. *Triton Binding Energies for Modern NN Forces and the π-π Exchange Three-Nucleon Force*. Physics Letters, **B409**(1997) 19–25. 12

[Nog00] A. Nogga, H. Kamada, and W. Glöckle. *Modern Nuclear Force Predictions for the α Particle*. Physical Review Letters, **85**(2000) 944–947. 47

[Pat96] H. Patberg, R. Großman, G. Nitzsche, L. Sydow, S. Vohl, H. Paetz gen. Schieck, J. Golak, H. Witała, W. Glöckle, and D. Hüber. *Deuteron Breakup Reaction $^2H(\vec{p},pp)n$ Induced by Polarized Protons at E_p = 19.0 MeV*. Physical Review, **C53**(1996) 1497–1505. 19, 21

[Pre75] M.A. Preston and R.K. Bhaduri. *Structure of the Nucleus*. Addison-Wesley, 1975. 50

[Pre92] W.H. Press, S.A. Teukolsky, W.T. Vetterling, and B.P. Flannery. *Numerical Recipes in FORTRAN: The Art of Scientific Computing*. Cambridge University Press, 1992. 128

[Pri39] H. Primakoff and T. Holstein. *Many-Body Interactions in Atomic and Nuclear Systems*. Physical Review, **55**(1939) 1218–1234. 2

[Rau91] G. Rauprich, S. Lemaître, P. Niessen, K.R. Nyga, R. Reckenfelderbäumer, L. Sydow, H. Paetz gen. Schieck, H. Witała, and W. Glöckle. *Study of the Kinematically Complete Breakup Reaction $^2H(\vec{p},pp)n$ at E_p = 13.0 MeV with Polarized Protons*. Nuclear Physics, **A535**(1991) 313–330. 19, 21

[Rob86] M.R. Robliotta and H.T. Coelho. *Taming the Two-Pion-Exchange Three-Nucleon Potential*. Nuclear Physics, **A460**(1986) 645–674. 11

[Rup92] G. Rupp and J.A. Tjon. *Bethe-Salpeter Calculation of Three-Nucleon Observables with Multirank Separable Interactions*. Physical Review, **C45**(1992) 2133–2142. 10, 11

[Sal98] F. Salinas Meneses. *Use of the $^1S_0$ Neutron-Proton Scattering Length as a Probe for Three-Nucleon Forces*. Ph.D. thesis, Duke University, 1998. 76, 124, 150, 175, 180, 220, 222

[Sch86] R. Schiavilla, V.R. Pandharipande, and R.B. Wiringa. *Momentum Distributions in A=3 and 4 Nuclei*. Nuclear Physics, **A449**(1986) 219–242. 11

[Set94] H. R. Setze. *Differential Cross Section for the Neutron-Induced Deuteron Breakup Reaction at E_n = 13.0 MeV*. Ph.D. thesis, Duke University, 1994. 73, 76, 124

[Set96] H.R. Setze, C.R. Howell, W. Tornow, R.T. Braun, W. Glöckle, A.H. Hussein, J.M. Lambert, G. Mertens, C.D. Roper, F. Salinas, I. Šlaus, D.E. González Trotter, B. Vlahović, R.L. Walter, and H. Witała. *Verification of the Space-Star Anomaly in nd Breakup*. Physics Letters, **B388**(1996) 229–234. v, 1, 19, 21, 22, 154, 175, 202, 205

[Sie95] P.J. Siemens and A.P. Vischer. *Covariant Phenomenological Field-Theory for Extended Hadrons*. Annals of Physics, **238**(1995) 167–199. 47

[Sit91] A.G. Sitenko. *Scattering Theory*. Springer-Verlag, 1991. 51

[Ste89] M. Stephan, K. Bodek, J. Krug, W. Lübcke, S. Obermanns, H. Rühl, M. Steinke, D. Kamke, H. Witała, Th. Cornelius, and W. Glöckle. *Neutron-Induced Deuteron Breakup Cross Section at 10.3 MeV*. Physical Review, **C39**(1989) 2133–2137. v, 1, 19, 21, 202, 205

[Sto94] V.G.J. Stoks, R.A.M. Klomp, C.P.F. Terheggen, and J.J. de Swart. *Construction of High-Quality NN Potential Models*. Physical Review, **C49**(1994) 2950–2962. 10

[Str89] J. Strate, K. Geissdörfer, R. Lin, W. Bielmeier, J. Cub, A. Ebneth, E. Finckh, H. Friess, G. Fuchs, K. Gebhardt, and S. Schindler. *Differential Cross Section of the ^{2}H(n,nnp) Reaction at E_n = 13 MeV*. Nuclear Physics, **A501**(1989) 51–85. v, 1, 19, 21, 22, 202, 205

[Tak51] M. Taketani, S. Nakamura, and M. Sasaki. *On the Method of the Theory of Nuclear Forces*. Progress of Theoretical Physics, **VI**(1951). 30

[Tjo81] J.A. Tjon. *The Three and Four Nucleon Systems (Theory)*. Nuclear Physics, **A353**(1981) 47c–60c. 15

[Tor86] W. Tornow, W. Arnold, J. Herdtweck, and G. Mertens. *Measurement of the Response of the Deuterated Scintillators NE 232 and NE 230 to Protons and Deuterons*. Nuclear Instruments and Methods in Physics Research, **A244**(1986). 156

[Tor96] W. Tornow, H. Witała, and R.T. Braun. *Determinations of the Neutron-Neutron Scattering Length a_{nn} from Kinematically Incomplete Neutron-Deuteron Breakup Data Revisited.* Few-Body Systems, **21**(1996) 97–130. 206

[Tor98] W. Tornow, H. Witała, and A. Kievsky. *Do Phase-Shift Analyses and Nucleon-Nucleon Potential Models Yield the Wrong ^3P_j Phase Shifts at Low Energies?* Physical Review, **C57**(1998) 555–561. 13

[Wig33] E. Wigner. *On the Mass Defect of Helium.* Physical Review, **43**(1933) 252–257. 27

[Wir84] R.B. Wiringa, R.A. Smith, and T.L. Ainsworth. *Nucleon-Nucleon Potentials With and Without $\delta(1232)$ Degrees of Freedom.* Physical Review, **C29**(1984) 1207–1221. 37

[Wir95] R.B. Wiringa, V.G.J. Stoks, and R. Schiavilla. *Accurate Nucleon-Nucleon Potential with Charge-Independence Breaking.* Physical Review, **C51**(1995) 38–51. 10

[Wit88] H. Witała, Th. Cornelius, and W. Glöckle. *Faddeev Calculations with Meson-Exchange N-N Interactions for the n-d Break-Up Process.* Few-Body Systems, **5**(1988) 89–105. 1, 15, 16

[Wit89] H. Witała, W. Glöckle, and Th. Cornelius. *Rigorous Faddeev Calculations for Elastic Neutron-Deuteron Scattering Around 8 MeV c.m. Energy.* Nuclear Physics, **A491**(1989) 157. 13, 150, 153, 174

[Wit91] H. Witała and W. Glöckle. *The Analysing Power in Elastic Nucleon-Deuteron Scattering. Information on Two-Nucleon ^3P Forces?* Nuclear Physics, **A528**(1991) 48–72. 13

[Wit94] H. Witała, D. Hüber, and W. Glöckle. *Analyzing Power Puzzle in Low Energy Elastic Nd Scattering.* Physical Review, **C49**(1994) R14–R16. 15

[Wit01] H. Witała, 2001. Private Communication. 14, 63, 203

[Woo93] S.A. Wood and W.A.Watson III. In D. Axen and R. Poutissou, editors, *Conference Record of the Eighth Conference on Real-Time Computer Applications in Nuclear, Particle, and Plasma Physics*, page 60, 1993. 129

[Yuk35] H. Yukawa. *Interaction of Elementary Particles.* Proceedings of the Physico-Mathematical Society of Japan, **17**(1935) 48–57. 28

[Zej97] J. Zejma, M. Allet, K. Bodek, J. Lang, R. Müller, S. Navert, O. Naviliat-Cuncic, J. Sromicki, E. Stephan, L. Jarczyk, St. Kistryn, J. Smyrski, A. Strzałkowski, W. Glöckle, J. Golak, D. Hüber, H. Witała, and P.A. Schmelzbach. *Cross Sections and Analyzing Powers A_y in the Breakup Reaction $^2H(\vec{p},pp)n$ at 65 MeV: Star Configurations.* Physical Review, **C55**(1997) 42–56. 22

[Zho01] Z. Zhou, A.S. Crowell, J. Deng, W. Glöckle, C.R. Howell, H. Kamada, B. Qi, R.A. Macri, X. Ruan, H. Tang, R.L. Walter, and H. Witała. *The Space-Star Anomaly in nd Breakup at 25 MeV.* Nuclear Physics, **A684**(2001) 545c–548c. 203, 205

Biography

Alexander Sheffield Crowell

Personal

- Born in Kingsport, TN on March 8, 1971

Education

- B.S. Physics and Mathematics, Wake Forest University Winston-Salem, NC, 1993
- A.M. Physics, Duke University, Durham, North Carolina, 1996

Positions

- Teaching Assistant, Duke University, 1993-1995
- Research Assistant, Duke University, TUNL, 1995-2001
- UNIX Systems Administrator, TUNL, 2000-2001

Honors

- James B. Duke Graduate Fellowship, Duke University, 1993-2001

Publications

D.E. González Trotter, F. Salinas, Q. Chen, A.S. Crowell, W. Glöckle, C.R. Howell, C.D. Roper, D. Schmidt, I. Šlaus, H. Tang, W. Tornow, R.L. Walter, H. Witała, and Z. Zhou. *New Measurement of the $^1S_0$ Neutron-Neutron Scattering Length Using the Neutron-Proton Scattering Length as a Standard.* Physical Review Letters, **83**(1999) 3788–3791.

Z. Zhou, A.S. Crowell, J. Deng, W. Glöckle, C.R. Howell, H. Kamada, B. Qi, R.A. Macri, X. Ruan, H. Tang, R.L. Walter, and H. Witała. *The Space-Star Anomaly in nd Breakup at 25 MeV.* Nuclear Physics, **A684**(2001) 545c–548c.

C.R. Howell, Q. Chen, D.E. González Trotter, F. Salinas, T.S. Carman, A.S. Crowell, A. Hussein, W.R. Gibbs, B.F. Gibson, G. Mertens, C.F. Moore, C. Morris, A. Obst, E. Pasyuk, C.D. Roper, I. Šlaus, S. Sterbenz, H. Tang, W. Tornow, R.L. Walter, C.R. Whiteley, M. Whitton, Z. Zhou, W. Glöckle, and H. Witała. *Recent High-Accuracy Measurements of the $^1S_0$ Neutron-Neutron Scattering Length.* Few-Body Systems Supplementum, **12**(2000) 451–456.